Study of Sun-like G Stars and Their Exoplanets

Submitted in partial fulfillment of the requirements for the degree of

Doctor of Philosophy

by

Mr. SHASHANKA R. GURUMATH

VIT®

Vellore Institute of Technology

(Deemed to be University under section 3 of UGC Act, 1956)
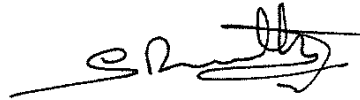
May, 2019

DECLARATION

I here by declare that the thesis entitled "Study of Sun-like G Stars and Their Exoplanets" submitted by me, for the award of the degree of *Doctor of Philosophy* to Vellore Institute of Technology, Vellore is a record of bonafide work carried out by me under the supervision of Prof. V. Ramasubramanian, Department of Physics, School of Advanced Sciences (SAS), Vellore Institute of Technology, Vellore, and Prof. K. M. Hiremath, Indian Institute of Astrophysics (IIA), Bengaluru.

I further declare that the work reported in this thesis has not been submitted and will not be submitted, either in part or in full, for the award of any other degree or diploma in this institute or any other institute or university.

Place: Vellore

Date: 13.05.2019

Signature of the Candidate

CERTIFICATE

This is to certify that the thesis entitled "Study of Sun-like G Stars and Their Exoplanets" submitted by Mr. SHASHANKA R. GURUMATH, Department of Physics, School of Advanced Sciences (SAS), Vellore Institute of Technology, Vellore for the award of the degree of *Doctor of Philosophy*, is a record of bonafide work carried out by him under our supervision, as per the Vellore Institute of Technology code of academic and research ethics.

The contents of this report have not been submitted and will not be submitted either in part or in full, for the award of any other degree or diploma in this institute or any other institute or university. The thesis fulfills the requirements and regulations of the University and in our opinion meets the necessary standards for submission.

Place: Vellore

Date: 13·05·2019

Signature of the Guides

(Dr. V. Ramasubramanian)

(Dr. K. M. Hiremath)

ABSTRACT

By employing exoplanetary physical and orbital characteristics, aim of this study is to understand the genesis, dynamics, chemical abundance and magnetic field structure of Sun-like G stars and relationship with their planets. With reasonable constraints on selection of exoplanetary physical characteristics, and by making corrections for stellar rate of mass loss, a power law relationship between initial stellar mass and their exoplanetary mass is obtained that suggests *massive stars harbor massive planets*. Such a power law relationship is exploited to estimate the initial mass (1.060 ± 0.006) $M_\odot$ of the Sun for possible solution of "Faint young Sun paradox" which indeed indicates slightly higher mass compared to present mass. Another unsolved puzzle of solar system is angular momentum problem, viz., compare to Sun most of the angular momentum is concentrated in the solar system planets. By analyzing the exoplanetary data, this study shows that orbital angular momentum of Solar system planets is higher compared to orbital angular momentum of exoplanets. This study also supports the results of Nice and Grand Tack models that propose the idea of outward migration of Jovian planets during early history of Solar system formation. Furthermore, we have examined the influence of stellar metallicity on the host stars mass and exoplanetary physical and orbital characteristics that shows a non-linear relationship. Another important result is most of the planets in single planetary stellar systems are captured from the space and/or inward migration of planets might have played a dominant role in the final architecture of single planetary stellar systems. Finally, with the host star chromospheric activity as a magnetic field proxy, following problems are investigated. At the present epoch, influence of planetary mass on the host star's magnetic activity is examined and it is found that host star's magnetic activity is independent of any planetary mass present in the vicinity of the host star. At the early epoch of planetary formation, the role of large-scale magnetic field on the planetary formation is examined which suggests that strong magnetic field inhibits more concentration of planetary mass in the protoplanetary disk.

Keywords: *Exoplanets*, *Sun*, *Solar system*, *stars:evolution*.

ACKNOWLEDGEMENT

life.

Last but not least, I wish to extend my profound sense of gratitude to **my parents - Prof. Renukaradhya Gurumath and Mrs. Kavita Gurumath, brother-Someshwar, sister-Manasa** and **all my family members** for all the sacrifices they made during my research and also providing me endless encouragement, moral and financial support. They have been an inspiration in every way.

Place: Vellore

Date: 13·05·2019

SHASHANKA R. GURUMATH

iii

TABLE OF CONTENTS

LIST OF FIGURES

LIST OF TERMS AND ABBREVIATIONS

CHAPTER 1

Introduction

The bright dots (mostly stars) in the sky of a dark night remained the source of curiosity till today. It is a source of inspiration that study of these bright dots (stars) is one of the oldest science in the world, known as Astronomy. In the olden days, due to apparent revolution of all these stars and Solar system planets in the celestial sphere, many scientists like Aristotle, Ptolemy and Aryabhata proposed the geocentric models. According to geocentric model, Earth is at the center of the universe and all other objects revolve around it. In 15th century, Nicolaus Copernicus, a Poland mathematician and astronomer revised the geocentric model by proposing Heliocentric model. According to heliocentric model, Sun is at the center of the universe and all other objects including Earth revolve around it. However, this new model is less welcomed during his period. Within a century after Nicolaus, his successors Tycho Brahe and Johannes Kepler studied the motion of planets in the sky. From the observed data, Kepler proposed three fundamental laws of planetary motion that accurately describe the motion of planets around the Sun. Successively, the Galileo Galilei, in late 16th century, was the first person to observe the celestial bodies through a telescope, invented by him. He discovered four moons of the Jupiter and stated that not all the celestial objects revolve around Sun, instead, there are many local binary and multi-systems like Earth-moon systems. Since then, the use of telescope revolutionized the understanding of astronomy as a whole. However, we waited almost 400 years after the discovery of telescope to detect planets outside the Solar system, that are commonly known as *Exoplanets*. Before understanding details of exoplanets that orbit around other stars, one has to better understand the nearest star, the Sun and the objects that orbit around it. Hence, in this chapter, we dis-

cuss and understand about the physical and dynamical characteristics of Sun and Solar system objects.

1.1   Solar System

Solar system is the home for us in this vast universe. It resides in the Milky Way galaxy approximately 8 kpc from the center of galaxy. The Solar system revolves around the galactic center with a speed of $\sim$ 230 km/s. Solar system consists of a star i.e., Sun, eight planets and thousands of other objects viz., asteroids, comets and dwarf planet that are revolving around the Sun. According to physical characteristics, eight planets of the Solar system are classified into terrestrial and Jovian/giant planets. The first four planets are categorized as terrestrial and next four are categorized as Jovian planets. These two classes of planets are separated by a belt of small objects known as *asteroids belt*. Radius of the Solar system is approximately to be $\sim$ 100 Astronomical Unit (AU) (1 AU = 1.4959 x 10^{11} m, which is the distance between Sun and Earth), because beyond that region the strength of Sun's gravitational force decreases. Most of the system's mass ($\sim$ 99%) is concentrated at the central object i.e., Sun, and majority of remaining mass is distributed in the planets. Let us understand the physical and chemical properties of the Sun in details.

1.2   The Sun

Sun is a main sequence star that belongs to a spectral class G2. It is formed around 4.5 billion years ago by gravitational collapse of inter stellar clouds of gas and dust particles. Due to the presence of high atomic number elements in the Solar system like Gold, Uranium, etc., it is believed that formation of Sun is triggered by the shockwaves that were due to explosion of nearby supernovae. As a result, cloud collapsed, the central object gained more mass and rest of the material formed a disk like structure around the Sun, where the planets are supposed to be formed. Due to more mass, the Sun's core experiences high pressure and high temperature, that triggers the nuclear fusion at core. Hence, presently by converting the Hydrogen into Helium through proton-proton

cycle, Sun produces the different forms of energy (heat, light and other radation). It is to be noted that nucleosynthesis occurs only in the core of the Sun, because temperature, pressure and density decreases as we move away from the center of the Sun. Figure 1.1 illustrates the radial variation of temperature, pressure, density and luminosity from Sun's center to its surface. Hence, the vertical cross section of the Sun (Figure 1.2) shows that it has different envelops at its interior with different physical and chemical properties that vary from surface to center.
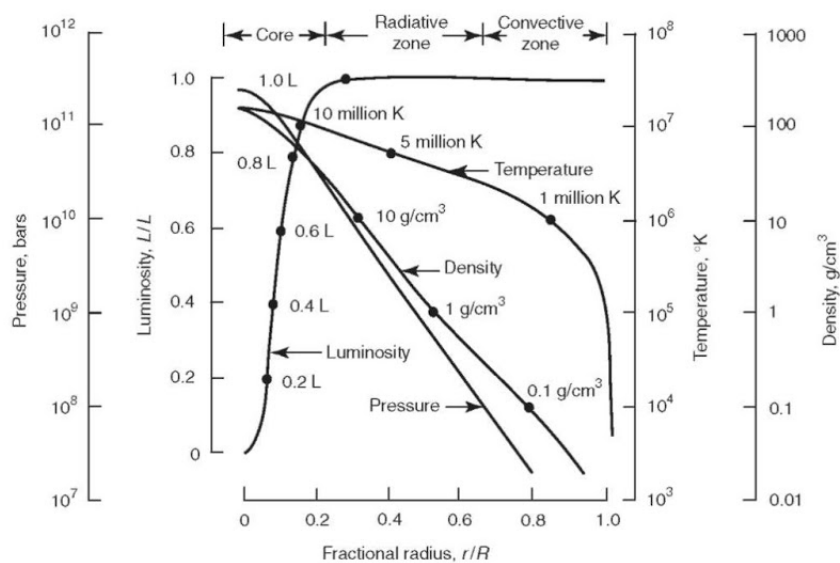
Fig. 1.1 Illustrates the Radial Variation of Temperature, Pressure, Density and Luminosity in the Interior of the Sun From Its Center to Surface. the X-Axis Represents the Fraction of Radius in Terms of Sun's Radius and Y-Axis Represents Different Physical Parameters. Image Credit: *http://what-when-how.com/space-science-and-technology/the-sun-as-a-star/*

1.2.1   Internal Structure of The Sun

Sun is a sphere of plasma that consists of hot gas in ionized state. Its radius is estimated to be $\sim 7 \times 10^8$ m. Figure 1.2 represents the internal structure of the Sun. Based on the different physical characteristics, the interior of Sun is classified into three main parts known as core, radiative zone and convection zone.
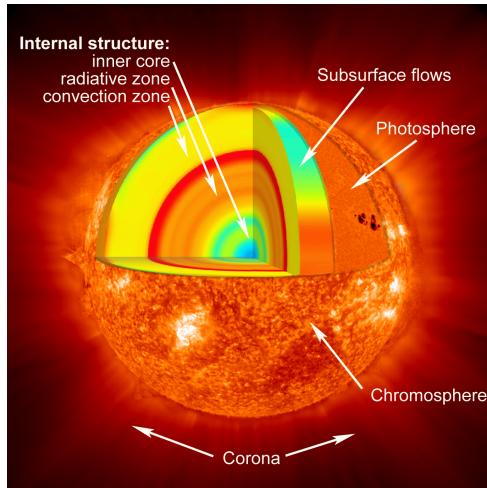
Fig. 1.2 Illustrates the Internal Structure and Atmosphere of the Sun. Image Credit: *http://web.utah.edu/astro/sun.html*

1.2.1.1 Core

Central part of the Sun is known as a *core* where majority of mass ($\geq 60\%$) is concentrated and its radius is estimated to be ~ 20 - 25% of the Sun's radius. Density at this region is estimated to be ~ 150 g/cm^3 and temperature is ~ 15 x 10^6 K. Due to high temperature and density in the radiative core, Hydrogen ions get more kinetic energy and colloid with each other to form the Helium. The process of conversion of Hydrogen into Helium is known as *proton-proton chain* or *p-p chain reaction*, which is graphically illustrated in Figure 1.3
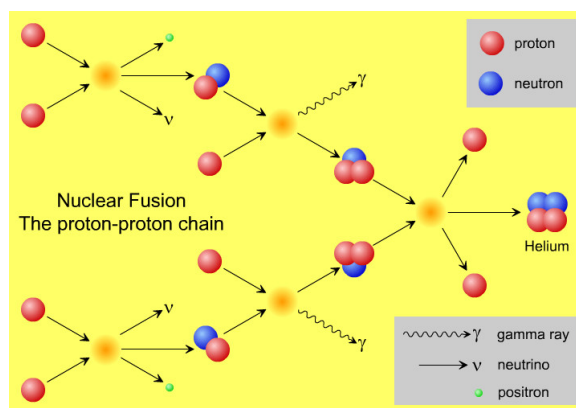
Fig. 1.3 Illustrates the Proton-Proton Cycle That Helps Us to Understand the Conversation of Hydrogen Into Helium. Image Credit: Randy Russell (Windows of the Universe Project).

At the beginning, two Hydrogen atoms combine to give a deuterium, positron (anti-

particle of the electron) and neutrino with a release of energy $\sim 1.4\ MeV$. The positron immediately combines with an electron and releases two gamma ray photons. Whereas, the neutrinos will escape from the Sun without interacting with any other particles. In the next stage, deuterium collides with a proton to form helium-3 with production of high energy photons of $\sim 6\ MeV$. In the last stage, two Helium-3 ions are combined to form a Helium atom with production of two protons/Hydrogen. Hence, in the entire process, four protons combine to form a Helium atom. The rate at which mass is converted into energy is $\sim 10^9$ kg/s. The energy produced in the core is transferred to the surface by radiative diffusion. Travel time of the light/photons from the Sun's radiative core to the surface is $\sim$ 20000-40000 years, this is mainly due to high density and large scattering with ions. However, few particles such as neutrinos, escape easily from the Sun because of their less interaction with other particles.

1.2.1.2 Radiative Zone

While moving away from the center of the Sun, region next to the core is known as *the radiative zone*. This zone almost covers the region between 0.25 - 0.75 solar radius. The temperature in this zone drops as we move towards the surface of the Sun. In the radiative zone, energy is transferred from higher temperature to lower temperature by collision of particles and electron/photon emission. Hence, the temperature gradient $(\frac{dT}{dr})$ is related to radiative flux (L_r) with an equation given by

$$\frac{dT}{dr} = -\frac{3K\rho}{16\sigma T^3}\frac{L}{4\pi r^2},\tag{1.1}$$

where c is speed of light, r is radius of star, ρ is the density and K is the mass absorption coefficient. The negative sign in the above equation indicates the temperature decreases as we move away from the center.

1.2.1.3 Convection Zone

The outer most layer of the Sun is known as *the convection zone*. In this region, the energy is transferred by the convection process. Energy transferred from the radiative zone to the base of the convective zone heats up the parcel of gas, that in-turn raises to-

wards the surface and expand and falls back by transferring energy to upper layers. With an assumption of the adiabatic movement of a parcel of gas, the temperature gradient $(\frac{dT}{dr})$ in case of convection zone is given by

$$\frac{dT}{dr} = \left(1 - \frac{1}{\gamma}\right) \frac{T}{P} \frac{dP}{dr},$$ (1.2)

where P is the pressure of gas and γ is adiabatic exponent (C_P/C_V) which is a ratio of the specific heat at constant pressure to constant volume.

1.2.2 Atmosphere of The Sun

Similar to the Earth, Sun has an atmosphere of hot gas which is extended to several solar radii above the photosphere. *Photosphere* is the inner most visible region of Sun, hence, it is also called as surface of the Sun. However, we don't find any solid surface except the boiling gas. Average temperature of the photosphere is $\sim$ 5770 K. The thickness of the photosphere is about 300 - 500 km. While observing the Sun, as we move from the center of the Sun's disk towards limb, the Sun appears to be dimmer and this phenomenon is known as *limb darkening*. This is due to the fact that as Sun rotates, light from the photosphere has to travel more distance in the Sun's atmosphere before it escape from the outer layers to reach the Earth. Due to rapid decrease in the temperature above the photosphere, photons get easily absorbed by the atoms at upper atmosphere. Hence, both the limbs appear to be darker compare to center of the Sun.

Since, photosphere is also known as the upper layer of convective zone, one can see the convection of hot gas bubbles via granulations formed in the photosphere. Figure 1.4 illustrates the typical image of granulations pattern in the photosphere. Bright center of each granulation indicates the raising of hot gas bubbles, whereas, dark lines at the boundary indicates the shrinking of cooled gas into the convection zone. In addition, many dark spots can also be found in the photosphere that usually appear in pairs known as *sunspots*. These spots appear dark because the temperature at these regions are less ($\sim$ 3500 K) than the ambient photospheric temperature. Details regarding these spots will be discussed in the following section 1.2.5.1.

The layer just above the photosphere is known as the *Chromosphere*. Due to its less

30   40   50   60

Photospheric granulation, G. Scharmer   Distance in units of
Swedish Vacuum Solar Telescope   1000 kilometers
10 July 1997
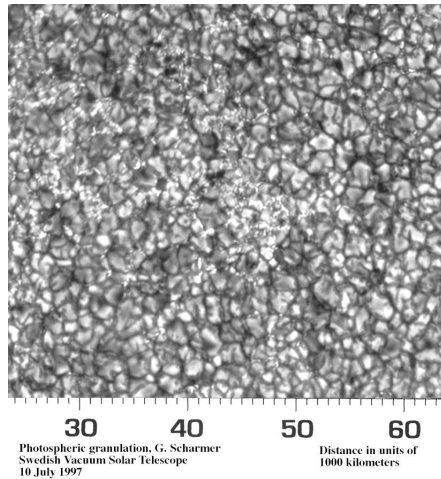
Fig. 1.4 Illustrates the Granulations That Are Observed in the Sun's Photosphere. Image Credit: Marshall Space Flight Center.

intense radiation compared to strongest radiation from the photosphere, one can not able to see it in normal conditions. However, during the period of total solar eclipses, one can able to see the chromosphere because, Moon completely blocks the light from the photosphere. The thickness of chromosphere is $\sim$ 4000 - 5000 km, and temperature varies from 4500 K (at the inner boundary) to 30000 K (at the out boundary). The spectrum of chromosphere shows many emission lines that belong to different elements. Hydrogen Balmer α line, at the wavelength 656.3 nm, is one of the prominent emission line among all. The origin of these emission lines in the chromosphere is due to Sun's magnetic activity that probably originates in the deep interior of the Sun.

Outer most layer of the Sun's atmosphere is known as *Corona* that extends around thousands of kilometers above the chromosphere and, can only be seen during the total solar eclipses. Corona is divided into two main parts, i.e., inner layer known as K corona and outer layer known as F corona. In the K corona, continuous spectrum is formed by the scattering of light. However, the spectrum from F corona shows the Fraunhofer absorption lines that are formed by the absorption of light from the dust particles. It is important to note that, in addition to absorption lines, one can also observe the strong emission lines in the spectrum that are produced from the hot plasma. The temperature of this plasma structure is estimated to be $\sim 10^6$ K and reason for this sudden jump in the temperature of the solar corona is not completely understood although many theories

were proposed to solve the reason behind the energy supply for coronal heating (Sakurai 2017). A typical image of corona is illustrated in Figure 1.5, where many magnetic activities occur, like coronal loops, flares, solar wind.
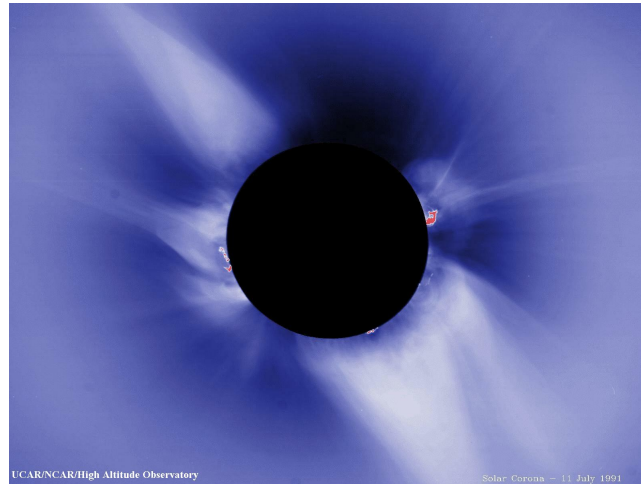
Fig. 1.5 Illustrates a Typical Image of Sun's Corona Observed by Using a Coronagraph. Image Credit: *https://solarscience.msfc.nasa.gov*

Fig. 1.6 Illustrates an Image of Sun's Dopplerogram. Image Credit: SOHO/MDI.

1.2.3 Solar Dynamics

Like any other celestial object, Sun also rotates about its own axis. The direction of Sun's rotation is same as the direction of planets orbital motion of the Solar system. Galileo Galilee is the first person to observe the Sun's rotation by tracing the Sunspots

over a period of time. Later, during early 19th century, it is discovered that Sun does not rotate like a solid body, instead its rotation changes with respect to latitude. This is because the Sun is a giant ball of hot gas and plasma. Near equator it takes about 24 days for one rotation about its own axis and rotation period increases with increasing latitude so that it takes about 36 days for one rotation near poles. The general equation that describes the differential rotation is given by

$$\omega = A + B \sin^2 \phi + C \sin^4 \phi, \tag{1.3}$$

where ω is rotation, A, B and C are the coefficients and, ϕ is latitude of the Sun's surface. Coefficients in the above equation are different for different detection techniques viz., tracing sunspots, magnetic features, coronal features, etc. In addition to tracing, one can also use the Doppler spectroscopy for measuring the Sun's rotation. The light from the receding side of Sun's surface is red shifted and light from the approaching side is blue shifted. Hence, by measuring the shift in the spectral lines, one can estimate the rotational velocity of Sun. Figure 1.6 illustrates a sample image of Sun's dopplerogram.

However, helioseismic inferences (following section 1.2.6) show that Sun's internal rotation is not same as its surface rotation. As we have already noticed in the Figure 1.1, Sun has different physical properties at different depths, mainly its mass and density is high at the center. Helioseismic inferences yield that Sun's core and radiative zone rotate like a rigid body and, differential rotation starts from the base of convection zone to the surface. The transition region between the rigid body rotation (radiative zone) and differential rotation (convection zone) is known as *tachocline*.

1.2.4 Chemical Abundances of The Sun

Before getting into the details of chemical composition of the Sun, let us understand identification of chemical elements in a star by using its spectrum. Due to high temperature, atoms are completely ionized in the Sun's interior. But as we move away from the center, ionized atoms will get neutralized due to decrease in temperature gradient. These neutral atoms absorb the light coming from the deep interior at a particular

wavelength that lead to the absorption lines in the spectrum.

Majority of composition of observable matter in the universe is Hydrogen and Helium. Hence, Sun's composition predominantly consists of these elements and is no different than composition of the universe. Whereas, Hydrogen and Helium are the only elements that are formed during early epoch of the *Big bang* of the universe. All other nuclei heavier than the helium (also called as metals by Astronomers) are produced in the cores of stars via nucleosynthesis. Hence, composition of most of the stars formed immediately after big-bang mainly consists of H and He and, these stars are known as *Population III* stars. *Population I and II* stars consist of chemically heavier elements than the *Population I* stars (Taketani et al. 1956). The higher elements in the stellar core are synthesized mainly due to the evolutionary nuclear chain reactions, viz., *proton-proton chain reaction, carbon cycle, Helium burning, Carbon burning, Oxygen burning, Silicon burning*, etc. Most of the elements higher than the Iron are formed by *neutron capture*. As the Sun is considered as a *Population I* star (G2 spectral class), in addition to H and He, it also consists of higher elements. There are almost 100 natural elements and more than 300 isotopes observed in the Solar system. Typical list of elements inferred from the Sun's spectrum is presented in the Table 1.1. It is interesting to be noted that the chemical abundance of the Sun's spectrum matches with the chemical composition of Asteroids and Meteorites, which suggests that the Sun and other objects of Solar system are formed from the same primordial clouds of gas and dust particles (Hayashi 1981).

Table 1.1 Chemical Abundance of the Sun

Element	% of total number of atoms	% of total mass
Hydrogen	91.2000	71.000
Helium	8.7000	27.100
Oxygen	0.0780	0.970
Carbon	0.0430	0.400
Nitrogen	0.0088	0.096
Silicon	0.0045	0.099
Magnesium	0.0038	0.076
Neon	0.0035	0.058
Iron	0.0030	0.140

1.2.5 Solar Cycle and Activity Phenomena

Although Sun appears to be quite, when one observes with a powerful telescope, its surface is full of many activity phenomena like sunspots, solar flares, coronal mass ejections, etc., that erupt from the surface and enter into interplanetary space. The source for all these activities is the magnetic field lines that are generated in the Sun's interior probably by a dynamo mechanism (Parker 1971). Let us study different activity phenomena that are occurring on the Sun.

1.2.5.1 Sunspots

Observations show that Sun is inherited by a large-scale weak magnetic field structure probably of primordial origin (Hiremath 1994, 2009, Hiremath and Gokhale 1995). Due to differential rotation of the Sun in the convection zone, the large scale magnetic field lines wound and due to buoyancy raise towards surface. These strong magnetic field lines inhibit significant amount of radiation emerging from the interior, which lead to decrease in temperature of the sunspot compared to the surrounding region. Hence, sunspots appear dark (Hathaway and Choudhary 2008). The strength of magnetic field of the sunspots is estimated to be $\sim$ 2000-3000 G. Generally, these spots appear in a pair with opposite magnetic polarities. The sunspot number changes with respect to time. Long term observation of number of sunspots suggests that they follow the sinusoidal behavior with approximately 11 year periodicity. This observed phenomenon is called the sunspot cycle. At the beginning of a cycle, sunspots appear near the latitude of $\pm 40^0$. As time progresses, these spots move towards equator. The shifting of sunspot belt with respect to different years is illustrated in Figure 1.7 which is known as *butterfly diagram*. After each sunspot cycle, the sign of magnetic field structure of Sun is flipped, which means Sun follows 22 year magnetic cycle also. The Figure 1.8 illustrates high resolution image of a sunspot obtained by Hinode space probe. One can notice from this picture that the central dark region in the sunspot is called as *umbra*, which is surrounded by a less dark region called as *penumbra*. The sizes of these sunspots are around 10000 km and, their lifetime varies from few days to several months depending on their size. There are few years in the 16th century when there was no sunspot activity.

This period of dearth of sunspot activity is called as *Maunder minimum*. However, origin of solar cycle and activity phenomena is not understood completely (Hiremath 1994, 2009).
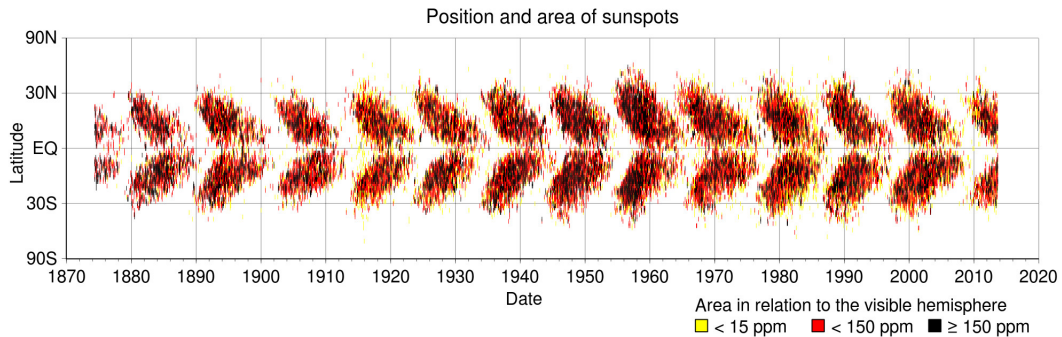
Fig. 1.7 Illustrates the Butterfly Diagram of Sunspots. the X-Axis Represents the Year and Y-Axis Represents the Sun's Latitude. Image Credit: NASA/Marshall Solar Physics.
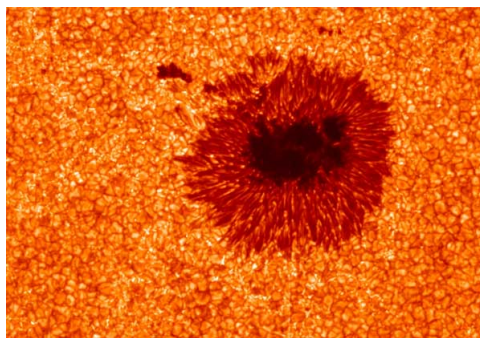
Fig. 1.8 Illustrates the Typical Image of a Sunspot. the Central Dark Region Is the *Umbra* Surrounded by Light Dark Region Known as *Penumbra*. Image Credit: Hinode Spacecraft.

1.2.5.2 Other Activity Phenomena

In addition to sunspot activity, other transient activity phenomena such as *flares, coronal mass ejection and prominences* originate from the Sun. A solar flare is a sudden burst of highly ionized gas from the Sun which contains enormous amount of energy. Flares on the Sun occur probably due to reconnection of magnetic field lines, that accelerate the charged particles. A major solar flare can emit $\sim 10^{25}$ joules of energy. Most of the energy released by a flare is in X-rays or UV range. Since flares can eject large

amount of highly energetic particles, they can affect the Earth's environment and also cause major hazards to Earth's orbiting satellites.

Solar prominence is a large loop of plasma ejected from the active region of photosphere moving through inner part of corona that consists of highly energetic gas particles. Life time of these prominences is about several months. When it bursts, enormous amount of highly charged particles release into the space. A typical length of a prominence is about 10^6 km.

In addition to afore mentioned activity phenomenon, a continuous stream of energetic particles are emitting from the Sun's corona in all directions. This phenomenon is known as *solar wind*. Typical speed of these particles is $\sim$ 400 km/s. Temperature near the corona is very high so that ambient plasma over comes the Sun's gravitational force. It is still not completely understood as to how the particles are accelerated to such a high velocities in the coronal region. Furthermore, we can differentiate the observed solar wind as *slow solar wind* (speed is $\sim$ 300-400 km/s) and *fast solar wind* (speed is $\sim$ 700-800 km/s). The slow wind originates from the Sun's equatorial region and fast wind originates from the coronal holes - the area in which the temperature of corona is low with low density plasma. The solar wind particles interact with the Earth's magnetic field and create the *Aurora* near the polar regions.

In addition to these activities, a large volume of plasma with magnetic fields ejects from the solar corona that is commonly known as *coronal mass ejections* (CME). Usually, CME's are associated with the solar flares and prominences. Similar to solar wind, CME's also have variations in their speeds ranging from 100 km/s to 3000 km/s. The speed of CMEs depend on the region from which it originates. CME's have a large impact on the Earth's atmosphere depending upon the direction of their magnetic field with respect to Earth's dipole magnetic field.

1.2.6   Helioseismology

Helioseismology is a branch of solar physics, where details about the internal structure of the Sun can be inferred by analyzing the observed surface seismic waves, particularly p and f-modes respectively. P-modes are created due to pressure perturbations that are

generated in the convection zone; g-modes are due to gravity waves in the stable strat-ified radiative core and, f-modes are due to surface gravity waves. There are about 10^7 p and f modes that sample at different parts of the solar interior. Such oscillations are globally distributed and can be observed mainly in the photosphere. These oscillations are detected by Doppler shifts in the spectral lines. Since these oscillations have ampli-tude of ~ 0.1 m/s, observation should be more accurate to measure the same. Figure 1.9 illustrates the simulated pattern of p-mode oscillations on the surface of the Sun.
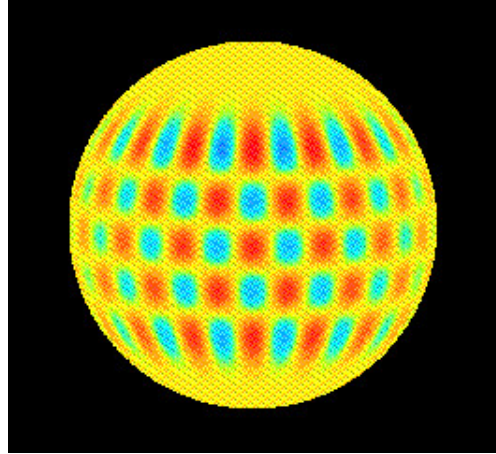
Fig. 1.9 Illustrates the Simulated Patterns of P-Mode Waves on the Surface and in the Interior of the Sun. the Blue and Red Colors Indicates the Oscillations of Waves in Opposite Direction. Image Credit: *http://soi.stanford.edu/*

Since the Sun's shape is nearly a spherical ball of gas, amplitude of oscillations can be represented as $A_{lmn}(r)P_l^m(\cos\theta)\ e^{i(\phi+\omega t)}$, where $A_{lmn}(r,\theta,\phi)$ is amplitude of observed oscillations, $P_l^m(\cos\theta)$ are Legendary polynomials, l is degree, m is azimuthal order and n is radial order of oscillations. Whereas, r, θ and ϕ are radial, latitudinal and azimuthal variables. By applying Fourier transformation and then spherical harmonics, one can decompose different oscillation modes and also frequencies can be estimated.

Similar to Zeeman effect that splits the spectral line, Sun's rotation splits the oscil-lation frequency. If V_{nlm} are frequency of the oscillations (where n is radial order, l is degree of the oscillation modes and m is azimuthal order), the δv_{nlm} is splitting of oscillation frequencies which is given as follows

$$\delta v_{nlm} = \int_0^R \int_0^\pi K_{nlm}(r,\theta)\omega(r,\theta)drd\theta, \tag{1.4}$$

where K_{nlm} are the kernels related to internal structure and $\omega(r, \theta)$ is the internal rotation that has to be inverted. A typical structure of Sun's internal rotation profile inverted from the observed rotational frequency splitting is illustrated in Figure 1.11.
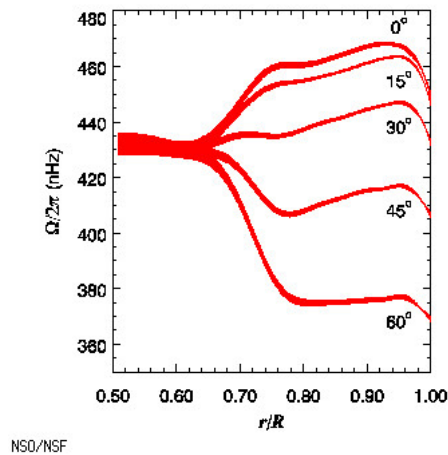
Fig. 1.10 Illustrates the Rotation Rate at Different Latitudes and Depths of Sun's Interior. Image Credit: NSO/NSF.
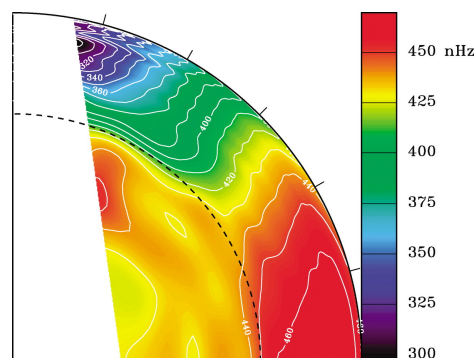
Fig. 1.11 Illustrates Iso-Rotational Contours of Sun's Internal Rotation at Different Depths and Latitudes. Image Credit: High Altitude Observatory.

1.3 Physical And Orbital Properties of Solar System Objects

Before understanding the solar system objects viz., planets, asteroids etc., first let us know the definition of these objects. According to International Astronomical Union (IAU), planetary systems are classified into *planet, dwarf planet and other objects.*

- Planet is a celestial object orbiting around the Sun/star that has a sufficient mass

for its self gravity to overcome the rigid body forces by maintaining hydrostatic equilibrium and cleared the neighborhood matter around its orbit.

- Dwarf planet is a celestial object orbiting around the Sun/star that has sufficient mass for its self gravity to overcome the rigid body forces by maintaining hydrostatic equilibrium, but it has not cleared the neighborhood matter around its orbit.

- Other objects constitute all small bodies of solar system that orbit the Sun viz., asteroids, dwarf planets, comets, etc.

Consequence of modified definition of planetary bodies in the Solar system kept *Pluto* into the *dwarf planet* category. The planets in the Solar system in increasing order of their distance from the Sun are *Mercury, Venus, Earth, Mars, Jupiter, Saturn, Uranus and Neptune.* The first four planets are considered as terrestrial planets and last four planets are considered as Jovian planets. These two categories are separated by a belt of small objects known as *asteroids belt*. The relative size of all the planets with respect to Sun are shown in the Figure 1.12. Similarly, the physical, orbital and atmospheric properties of Solar system planets are presented in Tables 1.2, 1.3 and 1.4 respectively. In Table 1.2, mass and strength of magnetic field of all the planets are expressed in terms of Earth's mass (M_E) and magnetic field (B_E). In the same table, in fifth column 'd' and 'h' means day and hour respectively. In Table 1.3, third column, 'd' and 'y' means day and year respectively. Whereas, 'g_E' and 'v_{esc}' in Table 1.4 of second and third column represents the acceleration due to gravity and escape velocity respectively.

1.3.1 Terrestrial Planets

A planet is considered as a terrestrial planet if it has a rocky/solid surface with iron dominated core. Total mass of all the terrestrial planets in Solar system is very much less than total mass of all the Jovian planets and their orbits are compactly arranged such that, they all orbit within ~ 1.5 AU from the Sun. The eccentricity of all the terrestrial planets are nearly zero except Mercury. Due to intense activity of the Sun in the early
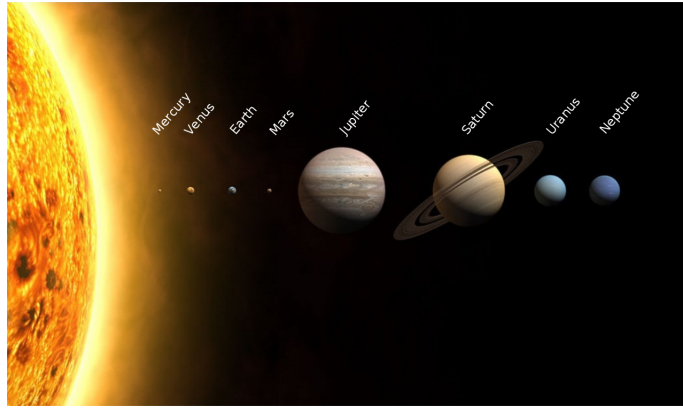
Fig. 1.12 Illustrates the Relative Size of All Solar System Planets With Respect to Sun. One Can Observe That Terrestrial Planets Are Very Small Compared Jovian Planets. Image Credit: Wikimedia Commons.

Table 1.2 Physical Properties of Solar System Planets. Data Credit: NASA.

Name	Mass M_E	Diameter km	Density g cm^{-3}	Rotation	Magnetic field B_E
Mercury	0.055	4879	5.427	58.785 d	0.0006
Venus	0.815	12,104	5.243	243.686 d	0.000
Earth	1.000	12,742	5.515	23.934 h	1.000
Mars	0.107	6,779	3.933	24.622 h	0.000
Jupiter	317.830	139,822	1.326	9.925 h	19,519
Saturn	95.159	116,464	0.687	10.656 h	578
Uranus	14.536	50,724	1.270	17.240 h	47.900
Neptune	17.147	49,244	1.638	16.110 h	27.000

evolutionary stage, probably most of the material present near the Sun might have been blown off to the inter stellar space. Hence, this is one of the reason that in addition to average low mass of planets, atmospheres of these planets are very thin. Let us study each terrestrial planet in the following sections.

1.3.1.1 Mercury

Among all other planets, Mercury is the nearest planet to the Sun with a least mass of ~ 0.06 Earth's mass. It orbits around the Sun in an elliptic orbit with an orbital eccentricity of 0.21 and a mean distance of ~ 0.39 AU. Due to high eccentric orbit, its distance varies from 0.31 to 0.47 AU. In addition, temperature of surface of the Mercury also varies drastically from 100 K (on the surface that faces away from Sun) to 700 K (on the surface that faces towards the Sun). Its diameter is estimated to be ~ 4800 km.

Table 1.3 Orbital Properties of Solar System Planets. Data Credit: NASA.

Name	Distance AU	Rotation	Eccentricity	i deg
Mercury	0.387	87.969 d	0.205	7.005
Venus	0.723	224.701 d	0.007	3.394
Earth	1.000	365.256 d	0.016	0.000
Mars	1.524	686.980 d	0.093	1.851
Jupiter	5.203	11.862 y	0.048	1.305
Saturn	9.537	29.457 y	0.054	2.484
Uranus	19.191	84.011 y	0.047	0.770
Neptune	30.069	164.790 y	0.008	1.769

Table 1.4 Atmospheric Properties of Solar System Planets. Data Credit: NASA.

Name	$\frac{g}{g_E}$	v_{esc} km s^{-1}	Temperature K	atm. press. (x Earth's)
Mercury	0.378	4.300	100 (night) - 725 (day)	10^{-15}
Venus	0.905	10.360	737	92
Earth	1.000	11.186	283 (night) - 293 (day)	1.000
Mars	0.379	5.030	184 (night) - 242 (day)	0.006
Jupiter	2.530	59.500	165	$\gg 1000$
Saturn	1.065	35.500	134	$\gg 1000$
Uranus	0.905	21.300	76	$\gg 1000$
Neptune	1.140	23.500	72	$\gg 1000$

By knowing mass and radius, its density is estimated to be ~ 5427 kg m^{-3}. It takes $\sim$ 87.969 days for one orbit around the Sun.

The observation of Mercury is very difficult because it always present in day light and can be visible in the horizon during Sunset or Sun raise. Since it does not have a natural satellite (moon), one can not accurately estimate the mass from Kepler's third law. The best estimation of mass is obtained using the data provided by a satellite Mariner 10 during 1974 and 1975. This space probe also observed many craters on the surface of the Mercury which are created during late stage of bombardment experienced by the Solar system. Figure 1.13 is one of the typical image taken by the Mariner 10 spacecraft.

Since Mercury has a very small size and high temperature, it does not have proper atmosphere like Earth. However, there is a thin atmospheric layer around the surface, composed with atoms of Helium, Oxygen and Sodium that are absorbed from the solar wind. As per the theoretical models, the internal structure of Mercury is dominated by
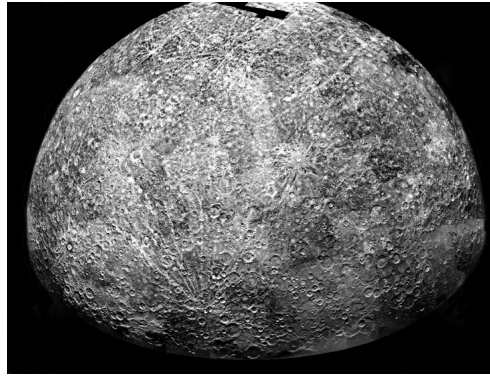
Fig. 1.13 Illustrates a Typical Image of Mercury Surface Taken From the Mariner 10 Spacecraft. One Can Observe the Many Number of Craters of Different Sizes on the Surface of the Mercury. Image Credit: *https://www.nasa.gov/image-feature/mariner-10-image-of-mercury*.

core with a density almost equal to the density of Earth. Hence, it is inferred that most of the composition of Mercury's core is Iron and Nickel.

The interaction between the Mercury and Solar wind suggests that, Mercury has a small intrinsic magnetic field. The strength of magnetic field estimated to be ~ 0.002 gauss, which is about 1% of the Earth's magnetic field. As per dynamo mechanisms, magnetic field structure is not a remnant from early times. It is assumed that magnetic fields are created by a electrically conducting core. Whereas, recent study by Hiremath (2012) suggests magnetic field structure of Mercury is of primordial origin that was inherited during early history of Solar system formation.

1.3.1.2 Venus

It is the brightest object in sky, after the Sun and the Moon. Since it is a second planet nearer to the Sun, it can only be seen during morning and evening. The mean distance between Sun and Venus is estimated to be ~ 0.723 AU. In earlier days, it is referred to as 'second Earth' because of the similarities in the mass, size and density. Due to its dense atmosphere, it is very difficult to probe the features of Venus by photography of visible light. By measuring the microwave radiation from the Venus, its temperature near the surface is estimated to be ~ 650 K.

Majority of the components of the Venus atmosphere are CO_2 (96%), Nitrogen (3.5%), sulphur dioxide (0.015%), water (0.01%), etc. The reason behind the low frac-

tion of water is mainly due to solar UV radiation that dissociates the water molecule into hydrogen and oxygen in the upper atmosphere of Venus. Due to thick atmosphere of Venus, only 1% of incident solar light can reach the surface. The reflected light from the surface is absorbed and re-emitted in the infrared region, which are blocked by carbon dioxide present in the atmosphere. This is the main reason for high temperature of Venus surface.

Mariner 2, in 1962, was the first spacecraft to probe the Venus. After five years, Russian spacecraft Venera 4 sent the data and pictures from below the clouds. The radar observation of Venus reveals the presence of mountains, craters and volcanoes on the surface of Venus. Venus has more volcanic activity than any other planet in the solar system. The strength of magnetic field of Venus is zero.

1.3.1.3 Earth

The third planet in the Solar system is the *Earth* and it has a natural satellite known as the *Moon*. Mass of the Earth is $M_E = 5.976 \times 10^{24}$ kg and its diameter is about 12,000 km. The Earth takes approximately 365 days for one rotation around the Sun and, 24 h for a rotation around its own axis. Its distance from the Sun is estimated to be $\sim 1.4959 \times 10^{11}$ meters.

Core of the Earth is divided into *inner* and *outer* core. The region below 5100 km from the surface is considered as the inner core, that constitute about 1.7% of Earth's mass and appears as solid because of the high pressure. Next to the inner core is the outer core that consists of 31% of Earth's mass. It is hot, electrically conductive layer composed of Fe-Ni, which is responsible for the generation of magnetic fields. The magnetic field is almost dipole with few considerable local variations. The strength of Earth's average magnetic field is estimated to be ~ 0.307 gauss at the surface. Mantle is the layer above the outer core that consists of about 49% of the mass and composed mainly silicon, magnesium and oxygen with small fraction of iron, aluminium and calcium. The outermost layer of Earth is known as *crust* with a thickness of about 10-70 km.

Similar to interior, Earth's atmosphere also consists of different layers. Major com-

ponents of Earth's atmosphere are nitrogen (77% by volume) and oxygen (21% by volume). Remaining part is composed by fraction of gases such as argon, carbon dioxide and water vapors. The lower part is known as *troposphere*, that extends upto 10-20 km above the Earth's surface. Next to *troposphere* is the *stratosphere* that extends up to 60 km. Main compositions of this layer are carbon dioxide, water vapor and ozone. One should note that, there is a decrease in the temperature from the surface to troposphere. However, temperature start increases as we move from base of the stratosphere. This temperature gradient is because of the interaction of particles with UV radiation from the Sun. The layer above the *stratosphere* is the *mesosphere* which extends upto 80 - 90 km. Here most of the atoms are in exited state because they directly absorbs the radiation from Sun. The last layer is *ionosphere* that extends upto 500 km. As the name itself resembles, the chemicals in this layer is in completely ionized state with a temperature around 1500 K.

1.3.1.4   Mars

The fourth planet from the Sun is the Mars which is the outermost among terrestrial planets. Its mass is almost one tenth of the Earth mass and diameter is half of the Earth's diameter. Through telescope, Mars appears to be a red disk with white cap at the poles that indicates the presence of ice. These polar white caps change with the seasons on the Mars. The rotation axis of Mars is tilted 25^0 to the ecliptic, which is almost same as Earth's axis. It takes around 24.62 hours for a rotation about its own axis and ~ 687 days around the Sun. *Phobos* and *Deimos* are the two moons of the Mars.

Similar to other planets, the craters can also be found on the surface of the Mars, especially near southern hemisphere. *Hellas* and *Argyre* are the largest craters found on the Mars with a diameter about 2000 km. Whereas, large lava basins and volcanoes can be found near northern hemisphere. Hence, both the hemispheres are elevated around 1 to 4 km in the polar regions. Many theories proposed the presence of water rivers during the ancient Mars just after its formation. However, at present, temperature and air pressure of Mars are too low for presence of liquid water. Chemical analysis of Mars

soil reveals that ratio of Ca/Si = 0 - 0.5, which is same as the Earth. Similarly, Fe/Si ~ 0.7, which is also comparable with the Earth's value of 0.3. Due to high content of iron in the form of FeO in the Mars soil, it looks red when we observe it through telescope. Like Venus, carbon dioxide (95%) is the main component of atmosphere with Nitrogen (2%) and Oxygen (0.1 - 0.2%) are other elements. However, due to very thin atmosphere, the greenhouse effect is very negligible. Despite of thin atmosphere, there are strong winds on the Mars with dust clouds. Usually, these winds appear when the Mars is at perihelion that causes the heating of surface, which makes a large temperature difference and turns into strong winds.

To date, any kind of global magnetic field of Mars is not detected. However, some part of the crust suggests a very small magnetic field structure that probably might have acquired from the primordial magnetic field (Bisikalo et al. 2017).

Figure 1.14 illustrates the relative size of all terrestrial planets with their internal structure. One can notice from this illustration that most part of Mercury is occupied by the central core.
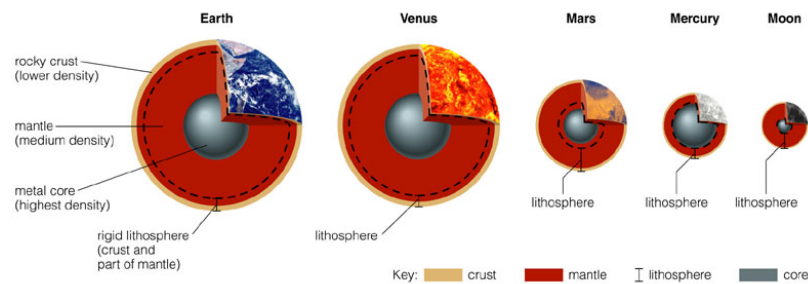
Fig. 1.14 Illustrate the Relative Size of All the Terrestrial Planets With Their Cores. Image Credit: Pearson Education.

1.3.2 Jovian Planets

There are four Jovian planets in the Solar system which are also known as gas giants, namely, *Jupiter, Saturn, Uranus and Neptune.* As their names itself resemble, they are very massive, bigger in size and spacing between the orbits are not as compact as terrestrial planets. Despite of more mass, the mean density of these planets is very low because of their large size and gaseous component. These planets are fast rotators ($\sim$ hours) and they posses strong intrinsic magnetic field structure. All the giant planets have many moons and ring like structures (that mainly consists of smaller bodies) that orbit around them. General internal structures of giant planets are also similar to terrestrial planets, however, due to absence of solid surface one has to infer their internal structures through seismic waves. Hydrogen and Helium are the major chemical compositions in these planets. In addition, due to their large orbital distances from the Sun, *ice*, ammonia and methane also main constituents of their composition especially in Uranus and Neptune. Hence, they are also known as *Ice giants*.

1.3.2.1 Jupiter

Jupiter is the fifth and nearest among the gas giants orbiting at a distance of ~ 5.2 AU from the Sun. It is the most massive planet among all the solar system planets with a radius about one-tenth of the Sun. Density and composition of Jupiter almost resembles the Sun because of high proportion of hydrogen and helium. Observation of Jupiter reveals banded structures with bright band known as *zones* and dark band known as *belt*. The gas flows upwards in zones, whereas, it flows downward in the belts. Hence, the temperature in the zones are lesser than the belts. There exists a large Great Red Spot (GRS) on the Jupiter, which is 14,000 km wide and 30,000 - 40,000 km long. In addition, there exists few small red and white spots with small lifetime. The rotation of these spots and bands around the Jupiter depends upon their latitude. Rotation period of Jupiter at the equator is around 10 hours, whereas, it is five times longer at the polar regions. Due to its high rotation Jupiter is flattened.

The central core of Jupiter consists of mass (around 10-20 times Earth's mass) which is mainly composed of iron. This core is surrounded by shell of silicate and other higher

elements containing hydrogen and carbon. The outermost layer is composed of mainly hydrogen and helium gases. Due to its high temperature (10000 K) and high pressure at deep interior of the Jupiter, the hydrogen dissociates into single atoms with high energy. Since this layer is electrically conducting region, it generates magnetic fields with a strength of 19,000 times stronger than the Earth. In addition, due to less amount of flux from the solar wind, the magnetosphere extends widely. Jupiter releases twice the energy that it receives from the Sun. The excess heat is coming from the energy released by gravitational contraction, that suggests still Jupiter is gradually cooling and contracting. The Figure 1.15 illustrates the image of Jupiter with belts, zones and GRS.

The Jupiter consists of many moons and ring like structures. *Io, Europa, Ganymede and Callisto* are major moons that are known as *Galilean satellites*. *Ganymede* is one of the largest moon of Jupiter as well as in the Solar system with a diameter $\sim$ 5300 km. 50% of mass of this moon is water and ice and, remaining is due to silicates. *Europa* is smallest among all the moons of Jupiter. Since it shows a small magnitude of magnetic field, it is believed that there exists a conducting material beneath the surface of this moon. *Io* is the innermost moon, with a size little larger than Moon. Volcanic activity on the surface of *Io* is higher than the Earth. *Callisto* is the outermost among all other moons. Its main composition is rocks (60%) and ice (40%) with fewer/no signs of tectonic activity.
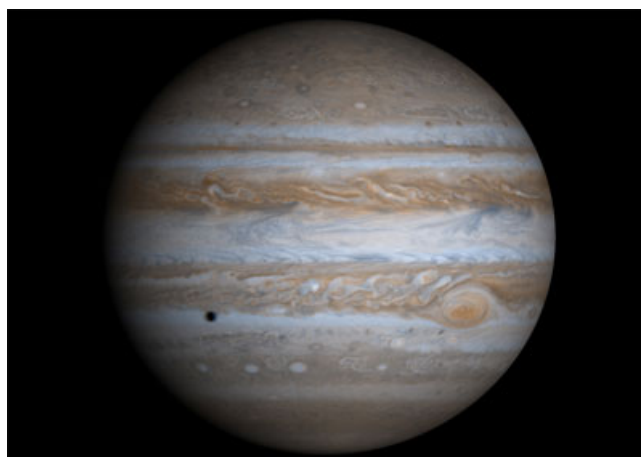
Fig. 1.15 Illustrates The Image of The Jupiter With White Bands Known as *Zones* and Dark Bands Known as *Belts*. The Big Red Dot is Called as GRS. Image Credit: NASA Jet Propulsion Laboratory.

1.3.2.2 Saturn

Saturn is the second largest planet in the Solar system with a mass around 95 times the Earth's mass and diameter around 120,000 km which is 10 times the Earth's diameter. The density of Saturn ($\sim$ 700 kg m^{-3}) is less than the water. Since its rotation axis is tilted by 27^0 with respect to orbital plane, one can observe both the poles of Saturn for every 15 years. From the periodic variation of magnetic field structure, the rotation period of Saturn is estimated to be $\sim$ 10 h 39 min. Similar to Jupiter, due to rapid rotation, Saturn is also flattened.

Saturn has a silicate and metal core of 5 Earth's mass. The metallic hydrogen in outer shell is not as thick as that of Jupiter because of the small size. The heat radiated by Saturn is 2.8 times that of incoming radiation from the Sun. This excess heat from the Saturn is generated by a mechanism where Helium gets separated and settling at the core. Similar to Jupiter, main atmospheric composition of Saturn is Hydrogen and Helium. There are more stronger winds on the Saturn than Jupiter because of the internal energy production. Magnetic field strength of Saturn is about 0.3 times that of Jupiter. Magnetic dipole axis is tilted about 1^0 with its spin axis.

One of most interesting aspect of Saturn is its ring structure which looks like a disk revolving around Saturn's equatorial plane. The size of particles in the ring structure are ranging from few centimeters to few meters that are composed of mainly water ice. The width and thickness of ring is 60,000 km and 100 m respectively. It has been shown that Saturn's ring structure is formed along with the Saturn's origin, that suggests particles in the ring structure are not from debris or broken moon. In addition to ring, there are 56 moons orbiting around Saturn. *Titan* is one of important and largest of all Saturn's moons with a diameter 5150 km. It has a very dense atmosphere with mainly nitrogen (98.4%) and methane. Temperature of *Titan* is 95 K with a pressure of about 1.5 - 2 bar.

1.3.2.3 Uranus

Compared to gas giants, Uranus is slightly different in its composition. Due to presence of methane in the atmosphere of Uranus, which absorbs red light, it appears to be greenish blue in color. Hydrogen (83%), Helium (15%) and methane constitute main at-

mospheric components. The clouds of Uranus also show banded structures like Jupiter. Interestingly, bands near the equator rotate slower than the poles. The rotation period of Uranus is around 17 h 14 m. In addition, the tilt of spin axis ($\sim 97^o$) is very large compared to other planets with a retrograde orbital motion.

The internal structure of Uranus consists of a rocky core with mantle of hydrogen and helium. In addition, water, ammonia and methane are dissociated into ions due to high pressure. The convection flows of these ions gives raise to magnetic fields at deep interior of the planet. The strength of magnetic field is about 0.003 times that of Jupiter with an axis tilted $\sim 60^0$ with respect to spin axis and, this is one of the interesting problem that needs to be solved.

Like other giants, Uranus also consists of ring structures that were discovered in 1977 during a stellar occultation (Bhattacharyya and Bappu 1977, Vasundhara et al. 1983). These rings were discovered by Bhattacharyya and Bappu (1977) from the Kavalur observatory, India. A total of 13 rings are discovered, among innermost is broad and diffuse, whereas, other rings are dark and narrow. The observations from Voyager 2 showed that these rings are made up of dust particles with a mean size of 1 meter. In addition to rings, there are 27 moons orbiting the Uranus. The biggest moon among all is named as *Miranda*.

1.3.2.4   Neptune

Neptune is often called as twin of Uranus, because its size and atmospheric compositions are comparable with Uranus. However, Neptune's mass is 18% higher and radius is 3% lesser than Uranus, hence, its density is higher than the Uranus. The rotation period of Neptune is 16 h 7 m. Probably, massive silicate-iron core may be a reason for Neptune's larger mass and smaller radius. This core is surrounded by a shell of water and methane. The outermost layer is gaseous with hydrogen and helium as its main components. Unlike Uranus, Neptune is more active body. Like Jupiter's GRS, Neptune also consists of a *Great Dark Spot* which is created because of the strong winds in its atmosphere. There are white bands on the Neptune, whose main composition is condensed methane. As mentioned earlier, the main atmospheric composition of Neptune

is similar to Uranus with a difference in helium fraction of $\sim 19\%$ higher than Uranus. Magnetic field of Neptune is dominated by dipole characteristics with a strength about half of the Uranus. Center of dipole is displaced from the center of the planet by a distance of 0.55 times the radius, which creates displacement of ($\sim 20^0$) with equatorial plane.

Similar to other gas giants, Neptune has 13 moons and rings. The largest of all the moons is known as *Triton* with a diameter of 27,000 km. This moon has thin atmosphere that is mainly composed of nitrogen. There are two rings at a distance of 53,000 and 62,000 km from the center of the planet.

1.3.3 Other Objects

In addition to planets, Solar system also consists of many other objects viz., asteroids, comets, dwarf planets such as *Pluto*, Kuiper belt and Oorts clouds.

1.3.3.1 Dwarf Planet - Pluto

According to the definition of IAU, *Pluto* is considered as a *dwarf planet* due to its low mass and it has not cleared its neighborhood. Due to its highly eccentric orbit (0.249), it passes through the Neptune's orbit while revolving around the Sun. Pluto's mass is unknown until the discovery of its moon *Charon* in 1978. Mass of Pluto is estimated to be ~ 0.002 Earth's mass with a radius around 1195 km. The density of Pluto is ~ 2100 kg m^{-3} that suggests it is an icy object. The internal structure suggests that it is made up of rocky core with icy mantel surrounded by a crust of methane and nitrogen.

The Charon orbits around the Pluto and these two objects are tidally locked. In addition, Pluto has two more satellites *Nix and Hydra*, that orbit counterclockwise with almost twice a period of Charon.

1.3.3.2 Asteroids

Asteroids are small objects with a negligible mass in the Solar system when compared to planets, whose sizes vary from few meters to several hundred meters. There are many asteroids between the region 2.2 AU and 3.5 AU that orbit around the Sun. Hence, this

region is known as *Asteroid belt*. First asteroid discovered in 1801 by Giussepe Piazzi, who named it as *Ceres*. Ceres is most massive and biggest among all the asteroids. The physical and orbital characteristics of each asteroid are different. Presently, there are more than 100,000 known asteroids and this number is increasing. Combined mass of all the asteroids present in the asteroid belt is estimated to be $\sim 1/1000$ of Earth's mass. With the help of *Titus-Bode law*, center of the asteroid belt is estimated to be ~ 2.9 AU.

Before understanding the composition of asteroids, one has to know the composition of meteorites, that are originated from the asteroids. Based on the laboratory analysis, meteorites are classified into *salt* that are mainly composed of silicate, *iron* that are mostly composed of iron with small fraction of nickel and, *stony-iron* which contains the mixture of *salt and iron* regions. In addition to analysis of meteorites, the spectroscopic observations of asteroids in visible and near infrared region reveal the information about their composition. Measuring the spectra of these asteroids and matching with the laboratory spectra help us to understand their composition. Asteroids are divided into six types based on their spectral characteristics. However, majority (80%) of them are belong to spectral type designated as C and S, whose main composition is carbonaceous chondrite materials and stony-iron respectively. In addition to the region between the Mars and Jupiter, around 500 - 1000 asteroids are also detected near Earth, that are known as *near-Earth Asteroids*. Majority of these asteroids' size are more than one kilometer.

1.3.3.3 Kuiper Belt and Oort's Clouds

Furthermore, as suggested by *Gerard Kuiper* in 1950's, there are many other small objects like asteroids, comets, etc., are found beyond the Neptune's orbit, which is known as *Kuiper's belt and Oort's cloud*. The total number of objects discovered in Kuiper's belt is more than 70,000 with some of their size is larger than Pluto. It has been showed that objects in the Kuiper's belt and Oort's cloud are remnant of materials from early accretion phase of Solar system planet formation.

1.3.3.4   Comets

Comets are small objects made up of ice, snow and dust particles with a typical diameter of 10 km. They have rocky core surrounded by ice and frozen gases. Edmund Halley is the first person to recognize these objects and postulated that comets have a specific orbits around the Sun. Since comets are very small in size, one can not able to detect or see the comets when they are very far away from the Sun. However, when they are passing nearer to Sun ($\leq$ 2 AU), heat from the Sun melts the snow and ice particles. These melted particles form an envelop around the nucleus of the comet known as *coma*. The energetic solar wind and radiation pressure pushes these particles away from the Sun that appears as a tail. The tail of a comet is divided into *ion tail* and *dust tail*. High energy solar winds are the main reason for ionized gas. Due to emission from the exited atoms, ion tail appears very bright. The dust tail is created due to radiation pressure. The materials in the comets are loosely bound to each other. Hence, evaporation of high fraction of mass from the comet due to high temperature and pressure may destroy the comet completely. In addition to ice and snow, other chemical elements present in the comets are carbon monoxide, carbon dioxide, methane, ammonia and formaldehyde.

There are two kinds of comets classified as *Jupiter family* of comets and extreme class of comets. Jupiter family comets have short orbit, with a small inclination, and the value of eccentricity is 0.5 - 0.7. Whereas, the comets that belong to extreme class family have major axis of few hundreds of AU and eccentricity is near to unity. In 1950, *Jan Oort* discovered a population of long distance comets orbiting around Sun at a distance of $\sim$ 50,000 AU. He proposed that there exists at least 10^{12} comets in outer part of Solar system, which is known as *Oorts cloud*. The total mass of Oorts cloud is estimated to be few Earth's mass. Within next few years, after Oort, another scientist *Gerard Kuiper* observed a separate population of comets orbiting with a short period of 200 years around the Sun with an orbital inclination $\leq 40^0$, revolving in a same direction as that of Earth. The perturbation from the passing stars send few comets into the inner orbit of Solar system that are known as long period comets. The region of these short period objects is just beyond the orbit of Pluto and is known as *Kuiper's belt*. It is showed that Oorts cloud objects and Kuiper belt objects have different origins.

Oorts cloud objects are formed nearer to giant planets and ejected into the outer space through their dynamical interactions with giant planets. However, Kuiper belt objects had no such interaction during their early stages.

1.4 Different Theories on Genesis of Solar System Formation

Any theory should better explain the formation of Sun, planets and all other small objects. Some of the key factors that are to be considered on the origin and formation of Solar system objects are listed below:

- the contrast of angular momentum distribution of the Sun and the planets

- mechanism of planetary formation within a short time of $\sim$ 50-100 Myrs

- coplanar orbits of the solar system planets

- orbital distribution of terrestrial and giant planets

- nearly circular orbits of solar system planets (except Mercury)

- explanation for all small objects viz., asteroid belt, comets, objects in Kuiper belt and Oort's could, etc.

In the following sections we explain briefly the few important theories that are proposed to understand the origin of Solar system.

1.4.1 The Laplace Nebular Hypothesis

Rene Descartes (1596-1650) assumed that space was filled with the 'universal fluid' with unknown nature that forms a vortex near the stars. Within such large vortices, small vortices will form which are birth place of planets. But there was no sound scientific basis for this model. A century later, German scientists Immanuel Kant (1724-1804), with the help of Newtonian mechanics showed that solar system is formed by a collapsing cloud of gas contracting under its own gravity. Planets were formed in the disk orbiting around the central mass.

By studying the solar system model from these two scientists, Pierre Laplace (1749-1827) proposed first well formulated theory on the origin of Solar system in 1796. Figure 1.16 illustrates the graphical picture of Laplace model. According to Laplace, spinning clouds of gas and dust particles collapse due to their own gravity. While contraction, to conserve the angular momentum, the central object spin rapidly by forming a disk like structure orbiting around it. Further contraction in disk gives raise to ring like structures composed of gas and dust particles. The planets will form inside these rings by condensation of small particles. Major drawback of this theory is that it could not successfully explain the distribution of angular momentum in the Solar system objects. Despite of having more mass ($\sim 99\%$), Sun possess very less angular momentum ($\sim 1\%$) of Solar system. To date, this is one of major unsolved problem on the genesis of Solar system formation.
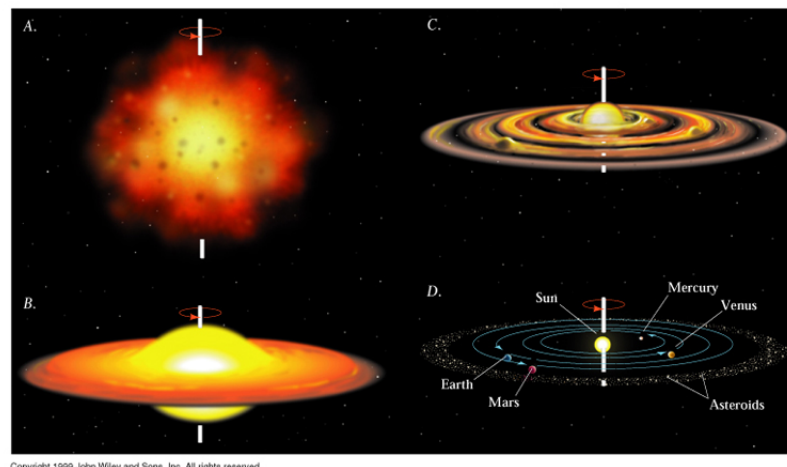
Fig. 1.16 Illustrates the Visualization of Laplace Theory of Solar System Formation. as Explained in Text, (A) Represents the Large Size of Collapsing Cloud of Gas and Dust Particles. (B) Contraction of Cloud Leads to Central Massive Object and a Disk Like Structure Around It. (C) Further Contraction Leads to Formation of Rings in the Disk. (D) Ultimately, Planets Will Form in the Rings by Obtaining the Final Structure of Solar System. Image Credit: Astronomy Online.

1.4.2 The Roche Model

Another scientist during Laplace period, Edouard Roche (1820-1883) suggested that majority of the mass of collapsing could would have condensed near the center with very less initial angular momentum. In 1873, Roche formulated a mathematical theory

in which the solar system is described as 'the Sun plus atmosphere', which clearly tells that solar system is formed by a collapsing clouds of gas with high central condensation. In this model, the atmosphere of Sun originally extends beyond the region of planets and shrinks as it cools. This model assumes that atmosphere is co-rotating with the Sun with an angular velocity (ω) and this is true upto the radius R_L given by

$$R_L^3 = \frac{GM_\odot}{\omega^2}, \tag{1.5}$$

where G and $M_\odot$ are the universal gravitational constant and Sun's mass respectively. The atmosphere beyond the R_L must go to free orbit around Sun. As system collapses R_L decreases rapidly leaving beyond the atmosphere. The atmosphere beyond the R_L, forms into the orbits of planets at a specific distances a given by

$$a^3 = \frac{GM_\odot}{\omega^2}. \tag{1.6}$$

Although this model partially explained the angular momentum problem, it is highly impossible to believe the existence of sufficient viscous coupling with such a diffused atmosphere. In addition, as per the Roche model, the nebular distribution at the outer region is very weak that it could not resists the tidal forces due to central mass. This is based on the work done by Roche who derived the *Roche limit*.

1.4.3 The Chamberlin and Moulton Planetesimal Theory

Thomas Chamberlin (1843-1928) and Forest Moulton (1972-1952) are two American scientists who developed a dualistic theory on Solar system formation. Around 1890's Chamberlin proposed that the planets are formed by condensation of nebular materials in the form of small objects known as *planetesimals*. Agglomeration of these planetesimals leads to formation of planets in later stages. The basic concern to this theory is that, due to slow rotation of outer particles compared to inner particles, the planets might have ended up with the retrograde spin. However, the elliptical orbits of planetesimals rule out this problem.

From 1900, Chamberlin and Moulton worked together for understanding the gene-

sis of Solar system formation. Since the nature of nebula was not known at that time, they interpreted the photograph of a spiral nebula as ejection of materials from a star. The ejected material further forms into the planets that are orbiting around a star. In a similar way, this model assumes that Sun was very active at the early stages with high prominences. The passing nearby star around the Sun pulls out the material from the prominence present on the active Sun in both the direction. The pulled out material formed into a spiral arms on both sides of Sun that extends up to Neptune's orbit. In order to explain the composition of terrestrial and Jovian planets it is assumed that material at the outermost part of the spiral arm might have originally coming from the surface of the Sun and material at the innermost part of spiral arm is from deep inside the Sun with high density. These prominences ejected from the Sun forms an irregular pulsations around the Sun which further cools down to form the planets. Since this theory describes in a qualitative way, without any details about the dynamical interactions of objects, this theory is not much appreciated in the scientific community.

1.4.4   The Jeans Tidal Theory

With a previous idea of formation of Solar system from the interaction of another star, James Jeans (1877-1946) has formulated a new theory which appears to be modification of Chamberlin-Moulton dualistic theory. The most important difference with the previous theory is the absence of ejection of prominences from the Sun by passing nearby star. Instead, the central object, the Sun, itself tidally interacted with another passing star within Roche limit. These interaction were so powerful that material from the Sun is escaped from it and formed into a filament as illustrated in the Figure 1.17. Due to gravitational instability, filaments break into small pieces that ultimately condensed into the planets.

One of the early supporter of Jeans theory, Harold Jeffrey (1891-1989), raised a first objection to this theory by saying that, since the massive stars are very rare, that might have resulted into the rare occurrence of planetary formation in the universe. Another question raised by Jeffrey is on the spin of Sun and Jupiter. Since composition and density of these objects are similar, both should have same spin/rotation. However spin

period of these objects are different by factor 65. One can also note that the presence of light elements (that might have destroyed around solar temperature) on Earth and other planets implies that they are not a part of an early Sun.
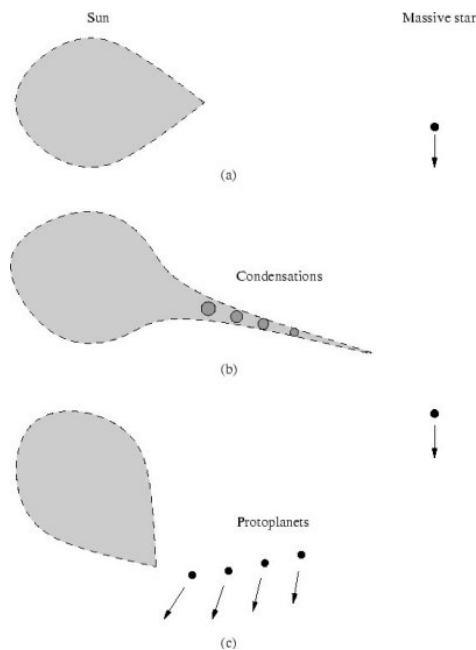
Fig. 1.17 Illustrates the Jean's Theory of Solar System Formation. (a) the Escape of Material From the Sun Due to Interaction With a Star, (b) Filament Like Structure Ejected From the Sun And, (c) Planets Formation by Attracting Protoplanets. Image Credit: Stephen Oxley, Doctoral Thesis, Univ. of York, 1999

1.4.5 The Solar Nebula Theory

During 1960s many laboratory experiments explained the characteristics of meteorites through the condensation of silicate vapors. This empirical results lead to an assumption that Solar system might have formed through the condensation of hot nebula. Subsequently, Solar system formation through condensation of hot nebula was abandoned. However, during 1970s, many theories were proposed on the basis of Laplace's nebular theory to explain the formation of Solar system which is known as Solar Nebula Theory (SNT). The concern that are explained by SNT are the distribution of angular momentum and formation of planets.

In 1974 Lynden-Bell and Pringle proposed a mechanism to explain the transfer of angular momentum from the core to disk of a collapsing cloud. If the nebula was turbulent then it could have produced the heat from it which is radiated away. Hence, as

nebula evolve, its energy become less with constant angular momentum. This mechanism happens only when the inner materials drifted inward and outer materials drifted outward. Due to this mechanism, materials gradually move inward that end up with in the central star. Near the central star, the gravitational force of central mass is neutralized with the spin of the material that produces diffuse objects with high angular momentum compared with the angular momentum of main sequence stars. Hence, further few mechanisms are required to explain the removal of angular momentum from central star.

1.4.6 Recent Important Models

The discovery of exoplanets (described in next chapter) with different physical and orbital characteristics revolutionized the concept of planetary formation. The planetary systems with hot-Jupiters, highly eccentric and inclined orbits that have much different architecture than the Solar system. Migration is one of the important mechanism during early stages of planetary formation. Recently, a model known as *Nice model* (Tsiganis et al. 2005), is proposed to explain the dynamics of Jovian planets by considering the migration scenario. According this model, the giant planets were in a compact orbits during early stages of Solar system. Just after the dissipation of initial gas from the disk, these giant planets were in co-planar, resonant and circular orbit. The remaining small planetesimals/dust particles orbiting inside the disk occasionally go through the gravitational interactions with the edges of giant planets. These interactions scatter majority of dust particles inside the disk and planets move outward in order to conserve the angular momentum of the system. These scattered dust particles simultaneously alter the orbits of Saturn, Uranus and Neptune. Once the resonance of giant planet cross, they attain the eccentric orbit. Mainly the orbit of Uranus and Neptune extends to planetesimals disk and scatters the small bodies present in that orbit. This leads to Late heavy bombardment during early stage of solar system evolution that have impact on the terrestrial planets.

Recently, another model known as *Grand Tack model* (Walsh et al 2011) is proposed to explain the influence of giant planets on the architecture of terrestrial planets, and low

mass Mars. According to this model, Jupiter is the first planet to form among the gas giants, beyond the snow line, with a core mass of ~ 10 Earth mass (Pollack et al. 1996) and started migrating inward. Simultaneously, Saturn grew at a larger distance than Jupiter in slower timescale. The inward migration of Saturn was faster compared to Jupiter's migration. Once the Jupiter and Saturn are in 2:3 mean motion resonance, it results in shifting the balance of disk torques acting on planet that causes the outward migration of those planets. As the disk dissipates, the migration slows down and stops at their current orbits. This inward-outward migration of Jupiter might have heavily influenced fraction of planetesimals near the Mars orbit, that results in low mass Mars and low density of present day asteroids belt. However, number of queries are raised for this model viz., whether inward-then-outward migration of Jupiter is possible, can any other simple model explains the formation of inner solar system, etc. Hence, still many models yet to be required to completely understand the origin and formation of Solar system.

CHAPTER 2

Exoplanets

Humans quest is to understand the origin and formation of the Solar system objects, origin of water and life on this Earth. Around 2000 years ago, concept of many worlds other than Earth was proposed by Epicurus (341-270 BC) who suggested that "there are infinite worlds both like and unlike this worlds of ours". However, another famous philosopher Aristotle (384-322 BC), from the same period stated "there cannot be more worlds than one." Since then many debates are going on regarding the existence of life elsewhere in the universe. In addition, humans are also searching for life outside the Earth. Some important and curious queries from the ancient time that are still yet to be answered - for example, "are there any planets outside the Solar system in this vast universe, that exactly resemble Earth?", "Are they common?" and "Do they have signs of life?". However, the detection of first exoplanet orbiting around a pulsar (Wolszczan and Frail 1992) and later around a Sun-like star (Mayor and Queloz 1995) gives a hope to answer all these interesting and philosophical questions.

Exoplanets are the planets outside the Solar system or the planets that are not bound to the Sun. These planets can be bound to other stars or they can be free-floating planets that are not bound to any stars. Planets do not generate their own light through nuclear reactions, instead they can only reflect their host stars light. Hence, it is very difficult to observe a planet that is very far from the Earth/Sun. The reflected light from a planet is billion times fainter than the light from its host star. Therefore, indirect methods are employed to discover the exoplanets. Although first exoplanet around Sun-like star is discovered around 1995, previously there were many attempts to discover the planets outside the Solar system. In the following section, previous attempts are briefly

described.

2.1 Brief History of Detection of Planets Outside the Solar System

The first discovery of an exoplanet was claimed during the mid of nineteenth century. Jacob (1855) suspected a planet around the star 70 Ophiuchi by astrometry method. Later, this conjecture was disproved by Moulton (1899). A century later, Struve (1952) proposed a theory on existence of Jupiter-like planets in a small orbit that can be discovered by the high precision spectroscopic and photometric techniques. Since during that period, all believed that a Jupiter-like planets can only exist in longer orbits (~ 5 AU from the star) like in the Solar system. A few years later, in 1960s, a Jupiter mass planet with an orbital period 24 years around Barnard's star was announced by van de Kamp (1963). However, these results turned out to be instrumental errors. In the year 1992, first two confirmed planets around a pulsar, PSR 1257+12, was announced (Wolszczan and Frail 1992). Pulsars are also known as the neutron stars, remnants of high mass stars ($\geq 8\ M_{\odot}$).

During early 1980s, Walker started to monitor the 21 bright Sun-like stars for search of Jupiter-like planet that orbits at a long distance from the host stars with a period of 12 years. In 1995, Walker et al. (1995) published his results with a conclusion that none of those 21 Sun-like stars host Jupiter mass (1-3 M_J) planets. In addition, they also announced that there is no evidence of short-period Jupiter mass planets around 45 Sun-like stars. In the same year, from the radial velocity method, Mayor and Queloz (1995) announced the discovery of first exoplanet that orbits the Sun-like star, 51 Pegasi, with a mass of 0.5 M_J, in a very short orbital period of 4.2 days. Previously, many people believed that architecture of Solar system planets is the base for all the models of planetary formation. However, discovery of such a massive planet in a very short orbit changed the view on the genesis of planetary formation. Further, many discoveries of massive planets in a short period orbit lead to a conclusion that all the nearby massive planets have undergone inward migration (Triaud 2016) during their early evolutionary stages.

At present, many detection methods are used to detect the exoplanets viz., radial

velocity, transit, microlensing, direct imaging, astrometry, timing, etc. The important methods are discussed in subsequent sections. To date around 3000 confirmed exoplanets are detected around various stars. Figure 2.1 illustrates the number of discovered exoplanets with respect to discovered years.
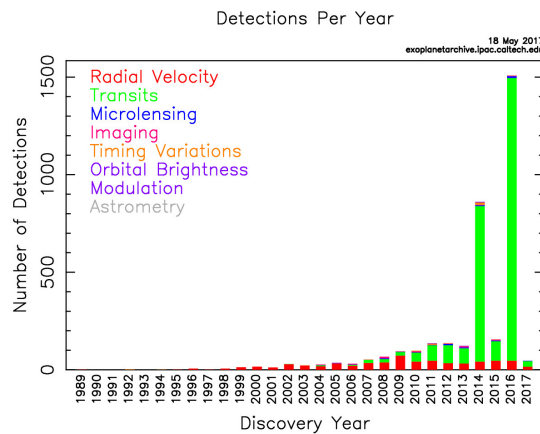
Fig. 2.1 Illustrates the Number of Confirmed Detected Planets For Different Years of Discovery. Image Credit: NASA Exoplanet Archive

2.2 Importance of Studying the Exoplanets

Until 1995, the only known planetary system is the Solar system. Earlier theoretical studies (Beauge and Aarseth 1990, Hartmann 1985, Hayashi 1981) of planetary formation were mainly concentrated on understanding the structure of the Solar system planets. According to previous studies, terrestrial planets were formed within a *snow line* (the region around a star where water can exists in liquid form) due to intense radiation from the stars in earlier stages. Similarly, all giant planets were formed beyond the snow line, because, due to less intense radiation from a star, more gas and dust particles can exist to form a planet. In the case of Solar system, *snow line* exists around 5 AU from the Sun (Jewitt et al. 2007). As explained in the earlier section, discovery of the first exoplanet changed the view of planetary formation. Until then nobody has expected a high mass planet (0.5 M_J) orbiting a star with a short period orbit (4.2 days). Discovery of similar kind of exoplanets in succeeding years lead us to rethink on the models of planetary formation.

At present, around 3000 exoplanets are discovered. Figure 2.2 illustrates the dis-

tribution of planetary masses with respect to their orbital periods. From this figure, apparently there are three branches of exoplanets viz., massive planets orbiting far from the host stars, massive planets orbiting near to the host stars, and low/intermediate mass planets orbiting within a range from less than one day to 200 days. The reason for such a three major classification of exoplanets is yet to be understood. Probably, all such detected exoplanets might have different formation mechanisms before attaining a stable structure. Some of the key problems that have to be answered by the physical and orbital characteristics of exoplanets are:

- whether all the planets/planetary systems have a typical Solar system like architecture.

- understanding the evolution history of Earth-like planets and how often one can detect them.

- understanding the interior, atmosphere and chemical composition of wide range of exoplanetary subgroups.

As mentioned in one of the afore mentioned key points, there are subgroups in the exoplanets viz., hot Jupiters, super-Earths, Super-Neptunes, etc., whose genesis need to be understood properly. Hot-Jupiter is a planet with mass ≥ 1 Jupiter mass orbiting very close (≤ 0.01 AU) to host star. Super-Earth is a planet with significantly larger than Earth with a mass less than 10 M_E. Super-Neptune is a planet which is massive than Neptune with a radius 5-7 times the Earth's radius.

In addition to all these more detailed scientific queries, one common question that arises in the minds of humans is the existence of extra-terrestrial life. Unlike Hollywood, if we could manage to find a primitive bacteria outside the Solar system, then it gives us a hope that we are not alone in this universe. The search for extraterrestrial intelligence (SETI) is one such team working towards the search for existence of life in the universe.

One can easily notice from the Figure 2.2 that, majority of exoplanets are discovered by using the *radial velocity method* and *transit method*. The planets discovered with the help of *microlensing method* and *direct imaging method* are detected if planetary orbital

period ≥ 1000 days. One can also notice that majority of planets discovered by using the transit method have very small orbital periods (~ 100 days). In addition, there are less crowded region in the Figure 2.2 that might have planets, but due to limitations in the present detection methods they might not have been discovered yet. Hence, one can say that different methods have their own pros and cons in discovering and characterizing the exoplanets. The details of detection and characterizing techniques of exoplanets are discussed in the next section.
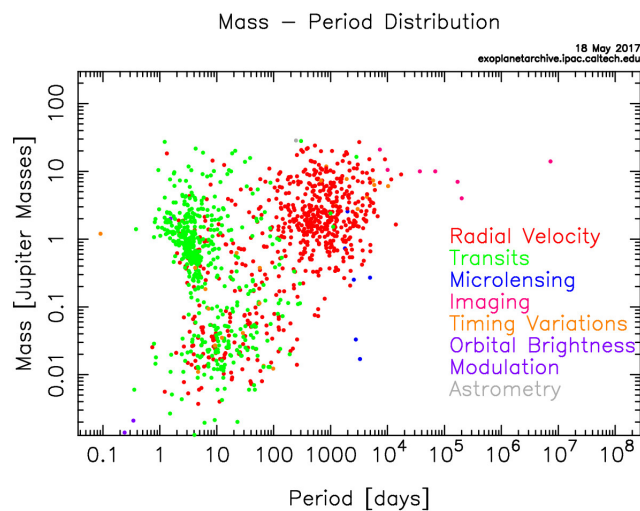
Fig. 2.2 Illustrates the Distribution of Planetary Masses With Respect to Orbital Periods of Presently Detected Exoplanets Discovered Until 18 May 2017. Image Credit: NASA Exoplanet Archive

2.3 Different Detection Methods And Characterization of Exoplanets

As mentioned in the earlier section, most of the exoplanets cannot be observed through ordinary telescopes. This is because, the reflected light from an exoplanet is very much fainter ($\sim 1/5000$) than the light from its host star. Therefore, many indirect methods are implemented to detect the exoplanets.

2.3.1 Radial Velocity (RV) Method

Radial velocity method is a technique in which the variations in the distance of an object is measured with respect to a reference point. In case of astronomy, Earth is considered as the reference point and radial variations of celestial objects are measured with respect

to it. The fundamental theory used in radial velocity technique to measure the spectral line variation of celestial objects is *Doppler theory*. According to Doppler theory, the frequency (or wavelength) of radiation emitted from an object increases (or decreases) as object approaches (or recedes) the reference point.

In astronomy, most of the times, these shifts can be observed only in case of binary systems, where two bodies are orbiting around a center of mass. During the late 19th and early 20th century, this technique is used to estimate the stellar masses in a binary system. By 1953, radial velocity measurements are taken for more than 15,000 stars (Wilson 1953), with a typical precision of 750 m s^{-1}. During the same period, *Struve (1952)* proposed that Jupiter like planets orbiting nearer (~ 0.02 AU) to their host stars can be detected via high precision radial velocity technique. However, during those days it did not get much attention. Later, in 1995 first exoplanet was discovered using radial velocity technique (Mayor and Queloz 1995).

Similar to a binary stellar system, when a star and planet orbit around their common center of mass, we observe a periodic shift in the spectral lines of a star in the stellar spectrum. Since exoplanet does not emit light, we can observe the spectral lines from a star alone. The motion of these two objects follow gravitational two-body problem orbiting each other in an elliptical orbit with a center of mass located at the focus. The fundamental equation between radial velocity and position of the orbit is given by

$$v_r = K[cos(\omega + f) + ecos\omega], \tag{2.1}$$

where, v_r is radial velocity of star at a distance r from the center of mass, K is semi-amplitude of radial velocity, e is eccentricity, ω angle between periastron direction and line of node and, f is the true anomaly. Value of K can be derived as $(v_{r,max} - v_{r,min})$/2 and

$$K = \sqrt{\frac{G}{1-e^2}} M_p sini (M_\star + M_p)^{-1/2} a^{-1/2}, \tag{2.2}$$

where, G is universal gravitational constant, $M_P \sin i$ is minimum planetary mass, i is the inclination angle between line of sight and objects position in the orbit, $M_\star$ is stellar

mass and a is semi major axis. Alternatively, by using Kepler's third law and assuming $M_p \ll M_\star$, above equation can also be written in more general form as

$$K_1 = \frac{28.432}{\sqrt{1-e^2}} \frac{M_p sini}{M_J} \left(\frac{M_\star + M_p}{M_\odot}\right)^{-2/3} \left(\frac{P}{1yr}\right)^{-1/3} ms^{-1}, \qquad (2.3)$$

where M_J is mass of the Jupiter, $M_\odot$ is mass of the Sun, and P is orbital period of the planet.

The preliminary physical parameters that can be estimated through the radial velocity method are orbital period (P), semiamplitude (K) and eccentricity (e). From these results and using equation 2.3, one can estimate the planetary minimum mass ($M_p sini$) with a reasonable assumption ($M_\star \gg M_p$). Since the inclination angle i is unknown, true mass of a planet cannot be estimated, which is important drawback of radial velocity method. However, for $i = \pi/4$ is generally used to calculate the planetary mass. The stellar mass can be estimated by using different methods as explained in the Chapter 4.

As explained earlier, the stellar radial velocity of star-planet around center of mass produces shifts in the spectral lines of the star's spectrum. From observers frame of reference, when a star is receding away with a velocity v and angle θ, changes in the wavelength ($\delta\lambda = \lambda_{obs} - \lambda_{em}$) is related to velocity with an equation given by

$$\lambda_{obs} = \lambda_{em} \frac{1 + \beta cos\theta}{(1 - \beta^2)^{1/2}}, \qquad (2.4)$$

where λ_{obs}, λ_{em} are the observed and emitted wavelength, and $\beta = \frac{v}{c}$. For $v \ll c$, and $\theta \ll \pi/2$ above equation takes the form

$$v_r = vcos\theta \approx \frac{\delta\lambda}{\lambda_{em}}c. \qquad (2.5)$$

There are many perturbations included in the measurement of radial velocities that are caused by gravitational redshifts, line asymmetries, blueshifts due to convections, etc. These effects introduce unknown errors up to ~ 1 m s^{-1} in the measured values for solar-type stars.

2.3.1.1 Limitations of The Radial Velocity Method

As explained earlier, since the inclination angle i cannot be measured from this method, the true mass of a planet remains unknown. This is one of the major limitations of the radial velocity method. In addition, many errors are introduced to the precision of radial velocity measurements by the different stellar physical and magnetic activities that are known as "stellar noise."

As the Sun-like stars possess an outer convective envelope, these stars produce p-mode oscillations at their surface. The typical periods for these oscillations are few minutes and typical amplitudes per mode are one meter per second in radial velocity (Bouchy and Carrier 2001). The observed radial velocity curves consist of the signals from these oscillations that make variations in RV curve accurate upto several meter per second. These oscillations increase with increasing stellar mean density, while RV signals increase with luminosity (L) to mass (M) ratio. Hence, oscillation periods are longer in early-type stars and due to their large L/M ratio, RV amplitudes are higher for early-type and evolved stars. Hence, low mass and non evolved stars are the best target stars for the search of exoplanets due to their less noise levels contributed from the p-mode oscillations. In addition, surface of the Sun and Sun-like stars filled with the *granulations and supergranulations*. Basically, these granulations are consequence of convective motion of gas such that it shows brighter upflows and darker downflows on the stellar surface. The typical velocities for these convective gas is around 1-2 km s^{-1}. Large number of granulations on the stellar surface average out the velocity field, but the jitter due to granulations is around few meter per second level (Palle et al. 1995).

The stellar magnetic activity also has its own influence on the noise level of RV signals through the starspots that have similar characteristics of Sunspots. These starspots appear randomly on a star's surface, evolve in time and co-rotate with the stellar rotation. The magnetic flux of these regions is less compared to the magnetic flux of other regions on the surface of a star. Therefore, as the star rotates, spots move from blueshifted to redshifted spectrum, that introduces variations in the measured amplitude of RV signals on timescale comparable to the star's rotation period. As mentioned earlier, the star spot magnetic flux varies with time. Like stellar rotation, magnetic ac-

tivity is very high for a star in its early evolutionary stages and gradually decreases as it evolves. Hence, stellar activity is a main problem while finding the signature of an exoplanet around a young star by causing RV variations about 10-100 m s^{-1}. The observation of a young star in the infrared region might be a possible solution for these limitations, because the influence of dark spots in these wavelength region is less than the visible region. Due to these difficulties, most of the astronomers focus on the old and slow rotating Sun-like stars for planet hunting.

2.3.2 Transit Method

Until 2009, majority of the exoplanets were discovered by the radial velocity method. From 2009 onwards, transit method is one of most successful method in detecting more number of exoplanets. Two most well-known space probes namely, *CoRoT and Kepler*, are succeeded in detecting majority of exoplanets through transit method. If one takes into account from the ground and space based observations, majority of exoplanets are detected by the transit. Hence, transit method is most successful detection method for exoplanet. In the following, we explain in detail the transit method.

When an object passes in between a star and an observer, it blocks the light from that star which results in dimming of star. This is the main principal behind the transit method. For example, since eclipses are also a type of transit, in case of solar eclipse, Moon blocks almost all the light coming from the Sun. This is because, the apparent size of Moon in sky is comparable with the size of Sun. However, in case of Venus transit during 2004 and 2012, since the apparent size of Venus is very small compared to size of the Sun, it blocks a small fraction of light as illustrated in Figure 2.3.

Similarly, as the exoplanets orbit around their host stars in line of sight to the observer, such planets periodically block minute fraction of light from the host stars. This periodic dip in the stellar flux is signature of the exoplanets that orbit around the host stars. Like transit, when an exoplanet goes behind the host star while orbiting, we call it as *occultation*. During occultation, we get only light from the host star. The process of transit and occultation are illustrated in Figure 2.4

During the transit, amount of flux blocked by a planet depends on the size of that
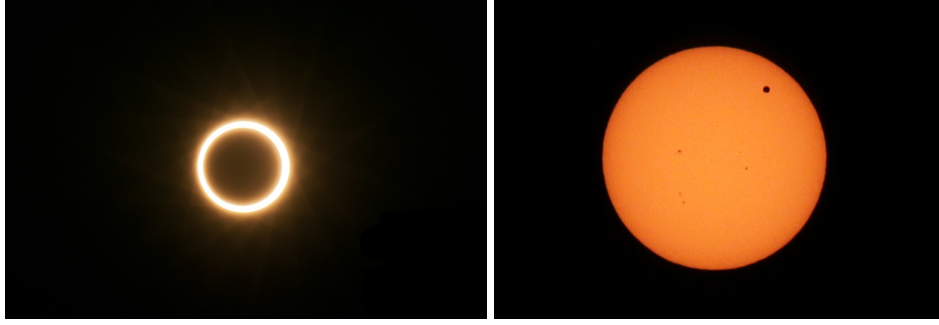
Fig. 2.3 Illustrates the Examples of Transits by Moon (Left Side Image) and Venus (Right Side Image) for the Sun. Image Credit: NASA.
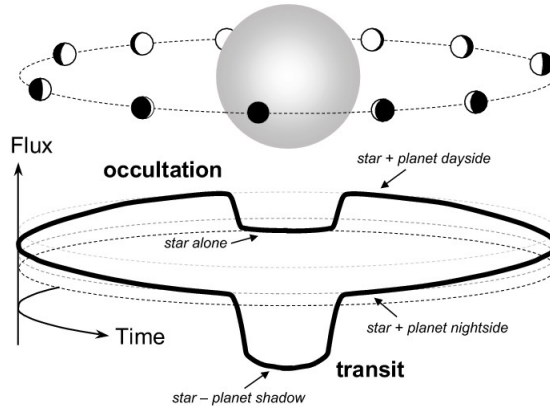
Fig. 2.4 Two Figures Illustrate The Transit And Occultation of a Planet That Orbits a Star. Image Credit: Winn (2010).

planet. The change in flux δf to that of stellar flux f is related with an equation given by

$$\frac{\delta f}{f} = \frac{R_p^2}{R_\star^2},$$

(2.6)

where R_p and $R_\star$ are planetary and stellar radii respectively. Hence, radius of an exoplanet can be accurately estimated by using this equation if one knows the radius and flux of a host star. The transits can be seen only when the star-planet system is nearly in edge-on. The shadow of a planet that orbits a star forms a cone on the celestial sphere as illustrated in Figure 2.5. The opening angle (θ) of the cone satisfies the condition $\theta = (R_\star + R_p)/a$, where a is orbital distance of a planet. This cone is called as penumbra inside of which transits are grazing. There is also an inner cone called antumbra, satisfy the condition $\theta = (R_\star - R_p)/a$, inside of which transits are non-grazing. The

information about e and ω of a planet can be estimated from Radial velocity method but not the inclination (i) of a planet, hence no information about eclipse is available. With reference to Figure 2.5, observer's celestial longitude is denoted by ω. The transit probability (p_{tra}) is calculated as the shadowed fraction of line of longitude, or more simply from the requirement $|b| \leq 1 + k$, where b is impact parameter as explained later in this section, and the knowledge that $\cos i$ is uniformly distributed for a randomly placed observer. If one may want to marginalize over all possible values of ω, then one can calculate the solid angle of the entire shadow band and divided by 4π (Winn 2010) giving

$$p_{tra} = \left(\frac{R_\star \pm R_p}{a} \right) \left(\frac{1}{1 - e^2} \right), \qquad (2.7)$$

From the above equation it is to be noted that, probability of transit of an exoplanet increases with decreasing its orbital distance.
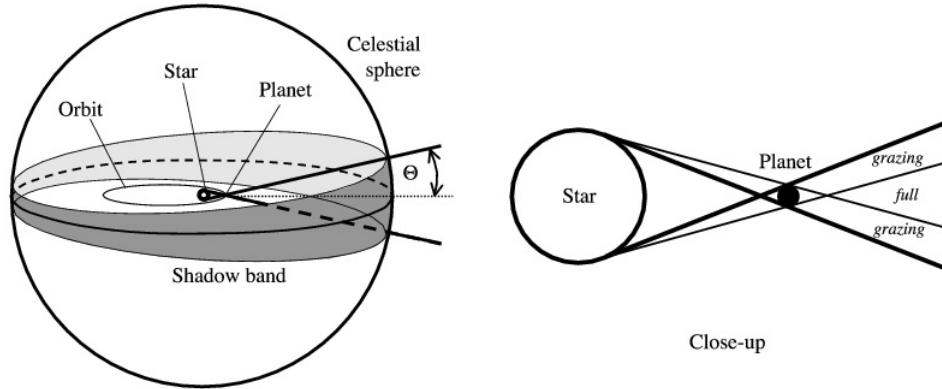
Fig. 2.5 Left side figure illustrates the geometry of planetary transits. The transits are visible if the observers are within the cone with opening angle θ. Right side figure illustrates grazing and non-grazing part of planetary transits.

Another important parameter known as *impact parameter* denoted by b, can be defined as the sky-projected distance between center of the star and center of the planet, which can be estimated from an equation given by

$$b = \frac{a \cos i}{R_\star} \left(\frac{1 - e^2}{1 + e \sin \omega} \right), \qquad (2.8)$$

where all the parameters are as defined earlier. The impact parameter has a significant

role in estimating the total transit duration, which is defined as the time during which any part of the star will be covered by a planet. Figure 2.6 graphically illustrates the transit time durations. The contact points t_I and t_{IV} are the beginning and end-time of a transit event respectively. Similarly, t_{II} and t_{III} are the beginning and end-time of a total transit event respectively. The total transit duration $T_{tot} = t_{IV} - t_I$. One can notice from the Figure 2.6 that transit duration is maximum if $b = 0$ and, it decreases as b increases. The length that planet has to travel across the stellar disk is given by

$$l = \sqrt{(R_\star + R_p)^2 - (bR_\star)^2}.$$ (2.9)

By using above equation and an assumption of circular orbit (distance around entire orbit is $2\pi a$) around the star with a simple geometry, the total transit duration can be estimated by an equation given by

$$T_{tot} = \frac{P}{\pi} sin^{-1} \left(\frac{\sqrt{(R_\star + R_p)^2 - (bR_\star)^2}}{a} \right).$$ (2.10)
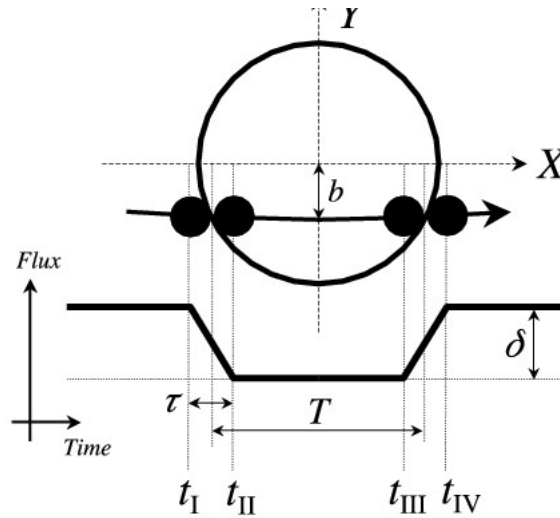
Fig. 2.6 Illustrates The Description of Beginning And End of a Transit of an Exoplanet. Image Credit: Winn (2010).

In addition, limb darkening is another factor affecting the transit events. During planetary transits, limb darkening causes larger flux decrease when a planet is at the center of a star than the planet is at edges of star. Since light has to travel more at

edges of star's disk, it come across cooler temperature at higher latitude of atmosphere. Hence, the resulting intensity profile I(X,Y) is described as

$$I \propto 1 - u_1(1 - \mu) - u_2(1 - \mu)^2, \tag{2.11}$$

where $\mu \equiv \sqrt{1 - X^2 - Y^2}$, X and Y indicate the coordinates and, (u_1, u_2) are constants that can be estimated from the atmospheric models. One can also relay on the fact that, light loss due to limb darkening depends on the frequency. Hence, one can also observe the transits at longer wavelengths to get-rid of limb darkening.

One should note that, the transit light curve alone will not help us to estimate the absolute physical and orbital parameters of an exoplanet. The transit light curve only reveals the information related to planet to star radius ratio ($R_p/R_\star$) and its orbital period (P). In order to estimate the planetary mass, one must also have the radial velocity signature of the planet, particularly the semiamplitude (K) value. By using the equation of semiamplitude in a barycentric motion and using Kepler's third law of motion, mass of a planet can be estimated by

$$\frac{M_p}{(M_p + M_\star)^{2/3}} = \frac{K_\star \sqrt{1 - e^2}}{sini} \left(\frac{P}{2\pi G} \right)^{1/3}. \tag{2.12}$$

Since the orbital inclination i of an exoplanet can be estimated from the transit method, absolute planetary mass of an exoplanet can be estimated. In addition, due to the assumption of $M_p \ll M_\star$, one can estimate the $M_p/M_\star^{2/3}$ but not absolute mass. The combination of stellar mean density ($\rho_\star$) and planetary mean density (ρ_p) can be estimated with the help of scaled stellar radius ($R_\star$/a) by using an equation (Seager and Mallen-Ornelas, 2003)

$$\rho_\star + k^3 \rho_p = \frac{3\pi}{GP^2} \left(\frac{a}{R_\star} \right)^3, \tag{2.13}$$

where k is $R_p/R_\star$ and all other symbols have their usual notation. In addition, planetary surface gravity g_p can be estimated by using the following equation (Southworth et al 2007)

$$g_p = \frac{2\pi}{P} \frac{\sqrt{1-e^2}K}{(R_p/a)^2 sini}.$$
(2.14)

Hence, using transit method one can accurately estimate the planetary surface gravity and stellar mean density. However, the uncertainties in planetary mass and radius depend on the stellar properties. Furthermore, spectroscopic measurement of a transit can help us to estimate the chemical composition of exoplanets atmosphere. Hence, one can also deduce the atmospheric composition of a transiting exoplanet. In addition, stellar rotation imposes the Doppler shift variations on the spectral line. That means, light from the approaching side of stellar disk blueshifted whereas, light from the receding side of the stellar disk is red shifted. During transit, when a planet covers the blueshifted part of the stellar disk, the integrated star light appears red shifted and *vice versa*. This effect is known as *Rossiter-McLaughlin (RM) effect*.

2.3.2.1 Transit Time Variation

Although majority of detected planets are known as single planetary systems, from the Solar system one can infer that there might be more number of planets in each stellar system (stars with planets) that might be discovered by improving the precision of current detection limits. In multiplanetary systems, the planets' motion is not only affected by the gravitational force of central star, but it is also affected by the gravitational force of another planet orbiting the same star. In case of transits, the gravitational perturbations due to another planet, changes the mid transit time, which is variations in the position of an exoplanet when it is at the center of stellar disk at each orbit. This effect is known as *Transit Time Variations*. The Figure 2.7 illustrates the variation of mid-transit times for the single and multiplanetary systems by taking the examples of Kepler-4 b and Kepler-36 c respectively.

In addition to inferring the existence of another planet, one can also estimate the combined mass of both the planets by means of several ways that depending on characteristics of orbits. The maximum transit timing deviation δt_{max} can be estimated by using following equation
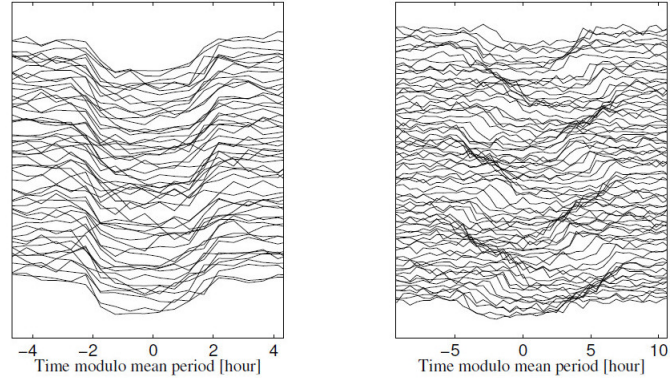
Fig. 2.7 Illustrates the Variation of Mid-Transit Time during TTVs. Image Credit: Winn (2010).

$$\delta t_{max} \approx \frac{P_1}{4.5j} \frac{m_2}{m_1 + m_2}, \qquad (2.15)$$

where j is the order of resonance, P_1 is the average time between transits, m_1 and m_2 are mass of the transiting planet and other planet respectively.

2.3.3 Microlensing Method

Microlensing method of detecting an exoplanet is based on the concept of gravitational lensing. In the gravitational lensing, the matter present between the observer and a distant light source is capable of bending the light from the source, that results in brightening the source. In 1936, Einstein derived the equations of microlensing by a foreground star aligned with a background star (Einstein 1936). This technique is suitable for detecting Earth-like low mass planet orbiting around a distant faint star or planet orbiting very far from its host star.

In microlensing technique, the foreground star and background star are called as lens and source respectively. The basic idea of detection of planet using this technique is, as the lens star passes close to the line of sight of background star, it distorts the image of a background star and split it into two images as shown in left side illustration of Figure 2.8. These distorted images form a curved path as the lens star passes in front of source star, and these two images have a typical separation of 1 mas, hence, unresolved. The total curved path during an entire period of an event forms a ring

51

around the source which is known as *Einstein ring*. However, the combined area of these two images (Einstein ring) is larger than the area of source, hence, we observe a change in brightness of source with respect to time as illustrated in right side illustration of Figure 2.8. If the lens star has a planet that orbit near the paths of distorted images, the planet further distort the image which leads to a short-lived signature (a sudden spike in the magnitude-time illustration) of a planet.
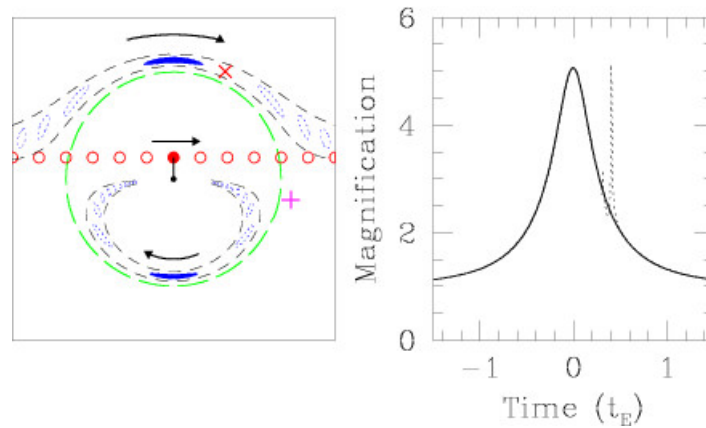
Fig. 2.8 Illustrates the Description of Microlensing of an Exoplanet. Image Credit: Gaudi (2010).

Consider an observer (O), lens (L) and source (S) as indicated in Figure 2.8. The lens and source are separated by a distance D_L and D_S from the observer respectively. The point mass M at L deflects the light by an angle α given by

$$\alpha = \frac{4GM}{hc^2} \tag{2.16}$$
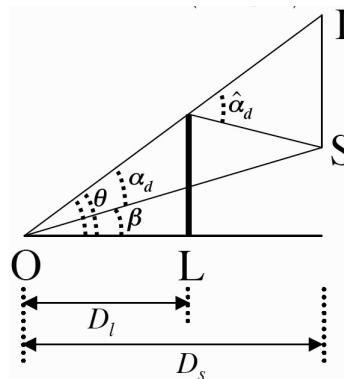
Fig. 2.9 Illustrates the Ray Diagram of Microlensing Event. Image Credit: Gaudi (2010).

where h is distance from lens mass to undeflected light ray with lens plane. One can notice from the Figure 2.8 that θ and β are the image and source positions w.r.t. line between O and L and, γ is angle between image and source which is given by

$$\gamma = \frac{D_S - D_L}{D_S}\alpha \approx \frac{\theta_E^2}{\theta} \qquad (2.17)$$

where

$$\theta_E = \sqrt{\frac{D_S - D_L}{D_S D_L}\frac{4GM}{c^2}}, \qquad (2.18)$$

which is known as Einstein radius. When β=0 in lens equation, the Einstein radius is given by $\theta = \theta_E$. By normalizing all the angles to Einstein angle, by defining $u = \beta/\theta_E$ and $y = \theta/\theta_E$ with some algebra one can get the equation for images given by

$$y_\pm = \frac{1}{2}(\sqrt{u^2 + 4} \pm 4). \qquad (2.19)$$

Among these two images, positive image will be always outside the Einstein ring and negative image will be always inside the Einstein ring. The amplified brightness of source during microlensing event is given by

$$A(u) = \frac{u^2 + 2}{u\sqrt{u^2 + 4}}. \qquad (2.20)$$

From this above equation, one can note that magnification is maximum when u=0. In these events, the value of u can change significantly within a short period time which is known as Einstein time t_E. The Einstein time is defined as time taken by lens to traverse an angular distance relative to the source, which is given by

$$u(t) = \sqrt{\frac{(t - t_0)^2 + u^2}{t_E^2}}, \qquad (2.21)$$

where u_0 is maximum brightness of event at time t_0, t_E is time taken to cross Einstein radius given by $t_E = \theta_E/\mu_{rel}$, μ_{rel} is proper motion of source relative to lens. If the foreground star consists of a planet, and it happens to be near the path of images, then it will create a perturbations on the primary microlensing events as shown in Figure

2.7. The duration of perturbation is given by $t_{E,p} = q^{1/2} t_E$, where $q = M_p M_\star$ and the magnification depends on the distance between the planet and image. The advantages of microlensing techniques are

- this technique is more sensitive to small mass planet than the other techniques.

- it is more sensitive to planets with orbital size of few AU.

- from this technique one can easily detect multi planets in a single light curve.

The limitations of this method are

- More number of stars have to be monitored continuously to find microlensing of few stars.

- the perturbation of light curve due to planet will not repeat.

- these planetary perturbations are short lived, so that they can be missed out easily.

2.3.4 Direct Imaging Method

Direct imaging is the only method where an exoplanet is captured using a telescope in the visible region. After 12 years of detection of first exoplanet, capturing of image of an exoplanet was successful in 2008 (Marois et al. 2008). Direct imaging of exoplanets is very difficult owing to the fact that the exoplanets do not emit light as stars do, instead they reflect the star's light and, the high contrast ratio between the star's light and planet's reflected light. On the other hand, the direct imaging technique is very useful when a planet is massive/huge at a large orbital distance. It is highly difficult to capture the image of hot-jupiters, because their orbital distances are very small. Thus, it needs very high angular resolution to separate the planet from a star. Therefore, the young planets orbiting in a protoplanetary disk are the prime candidates for direct imaging method. These young planets not only are situated far from the host star, but also have high temperature and large size. Direct imaging is also suitable for the nearby stars rather than distant stars. In addition, the spectroscopic analysis of reflected light coming from the planet reveals about the clouds, atmospheric structure and chemical composition (Burrows and Orton 2010, Meadows and Seager 2010).

In the direct imaging technique, the photon counts both from a planet and parent star are important, because this information yields the contrast of a planet. In this case, the *contrast* C is defined as the ratio of planet's brightness to the star's brightness, which is expressed as a ratio:

$$C = \frac{f_\lambda(p)}{f_\lambda(s)} = \frac{\dot{N}_\lambda(p)}{\dot{N}_\lambda(s)}, \quad (2.22)$$

where $f_\lambda(p)$, $f_\lambda(s)$ indicate the intensity flux from a planet and its host star respectively, as a function of apparent magnitude in a particular wavelength (λ) region. The same ratio can be expressed in terms of photon fluxes such that $\dot{N}_\lambda(p)$ and $\dot{N}_\lambda(s)$ are the photon flux of a planet and host star respectively. The photon flux $\dot{N}_\lambda$ at a particular wavelength is mainly dependent on the effective temperature of the object and solid angle $\Omega = \pi(r/d)^2$ steradian, where 'r' and 'd' are radius and distance of an exoplanet from its host star.

By using Kepler's third law, one can easily estimate the semi-major axis a, furthermore eccentricity e can also be estimated. If one knows the distance (d) of a star, then maximum angular separation of planet from the host star can be estimated by using following equation:

$$\theta = a(1 + e)/d, \quad (2.23)$$

where θ is angular separation in $arcsec$, a is in AU and d is in parsec.

The spectrum of a planet consists of light reflected from the host star, thermal emission and other features. The visible brightness of a planet is known as *geometric albedo* which is defined as the ratio of flux reflected from the planet at zero phase angle to flux from the host star that is incident on the planet. Similarly, one can also estimate *Bond albedo* (A_{Bond}) which is the fraction of luminosity reflected from the planet when stellar luminosity is incident on the planet. When flux (f) of a star traveled through a distance a and incident on a planet, part of it get absorbed and radiated again. From this radiated flux, the radiative equilibrium temperature of planet can be estimated using an equation given by

$$T_{equil} = \left(\frac{1 - A_{Bond}}{4f} \right)^{1/4} \left(\frac{r_s}{a} \right)^{1/2} T_s, \tag{2.24}$$

where T_s is temperature of a star, r_s is stellar radius and all other symbols have their usual notations.

Direct imaging method also has its pros and cons like other exoplanetary detection methods. The main advantage of direct imaging is the reflected star light coming from the exoplanet. Spectroscopic analysis of light from the exoplanets in broad and narrow wavelength band helps us to measure the different physical and orbital parameters of exoplanet viz., mass, radius, temperature, rotation rate, atmospheric characteristics, etc. Similarly the main disadvantage of this method is high contrast of star. Hence, through this technique, it is very difficult to capture the image of an exoplanet around a distant star. The direct image of an exoplanet is given in the Figure 2.10.
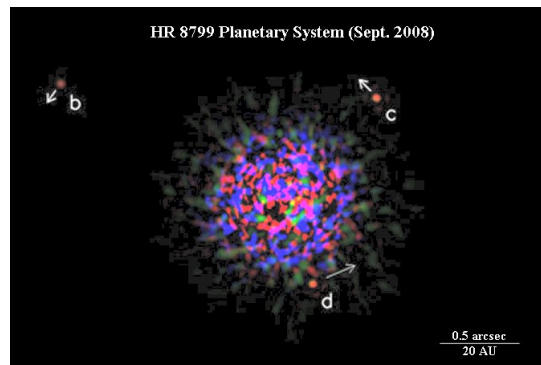
Fig. 2.10 Illustrates the Direct Image of Exoplanets Around a Star HD8799. Image Credit: Marois et al. (2008)

2.4 Challenges of the Exoplanetary Systems

2.4.1 Observational Challenges

Exoplanetary field is mainly driven by observations. As we have discussed in the beginning of this chapter, earlier many attempts were made for detection of planets outside the solar system. Struve (1952) was the first person to propose that detection of massive planet can be possible if the radial velocity precisions are improved. After almost four decades later we succeeded in detection of planet around Sun-like star (Mayor and

Queloz 1995) by radial velocity method. Similarly, with the help of transit method we have succeeded to detect low mass planets that orbit near the host stars. However, as we move away from the host stars, both probability of planetary transit and radial velocity amplitude decreases. Mainly detection of low mass planets between 5-30 AU is the main challenge to current observational astronomy. Microlensing is the favorable method for detecting such low mass planets orbiting at distance more than 5 AU. But it needs continuous monitoring of a star for longer period and it is one time phenomenon. In addition, detection of free-floating planet is possible through microlensing method. This will increase in understanding the mechanism of planet formation beyond the snow line. Hence, increasing the precisions of different detection techniques to a higher level, will increase the counts of exoplanets that might have different physical and orbital characteristics. In addition, with the precision improvement, one can also fill the less crowded/empty regions that are present in Figure 2.2 that helps in understanding the planetary formation.

One should also note that estimation of different physical and orbital characteristics of exoplanets needs accurate measurement of stellar properties. Errors in the stellar physical parameters have their own influence on the accuracy of exoplanetary parameters. For example, in transit technique, the preliminary information that we get from the light curve is ratio of planet's radius to star's radius. If star has an uncertainty of 30% in its radius, then this uncertainty in turn affects the accurate estimation of planet's radius. Hence, in oder to estimate the accurate physical and orbital properties of exoplanets, one should precisely observe and study the host stars. Asteroseismology is one promising technique that helps in precise measurement of stellar parameters. Astrometry is also one of the detection method of exoplanet from which absolute planetary mass can be estimated. However, this technique is useful only for nearby stars, because for distant star, it is highly difficult to measure the variations. Improving this technique will also helps in accurate measurement of radius and distance of the star and also confirms the binary systems.

2.4.2 Theoretical Challenges

As explained earlier in this chapter, before the detection of first exoplanet, all the planetary formation theories were proposed on the basis of Solar system's planetary architecture. Before the detection of first exoplanet, majority of people never expected a Jupiter like planet in a short period orbit ($\leq$ 10 days). However, detection of exoplanets with the wide range of physical and orbital characteristics viz., hot-Jupiters, planets with more eccentric orbits, compact orbits than the solar system planetary orbits, etc., gave us a new insight on planetary formation theories. Although, people proposed the new theories and contributed towards understanding of planetary formation, still there exist few unsolved problems which need a rigorous study. One such unsolved problem is understanding the origin and formation of hot-Jupiters and giant planets. Any theory which explains the formation of giant planets should also explain the origin of four gas giants of Solar system. A study by Udry and Santos (2007) shows that occurrence frequency of giant planet and stellar metallicity has a strong correlation. *Core accretion models* (Seager 2010, and references therein) predict this trend while *Disk instability models* (Boss 1997) are not. Hence, one has to understand the role of stellar metallicity and the amount of dust particles in the protoplanetary disk towards understanding the planetary formation.

Similarly, migration of planets occur during the early stages of planetary formation mainly because of the interaction between young planet and gaseous disk from which they are formed. It is showed that (Seager 2010), low mass planets undergo Type I migration, because density of disk is unaffected by the presence of mass. Whereas, the high mass planets undergo Type II migration where presence of planet alters the density of disk (Lubow and Ida 2010, and references therein). Previous studies (Cumming 2010, Winn and Fabrycky 2015, Triaud 2016, and references therein) came to a conclusion that giant planets are formed far away from the host star, then migrated inward and formed as hot-Jupiters by tidally locking with the parent stars. However, still one has to investigate the stopping mechanism of inward migration. It is also interesting to know the role of magnetic field structure during the initial stage of planetary formation.

CHAPTER 3

Missions for Detection of Exoplanets

In the previous chapter, we have briefly described the different detection techniques of exoplanets. Many people all over the world are trying to detect more exoplanets to understand their evolution and also to search for habitable planets elsewhere in the universe. In the last two decades, many ground and space based missions were launched for exoplanetary search. In the following we briefly describe different ground and space based few such exoplanetary missions and their instrumentations.

3.1   Ground Based Observations

3.1.1   High Accuracy Radial Velocity Planet Searcher (HARPS)

High Accuracy Radial Velocity Planet Searcher, in short HARPS is a high precision radial velocity planet finder installed on ESO's 3.6 m telescope at La Silla Observatory in Chile. It is fiber-fed echelle spectrograph, works on the principles of radial velocity method. By measuring the radial velocity profiles of host stars with a high precision of 1 m/s, this instrument helps us to detect the low mass exoplanets.

The instrument is placed in a vacuum chamber with highly controlled temperature (17° C with a variation of 0.01^o C) and pressure (below 0.01 mbar), so that the spectral drifts should not affect the precision. Between two fibers, one of the instrument collects the light from a star and another fiber is used to measure simultaneously a Th-Ar reference spectrum. These two fibers have an aperture with a special resolution of 1 arcsec and a spectral resolution of 115,000. The spectral range covered by this instrument is from 380 nm to 690 nm. The detector consists of mosaic of two 2k4 CCD's with pixel size of 15 μm. Figure 3.1 illustrates the anatomy of HARPS spectrograph.
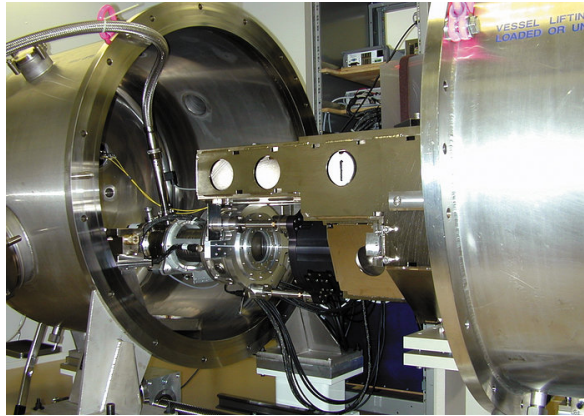
Fig. 3.1 Illustrates an Image of HARPS Spectrograph During Laboratory Tests. Credit: ESO.

The least mass of an exoplanet discovered by HARPS instrument is around 1.9 Earth mass[1]. This instrument is also used for follow-up measurements of exoplanets detected by space probes like CoRoT, Kepler etc. Through photometric measurements of space probes one can only estimate the radius of a planet. The planetary mass of those planets are measured by radial velocity techniques by HARPS. In addition to the planet finding, another science objective of HARPS instrument is to measure the seismic oscillations from the host stars that can be used to estimate the accurate stellar properties. This mission is led by Michel Mayor and the instrument made available to the scientific community from 2003 onwards.

3.1.2 High Accuracy Radial Velocity Planet Searcher for Northern hemisphere (HARPS-N)

The HARPS-N spectrograph is an analog of the instrument HARPS. This spectrograph also works on the principle of radial velocity method. HARPS-N is located in the Northern hemisphere and installed at the Telescopio Nazionale Galileo (TNG), a 3.58 meter Italian telescope which is located on La Palma, Canary Islands, Spain. The main scientific aim of this mission is to discover and characterize the low mass terrestrial planets by combining transit and radial velocity methods. Since it covers the northern hemisphere which consists of Cygnus and Lyra constellations, it can also be used for the follow-up study of Kepler mission exoplanet candidates. As for the instrumenta-

---

[1]http://www.eso.org/sci/facilities/lasilla/instruments/harps/science.html

tion, it resembles the HARPS. The HARPS-N Project is a collaboration between the Astronomical Observatory of the Geneva University (lead), the CfA in Cambridge, the Universities of St. Andrews, Edinburgh, the Queens University of Belfast and, the TNG-INAF Observatory.

3.1.3 Hanle Echelle Spectrograph - HESP

Hanle Echelle Spectrograph is a high resolution (R = 30,000 and 60,000) fibre-fed spectrograph installed at 2m Himalayan Chandra Telescope (HCT). It covers a wide range of wavelengths starting from 350 nm to 1000 nm. Coverage of broad range of wavelengths enables the detailed study of key elements in stellar nucleosynthesis. In addition, due to high mechanical stability and double fibre mode, it provides precise radial velocity measurements that helps to study the binaries, exoplanets and asteroseismology. The accuracy of radial velocity measurements is 20 ms^{-1} with double fibre mode. Observations are made for the objects brighter than the 11 magnitude.

A detailed study of different chemicals in stars and their abundances are necessary in order to understand the evolutionary status of star in HR diagram. Deriving chemical composition of a star requires unblended spectral lines with high resolution (R = 60,000) which is possible with HESP. Hence, stellar compositions can be well studied with this instrument. Furthermore, by using Doppler imaging technique (DPI), one can also study and monitor the star spots. DPI is most reliable tool to estimate the spatial distribution of temperature and chemical abundance at the surface of a star. In addition, oscillations from a star can also be measured accurately by this spectrograph that helps in exploring physics of the stellar interior and its chemical abundances. This spectrograph is developed by people from Indian Institute Astrophysics, Bengaluru in collaboration with IRL (Industrial Research Lab, Kiwi Star), New Zealand.

3.1.4 SuperWASP

SuperWASP stands for Wide Angle Search for Planets. It is a major planetary detection mission from UK. This mission is carried out by several academic organizations and, currently funded by Warwick University and Keele University. Between two ma-

jor observatories of this mission, one is situated on the island of La Palma known as SuperWASP-North and another is situated at the site of the South African Astronomical Observatory (SAAO), South Africa, known as SuperWASP-South that continuously monitor stars in the sky for periodic dip in their brightness i.e., it performs transit photometry.

Each observatory consists of eight wide-angle cameras with an aperture of 11.1 cm that allow us to monitor millions of stars continuously. These cameras are backed with the high quality CCDs of 2k x 2k. The field of view of these cameras is 7.8 x 7.8 degree with plate scale of 13.7 arcsec/pixel. The operating temperature is -50° C which is maintained by 3 stage peltier cooler. The amount of data collected by all the cameras each night crosses 50 gigabytes, which is automatically processed by the pipelines. The pipeline reduces the raw images by removing the noise, pixel sensitivity, dirt, etc., through flat-field, bias, and dark-current. Later, photometric analysis is carried out to measure the dip in the brightness of a star.

3.1.5   HATNet Project

The Hungarian-made Automated Telescope Network is a small exoplanet survey project used to discover the exoplanets through transit survey. This project make use of seven small telescopes that are connected geographically to measure the transit events. From 2003, till now there are 60+ exoplanets discovered by this project. Five of the HATNet telescopes are situated at the Fred Lawrence Whipple Observatory (FLWO) at Mount Hopkins in Arizona, USA, and another two are situated at Mauna Kea Observatory in Hawaii, USA. This large separation of basis of telescopes helps to monitor the sky continuously and consider better part of 24-hours which reduces the chance of false-positive. The telescopes with 200 mm f/1.8 lenses are attached to the large format of CCD cameras. All the operations are fully automated and make decision of which stars to be observed and at what time, based on the weather conditions.

3.2 Space Based Observations

3.2.1 CoRoT Space Telescope

The first space telescope launched towards the detection of exoplanets is the *CoRoT* in 2006. This mission is led by French Space Agency (CNES) in collaboration with European Space Agency (ESA). CoRoT stands for *Convection, Rotation and planetary Transits*. As the name "Convection and Rotation" indicates that, it helps us to probe the stellar interiors through the techniques of asteroseismology. As explained in the first chapter, frequency, amplitude and lifetime of these oscillation modes help us to determine important properties of the star like, its mass, radius, internal structure, rotation profile, etc. Similarly, the name "planetary transits" indicates the detection of exoplanets through the transit method. CoRoT was the first mission to detect rocky planets with a size of several times the Earth's size around nearby stars. CoRoT is most sensitive to the planets with orbital period ≤ 50 days. Initially, mission was scheduled for 2.5 years, but was extended up to 2013.

The CoRoT space telescope consists of a primary mirror with an aperture of 30 centimeter, wide-field two cameras - one for exoplanet search and another for asteroseismology which operates in the visible region. The field of view is square of 2.8 x 2.8 degree. Half of this area is used for asteroseismology and another half is for planetary transit. In addition, a prism is used to separate colors and utilizes to study the stellar activity during planetary transits.

Some of the notable planets discovered by CoRoT is Corot-7 b which is the first confirmed rocky planet with mass 7.3 M_E and radius 1.7 R_E (where M_E and R_E are mass and radius of Earth). CoRoT also discovered many hot-Jupiters namely Corot-10b, CoRoT-16b, CoRoT-20b and CoRoT-23b, with highly eccentric orbits. The detailed information on CoRoT data can be found in Baudin et al. (2006).

3.2.2 Kepler Space Telescope and K2

Kepler space telescope is a scientific mission, launched in 2009 to discover the Earth-size planets that probably orbit in a habitable zone around the host stars in Milky Way
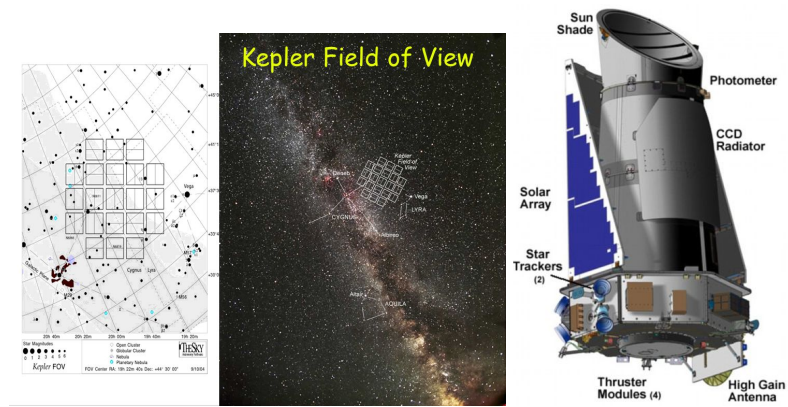
Fig. 3.2 Illustrates the Field of View and Anatomy of the Kepler Space Telescope. Image Credit: Nasa

galaxy. Kepler space telescope used the transit technique to discover the exoplanets around host stars. The photometer present in this telescope continuously monitors over 150,000 stars for detecting planets. The field of view for this telescope is fixed towards the constellations *Cygnus and Lyra*. Figure 3.2 illustrates the field of view of Kelper space telescope and anatomy of the telescope. Through Kepler science, one can also predict the fraction of stars in the Milky Way galaxy that might harbor the planets.

The main goals of Kepler space telescope are:

- to determine the fraction of stars that have Earth-like planets in their habitable zones.

- study the architecture of these planets in multiplanetary systems.

- to understand the mass, size and density of short period giant planets like hot-Jupiters.

- to estimate the accurate physical properties of host stars by using asteroseismic method.

The spacecraft consists of a primary aperture of 0.95 m and its field of view is 105 deg square. The photometer is composed of 42 CCDs with dimension 50x25 mm. Each CCD has a pixel density of 2200x1024. To prevent the saturation, each CCD is read out every three seconds. The spectral band pass for instrument is 400 nm to 850 nm. These collected data are stored and are transmitted to Earth once in a month. Initially this

mission was planned for the period of three and half years. However, due to high noise in the data and importantly, failure of two reaction wheels that were used for pointing spacecraft that lead to discontinuation of the Kepler mission in 2013.

In late 2013, a new proposal was accepted for utilizing the remaining power of Kepler telescope and named it as $K2$ "Second Light". The field of view in K2 mission is set towards the constellation *Lio-Virgo* and another field is set towards "head" of the constellation *Scorpius*. The main objectives of K2 mission are:

- detecting hot and cool planets around bright small stars whose transit spectroscopy helps us to understand their atmosphere.

- detect hot planets around young stars to understand the probable planetary migration scenarios during early evolutionary stages.

- estimation of stellar properties through asteroseismology.

3.2.3 Astrosat

Astrosat is the first Indian space telescope that observe the celestial objects in different wavelength bands simultaneously. Indian Space Research Organization (ISRO) launched this telescope on 15th September, 2015, from Satish Dhawan Space Centre, Sriharikota. This satellite revolves around the Earth in near-equatorial orbit around 650 km. Astrosat mission consists of five payloads for simultaneous observations at different wavelength regions. The five payloads present in Astrosat are:

- Ultraviolet Imaging Telescope (UVIT) - this covers the region from far-UV to optical. It has 28 arcmin diameter field of view and an angular resolution of 1.8" for UV channels and 2.5" for visible channels.

- Large Area Xenon Proportional Counters (LAXPC) - this instrument is used to study the low-resolution spectral studies and X-ray timings over an energy band of range 3-80 keV.

- Soft X-ray Telescope (SXT) - this instrument performs the X-ray imaging in 0.3 -8 keV energy band range.
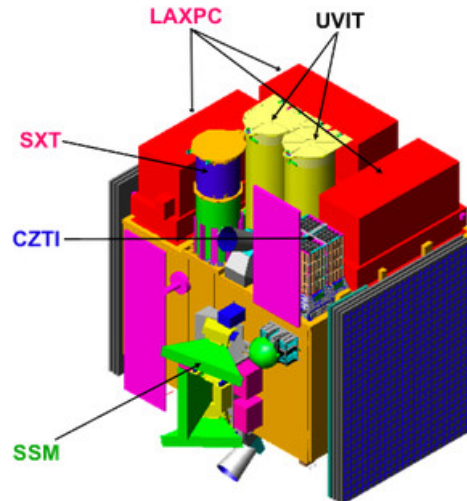
Fig. 3.3 Illustrates the Anatomy of Astrosat Telescope With Different Payload's On Board Position. Image Credit: ISRO

- Cadmium-Zinc-Telluride coded-mask Imager (CZTI) - It consists of Cadmium-Zinc-Telluride detector array of 1000 cm^2 geometric area with $\sim$ 100% efficiency. This covers the X-rays from 10-150 keV energy band range with 6 degree field of view.

- Scanning Sky Monitor (SSM) - It is used to locate the transient X-ray sources in the sky. To do so, it consists of a one dimensional proportional counters with coded mask.

Figure 3.3 illustrates the graphical picture of astrosat telescope with different payloads on board. Since, the astrosat is a multi-wavelength space observatory, one can also study the exoplanets and their host stars at different wavelength regions. For example, the interactions between stellar wind and magnetosphere of the exoplanets may produces the aurora that can be easily detected in UV regions. Observations of transit of many nearby exoplanets may give clues for such auroras that enhances the knowledge of magnetic field structure of exoplanets.

3.3 Future Space and Ground Based Probes for Detection of Exoplanets

3.3.1 James Webb Space Telescope

The James Webb Space Telescope (JWST) is a NASA's ongoing program in collaboration with the European Space Agency and Canadian Space Agency. It is scheduled to launch in October 2018. This telescope is positioned at the Sun-Earth Lagrangian point L2, which is ~ 1.5 x 10^6 km beyond the Earth. The James Webb Space Telescope will not only helps us to detect the exoplanets, in addition, one can also understand the formation of galaxies, stars, and planets. The main goals for the JWST can be categorized into four themes:

- With the strong infrared vision, this telescope is expected to catch the light from early universe that helps to understand the formation of stars and galaxies.

- High infrared sensitivity of JWST helps to compare the fainter, earlier galaxies with today's galaxies with different form.

- By observation of massive star forming regions, clouds of gas and dust particles, it enables us to study the stars and protoplanetary disks.

- Through transit observations of exoplanets, it enables us to study the atmosphere of exoplanets and study the building blocks of life elsewhere in the universe.

JWST offers high resolution and is sensitive from the visible region to mid infrared region. NASA called this telescope as a successor of Hubble Space Telescope. The diameter of primary mirror of JWST is 6.5 meters, which is almost five times higher light collecting area than the Hubble Space Telescope. The Integrated Science Instrument Module (ISIM) of JWST consists of following four main science instruments

- Near-Infrared Camera - It is a primary imager which covers infrared wavelength range from 0.6 to 0.5 microns. This camera is supplied with the coronagraphs that are used to observe the fainter objects by blocking the brighter objects. This camera is being built by the University of Arizona and Lockheed Martin.

- Near-Infrared Spectrograph - As the name itself suggest this instrument operates in the wavelength range 0.6 to 0.5 microns. Spectrograph disperses the light from an object into a spectrum. By analyzing the spectrum one can accurately estimate the chemical composition and other physical properties. The spectrograph used in this telescope has a remarkable multi-object capability such that it can simultaneously observe 100 objects. This is the first space spectrograph with such a capacity which is provided by ESA.

- Mid-Infrared Instrument - It consists of both camera and a spectrograph that collects light from wavelength range of 5 to 28 microns. The detectors in this instrument gathers light from the distant faint galaxies, star forming regions, comets and objects in Kuiper's belt. The wide-field, broadband camera obtains good quality images and mid-resolution spectroscopy can be done by spectrograph. This instrument is provided by the European Consortium with the European Space Agency (ESA), and by the NASA Jet Propulsion Laboratory (JPL).

- Fine Guidance Sensor - It helps the telescope to point the targeted object precisely, so that it can take a good quality images. It is provided by the Canadian Space Agency.

With all such highly equipped instruments, JWST has hope to reveal the details of the universe.

3.3.2 CHEOPS Mission

The CHEOPS stand for CHaracterising ExOPlanet Satellite which is jointly organized by European Space Agency (ESA) and Swiss Space Office. This is the first small class mission from ESA selected in 2012 and probably will be launched in 2018. This space probe consists of high ultra-precision photometric observatory, that analyzes the already detected transiting exoplanets around bright stars. This telescope can able to determine the accurate radii of exoplanets whose mass has already been estimated by ground based spectroscopic analysis. The main science objective of this mission is to study the structure of super-Earths to Neptune mass exoplanets whose radius varies from 1-6 R_E.
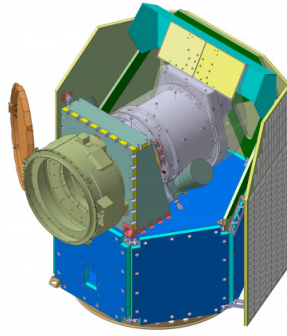
Fig. 3.4 Illustrates the Planned Accommodation of CHEOPS mission Instruments. Image Credit: ESO.

By knowing precise knowledge of mass and radius of these exoplanets, CHEOPS will provide new constraints on the origin and evolution of these exoplanets. In addition, CHEOPS will

- investigates the atmosphere of hot-Jupiters in order to study the mechanism for energy transport from day side to night side.

- recognizes planets with significant atmosphere based on their mass, size, orbital distance, etc.

- obtain mass-radius relation within a mass range by using with handful of data and to a precision that never achieved before.

The CHEOPS mission consists of a medium size telescope with a primary mirror of 30 cm. The telescope will be mounted on a stiff optical bench which shall be thermally decoupled. A Sun shield is placed on the platform to protect the telescope from radiation. The energy supply can be done by the solar panels mounted on a platform. The satellite will have a hexagonal base structure with a dimension 1.5 x 1.5 x 1.5 meters as illustrated in Figure 3.4. This telescope operates in a wavelength region between 0.4 to 1.1 μm. This telescope orbits the Earth in low Earth orbit ($\sim$ 650-800 km altitude) for a period of 5 years.

3.3.3 TESS - Transiting Exoplanet Survey Satellite

The Transiting Exoplanet Survey Satellite is a first space-borne all sky transit survey telescope by NASA designed to detect mainly small exoplanets around the bright stars near solar neighborhood. In addition, TESS also detects the planets ranging from Earth size to gas giants. The TESS will monitor for a periodic dip in the brightness of 200,000 stars during its two year period. It is expected that around 1500 exoplanets can be detected, among which $\sim$ 500 are of Earth-size and super Earth size planets. Since the targeted stars from the TESS are 30-100 times brighter than the Kepler mission, it is easier to characterize with follow-up observations, which provide refined measurements of planetary properties.

The TESS payload consists of a Data Handling Unit and four cameras. Each camera is provided with a lens and a detector assemblies with four CCDs. The field of view of each camera is 24 x 24 degree with bandpass range 600 - 1000 nm.

The main science objective of TESS is to survey the stars with spectral range F5-M5 for the search of Earth-size and super-Earth size exoplanets. It covers the area of sky which is 400 times larger than the area covered by Kepler. Since, this telescope searches for exoplanets around the bright stars, one can also make a follow-up observations of TESS candidates through ground based telescopes. TESS will transfer the collected data to Earth every two weeks. It orbits around the Earth in 2:1 lunar resonant orbit that is never used before by any spacecraft. It is expected to launch in 2018.

3.3.4 Thirty Meter Telescope - TMT

Thirty Meter Telescope (TMT) will be one of the biggest telescopes in the world that has very huge light gathering power (about 10 times higher than the Keck telescope). India is also one of the member in this mission along with Canada, Japan, USA and China. With this telescope one can observe an object from near-ultraviolet to mid-infrared. One of the biggest advantage of TMT compared to other ground based telescopes is the in-built adaptive optics (AO) system. The AO system helps to correct the atmospheric extinction and enables the better observation. The main science objectives of this telescope are

- to study the cosmology and early universe

- galaxy formation and intergalactic medium

- to understand the birth and early stages of stars and planets

- detection and understanding exoplanets

- understanding the Solar system objects

The primary design of TMT consists of a primary mirror which is 30 m in diameter with 492 segments of 1.44 meter, a secondary mirror with 3.1 m diameter and, a tertiary mirror located at center of the primary mirror with elliptical shape. The first light instrument of TMT consists of Wide Field Optical Spectrometer (WFOS), Infrared Imaging Spectrometer (IRIS) and Infrared Multi-object Spectrometer (IRMS). The WFOS will enables the long-slit observation of single objects and short-slit observations of many objects simultaneously. The IRIS is used in diffraction limited imaging and integral field spectroscopy at the wavelength range 0.8 - 2.5 μm. The expected launch of this telescope is around 2022.

These are few glimpses of exoplanetary missions. In addition to these missions, there are still many more exoplanetary groups and missions all over the world involved in detection of the exoplanets. After their detection, through follow-up observations, one can easily estimate the physical and orbital properties of exoplanets as explained in Chapter 2. All these physical and orbital properties of exoplanets and their host stars are publicly available in The Extrasolar Planets Encyclopaedia [2] and The Exoplanet Orbit Database [3]. With the help of these databases, in the next chapters, we investigate the genesis and formation of planetary systems in general and Solar system planets in particular.

---

[2]http://exoplanet.eu/catalog/
[3]http://exoplanets.org/

3.3.5 PLAnetary Transits and Oscillations of stars - PLATO

PLATO is a space based observatory by ESA's Cosmic Vision Program. The mission was proposed to ESA in 2007 and recently in June 2017 the Science Programme Committee approved the same. With a theme of understanding the conditions for planet formation and emergence of life, primary goal of PLATO mission is to detect and characterize the terrestrial planets around bright solar-type stars by transit method. It aims at detecting the terrestrial planets in habitable zones around bright stars. Further, PLATO will provide the better information on key parameters like planetary radii, density, stellar irradiation etc. In addition, one can also make the observation of stellar oscillations for solar-type stars that helps to accurately determine a star's mass, radius, age, etc.

The PLATO is targeting the bright stars with visual magnitude $\geq$ 11-13. For these stars, continuous high precision photometric observations will be carried out in visible range. The payload consists of 24 'normal' cameras with CCD-based focal planes. These cameras are read out with a cadence of 25 s. The 'normal' cameras are arranged in four groups. Each group consists of six cameras with same field of view but offset by a 9.2^o angle from payload module +Z axis. This arrangement allows the observer to survey a total field of about 2250 deg^2 per pointing. This arrangement will be mounted on the optical bench. Cameras are placed on a fully dioptric design with 6 lenses. Each camera has an 1100 deg^2 field-of-view. The lens will have diameter of 120 mm and is equipped with a focal plane array of 4 CCDs each with 4510 x 4510 pixels of 18 m size.

PLATO is scheduled to be launch by 2026 to Sun-Earth Lagrangian point L2. The telescope operates for 4 years of nominal science operations. In addition, satellite built and verified for an in-orbit lifetime of 6.5 years.

CHAPTER 4

Mass Relationship Between Sun-like Stars and Their Exoplanets

Stars are the basic components of the galaxies, that produce heat, light, and other forms of energy through nucleosynthesis in their core. Stars are mainly composed of hot and ionized gases known as plasma. All we get from a star is the light rays from which one needs to understand its physical and chemical properties. By analyzing a stellar spectrum produced by light rays of a star, one can deduce many physical properties viz., stellar temperature, luminosity, density, mass, etc. Similarly, the chemical composition of a star can be deduced from the absorption lines that are present in the stellar spectrum. The absorption lines that are produced at different wavelengths indicate the different elemental compositions. Based on the spectral characteristics, stars are mainly divided into seven types named as O, B, A, F, G, K, M. The stars belong to first three spectral type (O, B, A) are considered to be early type stars and those belong to later four type (F, G, K, M) are considered as late type stars. The early type stars are massive, that results in high luminosity, high temperature, high rotation rate, etc. Late type stars are less massive, less luminous, cooler with longer life time. Hence, one can say that mass of a star is one of the important properties that decides its life time/evolution and affects significantly its other physical and chemical properties. Before investigation of importance of mass of a star on its structure, in the following, let us understand didactically how mass of a star is estimated.

4.1 Estimation of Mass of Stars

4.1.1 From Binary Stars

A star can either be in a single system where it orbits around the center of the galaxy without any companion or it can be in a binary system where two stars revolve around common center of mass. Though our Sun is a single star, majority ($> 70\%$) of stars exist in our galaxy are part of a binary system. The brighter star in a binary system is considered as the primary star while fainter is a secondary star. Based on the method of discovery, binary stars are classified as Visual binaries, Astrometric binaries, Spectroscopic binaries and Photometric binaries.

4.1.1.1 Visual Binaries

Usually it is very difficult to resolve the components of a binary system if their orbital separation is small and especially when a primary star is much brighter than the secondary star. However, if the separation between the stars is grater than one arc second, then stars can be resolved into two components and such systems are known as *Visual binaries*. The relative position of stars in such a system changes with respect to time. The first Visual binary system is discovered in 1830 for the star ξ UMa.

If two stars are orbiting each other with a common center of mass, then the mass ratio of stars is given by

$$\frac{M_1}{M_2} = \frac{a_1}{a_2}, \tag{4.1}$$

where M_1 and M_2 are stellar mass and a_1 and a_2 are distances of primary and secondary objects respectively from the center of mass. Furthermore, $a = a_1 + a_2$, where a is semimajor axis of elliptical orbit. By knowing the distance of binary system, absolute size of an orbit can be estimated. Similarly, monitoring the stars over a period of time gives us the orientation of the orbits and orbital period (P). Knowing the orbital period the total mass of system can be estimated by using Kepler's third law given by

$$P^2 = \frac{4\pi^2}{G(M_1 + M_2)}a^3, \tag{4.2}$$

where G is gravitational constant.

4.1.1.2 Astrometric Binaries

In these binary systems the secondary component cannot be resolved. However, from the variable proper motion of primary (brighter) star over a period of time, one can infer the presence of its companion. By knowing the mass of primary component (from its luminosity; as explained in the next section), mass of the second component can be estimated. The first astrometric binary system discovered (in 1830) is Sirius.

4.1.1.3 Spectroscopic Binaries

Spectroscopic binaries appear as single star even in the powerful telescope. However, from the periodic variation in spectral lines in their spectra one can infer the presence of another star. The orbital motion of each star around center of mass produces the Doppler shift in the spectral lines that is directly proportional to the radial velocity. From the periodic shifts in the spectral lines, one can estimate the orbital period (P) of a star around the center of mass. Since we could not able to determine the inclination i (the angle between line of sight and normal of the orbital plane), the true mass of stars can not be found.

From the Doppler shift measurement one can estimate the observed velocity (v), that is related to true velocity (v_0) by a equation given by

$$v = v_0 sin(i). \tag{4.3}$$

If M_1 and M_2 are the masses of stars in a binary system and, a_1 and a_2 are the distances of stars from the center of mass, then one can write it as $M_1 a_1 = M_2 a_2$ and $a = a_1 + a_2$. Hence, orbital radius of an object 1 is given by

$$a_1 = \frac{a M_2}{M_1 + M_2}. \tag{4.4}$$

Similarly, true orbital velocity of an object is estimated from

$$v_{0,1} = \frac{2\pi a_1}{P}.$$

(4.5)

Using this true orbital velocity, the observed orbital velocity (4.3) is written as follows

$$v_1 = \frac{2\pi a_1 sini}{P}.$$

(4.6)

Using equation (4.4) in (4.6) we have

$$v_1 = \frac{2\pi a}{P} \frac{M_2 sini}{M_1 + M_2}.$$

(4.7)

Solving for a and using Kepler's third law, mass function equation is given by

$$\frac{M_2^3 sin^3(i)}{(M_1 + M_2)^2} = \frac{v_1^3 P}{2\pi G}.$$

(4.8)

Similarly, by knowing v_2 and from equation (4.6) we have

$$\frac{v_1}{v_2} = \frac{a_1}{a_2},$$

(4.9)

and from the definition of center of mass, we have

$$M_1 = \frac{M_2 v_2}{v_1}.$$

(4.10)

Substituting above equation in (4.8) gives the value of $M_2 sin^3(i)$. Similarly, $M_1 sin^3(i)$ can be estimated. The true mass of these stars can not be estimated until the inclination is known.

4.1.1.4   Photometric Binaries

In the photometric binaries, the motion of stars around the center of mass causes the periodic variation in the brightness of system. When a star passes in front of a another star in binary system, it blocks the significant amount of light, hence, these are also known as *eclipsing binaries*. The inclination of the orbit in these systems are near to

90^0 in order to undergo the eclipse. Hence, these are the only *Spectroscopic binaries* for which inclination can be determined.

In addition to method of detection, the binaries are also classified based on their orbital separation as:

- Distant binaries: The orbital separation between the companion is around 10 to 100 AU.

- Close binaries: The orbital separation in these system is within 1 AU.

- Contact binaries: In these systems separation is very close so that both stars are almost touch each other.

4.1.2 Luminosity-Mass Relationship

As we have already mentioned earlier, along with the binary systems, the Milky way galaxy also consists the single star systems. The masses of these single stars can be estimated by an empirical mass - luminosity relation given by

$$\frac{L}{L_\odot} = \left(\frac{M}{M_\odot} \right)^x, \tag{4.11}$$

where, L and $L_\odot$ are the luminosity of a star and the Sun respectively. Similarly, M and $M_\odot$ are mass of a star and the Sun respectively. The value of exponent x is used as 3.5 for main sequence stars. Kuiper (1938) is the first person to obtain the mass-luminosity relationship by using the binary systems.

4.1.3 Asteroseismic Method

Asteroseismology is one of the advanced method to estimate the stellar properties by using the oscillation/frequency spectra of a star. From this method, one can accurately model the internal structure of a star. The oscillations from a star mainly consist of two modes namely p-mode and g-mode (Hiremath 2013, 2016, and references there in). The p-mode waves are acoustic in character with frequency ranging from 1-5 mHz in case of Sun. Usually p-mode oscillations can be observed on the surface of a star. Whereas, restoring force for the g-modes is due to internal gravity waves that have low frequency

compared to p-modes. The detailed explanation for the extraction of different stellar properties from the observed astrosiesmic parameters are given by Chaplin and Miglio (2013).

4.2 Estimation of Age of a Star

Age is another fundamental physical parameter of a star that is essential for understanding evolutionary status. As star ages, its mass, dynamics such as rotation, magnetic activity and chemical abundances change with respect to time. Presently, we do not have any direct method to measure the age of a star. That is why different theoretical and empirical models are used to estimate the age of a star (Lebreton et al. 2014, Soderblom et al. 2014, and references therein). Age of a host star can be estimated mainly from the following methods.

In the *Isochrone method*, age can be estimated by placing a star on the curves in the HR diagram that represent different stellar masses with age. Models that are used in the Isochrone methods are based on the well-understood stellar physics. Errors of estimated ages from this method are usually significant (20-50%). Older Isochrones represent the stars with redder main sequence (Yi et al. 2001).

Since decline of rotation rate of a star with time is well understood, the *rotation rate* of a star can be used as an indicator of a stellar age. Hence, by determining rotation rate of the stars for different evolutionary periods, age of a star (Epstein and Pinsonneault 2014) can be estimated. Similarly, Lithium abundance on the surface of a star decreases over a period of time, although process from which Lithium of host stars is depleted is unambiguously not understood. Hence, Lithium abundance of a star can be used as an estimator of age.

In the *method of evolutionary track*, ages of stars are estimated by evolving stellar structure equations such that computed mass, radius and luminosity must match with the observed mass, radius and luminosity of a star.

In addition to afore mentioned methods, recently *the asteroseismic method* yields best estimation of age of a star (Lebreton et al. 2014). As described in Chapter 1, the accurate determination of oscillations from the different depth of a star help us to

model the internal structure of a star precisely. With these precisely estimated internal parameters and with the stellar models, one can estimate the stellar age unambiguously. The detailed explanation on the extraction of different stellar properties can be found in Brown and Gilliland (1994).

4.3   Different Techniques to Measure the Mass Loss From the Stars

Stellar mass loss is a fundamental phenomenon where large fraction of stellar mass is continuously ejecting into the inter stellar medium due to various dynamical interactions. Understanding mass loss of a star is crucial, because it varies with different stellar evolutionary stages. Similarly, stars with different rate of mass loss have different evolutionary stages. For example, mass loss rate is high for a star during early (Pre-Main Sequence(PMS), T-tauri) stages of stellar evolution due to intense activity, whereas, it decreases in the main sequence stage. Again, mass loss is dominant in the Red (super) giant stage of a star. Rate of mass loss is small for massive stars ($\sim 7 \ M_\odot$, where $M_\odot$ is mass of the Sun) when they are on the main sequence stage and increases with the late stage of stellar evolution (Huang et al. 1990). For the sun like stars, mass loss rate by stellar wind might be 200 - 10000 times more in early stage of stellar evolution (Linsky and Wood, 2004).

Mass loss in a star can occur via stellar wind, coronal mass ejection, and mass transfer (in binary systems). The speed of the particles ejecting from the star is $\sim$ 400 - 700 km s^{-1} in main sequence stage. Mass loss can be observed mainly from the *P Cygni Profiles* and *Emission lines* in the spectral profile of a star. When the strong stellar wind or gas is expanding from a star towards the observer, along with the strong emission lines, there exists a corresponding blue shifted absorption lines. These spectral line profiles with strong emission correspond to blue shifted absorption lines are known as P Cygni profiles. Figure 4.1 illustrates an example of P Cygni profile.

One can notice from the Figure 4.1 that by measuring the width of a blue shifted absorption lines one can easily estimate the wind velocity (*v*) of the stellar wind. From the knowledge of the velocity of stellar wind, density profile $\rho(r)$ of gas around a star and utilizing mass continuity equation, the rate of mass loss can be estimated as follows

Formation of a P-Cygni Line- Profile
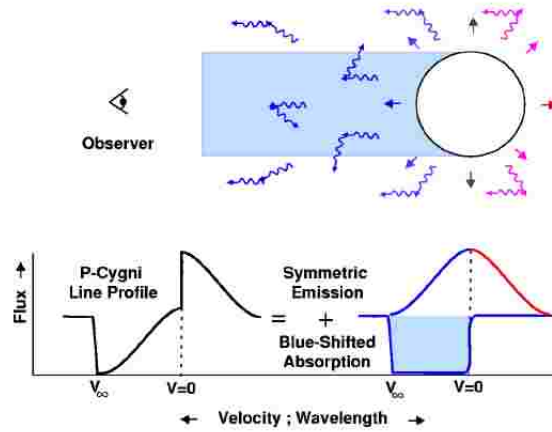
Fig. 4.1 Illustrates the Formation of P-Cygni Line Profile. Image Is Taken From the Website *www.bartol.udel.edu*

$$\dot{M} = 4\pi r^2 \rho(r) v(r), \tag{4.12}$$

where, $\dot{M}$ is the rate of mass loss, r is the radius from the star.

Similarly, the emission lines in the stellar spectral line profile are also used for estimating the mass loss of a star. H_α is most notable spectral line used to estimate the mass loss. In addition, Paschen and Brackett lines of He-II are also used. Since, as the gas departs away from the star, it leads to Doppler shift and, the widths of Doppler shift for these lines are typically few hundred kms^{-1}. By determining the total line luminosity of these lines the mass loss can be estimated by

$$\dot{M} \sim v\sqrt{L}, \tag{4.13}$$

where, v is the wind velocity.

4.4 Motivation

Formation and evolution of a planet around a central star are still a mystery. Right from the Kant and Laplace theory (as we described in chapter 1, section 1.4), to date, many theories showed that formation of the stellar system begins with the self gravitational collapse of interstellar clouds of gas and dust particles which is commonly known as a nebula (McNally 1971, McKee and Ostriker 2007). In later stages, to conserve the angular momentum of collapsing clouds, a disk is formed around the central star known as protoplanetary disk (Roberge and Kamp 2010). Small centimeter sized dust particles in the protoplanetary disk coagulate to form kilometer-sized protoplanets, and in later stages as planets, within a small span of 100 million years.

Similarly, the Sun and eight planets of the Solar system also might have originated from a dense interstellar cloud known as the solar nebula that consists of gas and dust particles (Woolfson 2014). Weidenschilling (1977) and Hayashi (1981) arrived at a conclusion that, Minimum Mass Solar Nebula with a dust mass ~ 0.02 solar mass is necessary to form all the eight planets in the Solar system. Later, many theories were proposed in order to understand the dynamical evolution of Solar system planets viz., the formation of Jovian planets, the low mass of terrestrial planets by considering migration scenario (Tsiganis et al. 2005, Walsh and Millar 2011) and, higher density of the solar nebula (Alibert et al. 2005, Crida 2009, Mordasini et al. 2012) during the early history of solar system formation. Faint young Sun paradox (FYSP) is one of the most interesting (Sagan and Mullen 1972) and one of the unsolved problems in Solar Physics that seeks a suitable explanation for liquid water on the Earth during the early evolutionary stages. Previously, many ideas were proposed to solve the FYSP, viz., deviation from the standard solar model (Gaidos et al. 2000), increase the fraction of greenhouse gases in the early Earth/Mars (Goldblatt and Zahnle 2011, Feulner 2012), etc. One of the promising solutions for FYSP is Sun's mass during an early stage of evolution must be slightly higher (1.03 - 1.07 $M_\odot$, where $M_\odot$ is the mass of the Sun; Güdel (2007) section 7.1.2) compared to the present mass.

The recent ground and space based observations revolutionized our understanding

of planetary formation by detecting the exoplanets. The exoplanets exhibit different variety of physical and orbital characteristics when compared to the Solar system planets. Many previous studies show unique relations between the properties of planets and host stars. For example, Udry et al. (2003) suggest a lack of massive planets in short period orbits (≤ 100 days) and, supports the migration scenario of planets. Cumming et al. (2008) arrived at a power law relationship between the orbital period and planetary minimum mass. Fischer and Valenti (2005) showed that the probability of occurrence rate of a planet depends on stellar metallicity. In addition, planets around metal poor stars have longer orbital periods, that suggests metallicity have a dominant role in the stellar system formation (Adibekyan et al. 2013). Exoplanets exhibit a wide range of eccentricities, especially most of the massive planets exhibit non-zero eccentricity (Marcy et al. 2005). The eccentricity of planets around evolved stars are less compared to the eccentricity of planets around young stars (Jones et al. 2014). Weiss and Marcy (2014) found a power law relationship between radius and mass of the exoplanets that have radii smaller than 4 earth radii, explaining the diversity of composition of planets.

Generally, the exoplanets are massive, have more eccentric orbits and revolve very close to their host stars (Udry and Santos 2007, Lammer et al. 2013). In contrast, planets within the vicinity (hereafter vicinity is the region within 1.5 AU from the host stars) of the Sun are less massive, have near zero orbital eccentricity (except Mercury) and, massive planets are orbiting very far from the Sun.

With the exoplanetary data, present study aims at a direction (i) to get clues from the distant stellar-planetary systems to understand Faint young Sun paradox, (ii) to examine whether any relationship exists between the stellar mass and planetary mass and, (iii) to examine whether present terrestrial mass in the vicinity of the Sun is compatible with mass of exoplanets in the vicinity of their host stars.

4.5   Data and Analysis

For the present study, physical and orbital characteristics of Sun-like G stars and their exoplanets are considered from the website *http://exoplanet.eu/catalog/*. The Sun-like G-type stars in the present study are defined based on the spectral G type provided

in the previously mentioned website. Further, we impose the following constraints on the physical properties of stars and exoplanets: (i) consider the host star that has $\leq 50\%$ error in its age, (ii) in order to avoid the ambiguity in considering the brown dwarf candidates, restrict the maximum planetary mass limit to 13 Jupiter mass and, (iii) avoid the binary stellar systems. With these constraints, we left with 114 host stars that have 147 exoplanets. Among 114 host stars, 17 are multi-planetary hosts with 49 planets. The relevant data is given in the Table 1 of Appendices section. In this table, first column represents the name of an exoplanet. Second and third columns indicate the planetary mass and its error in terms of Jupiter's mass respectively. Fourth and fifth columns subsequently describe the orbital distance of a planet and its error in terms of AU. Sixth and seventh columns represent the stellar mass and its error in terms of Sun's mass respectively. Last three columns subsequently indicate the spectral type, age (in Gyrs) and error in age.

One can argue that data bias ((i) high mass planets in the vicinity of stars and (ii) high uncertainties in the stars ages) can lead to misleading results. However, when one examines the data presented in Table 1, following two important facts completely rule out such biases. For example, in addition to hot-Jupiters, the data set also consists of many low-mass planets in the vicinity of their host stars viz., Kepler-10 b, Kepler-11 b, HD 20794 b, HIP 68468 b, etc. In addition, majority of stars in the data set have less than 30% uncertainties in their estimated ages, which helps in removing the inconsistencies that arise in estimating the stellar rate of mass loss. Further, one can also notice that the error bars in the stellar and planetary masses are small (on average 10%). Hence, present data set is most appropriate to extract the useful scientific results.

4.6 Estimation of Mass Loss From the Host Stars

The solar type stars lose their mass heavily when they were young (Linsky et al. 2004) and, the rate of mass loss decreases as the stars evolve (Wood et al. 2002). This is because, at later evolutionary stages of Sun-like stars, the rotation rate decreases (Hartmann 1985) that results in less magnetic activity. However, mass loss is small for massive stars ($\sim 7 M_\odot$) in their main sequence stage and increases with the late stage of

$$M_\star/M_\odot = 10^{(0.056\pm0.040)}(T_\star/T_\odot)^{-(0.247\pm0.110)}$$
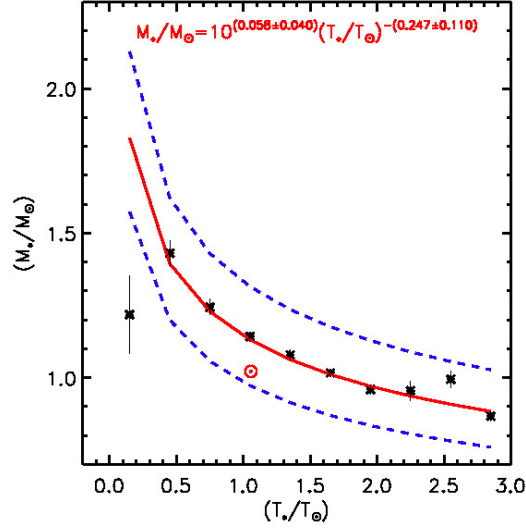
Fig. 4.2 Illustrates the Dependence of Stellar Mass With Its Age. the Continuous Line Indicates the Best Power Law Fit Between Both the Variables and the Dashed Lines Indicate the One Sigma Error Level. ⊙ Symbol Indicates the Position of the Sun.

stellar evolution (Huang et al. 1990). Hence, stellar mass loss eventually affects the internal structure of a star. The rate of mass loss of host stars ranges from 10^{-14} to 10^{-4} $M_\odot$ /year (Ridgway et al. 2009) depending upon the different stellar properties viz., stellar mass, luminosity, radius, and temperature. Since the stars are very active in their early evolutionary stages (Hiremath 2009 and references therein), there might have more chance of losing heavy mass from them, that might also affects the nearby planets.

4.6.1 Rate of Mass Loss Estimated From the Host Stars That Have Exoplanets

Since we do not know whether the rate of mass loss is same for stars with and without exoplanets, first an attempt is made to understand the variation of stellar masses (that have exoplanets) with their ages. Figure 4.2 (star's mass $M_\star$ and star's age $T_\star$ are normalized with the Sun's mass $M_\odot$ and age $T_\odot$ respectively) illustrates a power law relationship between stellar mass and age such that $\frac{M_\star}{M_\odot} \sim (\frac{T_\star}{T_\odot})^{-0.247}$. In this figure, the x-axis is binned with a size of 0.3 $\frac{T_\star}{T_\odot}$, and the y-axis represents the average stellar mass in that bin with an error bar estimated from the ratio $\frac{\sigma}{\sqrt{n}}$ (where σ is a standard deviation and n is the number of data points in each bin). Such an empirical power law suggests that the stellar rate of mass loss is high during the initial evolutionary stages.

With the present data set that consists of stellar mass and age and, by making use of numerical differentiation, the rate of mass loss $\frac{d(M_\star/M_\odot)}{d(T_\star/T_\odot)}$ for each star is estimated. Now onwards, $\frac{M_\star}{M_\odot}$ and $\frac{T_\star}{T_\odot}$ are represented as M and t respectively. Further, we find that estimated $\frac{dM}{dt}$ fits a power law relation with the stellar mass. By making use of this power law relation, the estimated (see Table 4.1, second column, second row) rate of mass loss of the Sun is found to be $\sim 10^{-11}$ $M_\odot$/yr, which matches very well in the range of mass loss computed by the previous studies (Drake et al. 2013, Cranmer 2017) if one considers mass loss due to coronal mass ejections also. Careful observation of data in Appendix (Table 1) reveals that dataset consists of few giant stars. Since these giant stars have the high rate of mass loss compared to other main sequence stars, one can argue that their presence significantly contribute to the high rate of mass loss of the stars. In order to confirm whether these giants have really affected the rate of mass loss, stellar mass versus age relationship without the giants is illustrated in Figure 4.3. Further, a relationship is examined between the rate of mass loss of stars (estimated as described above) and their stellar masses that yields the rate of mas loss of Sun to be $\sim 0.9 \times 10^{-12}$ $M_\odot$ /yr which is almost equal to the previously estimated value. Both these results strongly suggest that contribution due to coronal mass ejections from the Sun substantially increases its present rate of mass loss that is estimated only from the solar wind. One can also notice that Sun's position in both the Figures (4.2 and 4.3) is just below the fitted line within one sigma error level. That means, Sun's evolutionary path is no different than the stars evolutionary path that have exoplanets.

Since stellar ages have appreciable but not very high magnitude of error bars, in order to validate the obtained law of mass loss, we have also verified from the data of 42 stars that have accurate stellar mass (average error in stellar mass is $\sim 3.07\%$) and stellar age (average error in stellar age is $\sim 11.80\%$) computed from the asteroseismic method (Metcalfe et al. 2014). Figure 4.4 illustrates the stellar mass versus age relationship for the stars (with no detected exoplanets) whose properties are accurately determined from the asteroseismic method. The x and y axes are binned as described earlier. Careful observation of Figures 4.2 - 4.4 reveals that, during early stellar age ($\leq$ 0.3 $\frac{T_\star}{T_\odot}$), stars with exoplanets experienced a high rate of mass loss compared to stars
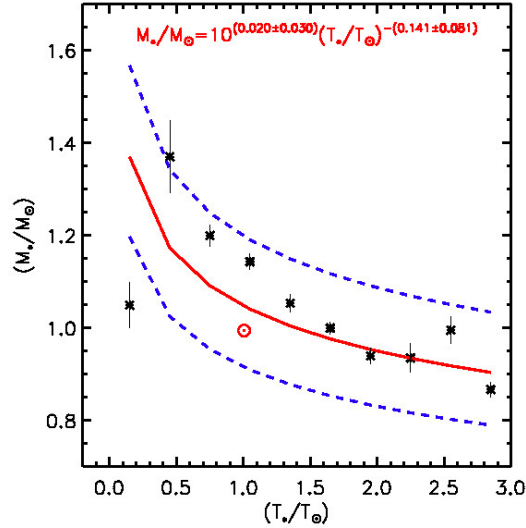
Fig. 4.3 Illustrates the Dependence of Stellar Mass With Its Age for the Dataset Without Giant Stars. The Continuous Line Indicates the Best Power Law Fit Between Both the Variables and the Dashed Lines Indicate the One Sigma Error Level. ⊙ Symbol Indicates the Position of the Sun.

without exoplanets. However, cause for the excessive rate of mass loss from the stars with exoplanets during early evolutionary stage is beyond the scope of this study.

4.6.2 Rate of Mass Loss Estimated From the Observations of Stars

There is every possibility that, a mismatch between the estimated and observed rate of mass loss of the Sun could be due to not using the observed rate of mass loss of host stars. Hence, the observed (direct estimation) rate of mass loss of host stars, irrespective of whether stars harbour planets or not, are considered from Cranmer and Saar (2011). With this data, a power law relationship is obtained between the rate of mass loss of stars and their masses. Using this power law relationship, the present rate of mass loss of the Sun is estimated to be $\sim 0.8 \times 10^{-12} M_\odot$/yr which is of the same order ($\sim 10^{-11} M_\odot$/yr) as estimated from the host star mass-age relationship. For additional check, an empirical rate of mass loss relationship given by de Jager et al. (1988) is also used to estimate the Sun's present rate of mass loss which is found to be of similar order ($\sim 10^{-14} M_\odot$/yr; see also Wood et al. (2005)). Obvious reason for the difference of rate of mass loss estimated by Wood et al. (2005) and our estimation is that, Wood et al. (2005) estimate the rate of mass loss due to stellar wind only.

$$M_\star/M_\odot = 10^{(0.032 \pm 0.032)}(T_\star/T_\odot)^{-(0.131 \pm 0.079)}$$
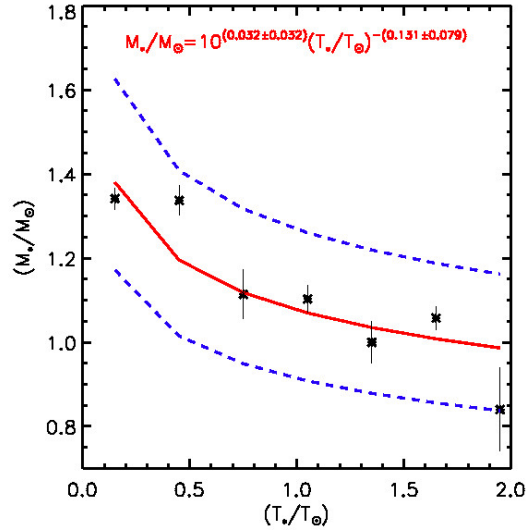
Fig. 4.4 Illustrates the Dependence of Stellar Mass With Its Age for the Stars Whose Properties Are Estimated From the Asteroseismic Method. the Continuous Line Indicates the Best Power Law Fit Between Both the Variables and the Dashed Lines Indicate the One Sigma Error Level.

All these three empirical rate of mass loss laws and estimated present Sun′s rate of mass loss are presented in the first two rows of Table 4.1. It is interesting to note that all the three empirical laws suggest power law relationships between the rate of mass loss of stars and their respective masses. Hence, it is obvious from these relationships that, high mass stars have a high rate of mass loss.

One can also notice from Table 4.1 that different mass loss laws yield different initial Sun's mass. Among all the mass loss laws, the estimated uncertainties in the exponents of power laws are least for the mass loss law that is estimated from the host stars data (second column, Table 4.1). In addition, the Sun's rate of mass loss estimated from this law very well matches with the rate of mass loss estimated by Drake et al. (2013). Hence, among these three relationships, best relationship is the one which is derived from the host stars data as described in section 4.6.1.

4.6.3 Computation of Initial Stellar Mass

With these three empirical power laws (as presented in the first row of Table 4.1) of rate of mass loss, initial stellar mass M_{ini} can be computed in the following way

$$M_{ini} = M_{pre} + \int_{t_1}^{t_2} \frac{\mathrm{dM}}{\mathrm{dt}} \mathrm{d}t, \qquad (4.14)$$

where M_{pre} is present stellar mass, t_1 and t_2 are initial and present ages of a star respectively.

On the right-hand side (RHS) of equation (4.14), the second term represents the total mass lost by a star from its initial age t_1 to present age t_2. Hence, by adding total lost mass to present mass, initial mass M_{ini} of a star can be estimated. In the present study, total mass lost (numerical integration of the second term in RHS is performed) from the host stars is estimated and is added to the present mass M_{pre} in order to get the initial mass M_{ini}. For estimating total rate of mass loss, initial ages of stars are assigned to be $\sim$ 50, 60, 70, 80, 90, 100 and 200 million years and, initial stellar mass is estimated for these ages. However, among all these assigned initial stellar ages, the estimated initial stellar masses converge and saturate at 50 million years than the other assigned ages. Hence, we accept 50 million years as the initial age of a star.

4.7   Results and Conclusion

After computing the initial stellar masses of the host stars, association between the initial stellar masses and the planetary masses is examined. In the case of multi-planetary systems, all the planetary mass is added that gives the information about the total amount of planetary mass for respective host star. As illustrated in Figure 4.5 we find that these two parameters are non-linearly (power law) dependent on each other. In Table 4.2, three power laws that relate the initial host star mass with the planetary mass are presented. In each case, to estimate the initial stellar mass, separate rate of mass loss correction is applied as mentioned in the first column of Table 4.2.

The power law between the initial stellar mass and planetary mass as illustrated in the Figures 4.5 suggest that, *the massive stars harbor massive planets in their vicinity*. These results are also consistent with the previous studies of observational (Laws et al. 2003, Johnson et al. 2007, Lovis and Mayor 2007, Johnson et al. 2010) and theoretical inferences (Ida and Lin 2005). For different spectral type, Lovis and Mayor
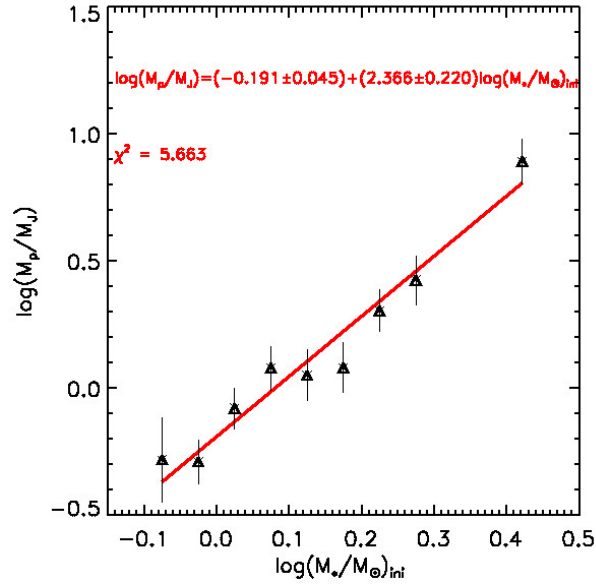
Fig. 4.5 Illustrates the Dependence of Present Mass of the Exoplanets With the Initial Mass of Star. the Continuous Line Indicate the Best Fit Line Between the Planetary Mass and Initial Stellar Mass.

(2007) present a relationship between exoplanetary mass and stellar mass. However, the present study is different than the previous studies as we have consistently applied the mass loss correction to the stellar mass and also quantitatively estimated the relationship between the stellar mass and the planetary mass.

4.7.1 Estimation of Initial Mass of The Sun

Although it is not proper to compare physics of the Solar system with physics of exoplanetary systems, since the Sun has similar physical characteristics such as mass, it is interesting to estimate Sun's lost mass and initial mass from the rate of mass loss relationships (see Table 4.1, second row). The estimated rate of mass loss of the Sun from the de Jager's empirical formula is no different than the present Sun's rate of mass loss, that is estimated only from the solar wind. This value almost matches with the rate of mass loss estimated by Wood et al. (2005) if one considers the contribution due to solar wind only. However, from the other two relations, indeed the Sun has an excess rate of mass loss. Especially, if one accepts the rate of mass loss due to coronal mass ejections (Drake et al. 2013, Cranmer 2017) also, then the rate of mass loss of the Sun increases by $\sim 10^3$ times compared to a rate of mass loss estimated from the solar wind alone

Table 4.1 Rate of Mass Loss of Stars With Planets

	Mass loss obtained from host star data	Mass loss obtained from observed data	Mass loss obtained from empirical relation
Rate of mass loss $\frac{dM}{dt}$	$10^{(-1.206\pm0.019)}\left(\frac{M_\odot}{\tau_\odot}\right)\left(\frac{M_\star}{M_\odot}\right)^{3.788\pm0.190}$	$10^{(-12.092\pm0.302)}\left(\frac{M_\star}{M_\odot}\right)^{3.974\pm1.394}$	$10^{-8.158}\left[\frac{(\frac{L_\star}{L_\odot})^{1.768}}{(T_{eff})^{1.676}}\right]$
Sun's rate of mass loss	$1.361 \times 10^{-11} M_\odot$ /yr	$8.090 \times 10^{-13} M_\odot$ /yr	$3.4435 \times 10^{-15} M_\odot$ /yr
Initial $M_\odot$	$1.061 \pm 0.006 \ M_\odot$	$1.003 \pm 0.006 \ M_\odot$	$1.000015 \ M_\odot$

where $M_\star$ - mass of the star, $\tau_\odot$ - age of Sun

Note: The dimension of a power law obtained from host stars data is $M_\star/yr$, whereas, power law obtained from the observed data has no dimension, because we have normalised the rate of mass loss of stars from the present Sun's rate of mass loss (estimated from solar wind alone).

Table 4.2 Relationship Between Host Stars Initial Mass and Planetary Mass

Corrections applied	$(\frac{M_p}{M_J})$ versus initial $(\frac{M_\star}{M_\odot})_{ini}$ relationships	Missing planetary mass in the vicinity of Sun
Host star data correction	$log(\frac{M_p}{M_J}) = (-0.191 \pm 0.045) + (2.366 \pm 0.220)log(\frac{M_\star}{M_\odot})_{ini}$	$0.738\pm0.172 \ M_J$
Observed mass loss correction	$log(\frac{M_p}{M_J}) = (-0.116 \pm 0.041) + (2.560 \pm 0.223)log(\frac{M_\star}{M_\odot})_{ini}$	$0.887\pm0.191 \ M_J$
Empirical mass loss correction	$log(\frac{M_p}{M_J}) = (-0.102 \pm 0.041) + (2.522 \pm 0.233)log(\frac{M_\star}{M_\odot})_{ini}$	$0.914\pm0.198 \ M_J$
Average initial planetary mass	$0.846\pm0.187 \ M_J$	

and hence, inevitably Sun must have an excess initial mass. As we have already mentioned in section 4.6.1, the best relation between the rate of mass loss and stellar mass is one which is obtained from the host stars data. Hence, by using rate of mass loss (Table 4.1, first row and second column) from host stars data we have estimated the Sun's initial mass which is found to be $\sim (1.061 \pm 0.006) M_{\odot}$. It is to be noted that our estimated initial mass is consistent with the initial mass as estimated in the previous studies (Whitmire et al. 1995, Sackmann and Boothroyd 2003, Güdel 2007, section 7.1.2). Moreover, the cumulative mass lost by the Sun during its evolution until present age is 0.061 $M_{\odot}$ which is about 1% of the solar mass as recently predicted by Cranmer (2017). Hence, during early evolutionary stages, indeed Sun's mass is slightly higher than the present mass. It is also to be noted that this estimated excess initial mass of the Sun is in the range (1.03 - 1.07 $M_{\odot}$; Güdel (2007), section 7.1.2) of Sun's initial mass that requires Earth to retain the liquid water (Minton and Malhotra 2007). This astrophysical solution is a possible reason for alleviating the long-standing problem of faint young Sun paradox.

4.7.2 Estimation of initial planetary mass in the vicinity of Sun

With the calculated Sun's initial mass and making use of empirical relationships as presented in Table 4.2, estimated average planetary mass in the vicinity of Sun is found to be $\sim (0.846 \pm 0.187) M_J$ (where M_J is the mass of Jupiter). In contrast, the present total planetary mass (that includes masses of all the terrestrial planets and asteroids) in the vicinity of Sun is $\sim 0.006\ M_J$ (~ 2 earth mass). One can notice that the difference between estimated and observed planetary mass of the terrestrial planets suggests that a substantial amount of planetary mass is missing in the vicinity of Sun. Probably during early phase of the Solar system evolution, some part of that missing mass might have accreted onto the Sun or some part might have blown off to space due to intense stellar radiation (X-rays, EUV radiations) or protoplanetary disk might have blown off by photoevaporation or part of this missing mass might have migrated outwards from the vicinity of Sun during the early history of Solar system formation. Another possibility could be due to dynamical barriers imposed by the gas giants (Izidoro et al. 2015)

for migration of super earths, although Kepler data do not support such a migration scenario (Chatterjee and Tan 2015). Hence, further clear understanding of deficiency in the present planetary mass in the vicinity of Sun from the perspectives of theory and analysis of the observed physical characteristics of exoplanetary data is necessary.

Since the Sun-like stars were very active during early evolutionary stages (Wood et al. 2005, Hiremath 2009), combined mass loss due to solar wind and coronal mass ejections might have affected the mass of the nearby planets. As for estimated initial planetary mass $(0.846 \pm 0.187)M_J$ in the vicinity of Sun, since the planets also lose mass due to intense radiation from the host stars, with a caveat we have to conclude that, unambiguous planetary mass loss correction is also necessary. Presently, the planetary mass loss is not well understood and mass loss correction for the planets is beyond the scope of this study. However, in case mass loss correction for the planets is also applied, estimated initial planetary mass might further increases and aggravates the deficiency of planetary mass in the vicinity of Sun.

4.7.3 Conclusions

To conclude this study, physical and orbital characteristics of Sun-like G stars and their exoplanets are used to seek (i) a possible solution for the faint young Sun paradox, (ii) a relationship between the stellar mass and planetary mass and, (iii) a reason for low planetary mass within the vicinity of Sun. By estimating the rate of mass loss of each star, we have obtained a non-linear relationship between the rate of mass loss of host star and its mass. In addition, by using the rate of mass loss of a star, its initial mass during early stage (~ 50 Myrs) is computed. For a possible solution for the faint young Sun paradox, initial mass of Sun is estimated to be $\sim (1.061 \pm 0.006)M_\odot$. Furthermore, it is found that, during early evolutionary stages, host star mass and planetary mass follows a non-linear relationship such that massive stars harbour massive planets. From the obtained relationship between initial stellar mass and their exoplanetary mass, initial planetary mass in the vicinity of Sun is estimated to be $\sim (0.846 \pm 0.187)M_J$, in excess of planetary mass concentrated at the present epoch. The excess solar planetary mass lost is conjectured with different views.

CHAPTER 5

Angular Momentum of Sun-like G Stars and Their Exoplanets

Angular momentum is one of the key parameter that controls the physical and orbital characteristics of a star and planet during their evolutionary stages. In a system like solar system, the total angular momentum is the combination of rotational/spin angular momentum of the central object (Sun) and orbital angular momentum of all the planetary bodies. Rotation of a star plays a central role in governing the dynamo-driven magnetic activities, stellar mass loss, surface chemical abundance, internal structures, etc. By estimating the rotation rate of a central star, one can easily estimate the spin angular momentum of a star.

5.1 Estimation of Stellar Rotation

We have various techniques to measure the stellar rotation. Let us discuss two important methods to estimate the stellar rotation.

5.1.1 Spectroscopic method

Abney (1877) is the first person to suggest the use of Doppler broadening of spectral lines to estimate the rotation of a star. The Doppler broadening for spectral line is given by

$$\Delta\lambda_L = (\lambda/c)V_{eq}\sin i, \qquad (5.1)$$

where V_{eq} is linear equatorial velocity, i is the inclination angle between the rotation axis and the line of sight. For a star with pole-on, we observe no Doppler shifts in the spectral lines, while for a star with rotation axis perpendicular to line of sight we can

get direct measurement of V_{eq}. The spectral line shifts at the locus of a stellar disk can be estimated by

$$\Delta\lambda = (\lambda/c)V_{eq}\sin i \cdot \cos(l) \cdot \sin(L), \qquad (5.2)$$

where l and L are latitude and longitude of a point on the stellar disk respectively. The rotation rate of slow rotating stars can be estimated by cross-correlation method. In this method, the spectrum of a star is compared with the standard template spectrum of a star with similar physical properties. Since the cross correlation function is proportional to the $vsini$ (which is calibrated by using a stars whose rotational rate are accurately estimated), the rotation rate for slow rotating stars can be estimated precisely. In addition, the Doppler imaging technique or Zeeman-Doppler imaging techniques are also used to measure the stellar rotation by using the relation exists between location of feature at the stellar surface and its position with line profile (Bouvier 2013). Continuous monitor of a star thus provides the reconstruction of surface brightness and magnetic mapping. Hence, it provides the direct measurements of star's rotational period.

5.1.2 Photometric Method

Determining rotation of a star by monitoring its spots is the oldest method used to determine the stellar rotation. Since the star spots can not be resolved due to their large distances, the luminosity of a star is monitored continuously to measure the change in the brightness of a star due to star spots. Hence, the recorded photometric light curves over a period of time gives a direct estimation of rotational period P_{rot}. Advantage of this method over spectroscopy is that, it is free from the orientation of stellar rotation axis. By knowing the rotational period of a star, the angular velocity ω can be estimated by

$$\omega = 2\pi/P_{rot}. \qquad (5.3)$$

5.2 Angular Momentum Problem of the Solar System

Despite having approximately $\sim 99\%$ of the total mass, the Sun posses about 1% of angular momentum (Okamoto 1969) of the Solar system. Since the proposed Laplace Solar system model, many theories have been formulated to solve the angular momentum problem of the Solar system. In the Sun-like stars, gravity waves play a significant role in the redistribution of angular momentum and mixing of elements on top of the radiative zone (Zahn et al. 1997, Kumar et al. 1999, Aarnio et al. 2012). Similarly, gravity waves transport angular momentum from the solar interior (Rogers and Glatzmaier 2006) to the outer part of Sun. A previous study (Burns 1975) obtained a power law relationship between the angular momentum of Solar system objects and their mass. Furthermore, asteroids, however, deviate from this power law by possessing more angular momentum (Quiroga 1984), which implies collision might have played a dominant role in transforming the angular momentum to smaller bodies of the Solar system. These interactions probably might have also lead to migration of the planets towards/away from the central star (Seager and Lissauer 2010). The migration of Jupiter mass planets is common during the early stages of stellar evolution, and it results in the formation of low mass or terrestrial planets and the asteroid belt (Raymond et al. 2006, Roig and Nesvorný 2015). Tsiganis et al. (2005), in their *Nice Model*, explain the resonance crossing of giant planets especially the Jupiter and Saturn by migration scenario. The Nice model suggests that, after the dissipation of gas and dust particles during early stages of solar system planetary formation, all gas giants orbits are nearer to the Sun than their present orbits. However, due to interactions between the giant planets and small planetesimals (that move inward) in the disk lead to outward migration of planets to conserve the angular momentum of the system. Similarly, Walsh and Millar (2011), in their *Grand Tack Model*, explained the influence of Jovian planets' migration (inward-then-outward) on the formation of terrestrial planets, especially on the low mass of Mars.

5.3   Angular Momentum of the Host Stars That Have Exoplanets

During the first few million years, the rotation rate of the central star is significantly affected by dynamic interactions between it and the the protoplanetary disk (Scholz 2013). In the pre-main sequence stage, the central protostar loses its angular momentum due to mass loss and interaction with accretion disk (Aarnio et al. 2012, Wolff et al. 2004). Furthermore, the magnetic interactions between the disk and central stars lead to an exchange of angular momentum (Vidotto 2014). The life time of a disk depends on the rotation of central star (Denissenkov et al. 2010, Gallet 2013), and once the central star reaches the main sequence stage, its rotational rate gradually decreases through stellar wind and attains a low magnetic activity compared to pre-main sequence stage (Mestel 1968, Collier-Cameron et al. 1991). Interestingly, during the main sequence stage, Sun-like stars with high rotation periods lose negligible angular momenta compared to host stars that have slow rotation periods (Lanza 2010), and these rotational periods are estimated from the spectroscopically determined projected rotational velocity (*v* sin*i*, where *v* is the equatorial rotational velocity, and *i* is the angle of inclination of the rotational axis).

Due to their high mass and magnetic activity, early type stars possess more angular momentum than late type stars (Tarafdar and Vardya 1971, Carrasco et al. 1982). Therefore, as a star evolves, its central mass plays a significant role in varying its angular momentum (Matt et al. 2015). Kraft (1967) obtained a power law relationship between the mean angular momentum per unit mass (hereafter *J*) and the mass of a star (*M*), such that $J \propto M^\alpha$, where α is an exponent. Recent analyses of the Kepler host stars confirm Kraft's power law relationship (Paz-Chinchón et al. 2015).

5.4   Motivation

Although it is not correct to compare physics of the Solar system with physics of exoplanetary systems, as the Sun has similar physical characteristics compared to physical characteristics of exoplanetary host stars, one can understand the formation and evolution of Sun and its planets through exoplanetary systems. By considering physical

and orbital characteristics of the exoplanets, present study has the following aims: (i) to seek possible answer to the unsolved problem of the Sun's low spin angular momentum, (ii) to examine whether the total (spin and orbital) angular momentum of the whole Solar system planets is compatible with the total angular momentum of Sun-like stars that have detected exoplanets, (iii) to ascertain whether magnitudes of orbital angular momenta (OAM) of the solar system planets are within the range of magnitudes OAM of the exoplanets, (iv) to determine whether planets in the vicinity (≤ 1.5 AU, hereafter vicinity is the region within 1.5 AU from the central star) of the Sun accreted mass onto the Sun during the early history of Solar System planetary formation and, (v) to investigate whether Solar system planets experienced orbital migration to their current positions.

5.5   Data And Analysis

We consider the physical and orbital characteristics of Sun-like G type host stars and their exoplanets. In this analysis, Sun-like stars are defined based on the spectral G type at different evolutionary stages that are provided in the Extrasolar Planets Encyclopedia website[1]. Exoplanetary masses, semi-major axes, orbital eccentricities, stellar masses, and stellar radii are also considered from the same website. The spectroscopically measured projected rotational velocities of the host stars were obtained from the Exoplanet Orbit Database website[2]. We find that there are nearly 483 G-type stars with exoplanets in the dataset, although some of the stars physical (mass and radius) and exoplanet's orbital (semi-major axis and eccentricity) parameters are missing. In addition, in order to avoid the ambiguity in considering the brown dwarf candidates, restrict the maximum planetary mass limit to 13 Jupiter mass. If one considers all the physical parameters of host stars and orbital parameters of planets, we are left with 275 exoplanetary data. Out of which finally we have 186 exoplanets that have estimated projected rotational velocities for their host stars.

This final dataset consists of 36 low mass (≤ 0.1 M_J) planets, out of which 6 have

---

[1] http://exoplanet.eu/catalog/
[2] http://exoplanets.org/table

masses approximately close to the Earth mass. The physical and orbital characteristics of the selected exoplanets and their host stars are provided as a Table 2 of Appendices. One can argue that data bias (majority are high mass planets in the vicinity of stars) can lead to misleading results. However, when one examines the data, following important fact completely rule out such biases. For example, in addition to hot-Jupiters, the data set also consists of low-mass planets in the vicinity of their host stars, such as Kepler-10, Kepler-11, HD 20794, etc.

Orbital angular momentum (OAM), L_p, of exoplanets (Berget and Durrance 2010) is computed (based on the central force between two objects) as follows:

$$L_p = M_p \sqrt{GM_\star a(1 - e^2)}, \tag{5.4}$$

where M_p is the mass of the exoplanet, G is the universal gravitational constant, a is the semi-major axis, e is the orbital eccentricity and $M_\star$ is the stellar mass. It is to be noted that the equation (5.4) is a valid approximation because the planetary mass is negligible when compared to stellar mass.

The spin angular momentum of the host stars, $J_\star$, is estimated by

$$J_\star = \left(\frac{v \sin i}{R_\star} \right) I_\star, \tag{5.5}$$

where $v \sin i$ is the projected rotational velocity of the star, i is the inclination about the rotation axis, $R_\star$ is the radius and $I_\star$ is the moment of inertia (= $(2/5)M_\star R_\star^2$) of a star calculated with a reasonable assumption of rigid body. In the case of Sun-like G stars, nearly 50% of the mass (Gibson 1973, Hiremath 2013, 2016) is concentrated in a 20% radius from the center, where density variation is roughly constant and, hence, this reasonable assumption that the star is a rigid body is valid.

If the rotational period ($P_\star$) of a star is known, the spin angular momentum, J_{spin}, can also be computed as follows:

$$J_{spin} = \frac{2\pi I_\star}{P_\star}. \tag{5.6}$$

It is to be noted that, both $J_\star$ and J_{spin} represent the spin angular momentum of a host

Table 5.1 The Physical and Orbital Characteristics of Solar System Planets. the First and Second Columns Represent the Name and Mass (In Terms of Jupiter Mass M_J) of the Planets, Respectively. the Eccentricity (*E*) and Semi-Major Axis (*A*) Are Given in Third and Fourth Columns. the Orbital (L_{ps}) and Total L_{totS} (Sum of Sun's Spin and Orbital) Angular Momenta Are Presented in the Last Two Columns.

Name	Mass (M_J)	e	a (AU)	$\log(L_{ps})$ (kg $m^2 s^{-1}$)	$\log(L_{tots})$ (kg $m^2 s^{-1}$)
Mercury	0.0001	0.2056	0.3870	38.9533	42.0456
Venus	0.0025	0.0068	0.7230	40.2668	42.0524
Earth	0.0031	0.0167	1.0000	40.4260	42.0556
Mars	0.0003	0.0934	1.5240	39.5450	42.0466
Jupiter	1.0000	0.0484	5.2032	43.2859	43.3101
Saturn	0.2994	0.0542	9.5374	42.8936	42.9512
Uranus	0.0457	0.0472	19.1920	42.2296	42.4482
Neptune	0.0539	0.0086	30.0705	42.3993	42.5584

star. However, $J_\star$ is estimated by using projected rotational velocity, whereas, J_{spin} is estimated by using rotational period of a star.

Using the formulae 5.4-5.6 and different physical characteristics of the host stars, we compute orbital, spin, and total (sum of spin and orbital) angular momenta of Sun-like stars that have detected exoplanets. These estimated angular momenta of host stars and exoplanets are presented in Table 3 of Appendices. Whereas, along with the physical and orbital characteristics, the estimated OAM and total angular momentum of Solar system planets are presented in Table 5.1.

5.6 Results And Conclusions

5.6.1 Orbital Angular Momentum of Exoplanets

First, we investigate a relationship between the exoplanetary mass and its OAM. Among the linear and non-linear (power law and exponential) fits, we get a best power law fit between the OAM of detected exoplanets and their respective masses. Since the OAM of detected exoplanets is directly proportional to the planetary mass (see equation 5.4), it is not surprising that the slope in the Figure 5.1 is ~ 1. However, aim of the present study is to find the range of OAMs of the exoplanets that vary with different planetary masses in the Milky Way Galaxy, and to examine whether the OAM of our Solar system

planets falls in this range.

As shown in Figure 5.1, the range of Solar system planetary masses, particularly related to terrestrial masses, are located at the lower end distribution of exoplanetary masses. We believe that this result may be due to undetected exoplanets at the lower mass range. The upper line in Figure 5.1, that represents OAM of Solar system planets, is almost parallel and slightly above the lower line that represents the OAM of detected exoplanets, suggesting that the OAM of Solar system planets is higher than the OAM of detected exoplanets. This resulting mismatch may be explained as follows. Observations show that, in addition to low mass planets, a majority of exoplanets that are within the vicinity of their host stars have a mass that is higher than the mass of Solar system terrestrial planets (Udry and Santos 2007). Therefore, in order to compensate for this mismatch, the masses of the Solar system planets have to be increased without altering their orbital distances. One can argue that instead of increasing the planetary mass, the orbital distances of solar terrestrial planets can be decreased. However, the detailed explanation for the same is given in section 5.6.4. We may also account for the low mass and high OAM of Solar system planets in different ways, *viz.,* the formation mechanism of Solar system may be different than the other stellar planetary systems. In early evolutionary stages, due to high solar activity (Hiremath 2009) (with heavy mass loss, the fast solar wind, intense coronal mass ejections, among others), the Solar system terrestrial planetary mass might have been displaced to the outer reaches of the Solar system. Presence of ^{6}Li in the host star indicates the accretion of mass onto the central star in early main sequence stage (Israelian et al. 2001, Reddy et al. 2002). This result implies that a part of the planetary mass in the vicinity of the Sun might have accreted onto the Sun. That means, probably present planetary mass in the vicinity of Sun might be lower than the mass during early epoch of the solar system formation. However, presently, it is not clear to us how, and in which epoch of the evolutionary history of the Solar system, the part of terrestrial planetary mass accreted onto the Sun.

On the other hand, it is interesting to estimate the magnitude of missing terrestrial planetary mass by using the relationship between L_p and $\frac{M_p}{M_J}$ that is obtained from the exoplanetary data and is given by
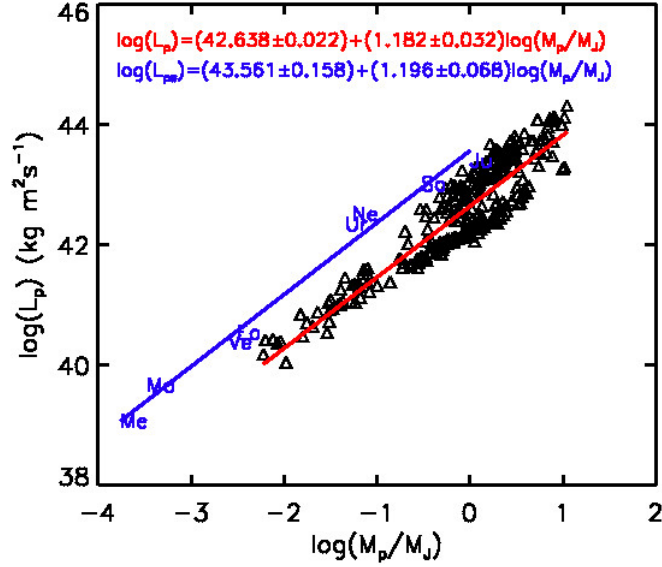
Fig. 5.1 The Non-Linear Relationship Between Orbital Angular Momentum of Exoplanets and Their Masses. the Best Fit Line Is Indicated by the Lower Continuous (Red) Line, While the Upper (Blue) Line Indicates the Best Fit Between the OAM of Solar System Planets With Respect to Their Masses. the Words (Me-Mercury, Ve-Venus, Ea-Earth, Ma-Mars, Ju-Jupiter, Sa-Saturn, Ur-Uranus and Ne-Neptune) Represent the Solar System Planets. Error Bars in L_p Are Negligible, Hence Is Not Plotted.

$$\log(L_p) = (42.638 \pm 0.022) + (1.182 \pm 0.032) \log\left(\frac{M_p}{M_J}\right). \tag{5.7}$$

Whereas the best fit between the OAMs of Solar system planets (L_{ps}) and their masses yields

$$\log(L_{ps}) = (43.561 \pm 0.158) + (1.196 \pm 0.068) \log\left(\frac{M_p}{M_J}\right). \tag{5.8}$$

One can infer, from equations (5.7) and (5.8), that, for one Jupiter planetary mass, the Solar system OAM is roughly ten times the OAM of detected exoplanets.

5.6.2   Spin Angular Momentum of Confirmed Planetary Host Stars

As we discussed earlier, the spin angular momentum of a star is estimated either by assuming it as a rigid body rotation and/or by considering the differential rotation of a star both in radial and latitude components. However, we know that the Sun and other sun-like stars actually rotate deferentially (Hiremath 2016). In this section, the angular momentum of stars are computed for three cases, namely, (i) rigid body rotation

102
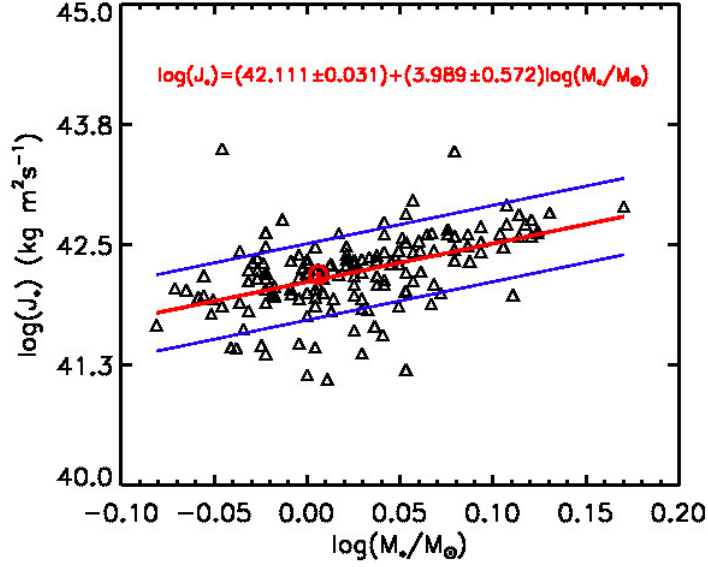
Fig. 5.2 The Power Law Distribution of Spin Angular Momentum *Vs* Mass of the Host Stars. the Central Line Indicates the Best Fit Line, and the Two Other Lines, Above and Below the Best Fitted Lines Are the One Standard Deviation Error Bars. the Sun's Position Is Indicated by Its Usual Notation ⊙. Note: Stars That Do Not Have Projected Rotational Velocities Are Not Plotted in This Figure.

(in which case where star is assumed to be rotating rigidly), (ii) differential rotation of convective envelop with decreasing core rotation and, (iii) differential rotation of convective envelop with increasing core rotation. Derivation of angular momentum, especially for the last two cases, and results for all the three cases are presented below.

5.6.2.1 Assumption of Rigid Body Rotation of Host Stars

When one makes this assumption of rigid body rotation, it is easy to derive equation for angular momentum as explained in equation (5.5) and (5.6) respectively. The dependency of the estimated spin angular momenta $J_\star$ of stars (by using equation 5.5) on stellar masses is examined for both linear and non-linear least square fits. The best fit yields a non-linear relationship which is illustrated in Figure 5.2, with a power law given by

$$\log(J_\star) = (42.111 \pm 0.031) + (3.989 \pm 0.572) \log\left(\frac{M_\star}{M_\odot}\right). \tag{5.9}$$

Interestingly, the simplified form of equation (5.9) resembles the Kraft (1967) law ($J_\star \propto M_\star^\alpha$, wherein α is 4.5). In our study, for the host stars that have detected exo-

planets, the value of exponent α is estimated to be ~ 4, which is close to the value of exponent in Kraft's law.

One can notice from Figure 5.2 that there is a lot of scatter in this relationship. Careful observation of data reveals that we have significant uncertainties ($\geq 30\%$) in the projected rotational velocities of host stars. Owing to this reason, these large error bars are not considered when subjecting least square fit between spin angular momentum and mass of the host stars. Instead, the deviation of observed data from the fitted line is used to compute errors in the estimated coefficients of the linear least square fit (Press et al. 1992, see section 15.2).

Hence, in order to reduce the scatter in the relationship between spin angular momentum and stellar mass, we consider photometrically estimated rotational period (most of the values have $\leq 20\%$ error) of Sun-like (F, G, K and M) stars that have detected exoplanets from the previous studies (Pinsonneault et al. 2012, Paz-Chinchón et al. 2015). By knowing rotational period (P) and from equation (5.6), the spin angular momentum J_{spin} of these host stars is computed. The resulting spin angular momentum *vs* stellar mass is illustrated in Figure 5.3 (a) wherein one can notice the least scatter. The best power law fit between the spin angular momentum of the stars and their masses yields

$$\log(J_{spin}) = (42.331 \pm 0.035) + (4.187 \pm 0.247) \log(\frac{M_\star}{M_\odot}). \qquad (5.10)$$

One can notice from the Figure 5.3 that probability of occurrence of Sun's position (as represented by symbol $\odot$) that falls within 1σ (where σ is a standard deviation of the best fit line) is very good ($\sim 95\%$; assuming Gaussian distribution).

As the Sun/stars rotate deferentially both in radial and latitude direction (Hiremath 2016), the computation of spin angular momentum of the Sun/stars with an assumption of rigid body rotation is not reasonable. Thus, for derivation of angular momentum, one has to consider the rotation profile of the stars that varies with its co-latitude and radial direction for precise estimation of its spin angular momentum. Although rotation profile inferred from the rotational splitting due to 'p' modes yield the core rotation upto nearly 0.2 solar radius, however, it is not clear whether radiation of core rotation increases or decreases towards center. Whereas, recent inference (Fossat et al. 2017) of

near core center due to 'g' modes yielded the core rotation substantially (nearly 4 times surface rotation) increases towards center. In this scenario of uncertain estimation of core rotation and in order to estimate the angular momentum, we make two assumptions regarding core rotation near the center ((i) radially increasing core rotation and, (ii) radially decreasing core rotation) and analytically derive the angular momentum equation. Before deriving these equations, we should have knowledge of angular momentum of deferentially rotating convective envelope which is derived in the following section.

5.6.2.2   Differential Rotating Convective Envelope

In this case, best way and reasonable rotation profile one can adopt is the one which satisfies the hydrodynamic stability criterian (Dubrulle and Knobloch 1993) and is given as follows:

$$r^2 \frac{d}{dr}\left(\frac{\Omega^2}{r^2}\right) > 0 \tag{5.11}$$

where r is the radial variable of star and Ω is angular velocity. Solution of above equation implies radially decreasing rotation rate from surface to base of the convection zone, which can be given as

$$\Omega(r) = \frac{\Omega_b r}{R_b}, \tag{5.12}$$

where Ω_b and R_b are angular velocity and radius at base of convective zone respectively. Spin angular momentum of the convective envelope (J_{con}) with variable density and rotation rate is given by

$$J_{con} = \int_0^{\frac{\pi}{2}} \int_{R_s}^{R_b} \rho(r)\Omega(r,\theta)r^4 dr d\theta, \tag{5.13}$$

where, $\rho(r) = \rho_0 e^{\frac{-r}{H}}$ (derived from hydrodynamic equilibrium), $\Omega(r,\theta) = \frac{\Omega_0}{r}\left(1 + \frac{\Omega_1}{\Omega_0}cos^2\theta\right)$, r is radial coordinate, θ is co-latitude, ρ_0 is average density of convective envelope, Ω_0 is surface rotation rate at the equator, Ω_1 is surface differential rotation rate, H is density scale height. By integrating the above equation, we obtain

$$J_{con} = \frac{\rho_0 \Omega_0 R_\star^5 \pi}{2} \left(1 + \frac{\Omega_1}{\Omega_0} cos^2\theta \right) (A1 + B1), \tag{5.14}$$

where $A1 = -H_1 e^{\frac{-x_b}{H_1}} (x_b^5 + 5H_1 x_b^4 + 20H_1^2 x_b^3 + 60H_1^3 x_b^2 + 120H_1^4 x_b + 120H_1^5)$,

$B1 = H_1 e^{\frac{-x_s}{H_1}} (x_s^5 + 5H_1 x_s^4 + 20H_1^2 x_s^3 + 60H_1^3 x_s^2 + 120H_1^4 x_s + 120H_1^5)$, $H_1 = (H/R_\star)$,

$R_\star$ is radius of a star, $x_s = R_s/R_\star$, $x_b = R_b/R_\star$, R_b and R_s are radii at the base and surface of a star.

It is to be noted that, the form of $\Omega(r,\theta)$ profile is assumed to be similar as that of convective envelope of the Sun from base of convection zone to the region near rotational shear close to the surface. We are neglecting shallow surface rotational shear which decreases around 0.93 $R_\odot$ to 1 $R_\odot$.

5.6.2.3 Rigidly Rotating Core With Radially Decreasing Rotation

Similarly, with an assumption of constant rotation rate at all latitude, the angular momentum of stellar core (J_{core}) is given by

$$J_{core} = \int_{R_b}^{R_c} \rho(r)\Omega(r)r^4 dr, \tag{5.15}$$

where $\rho(r) = \rho_b e^{\frac{-r}{H}}$, $\Omega(r) = \frac{\Omega_b r}{R_b}$, ρ_b is average density at the base of convection zone, Ω_b is rotation at the base of convection zone. By integrating the above equation (5.14), we obtain

$$J_{core} = \frac{\rho_b \Omega_b R_\star^6}{R_b} (A2 + B2), \tag{5.16}$$

where $A2 = -H_1 e^{\frac{-x_c}{H_1}} (x_c^5 + 5H_1 x_c^4 + 20H_1^2 x_c^3 + 60H_1^3 x_c^2 + 120H_1^4 x_c + 120H_1^5)$,

$B2 = H_1 e^{\frac{-x_b}{H_1}} (x_b^5 + 5H_1 x_b^4 + 20H_1^2 x_b^3 + 60H_1^3 x_b^2 + 120H_1^4 x_b + 120H_1^5)$, $x_c = R_c/R_\star$, R_c is core radius and $R_\star$ is radius of the star.

Above mentioned analytical equations (5.14 and 5.16) are used to compute the spin angular momentum of each host stars. However, in order to make use of these equations one should know the information of different properties of stellar interior viz., mass, rotation rate and depth of convective zone and core. As we already know that probing the properties of stellar interior is a difficult task. However, stellar evolutionary studies

suggest that mass, rotation rate, magnetic field of a star decreases with age. Skumanich (1972) showed that rotation rate of stars decreases with age which is well known as *Skumanich law*. However, Skumanich considered all G stars irrespective of whether they harbor planet or not. In order to confirm Skumanich law in case of the stars that have planets, we examined the variation of rotation rate of host stars with stellar age and obtained a non-linear relation given by

$$log(\Omega) = (-5.479 \pm 0.037) - (0.316 \pm 0.045)log(\frac{\tau_\star}{\tau_\odot}), \qquad (5.17)$$

where $\tau_\star$ and $\tau_\odot$ are host star's age and Sun's age respectively.

Above equation can be converted into a power law of the form $\Omega = 10^{-5.479} \left(\frac{\tau_\star}{\tau_\odot}\right)^{-0.316}$. Interestingly, for the stars that harbor planets, decay of the exponent of the age ($\frac{\tau_\star}{\tau_\odot}$) is larger (less negative index) compared to the power law index of Skumanich. This suggests that the stars that harbor the planets their rotation rates decrease slowly compared to the stars without planets (assuming that Skumanich sample of data mostly consists of stars without planets). Since the information of stellar age is not known, for most of the stars collected from in Pinsonneault et al. (2012), Paz-Chinchón et al. (2015), we use the above equation to estimate the stellar ages of host stars. With the information of estimated age of host stars and, mass and depth of convection zone of the Sun, the mass and depth of convective zone of other host stars are computed with a simple assumption that these properties vary as the inverse square root of their ages. By knowing the information regarding mass and depth of convective zone, its density can be easily estimated. The remaining mass and radius of a star is used to estimate the density of star's core. Thus, with these informations and making use of equations (5.14 and 5.16), we have estimated the spin angular momentum of outer convection envelope and core of host stars. The spin angular momentum of whole star (J_{spin}) is obtained by adding J_{con} and J_{core} respectively. Spin angular momentum of host stars with radially decreasing core rotation are compared with stellar mass and obtained a non-linear relationship as follows

$$log(J_{spin}) = (43.228 \pm 0.070) - (3.142 \pm 0.492)log(\frac{M_\star}{M_\odot}). \qquad (5.18)$$

This non-linear relationship is illustrated in Figure 5.3 (b). Contrary to the first case of angular momentum due to rigid body rotation, it is interesting to note that, the J_{spin} of the stars is inversely proportional to their stellar masses. One can also notice that the Sun's position in this figure is significantly lower side of one sigma error bar. This implies Sun's spin angular momentum is very small compared to other stars.

5.6.2.4 Differentially Rotating Convective Envelop with Increasing Core Rotation

In the previous case, we have considered the decreasing radial variation of rotation profile from base of convective zone towards center of a star which satisfies the hydrodynamic stability criterian as given in equation (5.11). However, recent study from Fossat et al. (2017) showed that the Sun's core rotates faster than its surface. Thus, in the following, with an assumption of increasing core rotation profile, similar to the Sun, in other sun-like stars, we analytically derive a formula for estimating the spin angular momentum of the host star. Here also we have considered a simple two component model of differentially rotating convective envelope and rapidly rotating core. Since we have considered the rotation profile of the convective envelope as similar to previous case (section 5.6.2.2, eq. 5.12), the estimation of spin angular momentum of convection zone (J_{spin}) is similar to the equation (5.14). However, similar to the previous case, we retain the assumption of constant core rotation rate at all latitudes. Spin angular momentum of the core is given by

$$J_{core} = \int_{R_b}^{R_c} \rho(r)\Omega(r)r^4 dr,$$ (5.19)

where $\rho(r) = \rho_b e^{\frac{-r}{H}}$, $\Omega(r) = \frac{\Omega_b R_b}{r}$ (similar decreasing rotation profile as described in equation 5.12 is used), ρ_b is density at the base of convection zone, Ω_b is rotation at the base of convection zone. After simplifying the above equation, we obtain

$$J_{core} = \rho_b \Omega_b R_b R_\star^4 (A3 + B3),$$ (5.20)

where $A3 = -H_1 e^{\frac{-x_c}{H_1}}(x_c^3 + 3H_1 x_c^2 + 6H_1^2 x_c + H_1^3)$, $B3 = -H_1 e^{\frac{-x_b}{H_1}}(x_b^3 + 3H_1 x_b^2 + 6H_1^2 x_b + H_1^3)$, $x_b = \frac{R_b}{R_\star}$, $x_c = \frac{R_c}{R_\star}$, R_c is radius at core of host stars and all other symbols
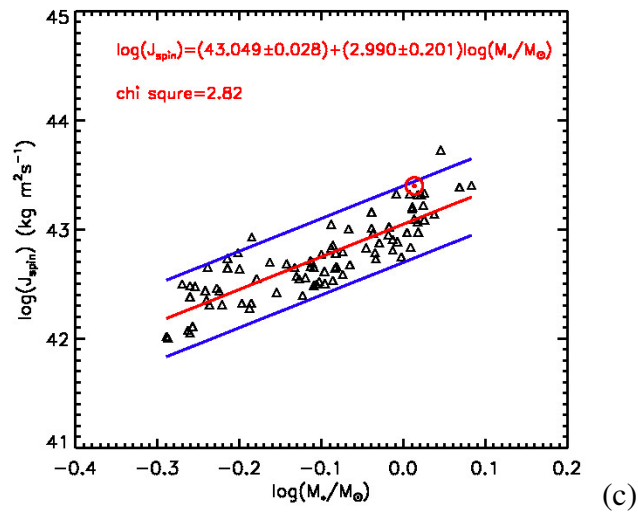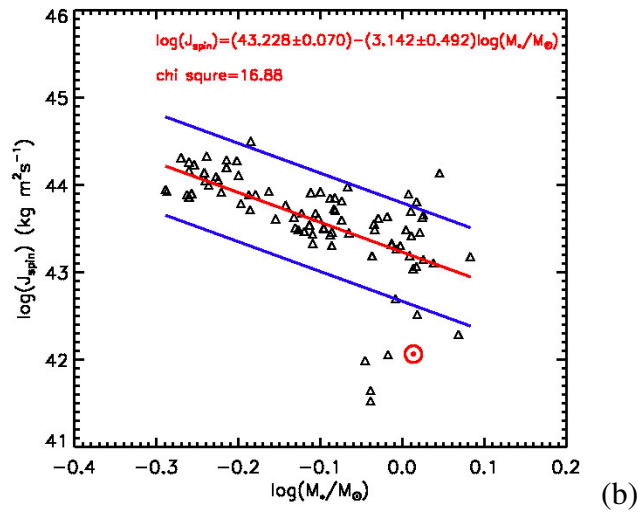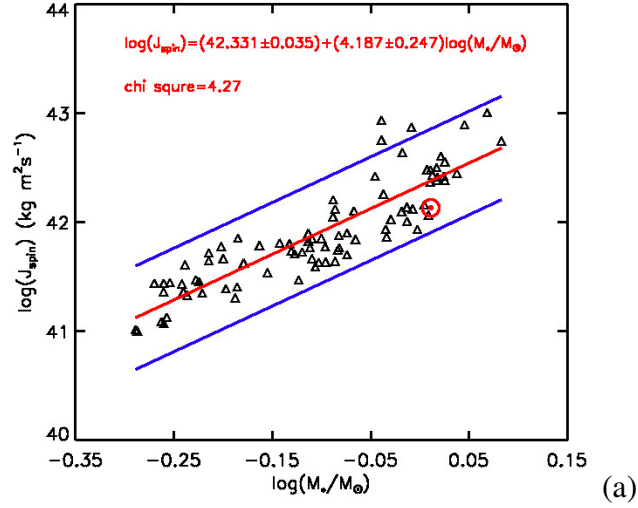
Fig. 5.3 The Power Law Distribution of Spin Angular Momentum *vs* Mass of Host Stars. The Spin Angular Momentum is Estimated by Assuming Rigid Body Rotation In Case of (a). Whereas, it is Estimated by Considering Decreasing Rotation Rate In Case of (b). In the Case (c), Spin Angular Momentum is Computed By Considering Fast Rotating Core. In All Three Cases, The Central Line Indicates the Best Fit, and the Other Two Lines, Above and Below the Best Fitted Lines Represent the One Standard Deviation Error Bars. The Sun's Position is Represented By its Usual Notation ⊙.

109

are as described earlier.

By using the above analytical equation, the spin angular momentum of stellar core is estimated and it is added with J_{con} in order to estimate the total spin angular momentum of a host star. The resultant J_{spin} of host stars is compared with the stellar mass and obtained a non-linear equation as follows

$$log(J_{spin}) = (43.049 \pm 0.028) + (2.990 \pm 0.201)log(\frac{M_\star}{M_\odot}). \qquad (5.21)$$

The above relationship is illustrated in Figure 5.3 (c) that suggests spin angular momentum increases with increase in stellar mass. In this case also we have obtained a power law relations similar to Kraft (1967). However, our power law relationship is purely for the host stars with planets. The Sun's position in this figure is well within one sigma error bars.

Among all the relationships (eq. 5.10, 5.17 and 5.20) between spin angular momentum of host stars and stellar mass, we find that, the power law presented in equation 5.20 is best on the basis of least error bars in the coefficients and least chi-square compared to other relationships. Owing to these important facts, in the following estimation of total angular momentum, we use this power law for the spin angular momentum.

Alves et al. (2010) compared the spin angular momentum of stars with and without exoplanets, and suggested that stars with confirmed exoplanets have more angular momenta than the stars without. It is plausible that the low spin angular momenta of stars (that have undetected planets) are the result of the distribution of angular momenta of stars to the spin and orbital angular momentum of undetected planets. Since stars with high planetary masses have high OAMs (Figure 5.1), we can speculate that stars with low OAM might have low mass planets that can be detected by future space probes.

5.6.3 Total Angular Momentum of The Confirmed Planetary Systems

Our final objective is to confirm whether total angular momentum (TAM) (spin + orbital) of the Solar system has a similar variation in the total angular momentum of detected planetary systems with respect to their planetary or stellar masses. Here, the total angular momentum of host stars are estimated by using two power laws (5.10 and
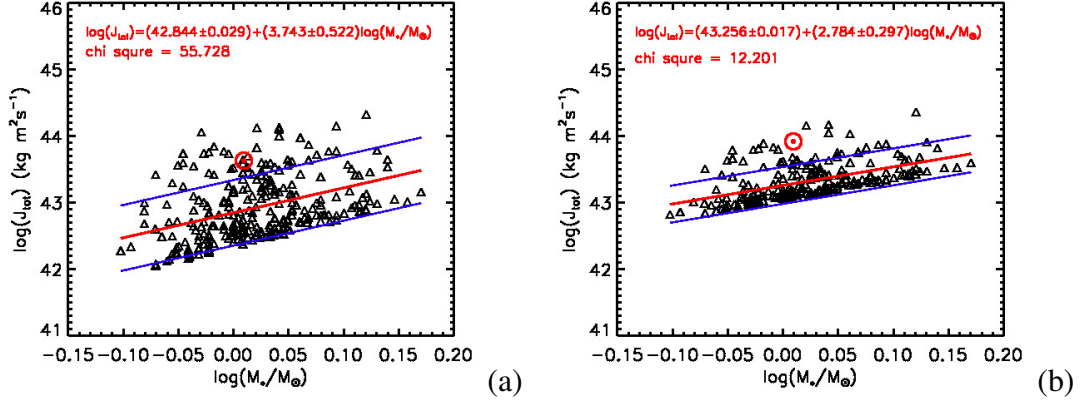
Fig. 5.4 (a) and (b) Illustrate The Power Law Dependence Between the Total Angular Momentum of the Stellar System and Its Stellar Mass. The Symbol ⊙ Outside the 1σ Line in Both the Figures Represents the Total Angular Momentum of the Solar System With Respect to the Sun's Mass.

5.20) related to spin and orbital angular momentum. This is essentially to compare the differences in magnitudes of TAMs estimated by considering the rigid body rotation and the differential rotation (increasing core rotation) respectively.

5.6.3.1 Total Angular Momenta vs Stellar Masses

Relationship between the total angular momentum (J_{tot}) of the host stars and their masses is illustrated in Figure 5.4. In case of Figure 5.4 (a), TAM is estimated by considering the case of rigid body rotation. Whereas, in case of Figure 5.4 (b), it is estimated by considering the case of differential rotation. From the constraint of least value of chi-square and least error bars in the coefficients, we find that, the best fit is the one when TAM is estimated by considering differential rotation with increasing core rotation and is given as follows

$$\log(J_{tot}) = (43.256 \pm 0.017) + (2.784 \pm 0.297) \log\left(\frac{M_\star}{M_\odot}\right). \qquad (5.22)$$

As shown in both the illustrations of Figure 5.4, the position of total angular momentum (as represented by symbol ⊙) of Solar system is slightly outside the 1σ error bars. Since it is known fact that most of the angular momentum of system resides in planets rather than the Sun, we can conclude that, during early stages of the Solar system formation, most likely Jovian planets might have migrated outward by acquiring

111

more orbital angular momentum. The same conclusion we drew in the previous section (5.6.1), where we inferred that, compared to confirmed planetary host stars, the Sun has a lower spin angular momentum.

It is important to note that if the best fit line is extended towards the lower stellar mass region, the minimum total angular momentum that a star can have is ~ 5.47 x 10^{38} kg $m^2 s^{-1}$, which is close to the spin angular momentum of a brown dwarf limiting mass ($0.08\ M_\odot$). This implies that the total angular momentum of a stellar system with a least stellar mass that generates energy from nuclear fusion reactions is $\sim 10^{38}$ kg $m^2 s^{-1}$.

5.6.3.2   Total Angular Momentum vs Planetary Masses

The dependence of total angular momentum (J_{tot}, estimated by considering rigid body rotation and differential rotation) with respect to planetary mass $\left(\frac{M_p}{M_J}\right)$ is examined for both linear and non-linear fits which are illustrated in Figure 5.5. For the two cases from which TAM is estimated, we obtained a best power law fit between J_{tot} and $\frac{M_p}{M_J}$ for the case when TAM is estimated by considering differential rotation, which is illustrated in Figure 5.5 (b). The central line in Figure 5.5 (b) represents the best power law fit, which is given by

$$\log(J_{tot}) = (43.355 \pm 0.013) + (0.304 \pm 0.019) \log\left(\frac{M_p}{M_J}\right). \qquad (5.23)$$

As shown in Figure 5.5 (b), two apparent relationships exist between the planetary mass and the total angular momentum of the stellar system. In fact, this relationship is pronounced if we consider the distribution of planets whose logarithmic mass is around -1. Hence, we have separately plotted for $\log\left(\frac{M_p}{M_J}\right) \leq$ -1 and for the value $\geq$ -1. These results are illustrated in the Figures 5.6 and 5.7, respectively. Among the two plots in Figure 5.6, the best fit yields a power law between TAM (estimated by considering differential rotation) and planetary mass ($\leq 0.1\ \frac{M_p}{M_J}$) is given by

$$\log(J_{tot}) = (43.286 \pm 0.090) + (0.175 \pm 0.059) \log\left(\frac{M_p}{M_J}\right). \qquad (5.24)$$

112
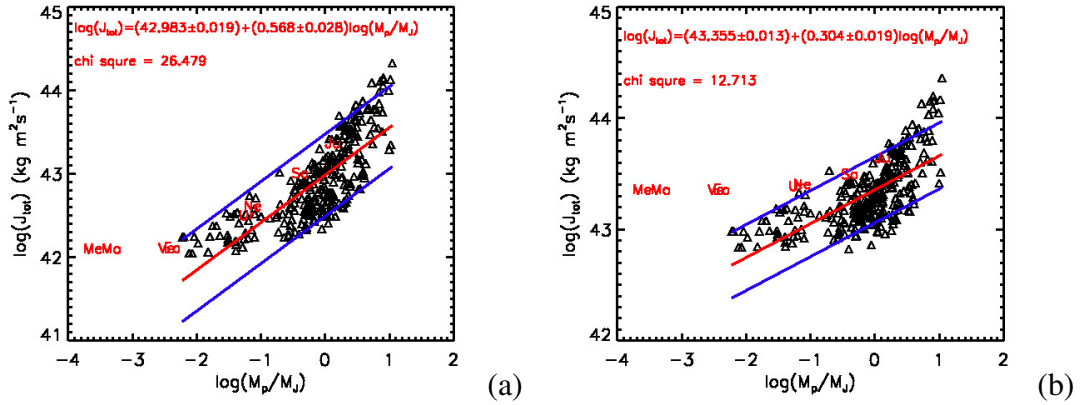
Fig. 5.5 (a) and (b) Illustrate The Power Law Dependence of the Total Angular Momentum of the Stellar System on Its Planetary Mass. Note the Different Range of Y-Axis Values When Compared to Two Plots.
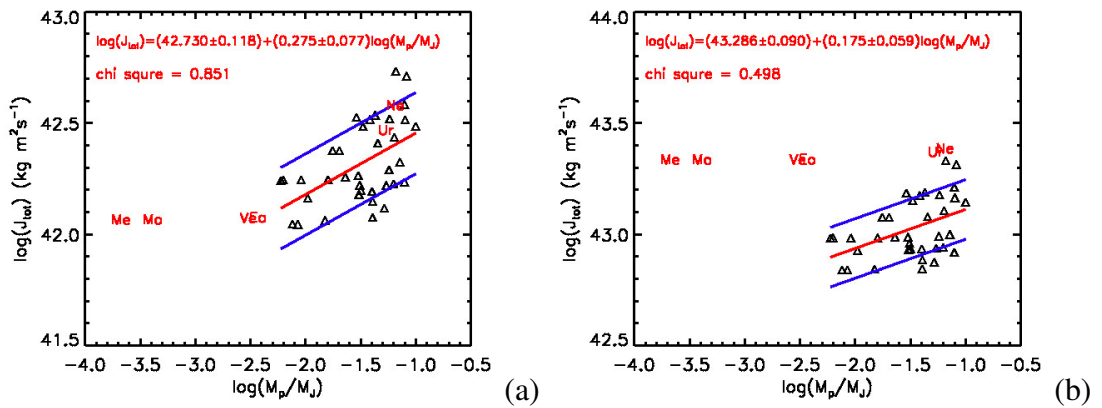
Fig. 5.6 (a) and (b) Illustrate The Power Law Dependence of the Total Angular Momentum of the Stellar System on Its Logarithmic Planetary Mass $\leq$ -1 For the Case of Rigid Body Rotation and Differential Rotation Respectively. Note the Different Range of Y-Axis Values When Compared to Two Plots.

Since we have very few data points (about $\sim 13\%$ of the total sample) in the lower mass range, we cannot make definite and meaningful conclusions regarding the J_{tot} - $\frac{M_p}{M_J}$ relationship. Nonetheless, one can see that the variation of total angular momentum of the solar terrestrial planets is aligned parallel to the x-axis. The obvious reason for this unusual variation is that the spin angular momentum of the Sun dominates in the J_{tot}, which means the OAM of Solar system terrestrial planets, that have a low mass, is smaller than the spin angular momentum of the Sun. Hence, one has to increase substantially the mass of terrestrial planets (see also section 5.6.4) in order to bring those (Me, Ma, Ve and Ea) to the best fitted universal line. In addition, one can also notice that the solar system planets in Figure 5.6 (b) are well above the other stellar-planetary systems.

Similarly, the dependency of total angular momentum (TAM) on mass for high mass planets (i.e., $\log\left(\frac{M_p}{M_J}\right) \geq$ -1) is illustrated in Figure 5.7. In case of Figure 5.7 (a), the TAM is computed by assuming rigid body rotation and in case of Figure 5.7 (b) it is computed on the bases of differential rotation. Based on the least error bars in the coefficients and minimum chi-square, a best fit is obtained in case of Figure 5.7 (b) which is of the form

$$\log(J_{tot}) = (43.319 \pm 0.013) + (0.497 \pm 0.032) \log\left(\frac{M_p}{M_J}\right). \qquad (5.25)$$

In Figure 5.7, Jupiter and Saturn (as represented by symbol Ju and Sa) are near the 1σ lines. In order to bring Jupiter and Saturn close to the best fitted line, their orbital distances need to be decreased substantially. The notations of Jupiter (Ju) and Saturn (Sa) near the best fit line represent J_{tot} after reducing the orbital distances to 1.30 AU and 1.43 AU, respectively. This result suggests that, in the early history of the Solar system, Jupiter's orbit around the Sun was smaller than its present orbit. Interestingly, these estimated orbital distances are almost similar to the orbital distances as estimated by the *Grand tack model* (Walsh and Millar 2011), which suggests that Jupiter has experienced the two phase migration described by inward (up to 1.5 AU) and then outward migration. Jupiter's two phase migration might have affected the protoplanetary disk near the Mars orbit and asteroid belt, which possibly might have reduced the early high
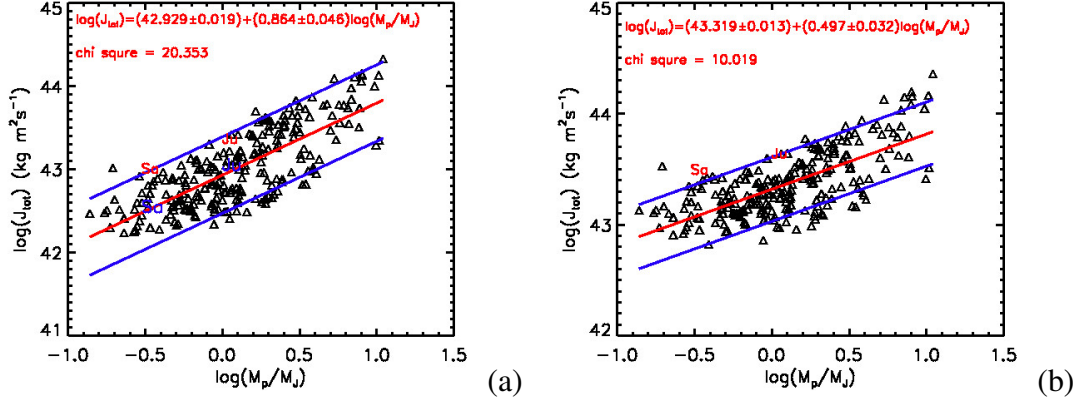
Fig. 5.7 (a) and (b) Illustrate The Power Law Dependence of the Total Angular Momentum of the Stellar System on Its Logarithmic Planetary Mass $\geq$ -1 For the Case of Rigid Body Rotation and Differential Rotation Respectively. Note the Different Range of Y-Axis Values When Compared to Two Plot.

mass Mars to present low mass Mars.

5.6.4 Clues for the Low Mass Planets and Missing Mass in the Vicinity of Sun

By using equation (5.8) and the total OAM of solar terrestrial planets (L_{ps}), we find that the present OAM of terrestrial planets is ten times higher than the OAM of exoplanets. Hence, we find a relation such that $L_p \sim 10^{-1}L_{ps}$ (where L_p is the OAM of detected exoplanets). Therefore, in order to match with the average OAM of the exoplanets (as shown in Figure 5.1), one has to either decrease the orbital distances of Solar system planets or increase the planetary mass. To decide this, dependency of planetary mass on the orbital distance a is examined and is illustrated in the Figure 5.8.

As shown in Figure 5.8 masses of the Solar system planets (as represented by Me, Ve, etc.) do not follow the stellar system planetary mass - semi major axis relationship. Figure 5.8 reveals two different distributions: (i) single planetary systems with the mass range of 0.1 - 10 Jupiter mass that are distributed independent of semi major axis and, (ii) a wide range of multiplanetary systems masses directly vary with the semi major axis. Therefore, masses similar to Earth-like planets can be detected if their stars have multiplanetary systems and are close to the host stars. In order to confirm whether two apparent distributions are drawn from the same parent distribution, an Anderson-Darling statistical test is performed on both the populations of single and multiplanetary

115
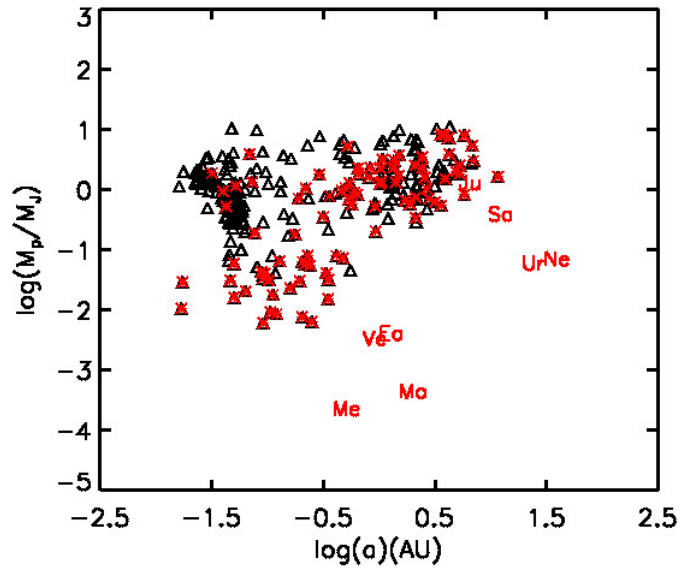
Fig. 5.8 The Relationship Between Planetary Mass and Its Semi-Major Axis. the Empty Triangles Indicate the Single Planetary Systems. the Triangles With Cross Marks Indicate the Multiplanetary Systems.
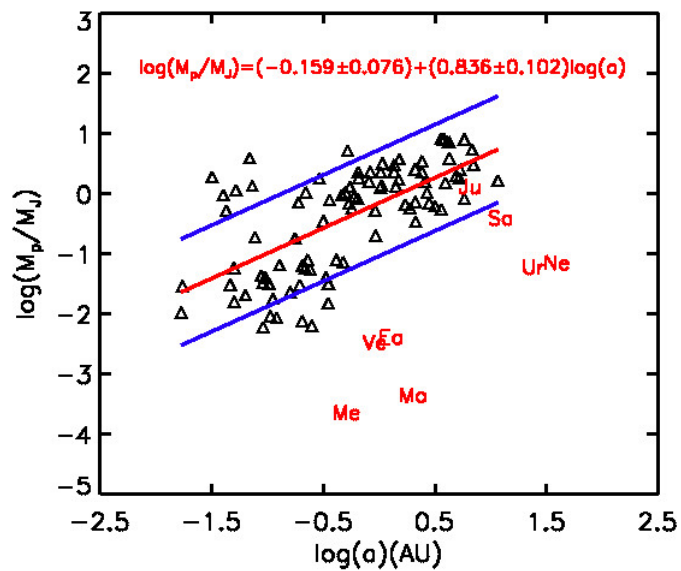
Fig. 5.9 The Power Law Dependence of Planetary Mass on Its Semi-Major Axes of Multiplanetary Systems.

systems that are presented in the Figure 5.8. The test results ($A^2 = 0.66$ and p-value = 0.08) for single planetary systems show that, the sample data is normally distributed. However, the test results ($A^2 = 3.14$ and p-value = 5.78 x 10^{-8}) for multiplanetary systems show that, this sample data is not distributed normally. This result suggests that both the populations are not drawn from the same parent distribution. Hence, we can infer that single and multiplanetary systems probably have different formation mechanisms.

Figure 5.9 illustrates the dependence of planetary masses on their semi-major axes (a), for the multiplanetary system, with a best power law fit given by

$$\log \left(\frac{M_p}{M_J} \right) = (-0.159 \pm 0.076) + (0.836 \pm 0.102) \log(a). \qquad (5.26)$$

As shown in Figure 5.9, the Solar system planets substantially deviate from the best fit line. In order for them to fall on the best fitted line, their semi-major axes need to be decreased or their masses need to be increased substantially. Equation (5.25) reveals that the estimated orbital distances (for the present solar terrestrial planetary mass) from the Sun are very small which is almost equal to the Roche limit. In this case, the chances of planetary destruction are more likely due to tidal forces. Therefore, mass of the terrestrial planets needs to be increased. By use of equation (5.25), the total missing mass of the solar terrestrial planets is estimated to be $\sim 2.5\ M_J$. Another way of masses of solar system planets very close to the best fitted line is to increase mass of the Jovian planets. Hence, if the masses of Jovian planets are increased, then their overall estimated mass ($\sim 40\ M_J$) will exceed the masses of brown dwarfs. This result inevitably leads to decrease of orbital distances of the Jovian planets, which suggests that these Jovian planets probably migrated outward during the early history of Solar system formation. This ultimate result is also compatible with the migration scenario as proposed by the Nice model (Tsiganis et al. 2005).

5.7 Conclusions

In conclusion, by considering the physical and orbital characteristics of the Sun-like G stars and their exoplanets, we have estimated the OAM of detected exoplanets and obtained a best power law fit with their planetary masses. We find that the OAM of Solar system planets is higher than the OAM of detected exoplanets, and the masses of terrestrial planets need to be increased to ensure compatibility between the OAM of the Solar system planets and the OAM of detected exoplanets. We speculate that the low mass of terrestrial planets in the vicinity of the Sun may be due to accretion of the planetary mass onto the Sun or transfer of the same planetary mass to the outer reaches of the Solar system.

Similarly, the spin angular momentum of the host stars is estimated for three cases of stellar rotation, namely, (i) rigid body rotation, (ii) differentially rotating convective envelope with slow rotating core and, (iii) differentially rotating convective envelope with fast rotating core. For all these cases, we have estimated the spin angular momentum of host stars and is compared to the stellar mass. Among these three cases, the best fit yields a power law relation for the case of differentially rotating convective envelope with fast rotating core. In this spin angular momentum-mass relationship, the Sun′s position falls well within one sigma error bars that suggests Sun's spin angular momentum is no different than other sun-like G stars. Furthermore, from the knowledge of orbital angular momentum of planets and spin angular momentum of host stars, total angular momentum of system is estimated. When the total angular momentum of the stellar system is compared with the host star and exoplanetary masses, the resultant relationship between J_{tot} - stellar masses shows that the solar system has more total angular momentum. This excess contribution is mainly because of the high OAM of Jovian planets. In order to reduce J_{tot}, present orbital distances, especially of the Jovian planets, need to be reduced substantially, i.e. similar to the ranges as proposed by *Grand Tack model* for Jupiter (1.5 AU) and 50% of reduced orbital distances for other Jovian planets. Furthermore, the relationship between J_{tot} and the exoplanetary mass show two different possible distributions: one for those planets whose logarithmic mass

is weighted by Jupiter mass is $\leq$ -1 and another for planets whose logarithmic mass is weighted by Jupiter mass is $\geq$ -1. Due to the presence of few data points in the lower mass range, we cannot make any definite conclusions; however, we can speculate that the detection of Earth-like planets is high when J_{tot} of the stellar system is $\sim 10^{42}$ kg $m^2 s^{-1}$. The fit of J_{tot} with the higher planetary mass range shows a clear power law relationship. If Jupiter and Saturn are brought closer to the best fit line, only their orbital distances would vary. In essence, this study suggests that Jovian planets (especially Jupiter and Saturn) migrated outwards in the early history of Solar system formation. The estimated orbital distances of Jupiter and Saturn in this study very well match with the initial orbital distances as proposed by the *Grand Tack model* (Walsh and Millar 2011).

Finally, planetary masses are compared with their respective orbital distances, and we find that, for multiplanetary systems, the planetary mass yields a best power law relation with its respective orbital distance, whereas, for single planetary systems, the planetary mass is independent of its orbital distance. These relationships reveal clues about the missing mass in the vicinity of the Sun and the migration scenario of Jovian planets that is compatible with migration scenario as proposed by Nice model (Tsiganis et al. 2005).

Metallicity of Sun-like G Stars and Their Exoplanets

6.1   Metallicity of Host Stars

Birth of a stellar system takes place in the nebula which consists of gas and dust particles that are basic ingredients for the formation of stars and planets. The amount of gas, dust particles, chemical composition or metallicity of the nebula play a significant role in the formation of planetary system (Ksanfomality 2004, Moriarty et al. 2014, Reboussin et al. 2015). Hence, study of stellar metallicity and its relation with different physical characteristics of host stars and their planets may lead to better understanding of the planetary system formation. Metallicity of a star is a measurement of fraction of metals present in that star. As explained in the chapter 1, all the elements with atomic number greater than two (i.e., Helium) are considered as metals. Total stellar composition of a star can be described by an equation given by

$$X + Y + Z = 1 \qquad (6.1)$$

where X indicates the fractional percentage of Hydrogen, Y indicates the fractional percentage of Helium and Z represents the fractional percentage of all metals present in a star. The Hydrogen mass fraction X can be given by $X = \frac{m_H}{M}$, where m_H is total mass of hydrogen present in a star and M is total mass of that star. Similarly Helium (Y) and other metals fractions (Z) can be expressed. For the Sun, values of these variables are approximately estimated as $X = 0.73$, $Y = 0.24$ and $Z = 0.02$.

Since the abundance of iron can easily estimated from the spectra of a star, often stellar metallicity is indicated by a symbol [Fe/H], which describes the total iron content

of a star compared to Hydrogen abundance. Usually the value of [Fe/H] is a logarithmic ratio of iron content of a star to the iron content of the Sun. Hence, if [Fe/H] is zero, then star's metallicity is similar to that of Sun. The positive and negative values indicate the metal rich and metal poor stars compared to the Sun's metallicity.

6.2 Motivation

The discovery of many exoplanetary systems (Boss et al. 2011, Lammer et al. 2010, Dressing and Charbonneau 2015) lead to many new models (de Wit and Seager 2013, Kerr et al. 2015) that further improved the knowledge of physics of planetary formation. In early studies it is found that the stars with planets have a higher metallicity than the stars without planets (Gonzalez et al. 2001b). However, low mass giant stars ($\leq$ 1.5 $M_\odot$) with planets do not show any difference in their metallicity when compared with giant stars without planets (Maldonado et al. 2013).

Previous studies (Gonzalez 2000, Santos et al. 2000) indicate that the detection of gas giants or hot Jupiters are more around the metal rich stars than the metal poor stars. That means, formation of giant planet is low around the metal poor stars (Fischer and Valenti 2005). Mordasini et al. (2012) showed that occurrence rate and mass of giant planets depend on the thickness and timescale of protoplanetary disk. On the other hand, occurrence rate of terrestrial planets or low mass planets is independent of the host star's metallicity (Buchhave et al. 2014). One explanation for the high mass planets around the metal rich stars is inward migration of planets during the early history of stellar system formation (Dawson and Murray-Clay 2013). Due to inward migration, high mass planets scatter the planetesimals (or gas and dust particles) that are present in the protoplanetary disk. These scattered planetesimals most likely accrete on the host stars convective envelope as a 'pollution' and hence, increases the stars metallicity (Vauclair and Vauclair 2014). During early evolutionary stage, accreted mass mix deep inside a star, whereas, in later stage, accreted mass mix only in a shallow convective envelope. For example, presence of ^{6}Li in the stellar system supports the accretion of planetary mass on the host star (Reddy et al. 2002, Santos et al. 2010, Mena et al. 2012). Hence, the effect of 'pollution' is one of the important factor that likely determines the final

metallicity of host stars and, the massive planets nearby host star may be a reason for increase in the metallicity of host stars during the early history of stellar system (stars with planets) formation.

Another explanation for high mass planets around metal rich stars is the metal rich nebula from which host stars and planets are formed (Gonzalez 2006). That implies, the metal rich protoplanetary disk around a host star (Gonzalez 2000, Bean et al. 2006) provides more gas and dust particles for the planetary formation. Adibekyan et al. (2012) confirmed that the rate of planetary formation is high in the galactic thick disk than in the galactic thin disk. This study also suggests that when the iron metal content is less, other metals play a major role in the planetary formation. The metal rich disk with high concentration of Si, Ca, Mg, Al etc., provides a good platform for the planetary core formation (Bodaghee et al. 2003). In addition, formation of terrestrial planets cannot be neglected around the metal rich stars (Wang and Fischer 2015), because, probability of formation of the solid core is high due to more number of dust particles in the disk, which eventually lead to solid planets that are within the snow line.

The volatile elements like carbon compounds and oxygen help in the formation of gaseous envelope or planetary atmospheres. Among various volatile materials, oxygen plays a major role in the planetary formation via ice accretion beyond the snow line and also by the oxides of Si, Mg, Al, Ca, etc., (Brugamyer et al. 2011). The silicate grains provide a good platform for the planetary formation and these grains with accretion of icy mantle may grow into gas giants. Interestingly, there is no significant difference in the abundance of [C/Fe] and [O/Fe] in stars with planets and stars without planets (Gonzalez et al. 2001, da Silva et al. 2011). Although contribution of these materials to metallicity of host star is insignificant, their major role in planetary formation cannot be neglected.

With this brief introduction, following are the aims of present study: (i) from the information of metallicity of host stars that have exoplanets, we try to understand how the metal content of a stellar nebula might have affected the planetary formation, (ii) we examine whether single and multiplanetary systems have similar mechanism of planetary formation or not, and the role of host stars′ metallicity in these mechanisms, (iii)

an attempt is made to confirm whether our solar system is also governed by the same universal mechanism of planetary formation and, (iv) we investigate whether stellar metallicity [Fe/H] is affected by average galactic metallicity that in turn might have influenced the planetary formation. Plan of present study is as follows. Description of the data used and the analysis are presented in section 6.3. Results with a brief discussion are presented in section 6.4, followed by overall conclusions in section 6.5.

6.3   Data and Analysis

In order to examine the role of metallicity in the planetary formation of Sun-like G stars, physical and orbital characteristics of exoplanets and their host stars of G type are considered from the website *http://exoplanet.eu/catalog/all_fields/*. Many previous studies make use of this catalog for understanding the physics of host stars, dynamics and atmospheres of their planets, *etc.* For example, estimation of metallicity of host stars (Lindgren et al. 2016) (Lindgren et al. 2016), atmospheric (Walsh and Millar 2011) and orbital (Antoniadou and Voyatzis 2016) studies of exoplanets, *etc.* Hence, this data set is most reliable to get answers for our aims.

We consider 225 exoplanets that belong to 179 host stars. Out of 225 exoplanets, 139 are detected by radial velocity method and remaining are detected by transit method. Among these, majority (148) of stars are single planetary hosts (only one planet for a star) and, 31 (with 77 planets) are multiplanetary hosts (more than one planet for a star). Although one can argue that single planetary hosts are due to limitations in detection techniques, at present it is not clear whether single planets are really single planets or due to limitations of the detection. It is also not clear, due to limitations of observational detection, how much percentage of data sample is due to single planet. However, in this study we assume that these are single planets.

With the present precision of detection techniques, number of planets that are detected from space and ground based missions are given in Table 6.1. From the distance measurements, we find that majority (171) of the exoplanets are within the solar neighborhood (≤ 300 pc). Relevant data related to the physical characteristics of planets and stars are presented in Table 4 of Appendices. As this exoplanetary catalog is compila-

Table 6.1 Number of Planets With Different Exoplanetary Detection Missions

Detection missions	no. of planets
CoRoT	14
HAT-P	09
HIP	03
HD catalog	125
Kepler	28
TrES	02
WASP	29
XO	01
Others	14

tion of ground and space based observations, observers have used different statistical techniques for estimating the error bars in the physical and orbital characteristics of exoplanets. For example, Hybrid Markov chain Monte Carlo (Gregory and Fischer 2010, Dumusque et al. 2014) and bootsrap (Barge et al. 2008) statistical method. However, basic errors that affect different physical parameters of the data are observational errors (Kovács et al. 2010, Wakeford et al. 2013).

In Table 4 of Appendices, first two columns represent the name of an exoplanet and its mass in terms of Jupiter's mass. Third and fourth columns represent the semi major axis and eccentricity respectively. Fifth and sixth columns represent the stellar metallicity [Fe/H] and stellar mass in terms of solar mass. Whereas, last column represents the stellar distance in parsec (pc).

6.4   Results and Discussion

Before examining a relationship between the stellar (planetary) mass with stellar metallicity, let us examine how far the exoplanets are located in the solar neighborhood and, if any influence of average galactic metallicity on the stellar metallicity irrespective of galactic latitude and longitude. Figure 6.1(a) illustrates the distribution of planets with their distances from the Sun. The x-axis represents the distances of host stars from the Sun and y-axis represents the number of planets. Similarly, Figure 6.1 (b) illustrates the distribution of stellar metallicities with their distances from the Sun. It is obvious and not surprising from Figure 6.1 (a) that exponential decrease of number of planets with the distance is due to faintness of the observed stars. That means, with the present

instruments, it is very difficult to precisely measure the radial velocity or transit curves of the exoplanets that are very far from the solar system. Hence, majority of exoplanets appear to occur within the solar neighborhood (≤ 300 pc). The Sun is situated in the galactic thin disk at about 20 pc above the galactic mid-plane. The gradient of radial variation of average metallicity in this galactic thin disk is 0.07 dex kpc^{-1} Gonzalez et al. (2001). It is interesting to check whether such a gradient of metallicity is also true if stars metallicity is influenced by galactic metallicity that in turn might have affected the planetary formation. In order to check this reasoning, irrespective of observed declinations (Dec) and right ascensions (RA), we combine different metallicities and same are plotted with respect to the observed stellar distances from the Sun. With the present data set, Figure 6.1 (b) illustrates the variation of stellar metallicity within the galactic thin disk. Since the majority of stars are within 300 pc, from the slope of Figure 6.1(b) (~ 0.08 dex kpc^{-1}) one can say that variation of average galactic metallicity within thin disk is negligible in the solar neighborhood. Of course, this is also evident from Figure 6.2 wherein distribution of stars with metallicity for different galactic coordinates is illustrated. There appears to be concentration of metal deficient stars (that have exoplanets) near both the galactic poles. Two illustrations (Figure 6.1 and 6.2) show that observed exoplanetary systems are within the proximity (~ 2 kpc) of the Sun. Whereas, from 2 - 8 kpc, there is no observational evidence of detection of exoplanets. Unless we have information of observed exoplanetary systems from all parts of galaxy, with the present dataset, it is difficult to conclude whether influence of galactic metallicity on the planetary formation exists or not.

6.4.1 Stellar Mass Versus Metallicity

Previous studies (Winn and Fabrycky 2015, and references therein) show that metal rich stars more likely harbor the planets. In addition, abundance of metallicity of stars with planets are more than the abundance of metallicity of stars without planets (Mortier et al. 2013). In these studies, results are obtained from an analysis of the host stars of all spectral types. However, it is interesting to know whether each spectral type, such as Sun-like G stars also follows the same trend or not. Importantly, it is essential to
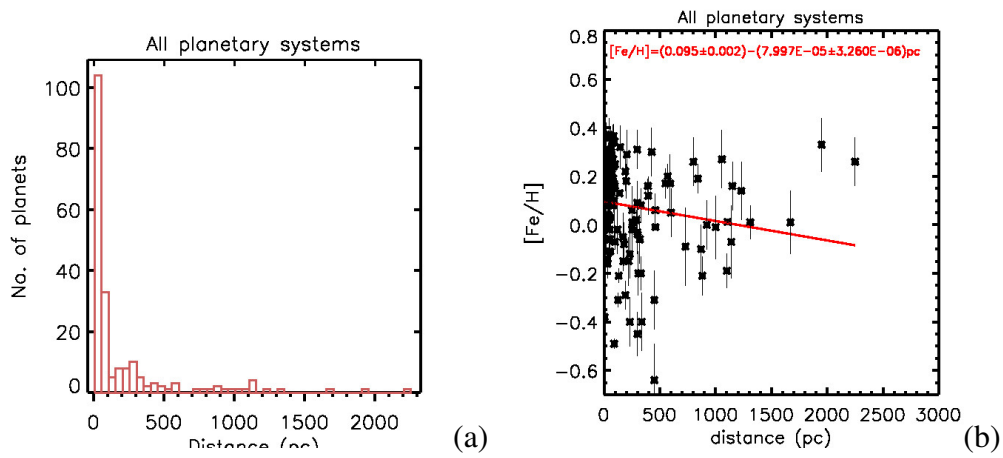
Fig. 6.1 (a) Illustrates the Distribution of Planets With Their Distances From the Sun. 6.1 (b) Illustrates the Dependency of Observed Stellar Metallicity With the Host Stars Distance From Solar System for All the Planetary Systems.
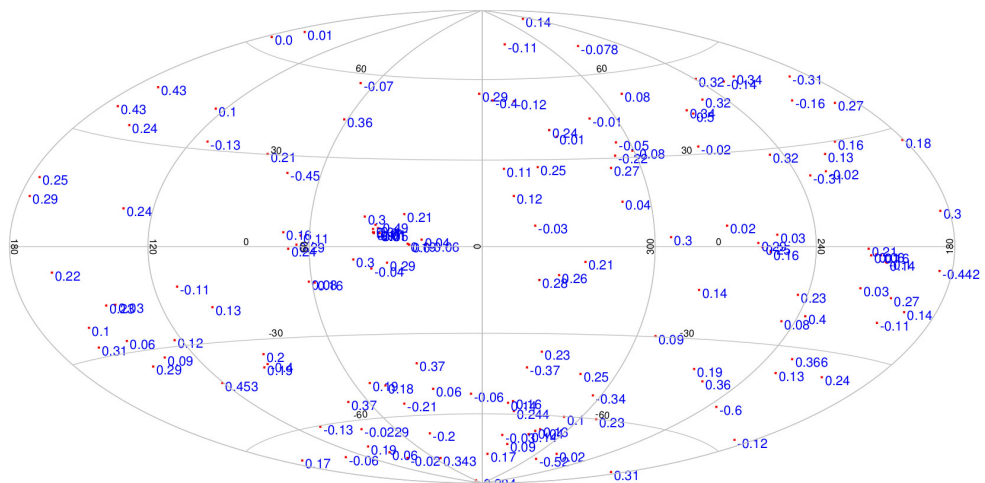
Fig. 6.2 Illustrates the Distribution of Stars (That Harbor Planets) With Metallicity for Different Galactic Coordinates Within the Observed Distance of 2.1 kpc.

126

understand the behavior of stellar metallicity in both single and multiplanetary systems. In order to assert these ideas, in Figure 6.3 (a) and 6.3 (b) we examine a relationship between stellar mass and stellar metallicity for all the planetary systems, irrespective of whether single or multiplanetary systems. In Figure 6.3 (a), x-axis represents the observed metallicity with a bin size of 0.1 dex in which stellar masses are collected, average and standard deviation (σ) are computed. Error in each bin is estimated from the ratio $\frac{\sigma}{\sqrt{n}}$ (where n is number of data points in each bin). Conventional usage is that, observed metallicity of a host star is a logarithmic value of ratio of star′s [Fe/H] to Sun′s [Fe/H]. In case, there is a linear relationship between host star′s metallicity and different physical parameters of their respective host star and planets, then logarithmic values of metallicity have to be converted into absolute values. Now onwards this transformation from logarithmic scale to linear scale is called as *absolute metallicity* and is denoted with a symbol abs[Fe/H].

In Figure 6.3 (b), we illustrate a relationship between the stellar mass and absolute metallicity, where the absolute metallicity values are binned with a size of 0.25. The average and standard deviations σ of stellar masses in each bin are calculated as explained earlier. Errors in each bin are estimated from the ratio $\frac{\sigma}{\sqrt{n}}$.

Compared to a relationship between stellar mass and absolute metallicity (Figure 6.3 (b)), we find a strong relationship between logarithmic stellar mass and observed metallicity [Fe/H] (Figure 6.3 (a)) with a best fit of following form:

$$log(\frac{M_\star}{M_\odot}) = (0.007 \pm 0.006) + (0.165 \pm 0.026)[Fe/H], \qquad (6.2)$$

where $M_\star$ is stellar mass in terms of Sun′s mass $M_\odot$. We conclude that a relationship illustrated in Figure 6.3 (a) is better than a relationship illustrated in Figure 6.3 (b) for the following reasons: (i) high correlation coefficient (99%) (ii) small value of chi-square 1.376. Hence, it is concluded that there exists a power law relationship between the stellar mass and the observed metallicity.

One can notice from Figure 6.3 (a) that, the host stars metallicity increases non-linearly with increasing in stellar mass. One can interpret this result as the metal rich stars are most likely originated in metal rich disks. Due to high fraction of dust and
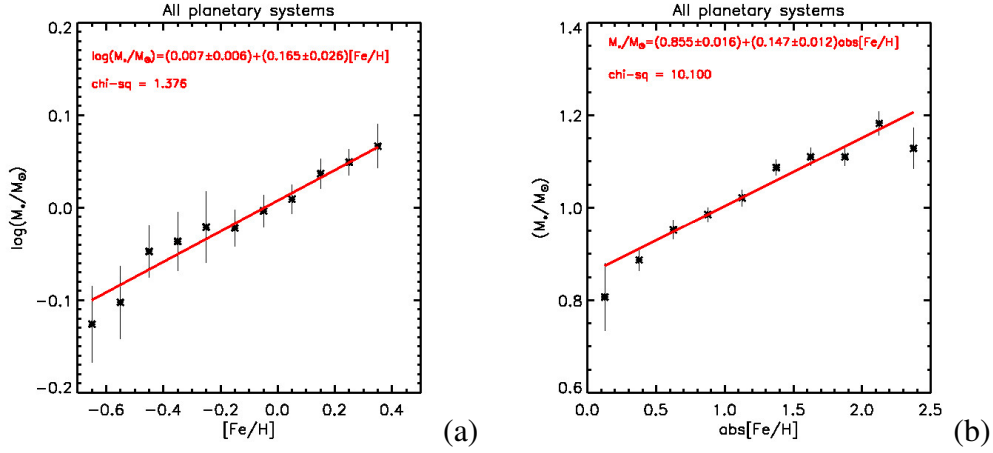
Fig. 6.3 (a) Illustrates the Dependency of Logarithmic Stellar Mass With the Observed Metallicity. (b) Illustrates the Dependency of Stellar Mass With the Absolute Metallicity for All Planetary Systems.

gas particles in a metal rich nebula, the rate of formation of a central star (or accretion of mass on the central star) is much higher than the rate of formation (or accretion of mass on the central star) in a metal poor nebula (Jones et al. 2016). The accretion process helps in acquiring more mass (i.e., more gas and dust particles that increases the chemical composition) by a central star. Hence, the metallicity of host star is directly proportional to the stellar mass in logarithmic scale.

As explained in the introduction, other plausible interpretation is that the accretion of disk or protoplanetary material or inward migration of planets add dust materials on the central star as a 'pollution' that ultimately increase the stellar metallicity. On the other hand, one can also argue that accretion of mass on a central star during later evolutionary stages may not increase the central mass substantially. Therefore, the effect of 'pollution' (accretion of mass) on the stellar mass is negligible, yet one can observe from the Figure 6.3 (a) that metallicity increases as the stellar mass increase. Thus, one may conclude that contribution to the final stellar metallicity from 'pollution' is small and most of stellar metallicity is likely to be of primordial composition of a nebula (Santos et al. 2004).

As the majority of stars in this analysis are single planetary systems, it is not clear whether multiplanetary systems follow a similar power law relationship. Thus, in order to delineate this combined data bias, in the following section, we investigate the stellar mass-metallicity relationship separately for single and multiplanetary systems. Another
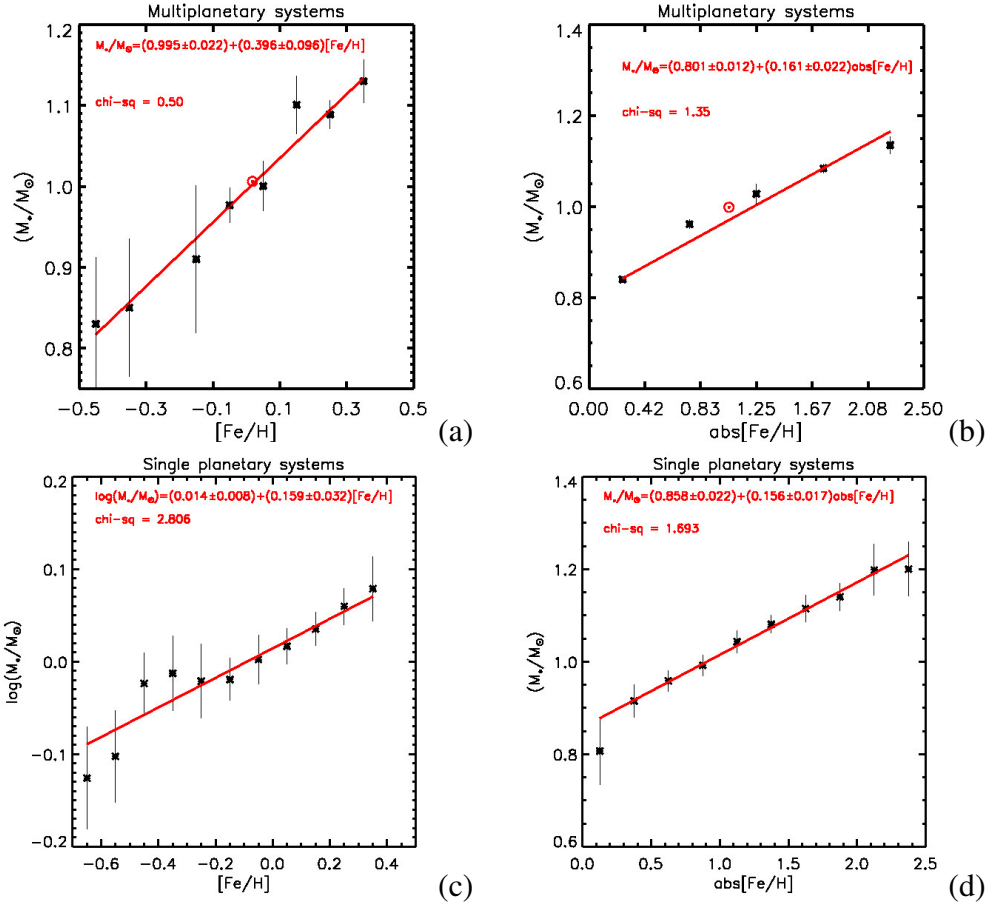
Fig. 6.4 For Multiplanetary Systems, 6.4 (a) and (b) Illustrate the Dependency of Stellar Mass With the Observed and Absolute Metallicity Respectively. for Single Planetary Systems, 6.4 (c) and (d) Illustrate the Dependency of Stellar Mass With the Observed and Absolute Metallicity Respectively. in Figures 6.4 (a) and (b), Metallicity of the Sun Is Represented by a Symbol ⊙.

aim of classification of this data is to examine whether single and multiplanetary systems originate in different ways or not. Hence, we investigate the relationship between stellar mass and metallicity for both single and multiplanetary systems in linear and non linear scales.

6.4.1.1 Stellar Mass Versus Metallicity: Multiplanetary Systems

In case of multiplanetary systems, Figures 6.4 (a) and (b) show the variations of stellar mass with observed and absolute metallicity respectively, with the best fits of following forms:

$$\frac{M_\star}{M_\odot} = (0.995 \pm 0.022) + (0.396 \pm 0.096)[Fe/H], \tag{6.3}$$

and

$$\frac{M_\star}{M_\odot} = (0.801 \pm 0.012) + (0.161 \pm 0.022)abs[Fe/H]. \quad (6.4)$$

Among both the fits, if we accept χ^2 as a constraint on goodness of fit, stellar mass versus observed metallicity is a best fit (eqn. 6.3). Both these relationships show a clear increasing trend between stellar mass and its metallicity. In both the Figures (6.4(a) and 6.4(b)), the symbol $\odot$ represents metallicity of the Sun.

6.4.1.2 Stellar Mass Versus Metallicity: Single Planetary Systems

Similar plots for single planetary systems are illustrated in Figures 6.4 (c) and 6.4 (d) respectively. In this case the best fit is obtained between the stellar mass and absolute metallicity, except that the stars that have same metallicity as those of multiplanetary systems produce massive planets. Hence, these results imply that origin and formation of single and multiplanetary systems appear to be entirely different.

Coefficients of different linear and non linear laws that show the dependency of stellar mass on its metallicity are summarized in Table 5 of Appendices. The first column in Table 5 of Appendices represents the different laws of fit, second and third columns represent the intercept (C1) and ratio of error in the intercept with respect to values of intercept ($|\frac{\delta C1}{C1}|$) respectively. Fourth and Fifth columns represent the slope (C2) and the ratio of error in the slope with respect to values of slope ($|\frac{\delta C2}{C2}|$) respectively, followed by chi-square (a measure of goodness of fit) in the sixth column for all planetary systems. Similar results are presented in other columns that represent the single and multiplanetary systems respectively.

6.4.2 Dependence of metallicity with the planetary physical properties

6.4.2.1 Occurrence Rates of Single and Multiplanetary Systems

In order to examine the occurrence rate of planets with metallicity, the number of planets in each bins is illustrated (Figure 6.5) against the stellar metallicity for both observed and absolute values. One can notice from Figures 6.5 (a) and (b) that the occurrence
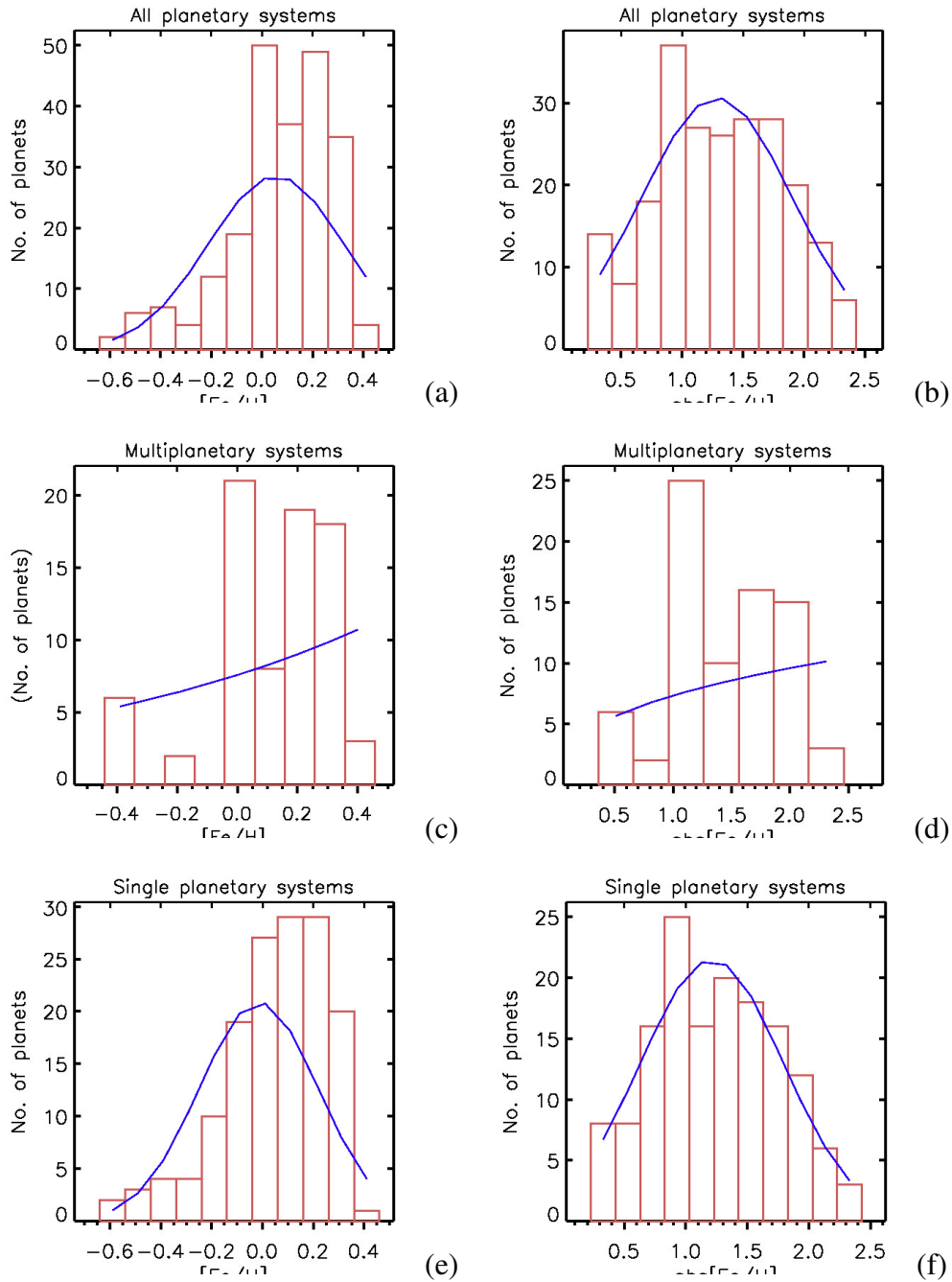
Fig. 6.5 Histograms Representation of Number of Planets Versus the Stellar Metallicity. 6.5(a) and 6.5(b) Illustrate the Dependency of Number of Planets With the Observed and Absolute Metallicity for All the Planetary Systems. 6.5(c) and 6.5(d) Illustrate the Dependency of Number of Planets With the Observed and Absolute Metallicity for the Multiplanetary Systems. 6.5(e) and 6.5(f) Illustrate the Dependency of Number of Planets With the Observed and Absolute Metallicity for the Single Planetary Systems.
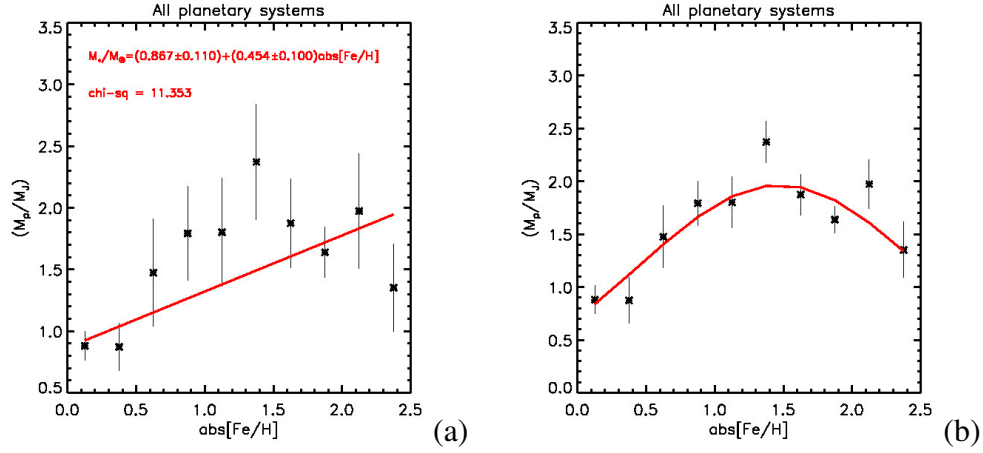
Fig. 6.6 (a) Illustrates the Linear Dependency of Planetary Mass With the Absolute Stellar Metallicity [Fe/H]. Whereas, (b) Illustrates the Normal Distribution of Planetary Mass With the Absolute Metallicity.

rates of planets are skewed Gaussian distributions with a peak around 0.0 to 0.2 dex in case of observed metallicity (Figure 6.5 (a)) and around 1.0 to 1.5 in case of absolute metallicity (Figure 6.5 (b)). For both the Figures 6.5 (a) and 5(b), best fits yield the lognormal and normal (Gaussian) distributions respectively. This apparent result strongly suggests that the occurrence rate of planets with stellar metallicity is a random phenomenon. This picture changes when we classify the data into two parts: (i) multiplanetary systems and, (ii) single planetary systems. As for multiplanetary systems, occurrence rate of planets with metallicity is not a random phenomenon, we get a power law relationship between both the variables. However, due to low statistics in the region of low metallicity ([Fe/H] < 0 or *abs*[Fe/H] < 1), with a caveat we conclude that more number of data-points are required to confirm an apparent power law relationship between both the variables in case of multiplanetary system. Whereas, single planetary systems follow lognormal and normal distributions as presented in Figures 6.5 (e) and (f) respectively. From these two classifications it appears that single planetary systems probably might not have been originated from the host star′s protoplanetary disk. This view will be strengthened from the results presented in the following sections.

6.4.2.2 Planetary Mass Versus Metallicity

As mentioned earlier, chemical composition of nebula affects the planetary physical properties and metallicity of the host stars. Previous study Nayakshin (2015) shows

that there is no correlation between the population of planets with metallicity except for gas giants that are present within few AU from the host star. In the present study we investigate the association between planetary mass with respect to stellar metallicity for single and multiplanetary systems. Probably this investigation may give hints on origin and formation of single and multiplanetary systems.

As metal rich stars show the tendency of increased occurrence rate of planets, it is interesting to examine whether planetary mass is dependent on the stellar metallicity. In order to confirm this conjecture, in Figure 6.6, irrespective of single and multiplanetary systems, we illustrate the dependence of planetary mass with respect to stars metallicity. Result presented in Figure 6.6 (a) shows that, for the absolute metallicity (linear-linear space), planetary mass is independent of host stars metallicity. Whereas in Figure 6.6 (b), a Gaussian or normal distribution fits very well for planetary mass-absolute metallicity relationship with the following form:

$$ln(\frac{M_p}{M_J}) = (-0.341 \pm 0.152) + (1.381 \pm 0.330)abs[Fe/H] - (0.469 \pm 0.142)abs[Fe/H]^2.$$
(6.5)

However, there is a data bias such that these fits are for the combined data set of single and multiplanetary systems. The data has been separated into single and multiplanetary systems in the following analysis.

Figure 6.7 (a) represents the dependency of planetary mass with respect to stellar absolute metallicity in case of multiplanetary systems. Whereas, in case of single planetary systems, Figures 6.7 (b) and (c) illustrate the dependency of planetary mass with respect to the absolute metallicity with linear and normal distribution respectively. As illustrated in Figure 6.7 (a), although there is a scatter, variation of planetary mass clearly shows an increasing trend with the host stars absolute metallicity and best fit yields the following relationship

$$\frac{M_p}{M_J} = (0.861 \pm 0.740) + (1.363 \pm 0.429)abs[Fe/H],$$
(6.6)

where M_p is the planetary mass in-terms of Jupiter mass M_J.

Similarly, the relation between planetary mass and absolute metallicity for single planetary system (Figure 6.7 (c)) is given by the best fit of normal distribution in the following way:

$$ln(\frac{M_p}{M_J}) = (-0.426\pm0.154)+(2.240\pm0.366)abs[Fe/H]-(0.953\pm0.165)abs[Fe/H]^2.$$

(6.7)

Both these results suggest that, single planetary systems on average produce massive planets and probably their origin is different compared to multiplanetary systems.

As for the results presented in Figure 6.7 (a), following is the reason for low planetary mass for the metal poor stars. Probably these metal poor stars might have originated with metal poor disks around them. These metal poor disks in turn might have less number of dust particles that eventually might have decreased the rate of planetary formation and hence less massive planets. Whereas in case of high metallicity stars with metal rich disks, the scenario of planetary formation probably might be exactly opposite. Due to more number of gas and dust particles in the protoplanetary disk, time period of planets core formation is less. Such a solid core rapidly acquires gas and dust particles as gaseous envelope to form massive or gas giants and grow big in size before dissipation of protoplanetary disk. Hence, the chance of formation of gas giants or massive planets is higher in case of metal rich stars.

6.4.2.3 Estimation of Solar System Planetary Mass

Although error bar in first coefficient of equation (6.6) is high, which is obtained from small sample of multiplanetary systems, it is interesting to estimate the total planetary mass of our solar system (a multiplanetary system) and compare it with the present observed planetary mass. We find that estimated total planetary mass of the solar system, by using equation (6.6), is $\sim 2.224 M_J$ which is roughly 1.5 times higher compared to the present observed planetary mass ($\sim 1.4 M_J$) (that includes masses of Asteroids, Kuiper belt and Oort's cloud objects). This result suggests that there is a missing planetary mass of $\sim 0.8 M_J$ in the solar system planetary bodies.

6.4.2.4 Estimation of Planetary Mass Beyond Solar System Kuiper Belt

Coming to picture of missing mass, if protoplanetary disk is in hydrostatic equilibrium, then density ρ varies as $\rho_0 e^{\frac{-r}{H}}$ (where ρ_0 is density at the center, r is distance from the center and, H is density scale height) where maximum density is concentrated near the center. In case we accept this reasonable density profile, then there is every possibility that maximum missing mass ($\sim 80\%$) might be accreted onto the Sun. Whereas a small ($\sim 20\%$) mass that is in plasma state might have transported along the magnetic field lines to a larger distances, probably beyond the present Kuiper belt objects. That means, about 20% of missing mass might have dumped into outer regions of the solar system. Interestingly, this 20% of missing mass turns out to be ~ 60 Earth's mass that is probably residing in the outer edge of the solar system unless it is ejected from the catastrophic events. Infact, this interesting estimation of missing mass might have formed as ninth and tenth or probably more planets in the outer region (~ 200 AU) of the solar system (Batygin and Brown 2016).

6.4.2.5 Single Planetary Systems: Wandering and Captured Planets

When we examine the results emerged from the histograms (Figures 6.5 (a), (b), (e) and (f)), and planetary mass-stellar metallicity relationships (Figures 6.6(b) and 6.7(c)), events are random and, there is no relationship between metallicity of the host stars and planets of the single planetary systems. That means, these planets probably are not formed in the host stars protoplanetary disks. Rather these planets might have been originated and were formed elsewhere in the galaxy, wandered and probably captured by the host stars. One can notice that, single planetary systems are majority in the present data set. However, with a power law, Figures 6.5 (c) and (d) confirm that planets in the multiplanetary systems are not random events. That means, these planets are not captured from the space, instead most likely they are originated in the protoplanetary disks around the host stars.
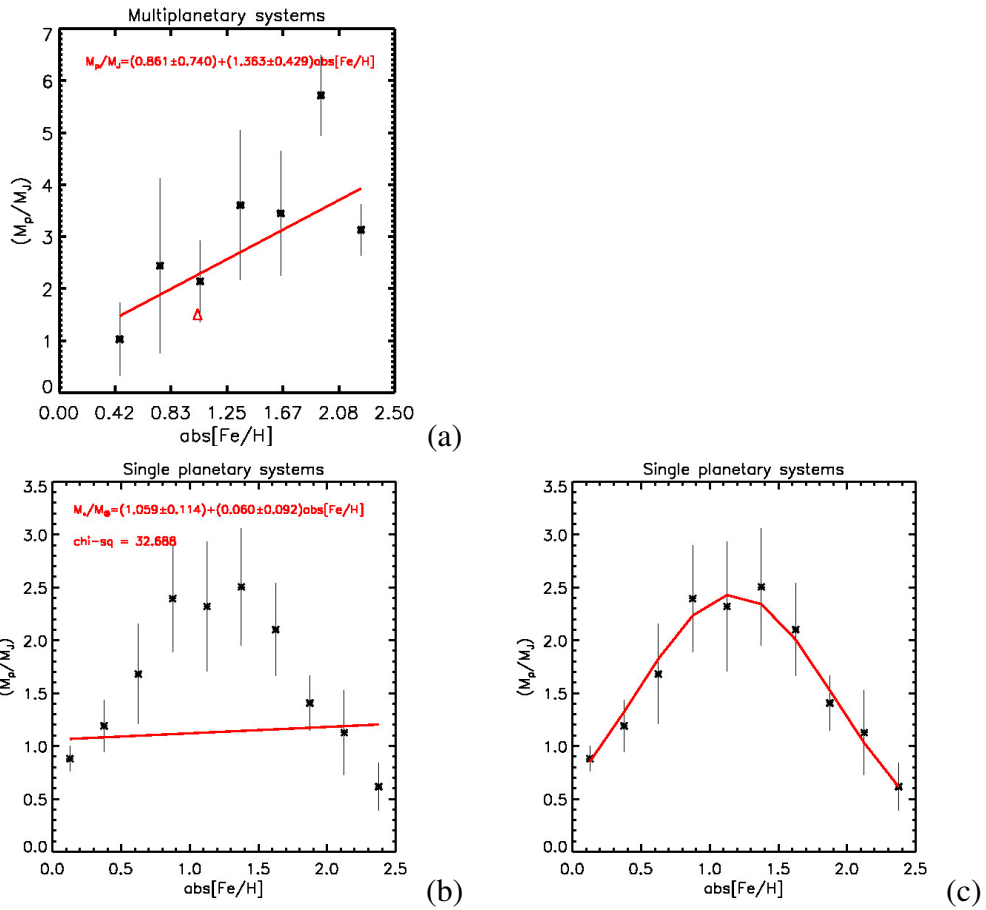
Fig. 6.7 (a) Illustrates the Dependency of Planetary Mass With Absolute Metallicity for Multiplanetary Systems. For Single Planetary Systems, (b) Represents the Linear Fit Between Planetary Mass and Absolute Metallicity. Whereas, (c) Represents the Normal Distribution. In Figure 6.7(a) Total Planetary Mass of Solar System is Represented by a Triangle.

6.4.3 Orbital Distances of Exoplanets Versus Stellar Metallicity

Planets prefer to form in the cooler region of protoplanetary disk. This is because, at high temperature, the rate of condensation of gas and dust particles is low due to high activity of central star, like Sun (Hiremath 2009). Hence most of the planets migrate before settling into the stable orbits around their host stars. Inspite of migration of the planets, it is interesting to examine whether orbital distances of planets depend upon the metallicity of the host stars. Thus, by separating data as single and multiplanetary systems we examined if any relationship exists between these two parameters.

In case of multiplanetary systems, Figure 6.8 illustrates the stable orbital distances of the planets as a function of absolute metallicity that clearly suggests a direct relationship. Although there are large error bars in the data, figure shows a linear increasing trend between stable orbital distance of planets and stellar absolute metallicity.

Similarly, in case of single planetary systems, we have not obtained any definite relation between stable orbital distance of planets and stellar metallicity. Since we have less number of data of multiplanetary systems compared to single planetary systems, there is every possibility of bias in our conclusion. In order to clear this ambiguity, we built random small sub-samples from the single planetary systems and these data sets are subjected to different (linear, non-linear, log-normal) least square fits. Results obtained from these sub-samples show that, 30% of data in single planetary systems follows log-normal distribution, 10% of data follows the power law distribution and remaining data doesn't show any relationship. Thus, from the present data set, we conclude that 30% of single planetary systems shows random distribution, which suggests either such planets are captured from the space or planetary migration scenario is dominant in these single planetary systems. These results also suggest that inward migration of planets and probably accretion of planetary mass on to the host stars is dominant in case of single planetary systems. This accretion of planetary mass on the central host star acts as a 'pollution' (Meléndez et al. 2009) and further increases the stellar metallicity. As for multiplanetary systems, it appears that inward migration is less compared to migration in case of single planetary systems. Since the analysis of samples of single planetary systems also shows 10% of data follows a power law, one can also conclude
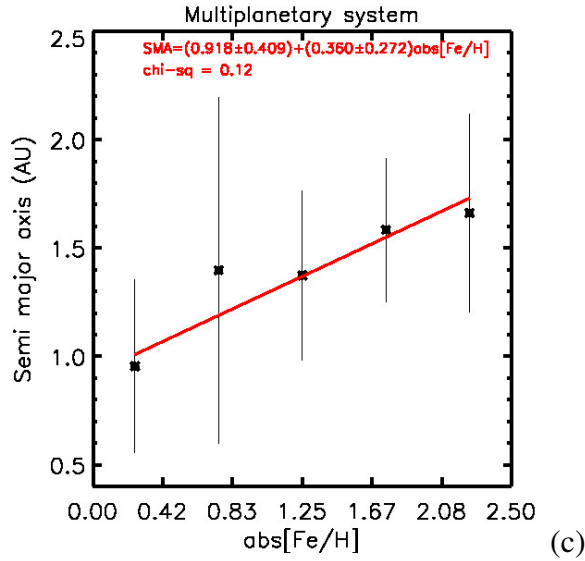
Fig. 6.8 Illustrates the Dependency of Semi-major Axis of Planets With the Absolute Metallicity for Multiplanetary Systems.

that such planetary systems may be part of multiplanetary planetary systems where only one planet has been discovered due to limitations in the present detection techniques.

6.5 Conclusions

To conclude this study, we have considered the physical characteristics of Sun-like G stars and their exoplanets with their orbital distances. Initially, an analysis has been done to examine the effect of galactic metallicity on the planetary formation. However, we conclude that with the present dataset of Sun-like stars, it is difficult to infer the influence of galactic metallicity on the stellar/planetary system formation. Further, the association between stellar mass with their metallicity is examined. We find that, there is a direct relationship between the logarithmic stellar mass and its metallicity that suggests most of the stellar metallicity is due to primordial origin. Hence, the contribution of 'pollution' to the final stellar metallicity is small.

The investigation of planetary mass with respect to their absolute stellar metallicity (abs[Fe/H]) for all planetary systems, doesn't show any significant dependence on each other. However, an analysis by separating the dataset into single and multiplanetary systems reveals that, in case of multiplanetary systems, planetary mass is linearly dependent on the stellar absolute metallicity. Whereas, we find a normal distribution

138

between the same variables in case of single planetary systems, that suggests most of the planets in single planetary systems might be captured from the space.

Interestingly, the relationship between planetary mass and abs[Fe/H] for multiplanetary systems suggests that there is a missing planetary mass ($\sim 0.8 M_J$) in the solar system. It is argued that majority ($\sim 80\%$) of missing planetary mass might have been accreted onto the Sun and a small fraction ($\sim 20\%$) might have been blown off to the outer part of the solar system during early evolutionary stage. This 20% of missing mass is estimated to be ~ 60 Earth mass that probably resides beyond the Kuiper's belt of the solar system.

Finally, a study of dependency of orbital distance on abs[Fe/H] reveals that both these variables are linearly dependent on each other in case of multiplanetary systems. Whereas, in case of single planetary systems, 30% of data follows a lognormal distribution and 10% data show power law fit very well between orbital distance and observed stellar metallicity. These results suggest that, single planetary systems might be multiplanetary systems where only a massive planet is detected. In addition, this result also suggests that inward migration of the planets might be dominant in case of single planetary systems during the early stages of orbital evolution.

Magnetic Field Structure of Sun-Like G Stars and Their Exoplanets

Magnetic field structure is one of the important physical property of a star which might have played a dominant role in the early history of star and planetary formation. This magnetic field structure might have been either of cosmic origin (Hiremath 1994, Hiremath and Gokhale 1995, and references therein) or locally generated by dynamo mechanism (Parker 1975). The turbulent plasma with rotation inside a star is the main reason for local generation of stellar magnetic field. Due to high rotation rate with deep convective layer, a star during early evolutionary stage like T-tauri phase, exhibit intense magnetic field structure than in the later evolutionary stages. Owing to strong magnetic field, one can also observe high stellar activity during early evolutionary stages. Once a star reaches the main sequence stage, the strength of magnetic field decreases due to decay in stellar rotation and smaller convective layer (Baliunas et al. 1996, and references therein). In addition, magnitude of other associated physical properties like angular momentum, stellar mass loss etc., also decrease which in-turn influence the stellar internal structure. Magnetic field structure also influences the other physical processes like accretion of disk mass on the central star, stellar rotation, angular momentum loss etc., during the early evolutionary stages. Hence, a study of role of stellar magnetic field structure is essential and important to understand genesis and evolution of stars and planetary systems (Fares et al. 2013). Before understanding the influence of magnetic field structure, let us briefly discuss the techniques that are used to estimate the magnitude and direction of magnetic field structure of the host stars, due to polarized property of its ambient medium.

Previously, there were no direct methods to observe and estimate strength of the

magnetic field of the host stars. Instead, indirect methods were used to observe the consequences of magnetic field structures viz., chromospheric emission, X-ray emission, etc., from which strength of magnetic field of a star can be estimated. The magnetic field of a star is first discovered by Babcock (1947) for a star *78 Vir*. During those days most of the magnetic fields of stars were detected by using the photographic techniques. In recent years, spectropolarimetry and time-series spectroscopy of Doppler-Zeeman effects are the primary tools for study of stellar magnetic field. Zeeman effect is the fundamental phenomenon from which one can detect the stellar magnetic fields and reconstruct their topologies. Such repeated measurements for a particular star help also to resolve the time-dependent uncertainties such as rotational modulation, pulsations, etc. In the following section, let us briefly discuss the *Zeeman effect*.

7.1   Zeeman Effect

The splitting of spectral lines due to presence of magnetic field structure is known as the *Zeeman effect*. The average distance between the splitted spectral lines from the primary spectral line mainly depends on the strength of magnetic field. This canonical method is used to measure the magnetic fields of the Sun and other stars. Due to presence of magnetic field structure, the energy levels of electrons is altered in according to the cross product between spin (S) and orbital angular momentum (L) and the magnetic field vector. Each energy level splits into (2J+1) states of energy with different magnetic quantum numbers, where J is total angular momentum quantum number. In addition to magnetic field, the difference between energy states is also depends on *Lande g factor* which is given by

$$g_i = \frac{3}{2} + \frac{S_i(S_i + 1) - L_i(L_i + 1)}{2J_i(J_i + 1)}. \tag{7.1}$$

where i = 0,1,2... When the transition occurs between two energy levels, the magnetic quantum number (M) must obey the selection rule i.e., ΔM = -1,0,1. The transition where $\Delta M = 0$ is known as π component and, transition with $\Delta M = -1$ or +1 is known as σ components. If one measures the energy shift in terms of the wavelength shift,

change in the wavelength $\Delta\lambda$ in $\mathring{A}$ is given by

$$\Delta\lambda = 4.67 \times 10^{-13} gB\lambda_0^2, \tag{7.2}$$

where λ_0 is wavelength when strength of magnetic field $B = 0$. Figure 7.1 illustrates the schematic diagram of Zeeman splitting with and without magnetic field structure.
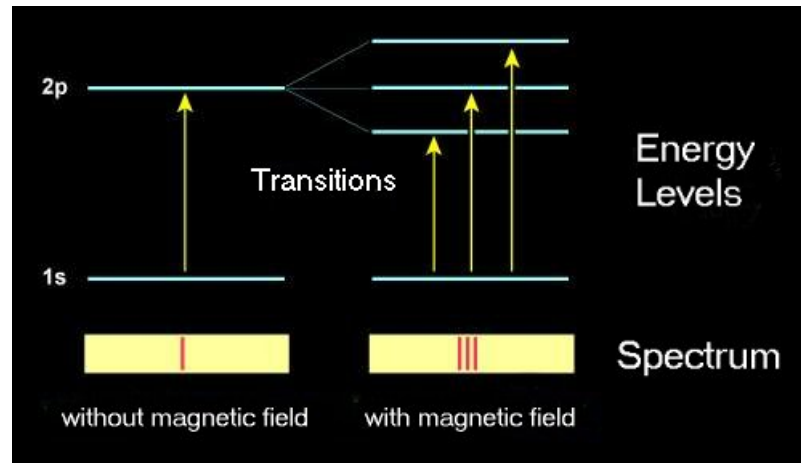
Fig. 7.1 Illustrates Schematic Diagram of Splitting of Energy Levels in The Presence of Magnetic Field. Image Credit: *http://www.asu.cas.cz/ solmag/english/zeeman.htm*

7.2 Polarization

Polarization is a property of electromagnetic waves where magnitude and direction of vibrating fields are in a specified direction. Similarly, the groups of Zeeman components (π and σ) also show different polarization states. The reason for different polarization states is that they are characterized by different magnetic moments. Furthermore, the observed polarization of Zeeman components depends on the angle between line of sight and magnetic field direction at the star. Figure 7.2 illustrates the different polarization states of π and σ components for the vertical uniform magnetic field structure. One can notice that, the energy of π component is not shifted and it is always linearly polarized. However, π component is not visible when the line of sight is parallel to magnetic field vector. On the other hand, σ components (σ_b due to $\Delta M = $ -1 and σ_r due to $\Delta M = $ +1) are shifted as per the equation 7.2 and they can be observed either in linear or circular polarization states based on the angle between line of sight and magnetic

field vector. If the observed line of sight is parallel (*longitudinal*) to magnetic field vector, then σ components are circularly polarized with opposite directions. If the observed line sight is perpendicular (*transverse*) to magnetic field vector, then σ components are linearly polarized with a direction perpendicular to polarization of π component.
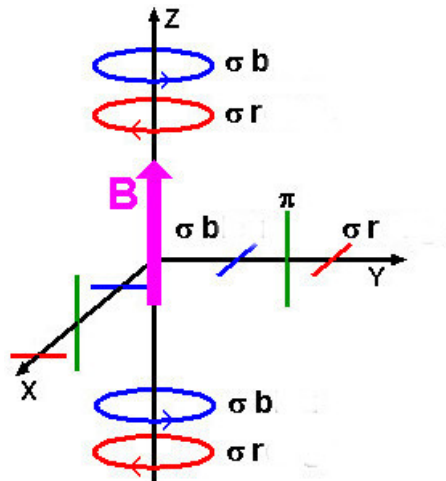
Fig. 7.2 Illustrates Polarization of π and σ Components. Image Credit: *http://www.eyes-on-the-skies.org/shs/Zeeman%20Effect.htm*

The shift of σ components from the π component is $\sim 10^{-2}$ $\mathring{A}$/kG at $5000\mathring{A}$. Thus, magnetic splitting of line is smaller when compared to other source of line broadening. Hence, magnetic splitting of line can be seen only in stars with strong magnetic fields in the high dispersion spectrogram. One should also note that estimation of magnetic field from the polarized line profiles from a star are considerably more complex. Because, the field is, in general, neither longitudinal nor transverse but at some intermediate angle to the line of sight. In addition, as the star is rotating, so that contributions to the magnetic flux from various parts of the stellar disk are Doppler shifted which leads to complex observed line profile. The detailed explanation for the measurement of magnetic field can be found in (Donati and Landstreet 2009, Reiners 2012).

7.3   Zeeman-Doppler Imaging

As the star rotates on its own axis, one can also measure the Doppler shift of individual features on the stellar surface, which carry the information about geometry of the star's surface. This method make use of dependency between wavelength position

across a rotationally broadened spectral line and spatial position across the stellar disk to reconstruct the surface maps of rotating stars. As we observe the star at different phases, we can have information about the magnetic field vector of a star at different projection angles. Hence, one can investigate the polarized light at different phases of a star. This technique assumes that field is not evolving and temperatures of magnetic regions are unknown. Since the activity at stellar surface depend on the strength of magnetic field, the assumption of not evolving field is questionable. Similarly, although the information about temperature of active regions on other stars is poorly understood, the high temperature adds more flux to the observed spectra. Hence, one has to take care of these two issues in this method. One of the important limitations of the Zeeman Doppler Imaging technique in cool stars is that, in order to measure the precise signatures of net polarization, high signal-to-noise ratios are required in polarized light. In order to achieve precise spatial resolution, individual exposures for Doppler Imaging must be kept short. Hence, simply integrating over long times in order to collect enough photons is not applicable. One can resolve this problem by using powerful telescopes and also add the information contained in the many spectral lines that contain similar information from the star.

7.4   Chromospheric Activty

As explained in the chapter 1, chromosphere is a layer above the photosphere of the Sun's atmosphere. In the stellar atmospheres with a radiative equilibrium, the energy transportation is mainly due to radiation. Any heat absorbed from the such radiation field is balanced by the thermal emission to maintain the outward flow of energy from the stellar interior. It is known fact that the temperature raises in chromosphere towards outer region, that results emission in prominent Fraunhofer lines such as Ca II H and K, this is one of the important phenomenon of the *chromospheric activity*. The chromospheric activity is strongly associated with the strength of large scale weak ($\sim$ 1 G) magnetic field and underlaying photospheric localized sunspot or starspots activity (Sivaraman and Livingston 1982, Nindos and Zirin 1998, Loukitcheva et al. 2009, Bertello et al. 2016). Hence, long-term observation of Ca II H and K lines helps in

understanding indirectly the variation of magnetic field structure of a star. Although Eberhard and Schwarzschild (1913) observed these lines a long back, Olin Wilson at the Mount Wilson Observatory (MWO) studied these emission lines for longer period. Further, Olin Wilson correlated these emission lines with age (Wilson 1963). In addition, Wilson and Vainu Bappu (1957) found a correlation between absolute visual magnitude (M_v) and widths of K emission line (W_0) for G, K and giant stars such that $M_v = 27.59 - 14.94 log(W_0)$, which is known as *Wilson-Bappu effect*. In addition to observation of H and K lines of other stars, long-term observations of same lines in case of Sun with Sun as a star (Egeland et al. 2017) are also available. The MWO measures activity index S, as a dimensionless ratio of the fluxes in the line cores (H and K at 396.849 nm and 393.368 nm respectively) to that in two nearby continuum band passes (R and V) on both sides of the H and K lines given by (Hall 2008)

$$S \propto \frac{H + K}{R + V}.$$ (7.3)

Since this S index has a color term from the reference bandpass, we can apply a transformation to obtain the parameter R_{HK}. The activity index R_{HK} is defined as the summation of emission in the narrow bands H and K and normalized with the bolometric luminosity of a star. The relations between MWO S index and R_{HK} is given by

$$R_{HK} = (1.34 \times 10^{-4}) C_{CF} S$$ (7.4)

where C_{CF} is color dependent function. The typical emission spectrum at cores of Ca II H and K lines is illustrated in the Figure 7.3.

7.5 Motivation

The magnetic fields are found in all type of stars starting from low mass M dwarfs to high mass O type stars. As described in the beginning of this chapter magnetic field structure plays an important role in all the evolutionary stages of a star. For example, the processes during early evolutionary stages like accretion, mass loss, turbulence etc., are influenced by the presence of magnetic field. Similarly, the strength of magnetic
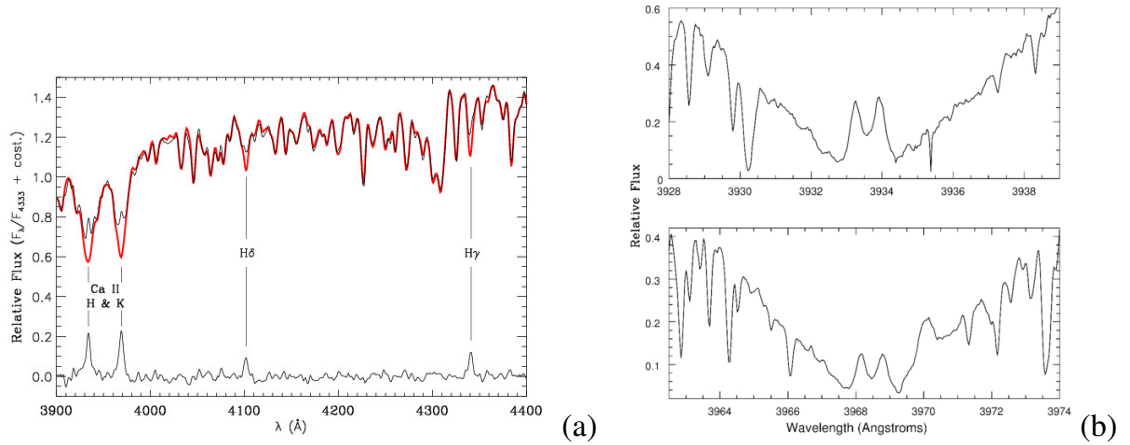
Fig. 7.3 (a) Illustrates Typical Emission at the Cores of Ca II H and K Lines and Other Prominent Emission Lines Image Credit: Gondoin et al. (2012). (b) The Right Upper Plot Illustrates the Emission in Ca II K Core and Right Lower Plot Illustrates the Emission in Ca II H Core. Image Credit: Ryon et al. (2009).

field structure during early stages of stars evolution also depends on other fundamental characteristics of a star like stellar mass, rotation rate, etc. In addition to all these processes, the magnetic fields also create other stellar activities like flares, star spots, coronal mass ejections, *etc*. These magnetic activities are very strong during early stages and strength decreases with time once a star reaches its main sequence stage. As there is one-to-one correspondence between magnetic activity and chromospheric activity due to chromospheric emission, hence, emission lines in Ca-II H and K core can be used as a proxy for stellar magnetic activity. There is a long-term behavior in stellar chromospheric activity of stars which is tightly linked with the long term variation of magnetic field structure of a star.

Magnetic fields play an important role in all the stellar evolutionary stages by affecting the physical and orbital characteristics of both central star (Singh et al. 1984) as well as the near-by orbiting planet. Magnetic fields also influence the star formation during the molecular cloud collapsing stage when the cloud's magnetic energy is equal to gravitational energy (Donati and Landstreet 2009). Such a strong equipartition magnetic field structure connects with the inner accretion disk and controls the outflow of material and angular momentum transport. The accretion of material present in the inner rim of circumstellar disk proceeds via magnetic field lines and dissipate within 10 Myr. Such interactions between central protostar and disk lead to slow down of the

146

rotation rate of the central star. Magnetic field structure of the accretion discs is also expected to impact the formation and migration of protoplanets (Armitage 2011). Magnetic field structure of the accretion disc and associated MHD turbulence can prevent the disc fragmentation through gravitational instabilities and also the formation of giant planets (Fromang 2005). In addition, presence of such a magnetic field structure can also modify the migration rate and angular momentum of protoplanets (Fromang et al. 2005; Machida et al. 2006). By affecting the inner regions of accretion discs, magnetic fields present during T-Tauri phase may stop the inward migration of giant planets formed earlier in the outer disc.

The companion (either a planet or brown dwarf) interacts with the central star through gravitation, tidal and/or magnetic fields. Cuntz et al. (2000) first detected such star-planet interactions (SPI) in a sample of stars which host close-in giant planets, where tidal and magnetic interactions are dominant. Shkolnik et al. (2003) claim that such SPI can be observed through synchronous enhancement in the Ca II H and K emission lines with planetary orbital periods. The variations in such an enhanced activity follow a period of P/2 (where P is orbital period of planet) in case of tidal interaction, whereas it follows a period P in case of magnetic interactions (Charbonneau 2004). Many models are proposed to explain the periodic variation of chromospheric enhancement in stars with Hot Jupiters (McIvor et al. 2006). Preusse et al. (2006) proposed a model based on the propagation of Alfven waves within the stellar wind flow relative to the planet. In addition, Scharf (2010) claimed SPI by obtaining a positive correlation between the X-ray luminosity and planetary mass of closely orbiting exoplanets. Over a large time scale, SPI have local and global consequences on a stellar system (stars with planets). These SPI interactions can either be tidal or magnetic. In case they are magnetic, then it helps us to study the magnetosphere of the exoplanets (Shkolnik et al. 2003). The interaction of magnetosphere of close-in exoplanets with their host stars may lead to extensive energy injection into planetary atmosphere which leads to high mass loss of the atmosphere. Hence, Lanza (2013) suggested to include such interactions in models of evaporation of planetary atmospheres. Owing to tidally locking of hot-Jupiters with their host stars, usually, strength of magnetic field structure of hot

Jupiter are supposed to be very weak compared to strength of magnetic field structure of that of Jupiter in the solar system.

Despite of many theories and observations which support enhancement in chromospheric activity due to presence of planets, there are also other studies which show that there is no correlation between the same two parameters. For example, it is found that there is no significant enhancement in the chromospheric emission lines or flux with the planetary orbital period and/or planetary mass for close-in planetary systems (Lenz et al. 2011, Miller et al. 2012, 2015). Canto Martins et al. (2011) study also supports the previous studies. However, star-planet interactions appear to be more complicated than the star-star interactions in close binaries. Shkolnik (2013) found no significant correlation between chromospheric activity and system parameters (a, M_p and M_p/a) in FUV and NUV region. However, this study shows that radial velocity (RV) of detected close-in planets is associated with excess FUV flux of the host star. Fares et al. (2013) suggest that stars with hot-Jupiters do not show peculiar behaviors in magnetic field structure when compared with stars without detected hot Jupiters.

With these brief introductions, aims of present study are two fold: (i) during the early epoch, probably when the planetary formation was at the nascent stage, to understand the influence of stellar magnetic field structure on the planet formation and, (ii) at the present observed epoch, whether presence of planets influence and enhance the stellar magnetic or chromospheric activity.

7.6   Data And Analysis

For the present investigation, physical and orbital characteristics of detected exoplanets of Sun-like G stars and physical properties of host stars such as mass, age are also considered from the Extrasolar Planets Encyclopedia website[1]. The value of chromospheric emission flux at the cores of CaII H and K lines (normalized with the bolometric flux of host star), which is a proxy for magnetic field of the host star, denoted by $\log(R_{HK})$, is extracted from the Exoplanet Orbit Database website[2].

---

[1]http://exoplanet.eu/catalog/
[2]http://exoplanets.org/table

From the data set, we find that there are nearly 500 detected exoplanets that orbit the G-type stars, although some of the stars′ physical (mass and radius) and exoplanets′ orbital (semi-major axis and eccentricity) parameters are missing. In addition, in order to avoid the ambiguity in considering the brown dwarf candidates, we restrict the maximum planetary mass limit to 13 Jupiter mass. If one considers all the physical parameters of host stars (by constraining the stellar mass range between 0.7 to 1.5 solar mass and considering the stars whose $\log(R_{HK})$ values are given) and orbital parameters of planets, we are left with 120 exoplanetary data.

We consider 120 exoplanets that belong to 86 host stars. Among these, majority (60) of stars are single planetary hosts (only one planet for a star) and, 26 (with 60 planets) are multiplanetary hosts (more than one planet for a star) with 18 low mass ($\leq 0.1\ M_J$) planets. Although one can argue that single planetary hosts are due to limitations in detection techniques, at present it is not clear whether single planets are really single planets or due to limitations of the detection. However, in this study we assume that these are single planets.

7.7 Results and Discussion

Before examining the influence of magnetic field structure on the planetary formation, first we examine the relationship between variation of chromospheric activity index (R_{HK}) with longitudinal magnetic field ($|B|$) of G-type stars. Idea of this exercise is to estimate the absolute value of strength of magnetic field from the proxy R_{HK} index. For this purpose data (stars with and without exoplanets) is used from the BCool survey (Marsden et al. 2014, Mengel et al. 2017). Prior to the analysis, it is to be noted that the chromospheric emission (which is normalized by the bolometric brightness) value provided in website[3] is in logarithmic scale. In case, there is a linear relationship between chromospheric activity and different physical parameters of their respective host star and planets, then logarithmic values are to be converted into linear scale which we called as actual (absolute) chromospheric emission values. Now onwards this transformation of $\log(R_{HK})$ into absolute scale is denoted with a symbol abs(R_{HK}). Figure

---

[3]http://exoplanets.org/table
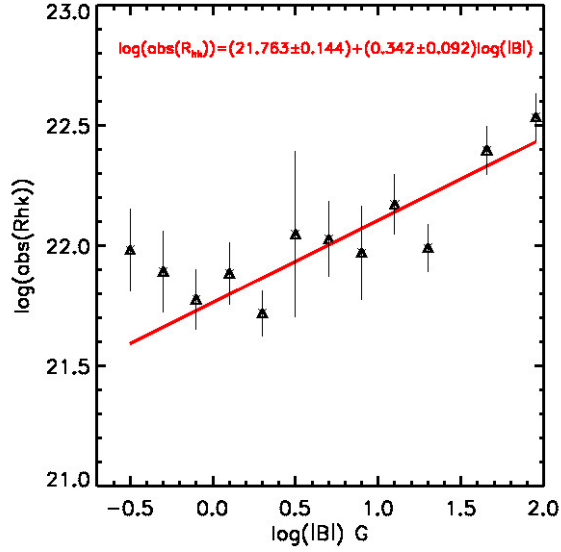
Fig. 7.4 Illustrates a Non-Linear Relationship Between the Chromospheric Activity Index and the Longitudinal Magnetic Field of Host Stars.

7.4 illustrates the relationship between absolute value of strength of magnetic field and chromospheric R_{HK} index. One can notice from this figure that there exists a linear relationship between $log(abs(R_{HK}))$ and $log(|B|)$ of host star for the present observed epoch with a following form

$$log(abs(R_{HK})) = (21.763 \pm 0.144) + (0.342 \pm 0.092)log(|B|). \qquad (7.5)$$

We get the same relationship (with similar order of coefficients and exponents) in case we use the host stars data with planets only. From the above equation we infer that the stellar chromospheric activity index is directly linked with the strength of line of sight component of stellar magnetic field structure. One make use of this relation of R_{HK} - |B| for estimation of longitudinal component of magnetic field of a star if we have the information about the chromospheric emission index. In the next section we investigate the variation of these magnetic activities with stellar age.

7.7.1 Magnetic Activity at the Present Epoch

7.7.1.1 Variation of Chromospheric Activity With Age

Magnetic (chromospheric) activity means, the activity due to chromospheric emission, starspots, sound and Alfen waves, etc., which is evident from the previous studies (Sivaraman and Livingston 1982, Nindos and Zirin 1998, Loukitcheva et al. 2009) on solar physics. Timescales of these activities vary from minutes to years. In addition to strength of magnetic field, the chromospheric activity of a star also decreases with the stellar age (Soderblom et al. 1991). The key reason for decline in the chromospheric activity is the reduction in stellar rotation with age. Hence, this reduction in the chromospheric activity is also used as an indicator of stellar age (Pace 2013). In the present study, we have also investigated the variation of chromospheric activity of host stars with stellar age. Figure 7.5 illustrates the relationship between absolute R_{HK} and stellar age that shows a power law relationship with the following form

$$Y = 10^{(-0.354\pm0.093)} X^{(-0.460\pm0.229)}, \tag{7.6}$$

X and Y represent the stellar age ($\tau_{\star}$) normalized with Sun's age ($\tau_{\odot}$) and absolute chromospheric activity index (abs(R_{HK})) normalized with the maximum value (1.056×10^{22} erg s^{-1} cm^{-2} Hz^{-1}) respectively. The x-axis in this figure which represents the stellar age is binned with the size of 0.3 ($\tau_{\star}/\tau_{\odot}$) and y-axis represents the average abs(R_{HK}) value within that bin with one sigma error bars. In addition, we have also investigated the variation of chromospheric activity with stellar age for G-type stars without detected planets from the BCool survey, which is illustrated in Figure 7.6. From this figure one can notice that there exists a power law relationship between these two parameters, with the following form

$$Y = 10^{(-0.398\pm0.146)} X^{(-0.500\pm0.424)}, \tag{7.7}$$

where the X and Y are defined as earlier, except the fact that in this case the maximum vale of abs(R_{HK}) is 1.544×10^{22} erg s^{-1} cm^{-2} Hz^{-1}. By observing the coefficients and
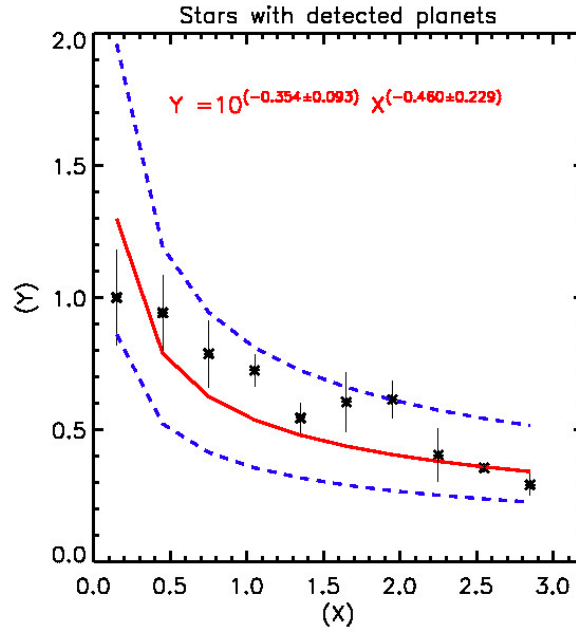
Fig. 7.5 Illustrates a Power Law Relationship Between the Chromospheric Activity Index (Indicated by Y) Normalized With Maximum Value and the Stellar Age (Indicated by X) Normalized With Sun's Age for the Stars With Detected Exoplanets. The Red Line Represents the Best Fit and Blue Dotted Lines Represent the One Sigma Error Bars.

exponents of equation 7.6 and 7.7, it is evident that variation of chromospheric activity for stars with and without exoplanets is almost same. This indicates that presence of planets around the host stars might not affect the magnetic activity of host star. However, one cannot rule out the slight magnetic or tidal interactions between the nearby planets with their host stars, that might have induced the negligible variations in the magnetic activity (Shkolnik 2013).

7.7.1.2 Variation of Chromospheric Activity With the Stellar Mass

Through models and observational evidences it is found that rotation rate of stars increases with increase in their masses. Since the chromospheric activity of a star strongly depends on the rotation rate of a star, it is interesting to know the relationship between stellar chrosmopheric activity and stellar mass. In Figures 7.7 (a) and 7.7 (b), we illustrate the association between abs(R_{HK}) and stellar mass for both stars with and without detected exoplanets respectively. The symbol X on the plot denotes stellar mass in terms of Sun's mass ($\frac{M_\star}{M_\odot}$) and Y denotes the absolute value of chromospheric emission.

152
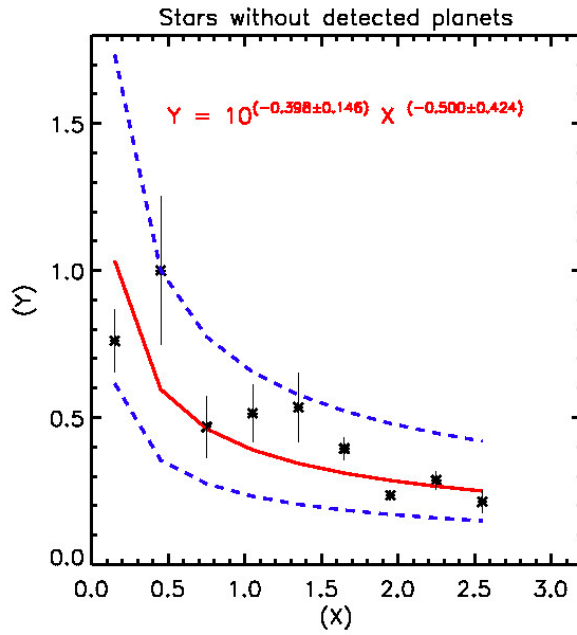
Fig. 7.6 Illustrates a Power Law Relationship Between the Chromospheric Activity Index (Indicated by Y) Normalized With Maximum Value and the Stellar Age (Indicated by X) Normalized With Sun's Age for the Stars Without Detected Exoplanets From BCool Survey. The Red Line Represents the Best Fit and Blue Dotted Lines Represent the One Sigma Error Bars.
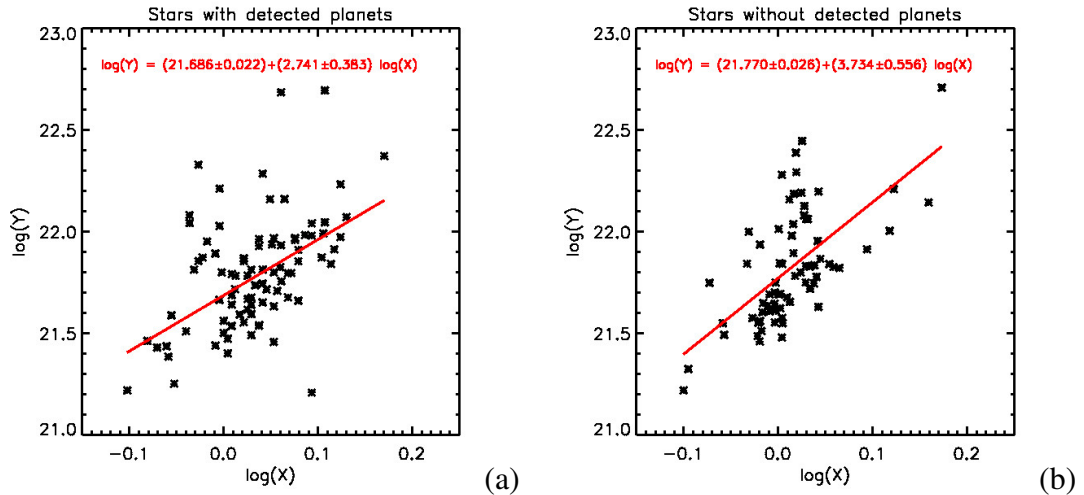
Fig. 7.7 (a) Illustrates the Dependency of Absolute Chromospheric Activity (Denoted With Symbol Y) on the Logarithmic Stellar Mass (Denoted With Symbol X) for Stars With Detected Exoplanets. (b) Illustrates the Dependency of Absolute Chromospheric Activity (Denoted With Symbol Y) on the Logarithmic Stellar Mass (Denoted With Symbol X) for Stars Without Detected Exoplanets. Red Lines in Both the Figures Indicate the Best Fit Line.

From the Figure 7.7(a), we have obtained a linear relationship between log(abs R_{HK}) and log($\frac{M_\star}{M_\odot}$) for stars with detected exoplanets, given by

$$log(Y) = (21.686 \pm 0.022) + (2.741 \pm 0.383)log(X), \qquad (7.8)$$

and for stars without planets with the following form

$$log(Y) = (21.770 \pm 0.026) + (3.734 \pm 0.556)log(X), \qquad (7.9)$$

where X and Y represent the stellar mass $\frac{M_\star}{M_\odot}$ and absolute chromospheric activity respectively. These relationships suggest that the chromospheric activity index increases with the increase in stellar mass for Sunlike G stars. In order to give more significance to the present result, we generated large sub-samples of smaller size and re-examined the relationship between stellar mass and chromospheric activity. The results show that a majority (90%) of sub-samples follow power law relationship between stellar mass and chromospheric activity. This increase of chromospheric activity with stellar mass might be due to increase in the stellar rotation rate. From the equations 7.8 and 7.9, one can also notice that, the exponent in case of stars without detected exoplanets is steeper than the exponent in case of stars with detected exoplanets. This indicates that magnetic activity increases rapidly with increase in stellar mass in case of stars without planets. In the next section, we have examined the influence of planets on the chromospheric activity.

7.7.2 Variation of Chromopheric Activity With Planetary Mass

As briefly discussed in the earlier section 7.5, there are many models that support and do not support the view that planets influence the host stars chromospheric activity. In this section, let us investigate with the present exoplanetary dataset, whether the presence of planets influence the stellar chromospheric activity or not. It is to be noted that, planetary mass (M_p) is normalized with their host star mass ($M_\star$), that represents the fraction of planetary mass that a stellar mass can contains and it is denoted by $\frac{M_p}{M_\star}$. Initially, we have examined the linear and non-linear relationships between the fraction
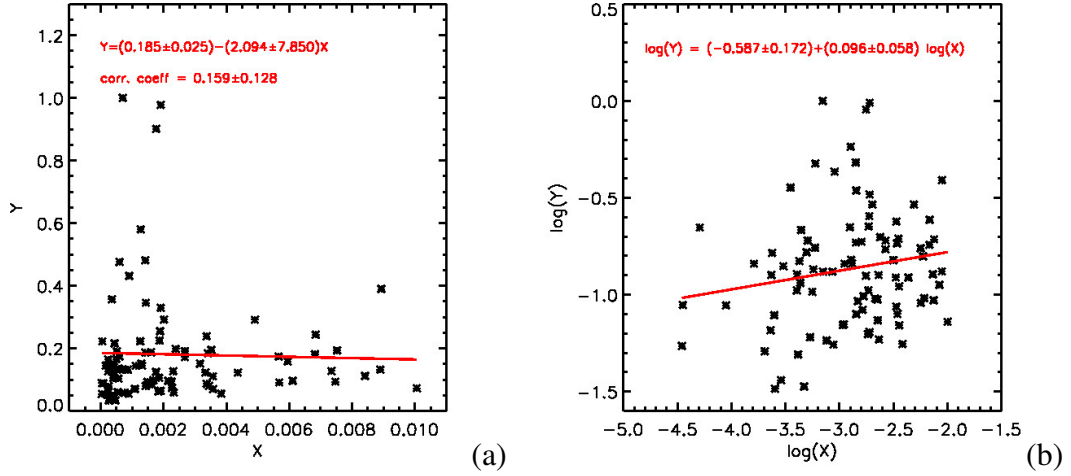
Fig. 7.8 (a) Illustrates the Linear Dependency of Absolute Chromospheric Activity (Denoted With Symbol Y) on the Ratio of Planetary Mass M_p with Stellar Mass $M_\star$ (Denoted With Symbol X). (b) Illustrates the Linear Dependency of Logarithmic Absolute Chromospheric Activity on the Logarithmic Ratio of Planetary Mass with Stellar Mass. Red Lines in Both the Figures Indicate the Best Fit Lines.

of planetary mass $\frac{M_p}{M_\star}$ and the absolute chromospheric activity. The results are illustrated in Figure 7.8 which suggests that there is no dependency of absolute chromospheric activity on the planetary mass. Although by observing the Figure 7.8 (b) one can argue that there is a slight increase in chromospheric activity with fraction of planetary mass, there is a lof of scatter in the association between the two variables. Hence, one can not argue that there is a non-linear relationship between those parameters based on this plot.

7.7.3 Magnetic Field Structure in the Early Epoch

7.7.3.1 Role of Magnetic Field Structure on the Planetary Formation

Magnetic field structure means, the field which is large-scale ($\sim$ dimension of star size) and which probably might be of primordial origin (Hiremath 1994, Hiremath and Gokhale 1995, and references therein). Timescales of this structure is $\sim$ magnetic diffusion timescale ($\sim$ billions of years). We have already discussed the influence of magnetic field structure on the planetary formation, from the magnetic field at the present epoch. It is interesting to estimate the initial magnetic field and examine whether such a field structure might have played a dominant role on the planetary formation. For

this purpose, we need to estimate magnitude of magnetic field (or R_{HK}) during the early epoch, probably during when planetary formation would have been at the nascent stage. In order to estimate the initial R_{HK} (here R_{HK} we mean abs(R_{HK})), we have applied the similar method that is described in Chapter 4 for computation of initial stellar mass. Since, we have data of R_{HK} and stellar age, through numerical differentiation the rate of magnetic decay ($\frac{dR_{HK}}{dt}$) at which the chromospheric emission also decreases is estimated. By using $\frac{dR_{HK}}{dt}$ for different ages of host stars, numerical integration is performed from present age to initial age and R_{HK} at the initial epoch is estimated. For different initial ages, starting from 10 Myrs, with interval of 10 million years, numerical integration is performed. We find that for 50 million years, the value of integral of R_{HK} saturates. Then we accept 50 million years as initial age during when probably chromospheric activity might have started. Considering the fact that nearby planets also lose their mass during evolution, a rough initial planetary mass $(\frac{M_p}{M_\star})_{ini}$ is estimated by using following equation

$$\left(\frac{M_p}{M_\star}\right)_{ini} = \left(\frac{M_p}{M_\star}\right)_{pre} + \left(\frac{M_p}{M_\star}(\tau_1 - \tau_2)\right), \qquad (7.10)$$

where $(\frac{M_p}{M_\star})_{pre}$ is present planetary mass, τ_1 is initial stellar age (50 Myrs) and τ_2 is present stellar age. Since we have initial R_{HK} and initial fraction of planetary mass with stellar mass $(\frac{M_p}{M_\star})_{ini}$, Figure 7.9 illustrates a best non-linear fit between these two variables that are related by the following equation

$$log\left(\frac{M_p}{M_\star}\right)_{ini} = (-2.725 \pm 0.099) - (0.937 \pm 0.293)log\left(\frac{abs(R_{HK})}{abs(R_{HK,max})}\right)_{ini}, \quad (7.11)$$

where abs($R_{HK,max}$) = 6.917×10^{22} erg s^{-1} cm^{-2} Hz^{-1}. One can observe from Figure 7.9 that the fraction of planetary mass decreases with increase in the magnitude of initial magnetic field structure. That means, stronger the magnetic field structure of the host star, lesser the planetary mass created in the surrounding host star in the accretion disk. This important result could be due to combined effect of large-scale magnetic field structure that was threaded in the accretion disk and effect due to strong stellar
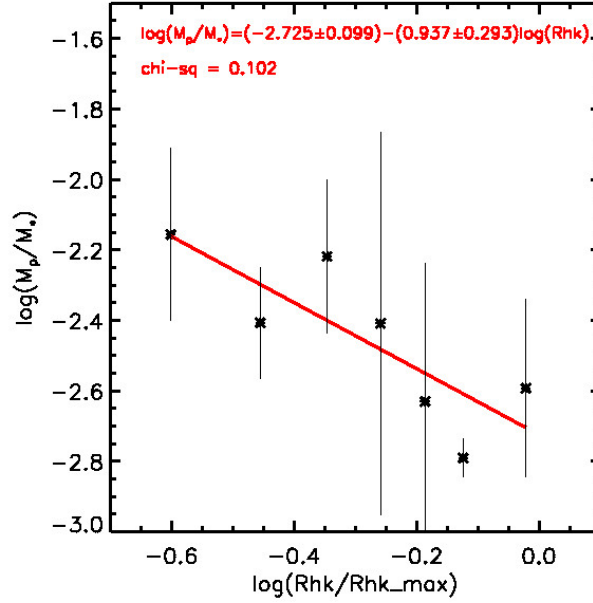
Fig. 7.9 Illustrates a Non-Linear Relationship Between the Initial Chromospheric Activity Index Normalized With Maximum Value and the Fraction of Initial Planetary Mass Normalized With Initial Stellar Mass for the Stars With Detected Exoplanets. The Red Line Represents the Best Fit.

magnetic activity. As for large-scale magnetic field structure, turbulence and differential rotation of accretion disk, unknown instabilities might have created less planetary mass. Similarly, during initial evolutionary stages, a star exhibits violent and frequent magnetic activities like stellar wind, flares, coronal mass ejections, etc., on its surface. Due to such violent activities, high amount energy is injected into nearby accretion disk that might have blown off the disk mass and planetary masses. Hence, these are the two combined possible reasons that might have yielded inverse relationship between the initial magnetic field structure (initial R_{HK}) and initial planetary mass.

7.8   Conclusions

To conclude this study, by considering the physical properties of Sun-like G stars and their exoplanets, for the present and initial epochs, we have examined association between chromospheric activity (a proxy for magnetic field structure and activity) of host stars with different physical properties of stars and their exoplanets. In order to understand how magnetic field structure of stars (with and without planets) decay with time,

an association between magnetic activity with respect to different ages is investigated. It is found that, a power law relationship between the chromospheric activity and stellar age suggests the magnetic activity decreases with time. Furthermore, analysis of magnetic activity with stellar age for stars with and without detected exoplanets reveals that presence of planets near the host star doesn't enhances the chromospheric activity of a star.

For the present observed epoch, association between stellar mass and magnetic activity for stars with detected exoplanets, shows a non-linear relationship that suggests activity increases with increase in stellar mass. This result is not surprising as magnetic activity of a star depends on the rotation which in turn depends upon the stellar mass. The same analysis yields the result for stars without detected exoplanets. It is found that magnetic activity in case of stars without planets increases steeper with increase in stellar mass than in case of stars with planets. The reason for rapid increase in magnetic activity may be due to other stellar parameters, that can be studied further.

An investigation is also carried out to study the presence of planetary mass in the vicinity of host star and its effect on the stellar magnetic activity. This investigation shows that there is no linear or non-linear dependency between the magnetic activity and presence of planetary mass, suggesting that the presence of planets do not affect the magnetic activity of host stars. Finally, the role of magnetic field structure during the early epoch of planetary formation is examined. It is found that strength of magnetic field structure and accumulated planetary mass during the planetary formation are inversely proportional to each other. This important result is interpreted as due to combined effect of embedded large-scale magnetic field structure (of the protoplanetary disk) and associated stellar activity during the early epoch.

CHAPTER 8

Summary of Thesis and Future Prospects

8.1 Summary of The Thesis

To summarize the thesis, initially in chapter 1, as the Sun is an important astrophysical object which is often used as a reference in this thesis, hence, the physical and chemical characteristics are explained followed by a brief overview of internal structure and its atmosphere. This overview yields the insight regarding variation of different properties like mass, density, temperature, etc., with respect to the radius of Sun. The description on Sun's surface and atmosphere gives an information about the different activity phenomena viz., sunspots, solar wind, solar flares, coronal mass ejection, etc. Furthermore, we have given detailed explanation on different physical and orbital characteristics of Solar system planets. Finally, the Chapter 1 ends with brief descriptions about the different theories (from Laplace and Kant model to latest Grand Tack model) that are proposed to understand the origin and formation of Sun and Solar system planets.

Humans quest is to understand the origin and formation of the Solar system objects, origin of water on the Earth that inturn supports the existence of life on the Earth. In addition, humans are searching for habitable worlds in the universe that might harbor life. For these important reasons astronomers started searching for the planets outside the Solar system. First planet outside the Solar system is detected in 1995 around a Sun-like star *51 Pegasi* (Mayor and Queloz 1995). In Chapter 2, a brief history of search for exoplanets is described followed by importance of studying the exoplanets. Subsequently, a brief explanation is presented on the important exoplanetary detection methods (radial velocity method, transit method, microlensing method and direct imaging method) and their limitations. In this chapter we find that the exoplanetary systems have different

physical and orbital characteristics compared to physical and orbital characteristics of the Solar system planets. For example, Solar system has a well-defined planetary architecture like terrestrial planets (orbiting near to Sun) and Jovian planets (orbiting away from the Sun), with small eccentricities (except Mercury), which are separated by asteroids belt. However, many of the detected exoplanets are massive compared to mass of Jupiter with different eccentric orbits and are also orbiting very near to their host stars. Different physical characteristics of these exoplanetary systems led to development of new theories on planetary formation. In the last section of Chapter 2, different challenges on the formation of exoplanetary systems are briefly presented.

Chapter 3 summarizes the practical use of these exoplanetary detectional techniques in different previous, on-going and future ground and space based missions. In the last two decades, many ground and space based missions are launched for exoplanetary search. With the handful of detected exoplanets, astronomers are beginning to model the atmospheres and interiors of exoplanets. Many models are developed for understanding the processes of planetary formation. However, we yet to know the origin and dynamics behind final architecture of multi-planetary systems and, to detect Earth's twin around nearby stars. In this chapter, we have discussed in detail the important ground and space based exoplanetary missions that have detected number (~ 3000) of exoplanets. In addition to the overview, the description of each mission contains its scientific goals, detailed instrumentation and major findings of that mission. In addition, we have also discussed the upcoming ground and space based missions dedicated to the search for exoplanets from different organizations all over the world.

As we have presented in the previous chapter, exoplanets have different physical and orbital characteristics when compared to physical and orbital characteristics of the Solar system planets. For example, many exoplanets are massive with a short period orbits, whereas, planets near the Sun are less massive. In order to understand the low planetary mass near the Sun, in Chapter 4, the physical characteristics of Sun-like G stars and, physical and orbital characteristics of their exoplanets are considered to examine the relationship between planetary masses and their stellar masses. Since host stars in the data set are from different ages, one has to go back to their initial ages to estimate

stars initial masses. Thus, rate of mass loss is computed for each star and their initial masses are estimated in order to check the relationship between initial stellar mass and their planetary mass. It is found that, during early history of stellar system formation, host stars masses and their planetary masses follows a power law relationship such that massive stars harbor massive planets in their vicinity. Interestingly this power law relationship yields the initial mass of the Sun that is estimated to be $\sim (1.061\pm0.006)$ M$_\odot$. It is concluded that, this slightly initial massive Sun with required luminosity probably explains the Faint Young Sun Paradox, one of the unsolved problem in solar physics. From the obtained relationship between stellar mass and exoplanetary mass, the possible initial planetary mass in the vicinity of Sun is estimated to be $\sim (0.846\pm0.187)$ M$_J$, in excess of planetary mass concentrated at the present epoch. By employing the same power law, the excess solar planetary mass lost is conjectured with different views.

In order to get the clues for understanding low spin angular momentum of the Sun, from the exoplanetary data, chapter 5 deals with the distribution of angular momentum between the host stars and their exoplanets. First we have estimated the orbital angular momentum (OAM) of detected exoplanets and obtained a best power law fit with their planetary masses. We also found that the OAM of Solar system planets is higher than the OAM of detected exoplanets. Similarly, the spin angular momentum of the host stars is estimated and is compared with the stellar mass. Best fit yields a power law relation, similar to Kraft (1967), with nearly the same exponent (~ 4.3). In this spin angular momentum-mass relationship, the suns position falls below the best fitted line. It is speculated that, during the early history of solar system formation, the Sun might have transferred its spin angular momentum to the planetary OAM, which might have resulted in the outward migration of Jovian planets from their previous orbital distances to the present orbital distances. Furthermore, when the total (spin and orbital) angular momentum (J_{tot}) of the stellar system with planets is compared with the host star and exoplanetary masses, the resultant relationship between J_{tot} - stellar masses shows that the Solar system has more total angular momentum. This excess contribution is mainly because of the high OAM of Jovian planets. In order to reduce J_{tot}, the orbital distances, especially of the Jovian planets, need to be reduced substantially, i.e. simi-

lar to the ranges as proposed by Grand Tack model for Jupiter (1.5 AU) and 50% less for other Jovian planets. In essence, this study suggests that Jovian planets (especially Jupiter and Saturn) probably are migrated outwards in the early history of Solar system formation. Finally, planetary masses are compared with their orbital distances, and we find that, for multiplanetary systems, the planetary mass yields a best power law relation with its orbital distance, whereas, for single planetary systems, the planetary mass is independent of its orbital distance. These relationships reveal clues about the missing mass in the vicinity of the Sun and the migration scenario of Jovian planets. It is speculated that missing mass in the vicinity of the Sun may be due to accretion of the planetary mass onto the Sun or migration of the same planetary mass to the outer reaches of the Solar system.

Chapter 6 deals with the influence of stellar metallicity on the stellar and planetary formation. Initially, we have examined the influence of galactic metallicity on the planetary formation. Due to the fact that, the distance of farthest exoplanetary system discovered in our dataset is ~ 2 kpc, which is small compared to the size of Milkyway galaxy, it is concluded that more observed data that spans all over the galaxy is needed. A non-linear relationship between the stellar metallicity and the stellar mass is obtained that suggests, present Sun's mass is 1% higher for its present metallicity. From this relationship it is concluded that, high dust/metal contents of nebula during the early phase of stellar formation leads to formation of massive stars. Furthermore, we have obtained different relationships between the stellar metallicity and the exoplanetary mass for single and multiplanetary systems. In case of multiplanetary systems, planetary mass is linearly correlated with the stellar metallicity, which suggests that rate of planetary formation increases with the metal content of stars. In case of single planetary systems variation of planetary mass and stellar metallicity best fit with a Gaussian distribution, suggesting that most of the planets in single planetary systems might have been captured from the space rather than originated in the same stellar planetary system. Whereas, the planets of multiplanetary system might have originated along with the formation of host stars.

The magnetic field structure is one of the important physical property of a star which

plays very important role in the star and planetary formation. The strength of magnetic field structure of a star is much higher during the early evolutionary stages, like proto-star or T-tauri phase,compared to later evolutionary stages (Hiremath 1994, Hiremath and Gokhale 1995, Küker et al. 2003). Once a star reaches its main sequence stage, along with magnetic field structure there is also deviation in magnitude of other physical properties like rotation, angular momentum, stellar mass loss etc., which in-turn modification of the stellar internal structure of the host stars. Magnetic field structure also plays an important role on the different physical processes like accretion of disk mass on the central star and planetary formation. Hence, study of stellar magnetic field structure increases the knowledge of stellar and planetary system evolution (Fares et al. 2013). In Chapter 7, an investigation has been carried out to understand (i) the variation of magnetic (chromospheric) activity with different physical properties of host stars and exoplanets and, (ii) the role of magnetic field structure on the planetary formation. We have obtained a non-linear relationship between the chromospheric activity and stellar age that suggests the magnetic activity decreases with stellar age. A similar kind of analysis has also been done for stars without exoplanets which also shows a same trend as of stars with detected exoplanets. This analysis reveals that presence of planets near the host star doesn't enhances the magnetic (chromospheric) activity of a star.

For the present observed epoch, association between stellar mass and magnetic activity for stars with detected exoplanets, shows a non-linear relationship that suggests activity increases with increase in stellar mass. This result is not surprising as magnetic activity of a star depends on the rotation which in turn depends upon the stellar mass. The same analysis yields the result for stars without detected exoplanets. It is found that stars without planets are magnetically more active than the stars with planets.

The investigation between planetary mass and magnetic activity shows that there is no linear or non-linear dependency between these parameters which suggests the presence of planets do not affect the magnetic activity of host stars. Finally, the role of magnetic field structure during the early epoch of planetary formation is examined. It is found that strength of magnetic field structure and accumulated planetary mass during the planetary formation are inversely proportional to each other. This important result is

interpreted as due to combined effect of embedded large-scale magnetic field structure (of the protoplanetary disk) and associated stellar activity during the early epoch.

8.2   Future Prospects

Before presenting the future prospects, in the following, let us recapitulate the important conclusions of this thesis study.

- A relationship between planetary mass and stellar mass indicates that massive stars harbor massive planets. This relationship also suggests that there is a missing planetary mass in the vicinity of the Sun.

- The Sun's initial mass is 6% higher than its present mass, which probably helps in solving the long standing faint young sun paradox in solar physics.

- Distribution between orbital angular momentum (OAM) and planetary mass (including solar system planets) suggests that OAM of exoplanets is less compared to OAM of solar system planets. This study also suggests that Jovian planets in the solar system are migrated outward during the early epoch of solar system formation. Our estimated position of Jupiter and Saturn before outward migration matches with the values estimated in *Grand Tack model*.

- Distribution between planetary mass and orbital distance of exoplanets indicates that the formation mechanisms of single and multiplanetary systems are different.

- A relationship between stellar mass and stellar metallicity suggests that for the present Sun's metallicity, Sun's mass is 1% higher,

- Most of the exoplanets in single planetary systems might have been captured from the space and/or migration in such planetary systems might have played a dominant role during their early stages of formation,

- At the present observed epoch, presence of planetary mass does not enhance the magnetic (chromospheric) activity.

- Magnetic field structure in the early history of host stars and planetary formation plays an important role such that large-scale strong magnetic field structure of protoplanetary disk decreases the concentration of more planetary mass in the vicinity of the host star.

As for the future study, following is the list of proposed problems to be investigated.

1) From the Chapter 4, we understood that a relationship between planetary mass and stellar mass for the Sun-like G type stars suggests that *massive stars harbor massive planets*. It is interesting to know whether stars of different spectral type follow the similar trend or not. A comprehensive study on the dependency of the planetary mass with stellar mass for the entire spectral range may helps in understanding the fraction of planetary mass that a stellar mass can harbor. Since the planetary mass is proportional to the amount of dust particles in the protoplanetary disks (Williams and Cieza 2011), with this analysis, one can also understand the amount of dust particles needed for formation of different planets like Earth-mass planets, super Earths, super Neptunes, etc., for entire spectral range. Furthermore, by inputing the Earth's mass in a relationship between initial stellar mass and planetary mass, one can estimate the stellar mass (belongs to M spectral type) that probably harbors the Earth-mass planets. Recently many Earth-like planets are discovered around other stars (Satyal et al. 2017), but current telescopes are not powerful to characterize the habitability of terrestrial planets. Although the model from Tian and Ida (2015) suggests that M dwarf are rare to harbor habitable planets, one has to use the upcoming telescopes like JWST, E-ELT, etc., that are powerful enough to characterize the habitable zone with Earth-like planets (Kopparapu et al. 2014), in-turn the possible signs of life.

As we have applied mass loss correction to the stellar mass, in a similar way mass loss correction has to be applied for the planetary mass in order to get a correct relationship between initial stellar mass and initial planetary mass. Since the stars are very active during early stages, planets nearby the host stars might have experienced heavy mass loss (Chadney et al. 2015), that results into the low/no atmosphere. Previously, Adams and Bloch (2013) studied the effect of stellar mass and tidal dissipation on the planetary survival. In order to confirm these models, more observational studies on

young stellar and planetary formation regions are required to understand the planetary mass loss.

2) A rigorous study has to be carried out in order to understand the dynamics played between central star and planets during early stellar system (stars with planets) formation. In particular a careful study is needed on the angular momentum transport between central star and planets. From Figure 5.5, we find the low statistics for the planetary masses that have less than -1 (on logarithmic scale). As many upcoming ground and space observation will be available in future, I would like to study for understanding the mechanism of angular momentum distribution in low and high mass planetary systems. During early evolutionary stages of planetary formation, angular momentum might have generally transported through the interactions of planetesimals with the protoplanetary disk (Armitage 2011, Williams and Cieza 2011). Interactions of protoplanets with the disk might have lead to either inward migration of planets by loosing orbital angular momentum or outward migration of planets by gaining the orbital angular momentum. Thus clear understanding of transport of angular and planetary dynamics during the early history of solar/stellar system formation is necessary.

3) Present study on metallicity of host stars and planetary physical and orbital characteristics suggests that, due to limitations in the detection techniques and unavailability of exoplanetary data from all part of the galaxy, one can not make a firm conclusion about influence of galactic metallicity on the planetary formation. Thus, more statistics from all part of the galaxy are required to analyze the influence of galactic metallicity on the planetary formation. Possibly upcoming ground and space observations will full fill the statistics.

In this thesis study, we have compared the stellar metallicity [Fe/H] with different stellar and planetary properties. In a similar way, one can study the occurrence variation of different chemical abundances (O, N, Mg, Si, etc.) with stellar and planetary physical and dynamical properties. Previous study by Bodaghee et al. (2003) shows that, in addition to Fe, other chemical elements (Si, Mg, Al, etc.) also provide a good platform for planetary formation. For example, in one of the study, it is found that oxygen plays a major role in formation of planetary atmosphere beyond the snowline

(Brugamyer et al. 2011). By studying the Lithium abundance in the stellar photosphere, one can infer the signature of accretion of disk/planetary mass on the star as a pollution (Reddy et al. 2002). Furthermore, since there is a strong association between the lithium abundance and magnitude of stellar rotation (Soderblom et al. 1993), one can understand how stellar rotation influences mixing the chemical abundances in the stellar interior. Hence, a comprehensive study of different chemical abundances with stellar and planetary properties may completely help in understanding stellar and planetary formations.

In one of the concluding points we say that planets in the single planetary systems might have been captured from the space rather than originated in the disk around a star. Similarly it is concluded that inward planetary migration scenario in a disk around the host star might have played dominant role during their early evolutionary stages. A study on the planetary atmosphere is the prime way to confirm whether planets are captured or migrated. In fact in one of the previous study (Madhusudhan et al. 2017), it is shown that study of atmospheric properties can be employed to understand the migration and formation of giant planets. Moreover, one has to find a way to differentiate whether the planets are captured or originated from the disk.

4) This thesis focuses is only on probing the relationship between the stellar and planetary properties of Sun-like G type stars. However, it is interesting to examine for other spectral types whether such a relationship holds good or not. Hence, probably a general relationship for all the spectral types will give a hint on complete picture of physics of planetary formation. With the help of future space probes (JWST, WFIRST etc.) and ground based missions (TMT, E-ELT, etc.) one can detect a very low mass planets like Mercury/super Mercury and study their formation.

REFERENCES

Aarnio, A. N., Matt, S. P. and Stassun, K. G. (2012), 'Mass Loss in Pre-main-sequence Stars via Coronal Mass Ejections and Implications for Angular Momentum Loss', *The Astrophysical Journal* **760**, 9.

Abney, W. D. W. (1877), 'effect of a star's rotation on its spectrum', *Monthly Notices of the Royal Astronomical Society* **37**, 278–279.

Adams, F. C. and Bloch, A. M. (2013), 'Evolution of Planetary Orbits with Stellar Mass Loss and Tidal Dissipation', *The Astrophysical Journal Letters* **777**, L30.

Adibekyan, V. Z., Figueira, P., Santos, N. C., Mortier, A., Mordasini, C., Delgado Mena, E., Sousa, S. G., Correia, A. C. M., Israelian, G. and Oshagh, M. (2013), 'Orbital and physical properties of planets and their hosts: new insights on planet formation and evolution', *Astronomy and Astrophysics* **560**, A51.

Adibekyan, V. Z., Santos, N. C., Sousa, S. G., Israelian, G., Delgado Mena, E., González Hernández, J. I., Mayor, M., Lovis, C. and Udry, S. (2012), 'Overabundance of α-elements in exoplanet-hosting stars', *Astronomy and Astrophysics* **543**, A89.

Alibert, Y., Mordasini, C., Benz, W. and Winisdoerffer, C. (2005), 'Models of giant planet formation with migration and disc evolution', *Astronomy and Astrophysics* **434**, 343–353.

Alves, S., Do Nascimento, Jr., J. D. and de Medeiros, J. R. (2010), 'On the rotational behaviour of parent stars of extrasolar planets', *Monthly Notices of the Royal Astronomical Society* **408**, 1770–1777.

Antoniadou, K. I. and Voyatzis, G. (2016), 'Orbital stability of coplanar two-planet exosystems with high eccentricities', *Monthly Notices of the Royal Astronomical Society* **461**, 3822–3834.

Armitage, P. J. (2011), 'Dynamics of Protoplanetary Disks', *Annual Review of Astronomy and Astrophysics* **49**, 195–236.

Babcock, H. W. (1947), 'Zeeman Effect in Stellar Spectra.', *The Astrophysical Journal* **105**, 105.

Baliunas, S. L., Nesme-Ribes, E., Sokoloff, D. and Soon, W. H. (1996), 'A Dynamo Interpretation of Stellar Activity Cycles', *The Astrophysical Journal* **460**, 848.

Barge, P., Baglin, A., Auvergne, M., Rauer, H., Léger, A., Schneider, J., Pont, F., Aigrain, S., Almenara, J.-M., Alonso, R., Barbieri, M., Bordé, P., Bouchy, F., Deeg, H. J., La Reza, D., Deleuil, M., Dvorak, R., Erikson, A., Fridlund, M., Gillon, M., Gondoin, P., Guillot, T., Hatzes, A., Hebrard, G., Jorda, L., Kabath, P., Lammer, H., Llebaria, A., Loeillet, B., Magain, P., Mazeh, T., Moutou, C., Ollivier, M., Pätzold, M., Queloz, D., Rouan, D., Shporer, A. and Wuchterl, G. (2008), 'Transiting exoplanets from the CoRoT space mission. I. CoRoT-Exo-1b: a low-density short-period planet around a G0V star', *Astronomy and Astrophysics* **482**, L17–L20.

Batygin, K. and Brown, M. E. (2016), 'Evidence for a Distant Giant Planet in the Solar System', *The Astronomical Journal* **151**, 22.

Baudin, F., Baglin, A., Orcesi, J.-L., Nguyen-Kim, K., Solano, E., Ochsenbeim, F. and Corot Scientific Committee (2006), Everything You Always Wanted to Know about CoRoT Data, *in* M. Fridlund, A. Baglin, J. Lochard and L. Conroy, eds, 'The CoRoT Mission Pre-Launch Status - Stellar Seismology and Planet Finding', Vol. 1306 of *ESA Special Publication*, p. 145.

Bean, J. L., Benedict, G. F. and Endl, M. (2006), 'Metallicities of M Dwarf Planet Hosts from Spectral Synthesis', *The Astrophysical Journal Letters* **653**, L65–L68.

Beauge, C. and Aarseth, S. J. (1990), 'N-body simulations of planetary formation', *Monthly Notices of the Royal Astronomical Society* **245**, 30–39.

Bertello, L., Pevtsov, A., Tlatov, A. and Singh, J. (2016), 'Correlation Between Sunspot Number and Ca ii K Emission Index', *Solar Physics* **291**, 2967–2979.

Bhattacharyya, J. C. and Bappu, M. K. V. (1977), 'Saturn-like ring system around Uranus', *Nature* **270**, 503–506.

Bisikalo, D. V., Shematovich, V. I., Gérard, J.-C. and Hubert, B. (2017), 'Influence of the crustal magnetic field on the Mars aurora electron flux and UV brightness', *Icarus* **282**, 127–135.

Bodaghee, A., Santos, N. C., Israelian, G. and Mayor, M. (2003), 'Chemical abundances of planet-host stars. Results for alpha and Fe-group elements', *Astronomy and Astrophysics* **404**, 715–727.

Boss, A. P. (1997), 'Giant planet formation by gravitational instability.', *Science* **276**, 1836–1839.

Boss, A. P., Hudgins, D. M. and Traub, W. A. (2011), New Worlds, New Horizons and NASA's approach to the next decade of exoplanet discoveries, *in* A. Sozzetti, M. G. Lattanzi and A. P. Boss, eds, 'The Astrophysics of Planetary Systems: Formation, Structure, and Dynamical Evolution', Vol. 276 of *IAU Symposium*, pp. 324–334.

Bouchy, F. and Carrier, F. (2001), 'P-mode observations on α Cen A', *Astronomy and Astrophysics* **374**, L5–L8.

Bouvier, J. (2013), Observational studies of stellar rotation, *in* P. Hennebelle and C. Charbonnel, eds, 'EAS Publications Series', Vol. 62 of *EAS Publications Series*, pp. 143–168.

Brown, T. M. and Gilliland, R. L. (1994), 'Asteroseismology', *Annual Review of Astronomy and Astrophysics* **32**, 37–82.

Brugamyer, E., Dodson-Robinson, S. E., Cochran, W. D. and Sneden, C. (2011), 'Silicon and Oxygen Abundances in Planet-host Stars', *The Astrophysical Journal* **738**, 97.

Buchhave, L. A., Bizzarro, M., Latham, D. W., Sasselov, D., Cochran, W. D., Endl, M., Isaacson, H., Juncher, D. and Marcy, G. W. (2014), 'Three regimes of extrasolar planet radius inferred from host star metallicities', *Nature* **509**, 593–595.

Burns, J. A. (1975), 'The angular momenta of solar system bodies - Implications for asteroid strengths', *Icarus* **25**, 545–554.

Burrows, A. and Orton, G. (2010), *Giant Planet Atmospheres*, pp. 419–440.

Canto Martins, B. L., Das Chagas, M. L., Alves, S., Leão, I. C., de Souza Neto, L. P. and de Medeiros, J. R. (2011), 'Chromospheric activity of stars with planets', *Astronomy and Astrophysics* **530**, A73.

Carrasco, L., Roth, M. and Serrano, A. (1982), 'Density scaling of the angular momentum versus mass universal relationship', *Astronomy and Astrophysics* **106**, 89–93.

Chadney, J. M., Galand, M., Unruh, Y. C., Koskinen, T. T. and Sanz-Forcada, J. (2015), 'XUV-driven mass loss from extrasolar giant planets orbiting active stars', *Icarus* **250**, 357–367.

Chaplin, W. J. and Miglio, A. (2013), 'Asteroseismology of Solar-Type and Red-Giant Stars', *Annual Review of Astronomy and Astrophysics* **51**, 353–392.

Charbonneau, D. (2004), A Review of the Current Status of Follow-Up Techniques to Study Known Extrasolar Planets, *in* A. K. Dupree and A. O. Benz, eds, 'Stars as Suns : Activity, Evolution and Planets', Vol. 219 of *IAU Symposium*, p. 367.

Chatterjee, S. and Tan, J. C. (2015), 'Vulcan Planets: Inside-out Formation of the Innermost Super-Earths', *The Astrophysical Journal Letters* **798**, L32.

Collier-Cameron, A., Jianke, L. and Mestel, L. (1991), Theory of Magnetic Braking of Late-Type Stars, *in* S. Catalano and J. R. Stauffer, eds, 'NATO Advanced Science Institutes (ASI) Series C', Vol. 340 of *NATO Advanced Science Institutes (ASI) Series C*, Cambridge University Press, p. 297.

Cranmer, S. R. (2017), 'Mass-loss Rates from Coronal Mass Ejections: A Predictive Theoretical Model for Solar-type Stars', *The Astrophysical Journal* **840**, 114.

Cranmer, S. R. and Saar, S. H. (2011), 'Testing a Predictive Theoretical Model for the Mass Loss Rates of Cool Stars', *The Astrophysical Journal* **741**, 54.

Crida, A. (2009), 'Minimum Mass Solar Nebulae and Planetary Migration', *The Astrophysical Journal* **698**, 606–614.

Cumming, A. (2010), *Statistical Distribution of Exoplanets*, pp. 191–214.

Cumming, A., Butler, R. P., Marcy, G. W., Vogt, S. S., Wright, J. T. and Fischer, D. A. (2008), 'The Keck Planet Search: Detectability and the Minimum Mass and Orbital Period Distribution of Extrasolar Planets', *Publications of the Astronomical Society of the Pacific* **120**, 531–554.

Cuntz, M., Saar, S. H. and Musielak, Z. E. (2000), 'On Stellar Activity Enhancement Due to Interactions with Extrasolar Giant Planets', *The Astrophysical Journal Letters* **533**, L151–L154.

da Silva, R., Milone, A. C. and Reddy, B. E. (2011), 'Homogeneous photospheric parameters and C abundances in G and K nearby stars with and without planets', *Astronomy and Astrophysics* **526**, A71.

Dawson, R. I. and Murray-Clay, R. A. (2013), 'Giant Planets Orbiting Metal-rich Stars Show Signatures of Planet-Planet Interactions', *The Astrophysical Journal Letters* **767**, L24.

de Jager, C., Nieuwenhuijzen, H. and van der Hucht, K. A. (1988), 'Mass loss rates in the Hertzsprung-Russell diagram', *Astronomy and Astrophysics Supplement Series* **72**, 259–289.

de Wit, J. and Seager, S. (2013), 'Constraining Exoplanet Mass from Transmission Spectroscopy', *Science* **342**, 1473–1477.

Denissenkov, P. A., Pinsonneault, M., Terndrup, D. M. and Newsham, G. (2010), 'Angular Momentum Transport in Solar-type Stars: Testing the Timescale for Core-Envelope Coupling', *The Astrophysical Journal* **716**, 1269–1287.

Donati, J.-F. and Landstreet, J. D. (2009), 'Magnetic Fields of Nondegenerate Stars', *Annual Review of Astronomy and Astrophysics* **47**, 333–370.

Drake, J. J., Cohen, O., Yashiro, S. and Gopalswamy, N. (2013), 'Implications of Mass and Energy Loss due to Coronal Mass Ejections on Magnetically Active Stars', *The Astrophysical Journal* **764**, 170.

Dressing, C. D. and Charbonneau, D. (2015), 'The Occurrence of Potentially Habitable Planets Orbiting M Dwarfs Estimated from the Full Kepler Dataset and an Empirical Measurement of the Detection Sensitivity', *The Astrophysical Journal* **807**, 45.

Dubrulle, B. and Knobloch, E. (1993), 'On instabilities in magnetized accretion disks', *Astronomy and Astrophysics* **274**, 667.

Dumusque, X., Bonomo, A. S., Haywood, R. D., Malavolta, L., Ségransan, D., Buchhave, L. A., Collier Cameron, A., Latham, D. W., Molinari, E., Pepe, F., Udry, S., Charbonneau, D., Cosentino, R., Dressing, C. D., Figueira, P., Fiorenzano, A. F. M., Gettel, S., Harutyunyan, A., Horne, K., Lopez-Morales, M., Lovis, C., Mayor, M., Micela, G., Motalebi, F., Nascimbeni, V., Phillips, D. F., Piotto, G., Pollacco, D., Queloz, D., Rice, K., Sasselov, D., Sozzetti, A., Szentgyorgyi, A. and Watson, C. (2014), 'The Kepler-10 Planetary System Revisited by HARPS-N: A Hot Rocky World and a Solid Neptune-Mass Planet', *The Astrophysical Journal* **789**, 154.

Eberhard, G. and Schwarzschild, K. (1913), 'On the reversal of the calcium lines H and K in stellar spectra.', *The Astrophysical Journal* **38**.

Egeland, R., Soon, W., Baliunas, S., Hall, J. C., Pevtsov, A. A. and Bertello, L. (2017), 'The Mount Wilson Observatory S-index of the Sun', *The Astrophysical Journal* **835**, 25.

Einstein, A. (1936), 'Lens-Like Action of a Star by the Deviation of Light in the Gravitational Field', *Science* **84**, 506–507.

Epstein, C. R. and Pinsonneault, M. H. (2014), 'How Good a Clock is Rotation? The Stellar Rotation-Mass-Age Relationship for Old Field Stars', *The Astrophysical Journal* **780**, 159.

Fares, R., Moutou, C., Donati, J.-F., Catala, C., Shkolnik, E. L., Jardine, M. M., Cameron, A. C. and Deleuil, M. (2013), 'A small survey of the magnetic fields of planet-host stars', *Monthly Notices of the Royal Astronomical Society* **435**, 1451–1462.

Feulner, G. (2012), 'The faint young Sun problem', *Reviews of Geophysics* **50**, RG2006.

Fischer, D. A. and Valenti, J. (2005), 'The Planet-Metallicity Correlation', *The Astrophysical Journal* **622**, 1102–1117.

Fossat, E., Boumier, P., Corbard, T., Provost, J., Salabert, D., Schmider, F. X., Gabriel, A. H., Grec, G., Renaud, C., Robillot, J. M., Roca-Cortés, T., Turck-Chièze, S., Ulrich, R. K. and Lazrek, M. (2017), 'Asymptotic g modes: Evidence for a rapid rotation of the solar core', *Astronomy and Astrophysics* **604**, A40.

Gaidos, E. J., Güdel, M. and Blake, G. A. (2000), 'The Faint Young Sun Paradox: An observational test of an alternative solar model', *Geophysical Research Letters* **27**, 501–503.

Gallet, F. (2013), Angular momentum evolution model for solar-like stars, *in* L. Cambresy, F. Martins, E. Nuss and A. Palacios, eds, 'SF2A-2013: Proceedings of the Annual meeting of the French Society of Astronomy and Astrophysics', pp. 85–89.

Gaudi, B. S. (2010), *Microlensing by Exoplanets*, pp. 79–110.

Gibson, E. G. (1973), *The quiet sun.*, NASA Special Publication, p. 7.

Goldblatt, C. and Zahnle, K. J. (2011), 'Faint young Sun paradox remains', *Nature* **474**, E1.

Gondoin, P., Gandolfi, D., Fridlund, M., Frasca, A., Guenther, E. W., Hatzes, A., Deeg, H. J., Parviainen, H., Eigmüller, P. and Deleuil, M. (2012), 'From CoRoT 102899501 to the Sun. A time evolution model of chromospheric activity on the main sequence', *Astronomy and Astrophysics* **548**, A15.

Gonzalez, G. (2000), Chemical-Abundance Trends among Stars with Planets (Invited Review), *in* G. Garzón, C. Eiroa, D. de Winter and T. J. Mahoney, eds, 'Disks, Planetesimals, and Planets', Vol. 219 of *Astronomical Society of the Pacific Conference Series*, p. 523.

Gonzalez, G. (2006), 'The Chemical Compositions of Stars with Planets: A Review', *Publications of the Astronomical Society of the Pacific* **118**, 1494–1505.

Gonzalez, G., Brownlee, D. and Ward, P. (2001), 'The Galactic Habitable Zone: Galactic Chemical Evolution', *Icarus* **152**, 185–200.

Gregory, P. C. and Fischer, D. A. (2010), 'A Bayesian periodogram finds evidence for three planets in 47UrsaeMajoris', *Monthly Notices of the Royal Astronomical Society* **403**, 731–747.

Güdel, M. (2007), 'The Sun in Time: Activity and Environment', *Living Reviews in Solar Physics* **4**.

Hall, J. C. (2008), 'Stellar Chromospheric Activity', *Living Reviews in Solar Physics* **5**, 2.

Hartmann, L. (1985), 'Mass loss from solar-type stars', *Solar Physics* **100**, 587–597.

Hathaway, D. H. and Choudhary, D. P. (2008), 'Sunspot Group Decay', *Solar Physics* **250**, 269–278.

Hayashi, C. (1981), 'Structure of the Solar Nebula, Growth and Decay of Magnetic Fields and Effects of Magnetic and Turbulent Viscosities on the Nebula', *Progress of Theoretical Physics Supplement* **70**, 35–53.

Hiremath, K. M. (1994), PhD thesis, Bangalore University, India, (1994).

Hiremath, K. M. (2009), 'Solar Forcing on the Changing Climate', *Sun and Geosphere* **4**, 16–21.

Hiremath, K. M. (2012), 'Magnetic field structure of Mercury', *Planetary and Space Science* **63**, 8–14.

Hiremath, K. M. (2013), *New Trends in Atomic and Molecular Physics: Advanced Technological Applications*, Springer Berlin Heidelberg, Berlin, Heidelberg, chapter Seismology of the Sun: Inference of Thermal, Dynamic and Magnetic Field Structures of the Interior, p. 331.

Hiremath, K. M. (2016), Reconstruction of Thermal and Magnetic Field Structure of the Solar Subsurface Through Helioseismology, *in* J.-P. Rozelot and C. Neiner, eds, 'Lecture Notes in Physics, Berlin Springer Verlag', Vol. 914 of *Lecture Notes in Physics, Berlin Springer Verlag*, p. 69.

Hiremath, K. M. and Gokhale, M. H. (1995), '"Steady" and "Fluctuating" Parts of the Sun's Internal Magnetic Field: Improved Model', *The Astrophysical Journal* **448**, 437.

Huang, R. Q., Jiang, S. Y., Han, Z. W. and Lie, Y. (1990), 'Evolution of a mass-losing star of 7 solar masses', *Astronomy and Astrophysics* **229**, 99–103.

Ida, S. and Lin, D. N. C. (2005), 'Dependence of Exoplanets on Host Stars' Metallicity and Mass', *Progress of Theoretical Physics Supplement* **158**, 68–85.

Israelian, G., Santos, N. C., Mayor, M. and Rebolo, R. (2001), 'Evidence for planet engulfment by the star HD82943', *Nature* **411**, 163–166.

Izidoro, A., Raymond, S. N., Morbidelli, A., Hersant, F. and Pierens, A. (2015), 'Gas Giant Planets as Dynamical Barriers to Inward-Migrating Super-Earths', *The Astrophysical Journal Letters* **800**, L22.

Jacob, W. S. (1855), 'On certain Anomalies presented by the Binary Star 70 Ophiuchi', *Monthly Notices of the Royal Astronomical Society* **15**, 228.

Jewitt, D., Chizmadia, L., Grimm, R. and Prialnik, D. (2007), 'Water in the Small Bodies of the Solar System', *Protostars and Planets V* pp. 863–878.

Johnson, J. A., Aller, K. M., Howard, A. W. and Crepp, J. R. (2010), 'Giant Planet Occurrence in the Stellar Mass-Metallicity Plane', *Publications of the Astronomical Society of the Pacific* **122**, 905–915.

Johnson, J. A., Butler, R. P., Marcy, G. W., Fischer, D. A., Vogt, S. S., Wright, J. T. and Peek, K. M. G. (2007), 'A New Planet around an M Dwarf: Revealing a Correlation between Exoplanets and Stellar Mass', *The Astrophysical Journal* **670**, 833–840.

Jones, M. I., Jenkins, J. S., Bluhm, P., Rojo, P. and Melo, C. H. F. (2014), 'The properties of planets around giant stars', *Astronomy and Astrophysics* **566**, A113.

Jones, M. I., Jenkins, J. S., Brahm, R., Wittenmyer, R. A., Olivares E., F., Melo, C. H. F., Rojo, P., Jordán, A., Drass, H., Butler, R. P. and Wang, L. (2016), 'Four new planets around giant stars and the mass-metallicity correlation of planet-hosting stars', *Astronomy and Astrophysics* **590**, A38.

Kerr, M., Johnston, S., Hobbs, G. and Shannon, R. M. (2015), 'Limits on Planet Formation Around Young Pulsars and Implications for Supernova Fallback Disks', *The Astrophysical Journal Letters* **809**, L11.

Kopparapu, R. K., Ramirez, R. M., SchottelKotte, J., Kasting, J. F., Domagal-Goldman, S. and Eymet, V. (2014), 'Habitable Zones around Main-sequence Stars: Dependence on Planetary Mass', *The Astrophysical Journal Letters* **787**, L29.

Kovács, G., Bakos, G. Á., Hartman, J. D., Torres, G., Noyes, R. W., Latham, D. W., Howard, A. W., Fischer, D. A., Johnson, J. A., Marcy, G. W., Isaacson, H., Sasselov, D. D., Stefanik, R. P., Esquerdo, G. A., Fernandez, J. M., Lázár, B. B. J., Papp, I. and Sári, P. (2010), 'HAT-P-15b: A 10.9 Day Extrasolar Planet Transiting a Solar-type Star', *The Astrophysical Journal* **724**, 866–877.

Kraft, R. P. (1967), 'Studies of Stellar Rotation. V. The Dependence of Rotation on Age among Solar-Type Stars', *The Astrophysical Journal* **150**, 551.

Ksanfomality, L. V. (2004), 'Regularity of Extrasolar Planetary Systems and the Role of the Star Metallicity in the Formation of Planets (Review)', *Solar System Research* **38**, 372–382.

Kuiper, G. P. (1938), 'The Empirical Mass-Luminosity Relation.', *The Astrophysical Journal* **88**, 472.

Küker, M., Henning, T. and Rüdiger, G. (2003), 'Magnetic Star-Disk Coupling in Classical T Tauri Systems', *The Astrophysical Journal* **589**, 397–409.

Kumar, P., Talon, S. and Zahn, J.-P. (1999), 'Angular Momentum Redistribution by Waves in the Sun', *The Astrophysical Journal* **520**, 859–870.

Lammer, H., Blanc, M., Benz, W., Fridlund, M., Foresto, V. C. d., Güdel, M., Rauer, H., Udry, S., Bonnet, R.-M., Falanga, M., Charbonneau, D., Helled, R., Kley, W., Linsky, J., Elkins-Tanton, L. T., Alibert, Y., Chassefière, E., Encrenaz, T., Hatzes, A. P., Lin, D., Liseau, R., Lorenzen, W. and Raymond, S. N. (2013), 'The Science of Exoplanets and Their Systems', *Astrobiology* **13**, 793–813.

Lammer, H., Dvorak, R., Deleuil, M., Barge, P., Deeg, H. J., Moutou, C., Erikson, A., Csizmadia, S., Tingley, B., Bruntt, H., Havel, M., Aigrain, S., Almenara, J. M., Alonso, R., Auvergne, M., Baglin, A., Barbieri, M., Benz, W., Bonomo, A. S., Bordé, P., Bouchy, F., Cabrera, J., Carone, L., Carpano, S., Ciardi, D., Ferraz-Mello, S., Fridlund, M., Gandolfi, D., Gazzano, J.-C., Gillon, M., Gondoin, P., Guenther, E., Guillot, T., den Hartog, R., Hasiba, J., Hatzes, A., Hidas, M., Hébrard, G., Jorda, L., Kabath, P., Léger, A., Lister, T., Llebaria, A., Lovis, C., Mayor, M., Mazeh, T., Mura, A., Ollivier, M., Ottacher, H., Pätzold, M., Pepe, F., Pont, F., Queloz, D., Rabus, M., Rauer, H., Rouan, D., Samuel, B., Schneider, J., Shporer, A., Stecklum, B., Steller, M., Street, R., Udry, S., Weingrill, J. and Wuchterl, G. (2010), 'Exoplanet discoveries with the CoRoT space observatory', *Solar System Research* **44**, 520–526.

Lanza, A. F. (2010), 'Hot Jupiters and the evolution of stellar angular momentum', *Astronomy and Astrophysics* **512**, A77.

Lanza, A. F. (2013), 'Star-planet magnetic interaction and evaporation of planetary atmospheres', *Astronomy and Astrophysics* **557**, A31.

Laws, C., Gonzalez, G., Walker, K. M., Tyagi, S., Dodsworth, J., Snider, K. and Suntzeff, N. B. (2003), 'Parent Stars of Extrasolar Planets. VII. New Abundance Analyses of 30 Systems', *The Astronomical Journal* **125**, 2664–2677.

Lebreton, Y., Goupil, M. J. and Montalbán, J. (2014), How accurate are stellar ages based on stellar models?. I. The impact of stellar models uncertainties, *in* 'EAS Publications Series', Vol. 65 of *EAS Publications Series*, pp. 99–176.

Lenz, L. F., Reiners, A. and Kürster, M. (2011), A Search for Star-Planet Interactions in Chromospheric Lines, *in* C. Johns-Krull, M. K. Browning and A. A. West, eds, '16th Cambridge Workshop on Cool Stars, Stellar Systems, and the Sun', Vol. 448 of *Astronomical Society of the Pacific Conference Series*, p. 1173.

Lindgren, S., Heiter, U. and Seifahrt, A. (2016), 'Metallicity determination of M dwarfs. High-resolution infrared spectroscopy', *Astronomy and Astrophysics* **586**, A100.

Linsky, J. L., Wood, B. E., Müller, H.-R. and Zank, G. P. (2004), Mass Loss of Solar-like Dwarf Stars and the Young Sun, *in* A. K. Dupree and A. O. Benz, eds, 'Stars as Suns : Activity, Evolution and Planets', Vol. 219 of *IAU Symposium*, p. 898.

Loukitcheva, M., Solanki, S. K. and White, S. M. (2009), 'The relationship between chromospheric emissions and magnetic field strength', *Astronomy and Astrophysics* **497**, 273–285.

Lovis, C. and Mayor, M. (2007), 'Planets around evolved intermediate-mass stars. I. Two substellar companions in the open clusters NGC 2423 and NGC 4349', *Astronomy and Astrophysics* **472**, 657–664.

Lubow, S. H. and Ida, S. (2010), *Planet Migration*, pp. 347–371.

Madhusudhan, N., Bitsch, B., Johansen, A. and Eriksson, L. (2017), 'Atmospheric signatures of giant exoplanet formation by pebble accretion', *Monthly Notices of the Royal Astronomical Society* **469**, 4102–4115.

Maldonado, J., Villaver, E. and Eiroa, C. (2013), 'The metallicity signature of evolved stars with planets', *Astronomy and Astrophysics* **554**, A84.

Marcy, G., Butler, R. P., Fischer, D., Vogt, S., Wright, J. T., Tinney, C. G. and Jones, H. R. A. (2005), 'Observed Properties of Exoplanets: Masses, Orbits, and Metallicities', *Progress of Theoretical Physics Supplement* **158**, 24–42.

Marois, C., Macintosh, B., Barman, T., Zuckerman, B., Song, I., Patience, J., Lafrenière, D. and Doyon, R. (2008), 'Direct Imaging of Multiple Planets Orbiting the Star HR 8799', *Science* **322**, 1348.

Marsden, S. C., Petit, P., Jeffers, S. V., Morin, J., Fares, R., Reiners, A., do Nascimento, J.-D., Aurière, M., Bouvier, J., Carter, B. D., Catala, C., Dintrans, B., Donati, J.-F., Gastine, T., Jardine, M., Konstantinova-Antova, R., Lanoux, J., Lignières, F., Morgenthaler, A., Ramìrez-Vèlez, J. C., Théado, S., Van Grootel, V. and BCool Collaboration (2014), 'A BCool magnetic snapshot survey of solar-type stars', *Monthly Notices of the Royal Astronomical Society* **444**, 3517–3536.

Matt, S. P., Brun, A. S., Baraffe, I., Bouvier, J. and Chabrier, G. (2015), 'The Mass-dependence of Angular Momentum Evolution in Sun-like Stars', *The Astrophysical Journal Letters* **799**, L23.

Mayor, M. and Queloz, D. (1995), 'A Jupiter-mass companion to a solar-type star', *Nature* **378**, 355–359.

McIvor, T., Jardine, M. and Holzwarth, V. (2006), 'Extrasolar planets, stellar winds and chromospheric hotspots', *Monthly Notices of the Royal Astronomical Society* **367**, L1–L5.

McKee, C. F. and Ostriker, E. C. (2007), 'Theory of Star Formation', *Annual Review of Astronomy and Astrophysics* **45**, 565–687.

McNally, D. (1971), 'Theories of star formation', *Reports on Progress in Physics* **34**(1), 71.

Meadows, V. and Seager, S. (2010), *Terrestrial Planet Atmospheres and Biosignatures*, pp. 441–470.

Meléndez, J., Asplund, M., Gustafsson, B. and Yong, D. (2009), 'The Peculiar Solar Composition and Its Possible Relation to Planet Formation', *The Astrophysical Journal Letters* **704**, L66–L70.

Mena, E. D., Israelian, G., Hernndez, J. I. G., Santos, N. C. and Rebolo, R. (2012), 'Be abundances in cool main-sequence stars with exoplanets', *The Astrophysical Journal* **746**(1), 47.

Mengel, M. W., Marsden, S. C., Carter, B. D., Horner, J., King, R., Fares, R., Jeffers, S. V., Petit, P., Vidotto, A. A., Morin, J. and BCool Collaboration (2017), 'A BCool survey of the magnetic fields of planet-hosting solar-type stars', *Monthly Notices of the Royal Astronomical Society* **465**, 2734–2747.

Mestel, L. (1968), 'Magnetic braking by a stellar wind-I', *Monthly Notices of the Royal Astronomical Society* **138**, 359.

Metcalfe, T. S., Creevey, O. L., Doğan, G., Mathur, S., Xu, H., Bedding, T. R., Chaplin, W. J., Christensen-Dalsgaard, J., Karoff, C., Trampedach, R., Benomar, O., Brown, B. P., Buzasi, D. L., Campante, T. L., Çelik, Z., Cunha, M. S., Davies, G. R., Deheuvels, S., Derekas, A. and Di Mauro, M. P. (2014), 'Properties of 42 Solar-type Kepler Targets from the Asteroseismic Modeling Portal', *The Astrophysical Journal Supplement Series* **214**, 27.

Miller, B. P., Gallo, E., Wright, J. T. and Dupree, A. K. (2012), 'On the detectability of star-planet interaction', *The Astrophysical Journal* **754**(2), 137.

Miller, B. P., Gallo, E., Wright, J. T. and Pearson, E. G. (2015), 'A comprehensive statistical assessment of star-planet interaction', *The Astrophysical Journal* **799**(2), 163.

Minton, D. A. and Malhotra, R. (2007), 'Assessing the Massive Young Sun Hypothesis to Solve the Warm Young Earth Puzzle', *The Astrophysical Journal* **660**, 1700–1706.

Mordasini, C., Alibert, Y., Benz, W., Klahr, H. and Henning, T. (2012), 'Extrasolar planet population synthesis . IV. Correlations with disk metallicity, mass, and lifetime', *Astronomy and Astrophysics* **541**, A97.

Moriarty, J., Madhusudhan, N. and Fischer, D. (2014), 'Chemistry in an Evolving Protoplanetary Disk: Effects on Terrestrial Planet Composition', *The Astrophysical Journal* **787**, 81.

Mortier, A., Santos, N. C., Sousa, S. G., Adibekyan, V. Z., Delgado Mena, E., Tsantaki, M., Israelian, G. and Mayor, M. (2013), 'New and updated stellar parameters for 71 evolved planet hosts. On the metallicity-giant planet connection', *Astronomy and Astrophysics* **557**, A70.

Moulton, F. R. (1899), 'The limits of temporary stability of satellite motion, with an application to the question of the existence of an unseen body in the binary system 70 Ophiuchi', *The Astronomical Journal* **20**, 33–37.

Nayakshin, S. V. (2015), Observations vs theory: from metallicity correlations of exoplanets and debris discs to HL Tau, *in* 'AAS/Division for Extreme Solar Systems Abstracts', Vol. 3 of *AAS/Division for Extreme Solar Systems Abstracts*, p. 115.09.

Nindos, A. and Zirin, H. (1998), 'The Relation of CA II K Features to Magnetic Field', *Solar Physics* **179**, 253–268.

Okamoto, I. (1969), 'On the Loss of Angular Momentum from the Protosun and the Formation of the Solar System', *Publications of the Astronomical Society of Japan* **21**, 25.

Pace, G. (2013), 'Chromospheric activity as age indicator. An L-shaped chromospheric-activity versus age diagram', *Astronomy and Astrophysics* **551**, L8.

Palle, P. L., Jimenez, A., Perez Hernandez, F., Regulo, C., Roca Cortes, T. and Sanchez, L. (1995), 'A measurement of the background solar velocity spectrum', *The Astrophysical Journal* **441**, 952–959.

Parker, E. N. (1971), 'The Generation of Magnetic Fields in Astrophysical Bodies.IV. The Solar and Terrestrial Dynamos', *The Astrophysical Journal* **164**, 491.

Parker, E. N. (1975), 'The generation of magnetic fields in astrophysical bodies. X - Magnetic buoyancy and the solar dynamo', *The Astrophysical Journal* **198**, 205–209.

Paz-Chinchón, F., Leão, I. C., Bravo, J. P., de Freitas, D. B., Ferreira Lopes, C. E., Alves, S., Catelan, M., Canto Martins, B. L. and De Medeiros, J. R. (2015), 'The Rotational Behavior of Kepler Stars with Planets', *The Astrophysical Journal* **803**, 69.

Pinsonneault, M. H., An, D., Molenda-Żakowicz, J., Chaplin, W. J., Metcalfe, T. S. and Bruntt, H. (2012), 'A Revised Effective Temperature Scale for the Kepler Input Catalog', *The Astrophysical Journal Supplement Series* **199**, 30.

Press, W. H., Teukolsky, S. A., Vetterling, W. T. and Flannery, B. P. (1992), *Numerical recipes in C. The art of scientific computing*, Cambridge: University Press, —c1992, 2nd ed.

Preusse, S., Kopp, A., Büchner, J. and Motschmann, U. (2006), 'A magnetic communication scenario for hot Jupiters', *Astronomy and Astrophysics* **460**, 317–322.

Quiroga, R. (1984), 'Angular momenta in the solar system', *Earth Moon and Planets* **30**, 137–147.

Raymond, S. N., Barnes, R. and Kaib, N. A. (2006), 'Predicting Planets in Known Extrasolar Planetary Systems. III. Forming Terrestrial Planets', *The Astrophysical Journal* **644**, 1223–1231.

Reboussin, L., Wakelam, V., Guilloteau, S., Hersant, F. and Dutrey, A. (2015), 'Chemistry in protoplanetary disks: the gas-phase CO/H_2 ratio and the carbon reservoir', *Astronomy and Astrophysics* **579**, A82.

Reddy, B. E., Lambert, D. L., Laws, C., Gonzalez, G. and Covey, K. (2002), 'A search for [6]Li in stars with planets', *Monthly Notices of the Royal Astronomical Society* **335**, 1005–1016.

Reiners, A. (2012), 'Observations of Cool-Star Magnetic Fields', *Living Reviews in Solar Physics* **9**, 1.

Ridgway, S., Aufdenberg, J., Creech-Eakman, M., Elias, N., Howell, S., Hutter, D., Karovska, M., Ragland, S., Wishnow, E. and Zhao, M. (2009), Quantifying Stellar Mass Loss with High Angular Resolution Imaging, *in* 'astro2010: The Astronomy and Astrophysics Decadal Survey', Vol. 2010 of *Astronomy*.

Roberge, A. and Kamp, I. (2010), *Protoplanetary and Debris Disks*, pp. 269–295.

Rogers, T. M. and Glatzmaier, G. A. (2006), 'Angular Momentum Transport by Gravity Waves in the Solar Interior', *The Astrophysical Journal* **653**, 756–764.

Roig, F. and Nesvorný, D. (2015), 'The Evolution of Asteroids in the Jumping-Jupiter Migration Model', *The Astronomical Journal* **150**, 186.

Ryon, J., Shetrone, M. D. and Smith, G. H. (2009), 'Comparing the Ca ii H and K Emission Lines in Red Giant Stars', *Publications of the Astronomical Society of the Pacific* **121**, 842.

Sackmann, I.-J. and Boothroyd, A. I. (2003), 'Our Sun. V. A Bright Young Sun Consistent with Helioseismology and Warm Temperatures on Ancient Earth and Mars', *The Astrophysical Journal* **583**, 1024–1039.

Sagan, C. and Mullen, G. (1972), 'Earth and Mars: Evolution of Atmospheres and Surface Temperatures', *Science* **177**, 52–56.

Sakurai, T. (2017), 'Heating mechanisms of the solar corona', *Proceeding of the Japan Academy, Series B* **93**, 87–97.

Santos, N. C., Delgado Mena, E., Israelian, G., González-Hernández, J. I., Gálvez-Ortiz, M. C., Mayor, M., Udry, S., Rebolo, R., Sousa, S. and Randich, S. (2010), Light elements in stars with exoplanets, *in* C. Charbonnel, M. Tosi, F. Primas and C. Chiappini, eds, 'Light Elements in the Universe', Vol. 268 of *IAU Symposium*, pp. 291–299.

Santos, N. C., Israelian, G., García López, R. J., Mayor, M., Rebolo, R., Randich, S., Ecuvillon, A. and Domínguez Cerdeña, C. (2004), 'Are beryllium abundances anomalous in stars with giant planets?', *Astronomy and Astrophysics* **427**, 1085–1096.

Santos, N. C., Israelian, G. and Mayor, M. (2000), 'Chemical analysis of 8 recently discovered extra-solar planet host stars', *Astronomy and Astrophysics* **363**, 228–238.

Satyal, S., Griffith, J. and Musielak, Z. E. (2017), 'Dynamics of a Probable Earth-mass Planet in the GJ 832 System', *The Astrophysical Journal* **845**, 106.

Scharf, C. A. (2010), 'Possible Constraints on Exoplanet Magnetic Field Strengths from Planet-star Interaction', *The Astrophysical Journal* **722**, 1547–1555.

Scholz, A. (2013), 'Angular momentum and disk evolution in very low mass systems ', *MmSAI* **84**, 890.

Seager, S. (2010), *Exoplanets*.

Seager, S. and Lissauer, J. J. (2010), *Exoplanets*, AZ: University of Arizona Press, pp. 3–13.

Shkolnik, E. L. (2013), 'An Ultraviolet Investigation of Activity on Exoplanet Host Stars', *The Astrophysical Journal* **766**, 9.

Shkolnik, E., Walker, G. A. H. and Bohlender, D. A. (2003), 'Evidence for Planet-induced Chromospheric Activity on HD 179949', *The Astrophysical Journal* **597**, 1092–1096.

Singh, H. P., Tandon, J. N. and Das, M. K. (1984), 'The effect of rotation on the luminosity of magnetic stars', *Astrophysics and Space Science* **100**, 219–225.

Sivaraman, K. R. and Livingston, W. C. (1982), 'CA II K2V spectral features and their relation to small-scale photospheric magnetic fields', *Solar Physics* **80**, 227–231.

Skumanich, A. (1972), 'Time Scales for CA II Emission Decay, Rotational Braking, and Lithium Depletion', *The Astrophysical Journal* **171**, 565.

Soderblom, D. R., Duncan, D. K. and Johnson, D. R. H. (1991), 'The chromospheric emission-age relation for stars of the lower main sequence and its implications for the star formation rate', *The Astrophysical Journal* **375**, 722–739.

Soderblom, D. R., Fedele, S. B., Jones, B. F., Stauffer, J. R. and Prosser, C. F. (1993), 'The evolution of the lithium abundances of solar-type stars. IV - Praesepe', *The Astronomical Journal* **106**, 1080–1086.

Soderblom, D. R., Hillenbrand, L. A., Jeffries, R. D., Mamajek, E. E. and Naylor, T. (2014), 'Ages of Young Stars', *Protostars and Planets VI* pp. 219–241.

Struve, O. (1952), 'Proposal for a project of high-precision stellar radial velocity work', *The Observatory* **72**, 199–200.

Taketani, M., Hatanaka, T. and Obi, S. (1956), 'Populations and evolution of stars', *Progress of Theoretical Physics* **15**(2), 89–94.

Tarafdar, S. P. and Vardya, M. S. (1971), 'On the Variation of Specific Angular Momentum Among Main Sequence Stars', *Astrophysics and Space Science* **13**, 234–248.

Tian, F. and Ida, S. (2015), 'Water contents of Earth-mass planets around M dwarfs', *Nature Geoscience* **8**, 177–180.

Triaud, A. (2016), 'Exoplanets: Migration of giants', *Nature* **537**, 496–497.

Tsiganis, K., Gomes, R., Morbidelli, A. and Levison, H. F. (2005), 'Origin of the orbital architecture of the giant planets of the Solar System', *Nature* **435**, 459–461.

Udry, S., Mayor, M. and Santos, N. C. (2003), 'Statistical properties of exoplanets. I. The period distribution: Constraints for the migration scenario', *Astronomy and Astrophysics* **407**, 369–376.

Udry, S. and Santos, N. C. (2007), 'Statistical Properties of Exoplanets', *Annual Review of Astronomy and Astrophysics* **45**, 397–439.

van de Kamp, P. (1963), 'Astrometric study of Barnard's star from plates taken with the 24-inch Sproul refractor.', *The Astronomical Journal* **68**, 515–521.

Vasundhara, R., Bhattacharyya, J. C., Rajamohan, R. and Mahra, H. S. (1983), 'Some further measurements of Uranian ring condensations', *Moon and Planets* **29**, 79–82.

Vauclair, S. and Vauclair, G. (2014), Consequences of the accretion of planetary matter on the chemical composition of the stars., *in* J. Ballet, F. Martins, F. Bournaud, R. Monier and C. Reylé, eds, 'SF2A-2014: Proceedings of the Annual meeting of the French Society of Astronomy and Astrophysics', pp. 285–289.

Vidotto, A. A. (2014), The effects of stellar winds and magnetic fields on exoplanets, *in* P. Petit, M. Jardine and H. C. Spruit, eds, 'Magnetic Fields throughout Stellar Evolution', Vol. 302 of *IAU Symposium*, pp. 228–236.

Wakeford, H. R., Sing, D. K., Deming, D., Gibson, N. P., Fortney, J. J., Burrows, A. S., Ballester, G., Nikolov, N., Aigrain, S., Henry, G., Knutson, H., Lecavelier des Etangs, A., Pont, F., Showman, A. P., Vidal-Madjar, A. and Zahnle, K. (2013), 'HST hot Jupiter transmission spectral survey: detection of water in HAT-P-1b from WFC3 near-IR spatial scan observations', *Monthly Notices of the Royal Astronomical Society* **435**, 3481–3493.

Walker, G. A. H., Walker, A. R., Irwin, A. W., Larson, A. M., Yang, S. L. S. and Richardson, D. C. (1995), 'A search for Jupiter-mass companions to nearby stars.', *Icarus* **116**, 359–375.

Walsh, C. and Millar, T. J. (2011), The Chemistry of Exoplanet Atmospheres, *in* J. Cernicharo and R. Bachiller, eds, 'The Molecular Universe', Vol. 280 of *IAU Symposium*.

Wang, J. and Fischer, D. A. (2015), 'Revealing a Universal Planet-Metallicity Correlation for Planets of Different Sizes Around Solar-type Stars', *The Astronomical Journal* **149**, 14.

Weidenschilling, S. J. (1977), 'Aerodynamics of solid bodies in the solar nebula', *Monthly Notices of the Royal Astronomical Society* **180**, 57–70.

Weiss, L. M. and Marcy, G. W. (2014), 'The Mass-Radius Relation for 65 Exoplanets Smaller than 4 Earth Radii', *The Astrophysical Journal* **783**, L6.

Whitmire, D. P., Doyle, L. R., Reynolds, R. T. and Matese, J. J. (1995), 'A slightly more massive young Sun as an explanation for warm temperatures on early Mars', *Journal of Geophysical Research* **100**, 5457–5464.

Williams, J. P. and Cieza, L. A. (2011), 'Protoplanetary Disks and Their Evolution', *Annual Review of Astronomy and Astrophysics* **49**, 67–117.

Wilson, O. C. (1963), 'A Probable Correlation Between Chromospheric Activity and Age in Main-Sequence Stars.', *The Astrophysical Journal* **138**, 832.

Wilson, O. C. and Vainu Bappu, M. K. (1957), 'H and K Emission in Late-Type Stars:

Dependence of Line Width on Luminosity and Related Topics.', *The Astrophysical Journal* **125**, 661.

Wilson, R. E. (1953), 'General catalogue of stellar radial velocities.', *Carnegie Institute Washington D.C. Publication* .

Winn, J. N. (2010), *Exoplanet Transits and Occultations*, University of Arizona Press, pp. 55–77.

Winn, J. N. and Fabrycky, D. C. (2015), 'The Occurrence and Architecture of Exoplanetary Systems', *Annual Review of Astronomy and Astrophysics* **53**, 409–447.

Wolff, S. C., Strom, S. E. and Hillenbrand, L. A. (2004), 'The Angular Momentum Evolution of 0.1-10 M$_{solar}$ Stars from the Birth Line to the Main Sequence', *The Astrophysical Journal* **601**, 979–999.

Wolszczan, A. and Frail, D. A. (1992), 'A planetary system around the millisecond pulsar PSR1257 + 12', *Nature* **355**, 145–147.

Wood, B. E., Müller, H.-R., Zank, G. P. and Linsky, J. L. (2002), 'Measured Mass-Loss Rates of Solar-like Stars as a Function of Age and Activity', *The Astrophysical Journal* **574**, 412–425.

Wood, B. E., Müller, H.-R., Zank, G. P., Linsky, J. L. and Redfield, S. (2005), 'New Mass-Loss Measurements from Astrospheric Lyα Absorption', *The Astrophysical Journal Letters* **628**, L143–L146.

Woolfson, M. (2014), *The Formation of the Solar System: Theories Old and New (2ND Edition)*, World Scientific Publishing Co.

Yi, S., Demarque, P., Kim, Y.-C., Lee, Y.-W., Ree, C. H., Lejeune, T. and Barnes, S. (2001), 'Toward Better Age Estimates for Stellar Populations: The Y^2 Isochrones for Solar Mixture', *The Astrophysical Journal Supplement Series* **136**, 417–437.

Zahn, J.-P., Talon, S. and Matias, J. (1997), 'Angular momentum transport by internal waves in the solar interior.', *Astronomy and Astrophysics* **322**, 320–328.

LIST OF PUBLICATIONS

Published Papers

1. **Shashanka R. Gurumath**, Hiremath K. M., V. Ramasubramanian, 2014. On the Relationship between Masses of Sun like G-stars and their Exoplanets. *New Advances in Physics*, 8, No. 1, pp.91-101.

2. **Shashanka R. Gurumath**, Hiremath K. M., V. Ramasubramanian, 2017. Metallicity of Sun-like G stars that have exoplanets. *Journal of Astrophysics and Astronomy*, 38(2), 19.

3. Hegde M., Hiremath K.M., Doddamani, V.H., and **Shashanka R. Gurumath**, 2015. Solar wind associated with near equatorial coronal hole. *Journal of Astrophysics and Astronomy*, 36, pp.355-374.

4. Ragadeepika Pucha, Hiremath, K.M. and **Shashanka R. Gurumath**, 2016. Development of a Code to Analyze the Solar White-light Images from the Kodaikanal Observatory: Detection of Sunspots, Computation of Heliographic Coordinates and Area. *Journal of Astrophysics and Astronomy*, 37, 3.

Papers Under Review

1. **Shashanka R. Gurumath**, Hiremath K. M., V. Ramasubramanian, 2017. Angular momentum of Sun-like G stars and their exoplanets. *Publication of Astronomical Society of Pacific*.

2. **Shashanka R. Gurumath**, Hiremath K. M., V. Ramasubramanian, 2017. Finding the Earths Twin: Hint from the Exoplanetary Data. *Astrophysics*.

3. **Shashanka R. Gurumath**, Hiremath K. M., V. Ramasubramanian and Hegde, M., 2017. A possible solution for the faint young Sun paradox: Clues from the exoplanetary data. *Journal of Astrophysics and Astronomy*.

4. Hiremath K. M., Rozelot, J. P., Pavan D. Grampurohith, **Shashanka R. Gurumath** and V. Ramasubramanian, 2017. Nearly Century Scale Variation of the Sun's Radius Data. *The Astrophysical Journal*.

Appendices

Table 1 Physical and Orbital Characteristics of Exoplanets and Their Host Stars Used In Analysis of Chapter 4.

Name	M_p (M_J)	a (AU)	$M_\star$ ($M_\odot$)	Spectral Type	$T_\star$ (Gyrs)
24 Sex b	1.990($\pm$0.380)	1.333($\pm$0.009)	1.54($\pm$0.08)	G5	2.70($\pm$0.40)
24 Sex c	0.860($\pm$0.220)	2.080($\pm$0.020)	1.54($\pm$0.08)	G5	2.70($\pm$0.40)
47 Uma b	2.530($\pm$0.060)	2.100($\pm$0.020)	1.03($\pm$0.05)	G0V	7.40($\pm$1.90)
47 Uma c	0.540($\pm$0.073)	3.600($\pm$0.100)	1.03($\pm$0.05)	G0V	7.40($\pm$1.90)
47 Uma d	1.640($\pm$0.480)	11.600($\pm$2.900)	1.03($\pm$0.05)	G0V	7.40($\pm$1.90)
61 Vir b	0.016($\pm$0.001)	0.050($\pm$0.000)	0.95($\pm$0.03)	G5V	8.96($\pm$3.00)
61 Vir c	0.057($\pm$0.003)	0.217($\pm$0.000)	0.95($\pm$0.03)	G5V	8.96($\pm$3.00)
61 Vir d	0.072($\pm$0.008)	0.476($\pm$0.001)	0.95($\pm$0.03)	G5V	8.96($\pm$3.00)
CoRoT-12 b	0.917($\pm$0.065)	0.040($\pm$0.001)	1.07($\pm$0.07)	G2V	6.30($\pm$3.10)
CoRoT-16 b	0.535($\pm$0.085)	0.061($\pm$0.001)	1.09($\pm$0.07)	G5V	6.73($\pm$2.80)
CoRoT-17 b	2.430($\pm$0.160)	0.046($\pm$0.001)	1.04($\pm$0.10)	G2V	10.70($\pm$1.00)
CoRoT-23 b	2.800($\pm$0.250)	0.047($\pm$0.004)	1.14($\pm$0.08)	G0V	7.20($\pm$1.00)
CoRoT-25 b	0.270($\pm$0.040)	0.057($\pm$0.003)	1.09($\pm$0.05)	G0V	5.20($\pm$1.30)
CoRoT-26 b	0.520($\pm$0.050)	0.052($\pm$0.001)	1.09($\pm$0.06)	G8IV	8.60($\pm$1.80)
CoRoT-28 b	0.484($\pm$0.087)	0.059($\pm$0.003)	1.01($\pm$0.14)	G8IV	12.00($\pm$1.50)
HAT-P-13 b	0.850($\pm$0.038)	0.042($\pm$0.001)	1.22($\pm$0.10)	G4	5.00($\pm$0.80)
HAT-P-15 b	1.946($\pm$0.066)	0.096($\pm$0.001)	1.01($\pm$0.04)	G5	6.80($\pm$1.60)
HAT-P-21 b	4.063($\pm$0.161)	0.049($\pm$0.001)	0.94($\pm$0.04)	G3	10.20($\pm$2.50)
HAT-P-22 b	2.147($\pm$0.061)	0.041($\pm$0.001)	0.91($\pm$0.03)	G5	12.40($\pm$2.60)
HAT-P-23 b	2.090($\pm$0.110)	0.023($\pm$0.000)	1.13($\pm$0.05)	G5	4.00($\pm$1.00)
HAT-P-28 b	0.626($\pm$0.037)	0.043($\pm$0.001)	1.02($\pm$0.04)	G3	6.10($\pm$1.90)
HAT-P-38 b	0.267($\pm$0.020)	0.052($\pm$0.001)	0.88($\pm$0.04)	G	10.10($\pm$4.80)
HATS-11 b	0.850($\pm$0.120)	0.046($\pm$0.001)	1.00($\pm$0.06)	G0	7.70($\pm$1.60)
HATS-19 b	0.427($\pm$0.071)	0.058($\pm$0.001)	1.30($\pm$0.83)	G0	3.94($\pm$0.50)
HATS-25 b	0.613($\pm$0.042)	0.051($\pm$0.001)	0.99($\pm$0.03)	G	7.50($\pm$1.90)
HATS-28 b	0.672($\pm$0.087)	0.041($\pm$0.001)	0.92($\pm$0.03)	G	6.20($\pm$2.80)
HATS-29 b	0.653($\pm$0.063)	0.054($\pm$0.001)	1.03($\pm$0.04)	G	5.50($\pm$1.70)
HATS-8 b	0.138($\pm$0.019)	0.046($\pm$0.001)	1.05($\pm$0.03)	G2V	5.10($\pm$1.70)
HD 10180 c	0.041($\pm$-)	0.064($\pm$0.001)	1.06($\pm$0.05)	G1V	4.30($\pm$0.50)
HD 10180 d	0.036($\pm$-)	0.128($\pm$0.002)	1.06($\pm$0.05)	G1V	4.30($\pm$0.50)
HD 10180 e	0.078($\pm$-)	0.269($\pm$0.004)	1.06($\pm$0.05)	G1V	4.30($\pm$0.50)
HD 10180 f	0.075($\pm$-)	0.492($\pm$0.007)	1.06($\pm$0.05)	G1V	4.30($\pm$0.50)
HD 10180 g	0.067($\pm$-)	1.422($\pm$0.026)	1.06($\pm$0.05)	G1V	4.30($\pm$0.50)
HD 10180 h	0.202($\pm$-)	3.400($\pm$0.110)	1.06($\pm$0.05)	G1V	4.30($\pm$0.50)
HD 102365 b	0.050($\pm$0.008)	0.460($\pm$0.040)	0.85($\pm$-)	G2V	9.00($\pm$3.00)
HD 104985 b	8.300($\pm$-)	0.950($\pm$-)	1.60($\pm$-)	G9 III	2.95($\pm$0.65)
HD 106270 b	11.000($\pm$0.800)	4.300($\pm$0.400)	1.32($\pm$0.09)	G5	4.30($\pm$0.60)
HD 10697 b	6.830($\pm$0.984)	2.160($\pm$0.120)	1.15($\pm$0.03)	G5IV	6.90($\pm$0.60)
HD 109271 b	0.054($\pm$0.004)	0.079($\pm$0.001)	1.04($\pm$0.02)	G5V	7.30($\pm$1.20)
HD 109271 c	0.076($\pm$0.007)	0.196($\pm$0.003)	1.04($\pm$0.02)	G5V	7.30($\pm$1.20)
HD 109749 b	0.280($\pm$0.016)	0.063($\pm$-)	1.20($\pm$0.10)	G3IV	10.30($\pm$2.90)
HD 11506 b	3.440($\pm$0.470)	2.430($\pm$0.120)	1.19($\pm$0.10)	G0V	5.40($\pm$1.60)
HD 11506 c	0.820($\pm$0.500)	0.639($\pm$0.017)	1.19($\pm$0.10)	G0V	5.40($\pm$1.60)
HD 117207 b	2.060($\pm$-)	3.780($\pm$-)	1.07($\pm$-)	G8V	6.68($\pm$2.20)

Table 1 Continue...

Name	M_p (M$_J$)	a (AU)	$M_\star$ (M$_\odot$)	Spectral Type	$T_\star$ (Gyrs)
HD 11755 b	6.500($\pm$1.000)	1.080($\pm$0.040)	0.90($\pm$0.10)	G5	10.20($\pm$1.30)
HD 12648 b	2.900($\pm$0.400)	0.540($\pm$0.020)	1.20($\pm$0.10)	G5	4.50($\pm$1.00)
HD 132406 b	5.610($\pm$-)	1.980($\pm$-)	1.09($\pm$0.05)	G0V	6.40($\pm$0.80)
HD 134987 b	1.590($\pm$0.020)	0.810($\pm$0.020)	1.07($\pm$0.08)	G5 V	9.70($\pm$3.70)
HD 134987 c	0.820($\pm$0.030)	5.800($\pm$0.500)	1.07($\pm$0.08)	G5 V	9.70($\pm$3.70)
HD 136418 b	2.000($\pm$0.100)	1.320($\pm$0.030)	1.33($\pm$0.09)	G5	4.00($\pm$1.00)
HD 13931 b	1.880($\pm$0.150)	5.150($\pm$0.290)	1.02($\pm$0.02)	G0	8.40($\pm$2.00)
HD 14067 b	7.800($\pm$0.700)	3.400($\pm$0.100)	2.40($\pm$0.20)	G9 III	0.69($\pm$0.20)
HD 149026 b	0.357($\pm$0.011)	0.042($\pm$0.000)	1.30($\pm$0.10)	G0 IV	2.00($\pm$0.80)
HD 149143 b	1.330($\pm$-)	0.052($\pm$-)	1.10($\pm$0.10)	G0 IV	7.60($\pm$1.20)
HD 154672 b	5.020($\pm$0.170)	0.600($\pm$0.170)	1.06($\pm$0.09)	G3IV	9.28($\pm$2.36)
HD 16175 b	4.770($\pm$0.370)	2.148($\pm$0.076)	1.35($\pm$0.09)	G0	5.30($\pm$1.00)
HD 162004 b	1.530($\pm$0.100)	4.430($\pm$0.040)	1.19($\pm$0.07)	G0V	3.30($\pm$1.30)
HD 16417 b	0.069($\pm$0.007)	0.140($\pm$0.010)	1.18($\pm$0.04)	G1V	4.30($\pm$0.80)
HD 165155 b	2.890($\pm$0.230)	1.130($\pm$0.040)	1.02($\pm$0.05)	G8V	11.00($\pm$4.00)
HD 168443 b	7.659($\pm$0.097)	0.293($\pm$0.001)	0.99($\pm$0.01)	G5	9.80($\pm$1.00)
HD 170469 b	0.670($\pm$-)	2.240($\pm$-)	1.14($\pm$0.02)	G5IV	6.70($\pm$1.10)
HD 171028 b	1.980($\pm$-)	1.320($\pm$-)	0.99($\pm$0.08)	G0	8.00($\pm$2.00)
HD 17156 b	3.195($\pm$0.033)	0.162($\pm$0.002)	1.27($\pm$0.01)	G0	3.38($\pm$0.47)
HD 175607 b	0.028($\pm$0.003)	-	0.71($\pm$0.01)	G6V	10.32($\pm$1.58)
HD 187085 b	0.750($\pm$-)	2.050($\pm$-)	1.22($\pm$0.10)	G0 V	3.30($\pm$1.20)
HD 18742 b	2.700($\pm$0.300)	1.920($\pm$0.050)	1.60($\pm$0.11)	G9IV	2.30($\pm$0.50)
HD 188015 b	1.260($\pm$-)	1.190($\pm$-)	1.09($\pm$-)	G5IV	6.20($\pm$2.32)
HD 20794 b	0.008($\pm$0.001)	0.120($\pm$0.002)	0.85($\pm$0.04)	G8V	14.00($\pm$5.00)
HD 20794 c	0.007($\pm$0.001)	0.203($\pm$0.003)	0.85($\pm$0.04)	G8V	14.00($\pm$5.00)
HD 20794 d	0.015($\pm$0.002)	0.349($\pm$0.006)	0.85($\pm$0.04)	G8V	14.00($\pm$5.00)
HD 209458 b	0.690($\pm$0.017)	0.047($\pm$0.000)	1.14($\pm$0.02)	G0V	4.00($\pm$2.00)
HD 212771 b	2.300($\pm$0.400)	1.220($\pm$0.300)	1.15($\pm$0.08)	G8IV	6.00($\pm$2.00)
HD 219077 b	10.390($\pm$0.090)	6.220($\pm$0.090)	1.05($\pm$0.02)	G8V	8.90($\pm$0.30)
HD 219828 b	0.066($\pm$0.004)	0.045($\pm$-)	1.24($\pm$-)	G0IV	5.80($\pm$1.20)
HD 221585 b	1.610($\pm$0.140)	2.306($\pm$0.081)	1.19($\pm$0.12)	G8IV	6.20($\pm$0.50)
HD 222155 b	1.900($\pm$0.530)	5.100($\pm$0.700)	1.13($\pm$0.11)	G2V	8.20($\pm$0.70)
HD 224693 b	0.710($\pm$-)	0.2339($\pm$-)	1.33($\pm$0.10)	G2IV	2.00($\pm$0.50)
HD 24040 b	4.010($\pm$0.490)	4.920($\pm$0.380)	1.18($\pm$-)	G0	6.68($\pm$1.52)
HD 30177 b	8.070($\pm$0.120)	3.580($\pm$0.010)	1.05($\pm$0.08)	G8 V	11.60($\pm$2.20)
HD 30177 c	3.000($\pm$0.300)	6.990($\pm$0.420)	1.05($\pm$0.08)	G8 V	11.60($\pm$2.20)
HD 34445 b	0.790($\pm$0.070)	2.070($\pm$0.020)	1.07($\pm$0.02)	G0	8.50($\pm$2.00)
HD 38529 b	0.930($\pm$0.110)	0.131($\pm$0.001)	1.48($\pm$0.05)	G4 IV	3.28($\pm$0.30)
HD 4308 b	0.040($\pm$0.005)	0.118($\pm$0.009)	0.85($\pm$-)	G5 V	7.10($\pm$3.00)
HD 4313 b	2.300($\pm$0.200)	1.190($\pm$0.030)	1.72($\pm$0.12)	G5 D	2.00($\pm$0.50)
HD 43691 b	2.490($\pm$-)	0.240($\pm$-)	1.38($\pm$0.05)	G0IV	2.80($\pm$0.80)
HD 5319 b	1.940($\pm$-)	1.750($\pm$-)	1.56($\pm$0.18)	G5IV	2.40($\pm$0.68)
HD 5319 c	1.150($\pm$0.080)	2.071($\pm$0.013)	1.56($\pm$0.18)	G5IV	2.40($\pm$0.68)
HD 72659 b	3.150($\pm$0.140)	4.740($\pm$0.080)	0.95($\pm$2.00)	G2 V	6.50($\pm$1.50)

Table 1 Continue...

Name	M_p (M$_J$)	a (AU)	$M_\star$ (M$_\odot$)	Spectral Type	$T_\star$ (Gyrs)
HD 72892 b	5.450($\pm$0.370)	0.228($\pm$0.008)	1.02($\pm$0.05)	G5V	8.00($\pm$3.00)
HD 74156 b	1.778($\pm$0.020)	0.291($\pm$0.003)	1.24($\pm$0.04)	G1V	3.70($\pm$0.40)
HD 74156 c	7.997($\pm$0.095)	3.820($\pm$0.044)	1.24($\pm$0.04)	G1V	3.70($\pm$0.40)
HD 75898 b	2.510($\pm$-)	1.190($\pm$-)	1.28($\pm$0.13)	G0	3.80($\pm$0.80)
HD 82886 b	1.300($\pm$0.100)	1.650($\pm$0.060)	1.06($\pm$0.07)	G0	7.00($\pm$2.00)
HD 9174 b	1.110($\pm$0.140)	2.200($\pm$0.090)	1.03($\pm$0.05)	G8IV	9.00($\pm$3.00)
HD 96167 b	0.680($\pm$0.180)	1.300($\pm$0.070)	1.31($\pm$0.09)	G5D	3.80($\pm$1.00)
HIP 11915	0.990($\pm$0.060)	4.800($\pm$0.100)	1.00($\pm$-)	G5V	4.00($\pm$0.60)
HIP 68468 b	0.011($\pm$-)	0.029($\pm$-)	1.05($\pm$0.01)	G3V	5.90($\pm$0.40)
HIP 68468 c	0.094($\pm$-)	0.665($\pm$-)	1.05($\pm$0.01)	G3V	5.90($\pm$0.40)
K2-24 b	0.066($\pm$0.017)	0.154($\pm$0.002)	1.12($\pm$0.05)	G9V	5.00($\pm$1.80)
K2-24 c	0.085($\pm$0.022)	0.247($\pm$0.004)	1.12($\pm$0.05)	G9V	5.00($\pm$1.80)
K2-60 b	0.426($\pm$0.037)	0.045($\pm$0.003)	0.97($\pm$0.07)	G4V	10.00($\pm$3.00)
K2-99 b	0.970($\pm$0.090)	0.159($\pm$0.006)	1.60($\pm$0.10)	G0IV	2.40($\pm$0.60)
KELT-8 b	0.874($\pm$0.066)	0.045($\pm$0.009)	1.21($\pm$0.06)	G2V	5.40($\pm$0.50)
Kepler-10 b	0.010($\pm$0.001)	0.016($\pm$0.000)	0.91($\pm$0.02)	G	10.60($\pm$1.50)
Kepler-10 c	0.054($\pm$0.005)	0.241($\pm$0.001)	0.91($\pm$0.02)	G	10.60($\pm$1.50)
Kepler-11 b	0.005($\pm$0.003)	0.091($\pm$0.003)	0.95($\pm$0.10)	G	8.00($\pm$2.00)
Kepler-11 c	0.009($\pm$0.005)	0.106($\pm$0.004)	0.95($\pm$0.10)	G	8.00($\pm$2.00)
Kepler-11 d	0.022($\pm$0.004)	0.159($\pm$0.005)	0.95($\pm$0.10)	G	8.00($\pm$2.00)
Kepler-11 e	0.030($\pm$0.006)	0.194($\pm$0.007)	0.95($\pm$0.10)	G	8.00($\pm$2.00)
Kepler-11 f	0.006($\pm$0.002)	0.250($\pm$0.009)	0.95($\pm$0.10)	G	8.00($\pm$2.00)
Kepler-11 g	0.950($\pm$0.950)	0.462($\pm$0.016)	0.95($\pm$0.10)	G	8.00($\pm$2.00)
Kepler-12 b	0.431($\pm$0.041)	0.055($\pm$0.001)	1.16($\pm$0.05)	G0	4.00($\pm$0.40)
Kepler-20 b	0.030($\pm$0.004)	0.046($\pm$0.001)	0.91($\pm$0.03)	G8	8.80($\pm$2.70)
Kepler-20 c	0.040($\pm$0.007)	0.094($\pm$0.002)	0.91($\pm$0.03)	G8	8.80($\pm$2.70)
Kepler-20 d	0.031($\pm$0.011)	0.350($\pm$0.010)	0.91($\pm$0.03)	G8	8.80($\pm$2.70)
Kepler-20 e	0.009($\pm$-)	0.063($\pm$0.001)	0.91($\pm$0.03)	G8	8.80($\pm$2.70)
Kepler-20 f	0.045($\pm$-)	0.139($\pm$0.003)	0.91($\pm$0.03)	G8	8.80($\pm$2.70)
Kepler-20 g	0.062($\pm$0.011)	0.205($\pm$0.002)	0.91($\pm$0.03)	G8	8.80($\pm$2.70)
Kepler-4 b	0.082($\pm$0.012)	0.045($\pm$0.001)	1.22($\pm$0.09)	G0	4.50($\pm$1.50)
Kepler-41 b	0.490($\pm$0.090)	0.029($\pm$0.001)	0.94($\pm$0.09)	G2V	7.40($\pm$3.40)
Kepler-412 b	0.939($\pm$0.085)	0.029($\pm$0.001)	1.16($\pm$0.09)	G3V	5.10($\pm$1.70)
Kepler-43 b	3.230($\pm$0.190)	0.044($\pm$0.001)	1.32($\pm$0.09)	G0V	2.80($\pm$0.80)
Kepler-44 b	1.020($\pm$0.070)	0.045($\pm$0.001)	1.19($\pm$0.10)	G2IV	6.95($\pm$1.70)
Kepler-66 b	0.310($\pm$0.070)	0.135($\pm$0.001)	1.03($\pm$0.04)	G0V	1.00($\pm$0.17)
Kepler-67 b	0.310($\pm$0.060)	0.117($\pm$0.001)	0.86($\pm$0.03)	G9V	1.00($\pm$0.17)
Kepler-75 b	9.900($\pm$0.500)	0.080($\pm$0.005)	0.88($\pm$0.06)	G8V	6.00($\pm$3.00)
Kepler-77 b	0.430($\pm$0.032)	0.045($\pm$0.001)	0.95($\pm$0.04)	G5V	7.50($\pm$2.00)
Pr 0211 b	1.880($\pm$0.020)	0.031($\pm$0.001)	0.93($\pm$0.01)	G9	0.79($\pm$0.03)
Pr 0211 c	7.950($\pm$0.250)	5.800($\pm$1.400)	0.93($\pm$0.01)	G9	0.79($\pm$0.03)
WASP-102 b	0.624($\pm$0.045)	0.040($\pm$0.000)	1.16($\pm$0.03)	G0	0.60($\pm$0.30)
WASP-110 b	0.515($\pm$0.064)	0.045($\pm$0.001)	0.89($\pm$0.07)	G9	8.60($\pm$3.50)
WASP-112 b	0.880($\pm$0.120)	0.038($\pm$0.001)	0.80($\pm$0.07)	G6	10.60($\pm$3.00)
WASP-119 b	1.230($\pm$0.083)	0.036($\pm$0.001)	1.02($\pm$0.06)	G5	8.00($\pm$2.50)

Table 1 Continue...

Name	M_p (M$_J$)	a (AU)	$M_\star$ (M$_\odot$)	Spectral Type	$T_\star$ (Gyrs)
WASP-12 b	1.404($\pm$0.099)	0.022($\pm$0.001)	1.35($\pm$0.14)	G0	1.70($\pm$0.80)
WASP-126 b	0.280($\pm$0.040)	0.044($\pm$0.001)	1.12($\pm$0.06)	G2	6.40($\pm$1.60)
WASP-127 b	0.180($\pm$0.020)	0.052($\pm$0.001)	1.08($\pm$0.03)	G5	11.41($\pm$1.80)
WASP-133 b	1.160($\pm$0.090)	0.034($\pm$0.001)	1.16($\pm$0.08)	G4	6.80($\pm$1.80)
WASP-157 b	0.576($\pm$0.093)	0.052($\pm$0.001)	1.26($\pm$0.12)	G2V	1.00($\pm$0.30)
WASP-19 b	1.114($\pm$0.040)	0.016($\pm$0.000)	0.90($\pm$0.04)	G8V	11.50($\pm$2.70)
WASP-26 b	1.028($\pm$0.021)	0.039($\pm$0.000)	1.12($\pm$0.03)	G0	6.00($\pm$2.00)
WASP-37 b	1.800($\pm$0.170)	0.043($\pm$0.001)	0.84($\pm$0.04)	G2	11.00($\pm$4.00)
WASP-46 b	2.101($\pm$0.073)	0.024($\pm$0.000)	0.95($\pm$0.03)	G6V	1.40($\pm$0.60)
WASP-5 b	1.637($\pm$0.082)	0.027($\pm$0.000)	1.00($\pm$0.06)	G5	3.00($\pm$1.40)
WASP-8 b	2.244($\pm$0.093)	0.080($\pm$0.001)	1.03($\pm$0.05)	G6	4.00($\pm$1.00)
WASP-95 b	1.130($\pm$0.040)	0.034($\pm$0.001)	1.11($\pm$0.09)	G2	2.40($\pm$1.00)
XO-1 b	0.900($\pm$0.070)	0.048($\pm$0.000)	1.00($\pm$0.03)	G1V	4.50($\pm$2.00)
XO-5 b	1.077($\pm$0.037)	0.048($\pm$0.000)	0.88($\pm$0.03)	G8V	8.50($\pm$0.80)

Table 2 Physical And Orbital Characteristics of The Host Stars And Their Exoplanets That are Used in Chapter 5.

Name	M_p (M_J)	a (AU)	e	$M_\star$ ($M_\odot$)	$R_\star$ ($R_\odot$)
18 Del b	10.300($\pm$1.030)	2.600	0.080	2.300($\pm$0.115)	8.500($\pm$0.850)
24 Sex b	1.990($\pm$0.320)	1.333	0.090	1.540($\pm$0.080)	4.900($\pm$0.080)
24 Sex c	0.860($\pm$0.285)	2.080	0.290	1.540($\pm$0.080)	4.900($\pm$0.080)
47 Uma b	2.530($\pm$0.065)	2.100	0.032	1.030($\pm$0.050)	1.240($\pm$0.040)
47 Uma c	0.540($\pm$0.069)	3.600	0.098	1.030($\pm$0.050)	1.240($\pm$0.040)
47 Uma d	1.640($\pm$0.385)	11.600	0.160	1.030($\pm$0.050)	1.240($\pm$0.040)
51 Peg b	0.468($\pm$0.007)	0.052	0.006	1.110($\pm$0.060)	1.266($\pm$0.046)
61 Vir b	0.016($\pm$0.001)	0.050	0.120	0.950($\pm$0.030)	0.940($\pm$0.029)
61 Vir c	0.057($\pm$0.003)	0.217	0.140	0.950($\pm$0.030)	0.940($\pm$0.029)
61 Vir d	0.072($\pm$0.008)	0.476	0.350	0.950($\pm$0.030)	0.940($\pm$0.029)
70 Vir b	6.600($\pm$0.660)	0.480	0.430	0.920($\pm$0.046)	1.968($\pm$0.047)
75 Cet b	3.000($\pm$0.300)	2.100	-	2.490($\pm$0.023)	10.500($\pm$1.000)
81 Cet b	5.300($\pm$0.530)	2.500	0.206	2.400($\pm$0.400)	11.000($\pm$0.100)
BD-10 3166 b	0.460($\pm$0.046)	0.046	0.010	0.990($\pm$0.049)	1.710($\pm$0.171)
CoRoT-1 b	1.030($\pm$0.120)	0.025	0	0.950($\pm$0.150)	1.110($\pm$0.050)
CoRoT-12 b	0.917($\pm$0.067)	0.040	0.070	1.078($\pm$0.072)	1.116($\pm$0.092)
CoRoT-13 b	1.308($\pm$0.066)	0.051	0	1.090($\pm$0.020)	1.010($\pm$0.030)
CoRoT-16 b	0.535($\pm$0.085)	0.061	0.330	1.098($\pm$0.078)	1.190($\pm$0.140)
CoRoT-17 b	2.430($\pm$0.160)	0.046	0	1.040($\pm$0.100)	1.590($\pm$0.070)
CoRoT-18 b	3.470($\pm$0.380)	0.029	0.080	0.950($\pm$0.150)	1.000($\pm$0.130)
CoRoT-2 b	3.310($\pm$0.160)	0.028	0	0.970($\pm$0.060)	0.902($\pm$0.018)
CoRoT-20 b	4.240($\pm$0.230)	0.090	0.562	1.140($\pm$0.080)	0.920($\pm$0.092)
CoRoT-22 b	0.038($\pm$0.035)	0.092	0.077	1.099($\pm$0.049)	1.136($\pm$0.064)
CoRoT-23 b	2.800($\pm$0.250)	0.047	0.160	1.140($\pm$0.080)	1.610($\pm$0.180)
CoRoT-25 b	0.270($\pm$0.040)	0.057	-	1.090($\pm$0.080)	1.190($\pm$0.085)
CoRoT-26 b	0.520($\pm$0.050)	0.052	0	1.090($\pm$0.060)	1.790($\pm$0.120)
CoRoT-27 b	10.390($\pm$0.550)	0.047	0.065	1.050($\pm$0.110)	1.080($\pm$0.120)
CoRoT-9 b	0.840($\pm$0.070)	0.407	0.110	0.990($\pm$0.040)	0.940($\pm$0.040)
GJ 3021 b	3.370($\pm$0.090)	0.490	0.511	0.900($\pm$0.045)	0.900($\pm$0.090)
HAT-P-1 b	0.525($\pm$0.019)	0.055	0.061	1.151($\pm$0.052)	1.174($\pm$0.030)
HAT-P-13 b	0.850($\pm$0.038)	0.042	0.014	1.220($\pm$0.100)	1.560($\pm$0.080)
HAT-P-15 b	1.946($\pm$0.066)	0.096	0.190	1.013($\pm$0.043)	1.080($\pm$0.043)
HAT-P-21 b	4.063($\pm$0.161)	0.049	0.228	0.947($\pm$0.042)	1.105($\pm$0.083)
HAT-P-22 b	2.147($\pm$0.061)	0.041	0.016	0.916($\pm$0.035)	1.040($\pm$0.044)
HAT-P-23 b	2.090($\pm$0.110)	0.023	0.106	1.130($\pm$0.050)	1.290($\pm$0.050)
HAT-P-25 b	0.567($\pm$0.056)	0.046	0.032	1.010($\pm$0.032)	0.959($\pm$0.037)
HAT-P-27 b	0.660($\pm$0.033)	0.040	0.078	0.945($\pm$0.035)	0.898($\pm$0.039)
HAT-P-28 b	0.626($\pm$0.037)	0.043	0.051	1.025($\pm$0.047)	1.103($\pm$0.069)
HAT-P-38 b	0.267($\pm$0.020)	0.052	0.067	0.886($\pm$0.044)	0.923($\pm$0.067)
HD 100655 b	1.700($\pm$0.150)	0.760	0.085	2.400($\pm$0.400)	9.300($\pm$1.100)
HD 102117 b	0.172($\pm$0.018)	0.153	0.106	1.030($\pm$0.050)	1.270($\pm$0.127)
HD 104985 b	6.300($\pm$0.630)	0.780	0.030	1.600($\pm$0.080)	10.870($\pm$0.360)
HD 106252 b	7.560($\pm$0.756)	2.700	0.470	0.960($\pm$0.048)	1.090($\pm$0.109)
HD 106270 b	11.000($\pm$0.800)	4.300	0.402	1.320($\pm$0.092)	2.500($\pm$0.100)

Table 2 Continue...

Name	M_p	a	e	$M_\star$	$R_\star$
	(M_J)	(AU)		$(M_\odot)$	$(R_\odot)$
HD 10697 b	6.380($\pm$0.530)	2.160	0.100	1.150($\pm$0.030)	1.720($\pm$0.170)
HD 108874 b	1.360($\pm$0.130)	1.051	0.070	1.000($\pm$0.050)	1.220($\pm$0.122)
HD 108874 c	1.018($\pm$0.300)	2.680	0.250	1.000($\pm$0.050)	1.220($\pm$0.122)
HD 109246 b	0.770($\pm$0.090)	0.330	0.120	1.010($\pm$0.110)	1.020($\pm$0.070)
HD 114729 b	0.840($\pm$0.084)	2.080	0.320	0.930($\pm$0.046)	1.460($\pm$0.146)
HD 11506 b	3.440($\pm$0.685)	2.430	0.220	1.190($\pm$0.020)	1.380($\pm$0.050)
HD 11506 c	0.820($\pm$0.405)	0.639	0.420	1.190($\pm$0.020)	1.380($\pm$0.050)
HD 117207 b	2.060($\pm$0.206)	3.780	0.160	1.070($\pm$0.053)	1.090($\pm$0.109)
HD 117618 b	0.178($\pm$0.020)	0.176	0.420	1.050($\pm$0.052)	1.190($\pm$0.119)
HD 117618 c	0.200($\pm$0.100)	0.930	0	1.050($\pm$0.052)	1.190($\pm$0.119)
HD 11964 b	0.622($\pm$0.056)	3.160	0.041	1.125($\pm$0.056)	2.180($\pm$0.290)
HD 11964 c	0.079($\pm$0.010)	0.229	0.300	1.125($\pm$0.056)	2.180($\pm$0.290)
HD 11977 b	6.540($\pm$0.654)	1.930	0.400	1.910($\pm$0.210)	13.000($\pm$1.300)
HD 120084 b	4.500($\pm$0.450)	4.300	0.660	2.390($\pm$0.060)	9.120($\pm$0.650)
HD 125612 b	3.000($\pm$0.300)	1.370	0.460	1.100($\pm$0.070)	1.050($\pm$0.080)
HD 125612 c	0.058($\pm$0.005)	0.050	0.270	1.100($\pm$0.070)	1.050($\pm$0.080)
HD 125612 d	7.200($\pm$0.720)	4.200	0.280	1.100($\pm$0.070)	1.050($\pm$0.080)
HD 12661 b	2.300($\pm$0.230)	0.830	0.377	1.070($\pm$0.053)	1.120($\pm$0.112)
HD 12661 c	1.570($\pm$0.157)	2.560	0.031	1.070($\pm$0.053)	1.120($\pm$0.112)
HD 134987 b	1.590($\pm$0.020)	0.810	0.233	1.070($\pm$0.080)	1.250($\pm$0.040)
HD 134987 c	0.820($\pm$0.030)	5.800	0.120	1.070($\pm$0.080)	1.250($\pm$0.040)
HD 136418 b	2.000($\pm$0.100)	1.320	0.255	1.330($\pm$0.090)	3.400($\pm$0.100)
HD 13931 b	1.880($\pm$0.150)	5.150	0.020	1.020($\pm$0.020)	1.230($\pm$0.060)
HD 14067 b	7.800($\pm$0.700)	3.400	0.530	2.400($\pm$0.200)	12.400($\pm$1.100)
HD 141937 b	9.700($\pm$0.970)	1.520	0.410	1.100($\pm$0.055)	1.060($\pm$0.106)
HD 142 b	1.250($\pm$0.150)	1.020	0.170	1.100($\pm$0.220)	0.860($\pm$0.040)
HD 142 c	5.300($\pm$0.700)	6.800	0.210	1.100($\pm$0.220)	0.860($\pm$0.040)
HD 142415 b	1.620($\pm$0.162)	1.050	0.500	1.090($\pm$0.054)	1.030($\pm$0.103)
HD 145377 b	5.760($\pm$0.100)	0.450	0.307	1.120($\pm$0.030)	1.140($\pm$0.114)
HD 1461 b	0.023($\pm$0.003)	0.063	0.140	1.080($\pm$0.040)	1.095($\pm$0.026)
HD 1461 c	0.018($\pm$0.002)	0.111	0	1.080($\pm$0.040)	1.095($\pm$0.026)
HD 147513 b	1.210($\pm$0.121)	1.320	0.260	0.920($\pm$0.046)	1.000($\pm$0.100)
HD 149026 b	0.356($\pm$0.012)	0.042	0	1.300($\pm$0.100)	1.497($\pm$0.069)
HD 150706 b	2.710($\pm$0.900)	6.700	0.380	0.940($\pm$0.800)	0.870($\pm$0.087)
HD 154672 b	5.020($\pm$0.170)	0.600	0.610	1.060($\pm$0.090)	1.270($\pm$0.090)
HD 154857 b	2.240($\pm$0.050)	1.291	0.460	1.718($\pm$0.026)	1.760($\pm$0.057)
HD 154857 c	2.580($\pm$0.160)	5.360	0.060	1.718($\pm$0.026)	1.760($\pm$0.057)
HD 16141 b	0.215($\pm$0.030)	0.350	0.280	1.010($\pm$0.050)	1.000($\pm$0.100)
HD 16175 b	4.400($\pm$0.440)	2.100	0.590	1.350($\pm$0.090)	1.870($\pm$0.040)
HD 163607 b	0.770($\pm$0.040)	0.360	0.730	1.090($\pm$0.020)	1.630($\pm$0.700)
HD 163607 c	2.290($\pm$0.160)	2.420	0.120	1.090($\pm$0.020)	1.630($\pm$0.700)
HD 164509 b	0.480($\pm$0.090)	0.875	0.260	1.130($\pm$0.020)	1.060($\pm$0.030)
HD 168443 b	7.659($\pm$0.097)	0.293	0.528	0.995($\pm$0.019)	1.510($\pm$0.060)
HD 168746 b	0.230($\pm$0.023)	0.065	0.081	0.880($\pm$0.010)	1.120($\pm$0.112)
HD 170469 b	0.670($\pm$0.067)	2.240	0.110	1.140($\pm$0.020)	1.220($\pm$0.070)
HD 171028 b	1.980($\pm$0.198)	1.320	0.590	0.990($\pm$0.080)	1.950($\pm$0.260)

Table 2 Continue...

Name	M_p (M_J)	a (AU)	e	$M_\star$ $(M_\odot)$	$R_\star$ $(R_\odot)$
HD 17156 b	3.191(±0.033)	0.162	0.676	1.275(±0.018)	1.508(±0.021)
HD 173416 b	2.700(±0.300)	1.160	0.210	2.000(±0.300)	13.500(±0.900)
HD 175541 b	0.610(±0.061)	1.030	0.330	1.650(±0.082)	3.850(±0.385)
HD 179079 b	0.080(±0.008)	0.110	0.115	1.087(±0.100)	1.480(±0.148)
HD 183263 b	3.670(±0.300)	1.510	0.357	1.170(±0.058)	1.210(±0.121)
HD 183263 c	3.820(±0.590)	4.250	0.253	1.170(±0.058)	1.210(±0.121)
HD 185269 b	0.940(±0.094)	0.077	0.300	1.280(±0.100)	1.880(±0.100)
HD 187123 b	0.520(±0.040)	0.042	0.010	1.060(±0.053)	1.170(±0.117)
HD 187123 c	1.990(±0.250)	4.890	0.252	1.060(±0.053)	1.170(±0.117)
HD 18742 b	2.700(±0.300)	1.920	0.230	1.600(±0.110)	4.900(±0.100)
HD 188015 b	1.260(±0.126)	1.190	0.150	1.090(±0.054)	1.100(±0.110)
HD 190360 b	1.502(±0.130)	3.920	0.360	1.040(±0.052)	1.200(±0.033)
HD 190360 c	0.057(±0.015)	0.128	0.010	1.040(±0.052)	1.200(±0.033)
HD 192699 b	2.500(±0.250)	1.160	0.149	1.680(±0.120)	4.250(±0.510)
HD 195019 b	3.700(±0.300)	0.138	0.014	1.060(±0.053)	1.380(±0.138)
HD 196050 b	2.830(±0.283)	2.470	0.210	1.170(±0.058)	1.290(±0.129)
HD 202206 c	2.440(±0.244)	2.550	0.267	1.130(±0.056)	1.020(±0.102)
HD 20367 b	1.070(±0.107)	1.250	0.230	1.040(±0.060)	1.180(±0.320)
HD 2039 b	4.900(±1.000)	2.200	0.670	0.980(±0.050)	1.210(±0.121)
HD 207832 b	0.560(±0.045)	0.570	0.130	0.940(±0.100)	0.901(±0.056)
HD 207832 c	0.730(±0.115)	2.112	0.270	0.940(±0.100)	0.901(±0.056)
HD 20794 b	0.008(±0.0009)	0.120	0	0.850(±0.040)	0.900(±0.030)
HD 20794 c	0.007(±0.0013)	0.203	0	0.850(±0.040)	0.900(±0.030)
HD 20794 d	0.015(±0.0019)	0.349	0	0.850(±0.040)	0.900(±0.030)
HD 208487 b	0.413(±0.050)	0.510	0.210	1.300(±0.065)	1.150(±0.115)
HD 209458 b	0.690(±0.017)	0.047	0.008	1.148(±0.022)	1.203(±0.061)
HD 210277 b	1.230(±0.030)	1.100	0.472	1.090(±0.054)	1.100(±0.050)
HD 212771 b	2.300(±0.400)	1.220	0.111	1.150(±0.080)	5.000(±0.100)
HD 213240 b	4.500(±0.450)	2.030	0.450	1.220(±0.061)	1.500(±0.150)
HD 216435 b	1.260(±0.130)	2.560	0.070	1.300	2.000
HD 216437 b	1.820(±0.182)	2.320	0.290	1.060(±0.053)	1.100(±0.110)
HD 217107 b	1.330(±0.050)	0.073	0.132	1.020(±0.051)	1.080(±0.108)
HD 217107 c	2.490(±0.250)	5.270	0.517	1.020(±0.051)	1.080(±0.108)
HD 219828 b	0.085(±0.008)	0.052	0	1.240(±0.062)	1.700(±0.160)
HD 222155 b	1.900(±0.600)	5.100	0.160	1.130(±0.110)	1.670(±0.700)
HD 222582 b	7.750(±0.650)	1.350	0.725	0.990(±0.049)	1.150(±0.115)
HD 224693 b	0.710(±0.071)	0.233	0.050	1.330(±0.100)	1.700(±0.300)
HD 28185 b	5.700(±0.570)	1.030	0.070	1.240(±0.062)	1.030(±0.103)
HD 28254 b	1.160(±0.080)	2.150	0.810	1.060(±0.053)	1.480(±0.060)
HD 290327 b	2.540(±0.155)	3.430	0.080	0.900(±0.045)	1.000(±0.010)
HD 30177 b	7.700(±1.500)	2.600	0.220	0.950(±0.050)	1.120(±0.112)
HD 30669	0.470(±0.060)	2.690	0.180	0.920(±0.030)	0.910(±0.040)
HD 33283 b	0.330(±0.033)	0.168	0.458	1.240(±0.100)	1.200(±0.100)
HD 34445 b	0.790(±0.070)	2.070	0.270	1.070(±0.020)	1.380(±0.080)
HD 37124 b	0.675(±0.017)	0.533	0.054	0.830(±0.041)	0.820(±0.082)

Table 2 Continue...

Name	M_p	a	e	$M_\star$	$R_\star$
	(M_J)	(AU)		$(M_\odot)$	$(R_\odot)$
HD 37124 c	0.652($\pm$0.052)	1.710	0.125	0.830($\pm$0.041)	0.820($\pm$0.082)
HD 37124 d	0.696($\pm$0.059)	2.807	0.160	0.830($\pm$0.041)	0.820($\pm$0.082)
HD 38529 b	0.780($\pm$0.078)	0.131	0.248	1.480($\pm$0.050)	2.440($\pm$0.220)
HD 39091 b	10.300($\pm$1.030)	3.280	0.610	1.100($\pm$0.055)	2.100($\pm$0.600)
HD 4203 b	1.820($\pm$0.050)	1.164	0.520	1.130($\pm$0.056)	1.330($\pm$0.133)
HD 4208 b	0.800($\pm$0.080)	1.700	0.040	0.870($\pm$0.043)	0.850($\pm$0.085)
HD 4308 b	0.040($\pm$0.005)	0.118	0.270	0.850($\pm$0.042)	0.920($\pm$0.092)
HD 4313 b	2.300($\pm$0.200)	1.19	0.041	1.720($\pm$0.120)	4.900($\pm$0.100)
HD 43197 b	0.600($\pm$0.080)	0.920	0.830	0.960($\pm$0.048)	1.000($\pm$0.001)
HD 44219 b	0.580($\pm$0.050)	1.190	0.610	1.000($\pm$0.050)	1.320($\pm$0.070)
HD 45350 b	1.790($\pm$0.140)	1.920	0.778	1.020($\pm$0.051)	1.270($\pm$0.127)
HD 49674 b	0.100($\pm$0.010)	0.058	0.049	1.070($\pm$0.053)	0.940($\pm$0.094)
HD 50499 b	1.710($\pm$0.200)	3.860	0.230	1.270($\pm$0.063)	1.380($\pm$0.138)
HD 52265 b	1.050($\pm$0.030)	0.500	0.350	1.200($\pm$0.060)	1.250($\pm$0.125)
HD 52265 c	0.350($\pm$0.090)	0.316	0.050	1.200($\pm$0.060)	1.250($\pm$0.125)
HD 5319 b	1.940($\pm$0.194)	1.750	0.120	1.560($\pm$0.180)	3.260($\pm$0.410)
HD 564 b	0.330($\pm$0.030)	1.200	0.096	0.920($\pm$0.030)	1.010($\pm$0.050)
HD 5891 b	7.600($\pm$0.400)	0.760	0.066	1.910($\pm$0.130)	8.700($\pm$0.200)
HD 6434 b	0.390($\pm$0.039)	0.140	0.170	0.790($\pm$0.039)	0.570($\pm$0.057)
HD 6718 b	1.560($\pm$0.105)	3.560	0.100	0.960($\pm$0.048)	1.020($\pm$0.030)
HD 68988 b	1.900($\pm$0.190)	0.071	0.140	1.200($\pm$0.060)	1.140($\pm$0.114)
HD 70642 b	2.000($\pm$0.200)	3.300	0.100	1.000($\pm$0.050)	0.840($\pm$0.084)
HD 72659 b	3.150($\pm$0.140)	4.740	0.220	0.950($\pm$2.000)	1.360($\pm$0.060)
HD 73267 b	3.060($\pm$0.070)	2.198	0.256	0.890($\pm$0.030)	1.040($\pm$0.104)
HD 73526 b	2.900($\pm$0.200)	0.660	0.190	1.080($\pm$0.050)	1.490($\pm$0.149)
HD 73526 c	2.500($\pm$0.300)	1.050	0.140	1.080($\pm$0.050)	1.490($\pm$0.149)
HD 73534 b	1.150($\pm$0.115)	3.150	0.046	1.290($\pm$0.100)	2.650($\pm$0.100)
HD 74156 b	1.880($\pm$0.030)	0.294	0.640	1.240($\pm$0.040)	1.640($\pm$0.190)
HD 74156 c	8.030($\pm$0.120)	3.400	0.340	1.240($\pm$0.040)	1.640($\pm$0.190)
HD 75289 b	0.470($\pm$0.047)	0.046	0.021	1.050($\pm$0.052)	1.250($\pm$0.125)
HD 75898 b	2.510($\pm$0.251)	1.190	0.100	1.280($\pm$0.130)	1.600($\pm$0.180)
HD 76700 b	0.230($\pm$0.023)	0.049	0.061	1.000($\pm$0.050)	1.330($\pm$0.133)
HD 80606 b	3.940($\pm$0.110)	0.449	0.930	0.980($\pm$0.100)	0.980($\pm$0.070)
HD 81040 b	6.860($\pm$0.710)	1.940	0.526	0.960($\pm$0.040)	0.860($\pm$0.040)
HD 82886 b	1.300($\pm$0.100)	1.650	0.270	1.060($\pm$0.074)	4.800($\pm$0.100)
HD 82943 b	4.800($\pm$0.480)	1.190	0.203	1.180($\pm$0.059)	1.120($\pm$0.112)
HD 82943 c	4.780($\pm$0.478)	0.746	0.425	1.180($\pm$0.059)	1.120($\pm$0.112)
HD 82943 d	0.290($\pm$0.031)	2.145	0	1.180($\pm$0.059)	1.120($\pm$0.112)
HD 8535 b	0.680($\pm$0.055)	2.450	0.150	1.130($\pm$0.056)	1.190($\pm$0.040)
HD 88133 b	0.300($\pm$0.030)	0.047	0.076	1.200($\pm$0.200)	1.930($\pm$0.193)
HD 89307 b	2.000($\pm$0.400)	3.340	0.250	1.028($\pm$0.040)	1.050($\pm$0.040)
HD 92788 b	3.860($\pm$0.386)	0.970	0.334	1.130($\pm$0.056)	0.990($\pm$0.099)
HD 92788 c	0.900($\pm$0.300)	0.600	0.040	1.130($\pm$0.056)	0.990($\pm$0.099)
HD 9446 b	0.700($\pm$0.060)	0.189	0.200	1.000($\pm$0.100)	1.000($\pm$0.100)
HD 9446 c	1.820($\pm$0.170)	0.654	0.060	1.000($\pm$0.100)	1.000($\pm$0.100)
HD 96167 b	0.680($\pm$0.180)	1.300	0.710	1.310($\pm$0.090)	1.860($\pm$0.070)

Table 2 Continue...

Name	M_p	a	e	$M_\star$	$R_\star$
	(M_J)	(AU)		$(M_\odot)$	$(R_\odot)$
HIP 14810 b	3.880($\pm$0.320)	0.069	0.142	0.990($\pm$0.040)	1.000($\pm$0.060)
HIP 14810 c	1.280($\pm$0.100)	0.545	0.164	0.990($\pm$0.040)	1.000($\pm$0.060)
HIP 14810 d	0.570($\pm$0.052)	1.890	0.173	0.990($\pm$0.040)	1.000($\pm$0.060)
HR 810 b	2.260($\pm$0.180)	0.925	0.161	1.110($\pm$0.070)	1.850($\pm$0.850)
Kepler-10 b	0.010($\pm$0.001)	0.016	0.060	0.910($\pm$0.021)	1.065($\pm$0.009)
Kepler-10 c	0.054($\pm$0.005)	0.241	0.050	0.910($\pm$0.021)	1.065($\pm$0.009)
Kepler-11 b	0.005($\pm$0.003)	0.091	0	0.950($\pm$0.100)	1.100($\pm$0.100)
Kepler-11 c	0.009($\pm$0.007)	0.106	0	0.950($\pm$0.100)	1.100($\pm$0.100)
Kepler-11 d	0.022($\pm$0.003)	0.159	0	0.950($\pm$0.100)	1.100($\pm$0.100)
Kepler-11 e	0.030($\pm$0.005)	0.194	0	0.950($\pm$0.100)	1.100($\pm$0.100)
Kepler-11 f	0.006($\pm$0.002)	0.250	0	0.950($\pm$0.100)	1.100($\pm$0.100)
Kepler-11 g	0.950($\pm$0.475)	0.462	0	0.950($\pm$0.100)	1.100($\pm$0.100)
Kepler-12 b	0.431($\pm$0.041)	0.055	0.010	1.166($\pm$0.054)	1.483($\pm$0.029)
Kepler-17 b	2.450($\pm$0.014)	0.025	0.011	1.160($\pm$0.060)	1.050($\pm$0.030)
Kepler-20 b	0.026($\pm$0.006)	0.045	0.320	0.912($\pm$0.035)	0.944($\pm$0.095)
Kepler-20 c	0.049($\pm$0.007)	0.093	0.400	0.912($\pm$0.035)	0.944($\pm$0.095)
Kepler-20 d	0.060($\pm$0.006)	0.345	0.600	0.912($\pm$0.035)	0.944($\pm$0.095)
Kepler-20 e	0.009($\pm$0.0009)	0.050	-	0.912($\pm$0.035)	0.944($\pm$0.095)
Kepler-20 f	0.045($\pm$0.004)	0.110	-	0.912($\pm$0.035)	0.944($\pm$0.095)
Kepler-22 b	0.110($\pm$0.011)	0.849	-	0.970($\pm$0.060)	0.979($\pm$0.020)
Kepler-4 b	0.082($\pm$0.0128)	0.045	0	1.223($\pm$0.091)	1.487($\pm$0.084)
Kepler-41 b	0.490($\pm$0.090)	0.029	0	0.940($\pm$0.090)	0.966($\pm$0.032)
Kepler-412 b	0.939($\pm$0.085)	0.029	0.003	1.167($\pm$0.091)	1.287($\pm$0.035)
Kepler-43 b	3.230($\pm$0.190)	0.044	0.025	1.320($\pm$0.090)	1.420($\pm$0.07)
Kepler-44 b	1.020($\pm$0.070)	0.045	0.021	1.190($\pm$0.100)	1.520($\pm$0.090)
Kepler-66 b	0.310($\pm$0.070)	0.135	-	1.038($\pm$0.051)	0.966($\pm$0.096)
Kepler-67 b	0.310($\pm$0.060)	0.117	-	0.865($\pm$0.043)	0.778($\pm$0.077)
Kepler-75 b	9.900($\pm$0.500)	0.080	0.569	0.880($\pm$0.060)	0.880($\pm$0.040)
Kepler-77 b	0.430($\pm$0.032)	0.045	0	0.950($\pm$0.040)	0.990($\pm$0.020)
Kepler-78 b	0.005($\pm$0.001)	0.010	-	0.810($\pm$0.050)	0.740($\pm$0.090)
KOI-192 b	0.290($\pm$0.090)	0.091	0.570	0.960($\pm$0.060)	1.350($\pm$0.200)
KOI-195 b	0.340($\pm$0.080)	0.041	0.180	0.910($\pm$0.060)	0.920($\pm$0.025)
ksi Aql b	2.800($\pm$0.280)	0.680	0	2.200($\pm$0.110)	12.000($\pm$1.200)
mu Ara b	1.676($\pm$0.167)	1.500	0.128	1.080($\pm$0.050)	1.245($\pm$0.255)
mu Ara c	0.033($\pm$0.003)	0.090	0.172	1.080($\pm$0.050)	1.240($\pm$0.255)
mu Ara d	0.521($\pm$0.052)	0.921	0.066	1.080($\pm$0.050)	1.240($\pm$0.255)
mu Ara e	1.814($\pm$0.181)	5.235	0.098	1.080($\pm$0.050)	1.240($\pm$0.255)
OGLE-TR-56 b	1.300($\pm$0.080)	0.022	0	1.170($\pm$0.040)	1.320($\pm$0.060)
ome Ser b	1.700($\pm$0.170)	1.100	0.106	2.170($\pm$0.250)	12.300($\pm$0.850)
omi UMa b	4.100($\pm$0.410)	3.900	-	3.090($\pm$0.070)	14.100($\pm$1.000)
TrES-2	1.253($\pm$0.052)	0.035	0	0.980($\pm$0.062)	1.000($\pm$0.036)
TrES-3	1.910($\pm$0.065)	0.022	0	0.924($\pm$0.040)	0.813($\pm$0.027)
WASP-104 b	1.272($\pm$0.047)	0.029	0	1.020($\pm$0.090)	0.930($\pm$0.230)
WASP-110 b	0.515($\pm$0.064)	0.045	0	0.892($\pm$0.072)	0.881($\pm$0.035)
WASP-112 b	0.880($\pm$0.120)	0.038	0	0.807($\pm$0.073)	1.002($\pm$0.037)

Table 2 Continue...

Name	M_p (M_J)	a (AU)	e	$M_\star$ ($M_\odot$)	$R_\star$ ($R_\odot$)
WASP-12 b	1.404($\pm$0.099)	0.022	0	1.350($\pm$0.140)	1.599($\pm$0.071)
WASP-16 b	0.855($\pm$0.059)	0.042	0	1.022($\pm$0.101)	0.946($\pm$0.054)
WASP-19 b	1.114($\pm$0.040)	0.016	0.004	0.904($\pm$0.045)	1.004($\pm$0.018)
WASP-21 b	0.300($\pm$0.010)	0.052	0	1.010($\pm$0.025)	1.060($\pm$0.040)
WASP-25 b	0.580($\pm$0.040)	0.047	0	1.000($\pm$0.030)	0.950($\pm$0.040)
WASP-26 b	1.028($\pm$0.021)	0.039	0	1.120($\pm$0.030)	1.340($\pm$0.060)
WASP-32 b	3.600($\pm$0.070)	0.039	0.018	1.100($\pm$0.030)	1.110($\pm$0.050)
WASP-34 b	0.590($\pm$0.010)	0.052	0.038	1.010($\pm$0.070)	0.930($\pm$0.093)
WASP-36 b	2.279($\pm$0.068)	0.026	0	1.020($\pm$0.032)	0.943($\pm$0.019)
WASP-37 b	1.800($\pm$0.170)	0.043	0	0.849($\pm$0.040)	0.977($\pm$0.042)
WASP-39 b	0.280($\pm$0.030)	0.048	0	0.930($\pm$0.030)	0.895($\pm$0.023)
WASP-4 b	1.237($\pm$0.060)	0.023	0	0.930($\pm$0.050)	1.150($\pm$0.280)
WASP-41 b	0.920($\pm$0.070)	0.040	0	0.950($\pm$0.090)	1.010($\pm$0.260)
WASP-44 b	0.889($\pm$0.062)	0.034	0	0.951($\pm$0.034)	0.927($\pm$0.070)
WASP-46 b	2.101($\pm$0.073)	0.024	0	0.956($\pm$0.034)	0.917($\pm$0.028)
WASP-47 b	1.140($\pm$0.050)	0.052	0	1.084($\pm$0.370)	1.150($\pm$0.030)
WASP-5 b	1.637($\pm$0.082)	0.027	0	1.000($\pm$0.060)	1.084($\pm$0.041)
WASP-50 b	1.437($\pm$0.068)	0.029	0.009	0.861($\pm$0.057)	0.855($\pm$0.019)
WASP-58 b	0.890($\pm$0.070)	0.056	0	0.940($\pm$0.100)	1.170($\pm$0.130)
WASP-6 b	0.503($\pm$0.028)	0.042	0.054	0.888($\pm$0.080)	0.870($\pm$0.036)
WASP-63 b	0.380($\pm$0.030)	0.057	0	1.320($\pm$0.050)	1.880($\pm$0.060)
WASP-8 b	2.244($\pm$0.086)	0.080	0.310	1.033($\pm$0.050)	0.953($\pm$0.058)
WASP-95 b	1.130($\pm$0.070)	0.034	0	1.110($\pm$0.090)	1.130($\pm$0.060)
WASP-96 b	0.480($\pm$0.030)	0.045	0	1.060($\pm$0.090)	1.050($\pm$0.050)
WASP-97 b	1.320($\pm$0.050)	0.033	0	1.120($\pm$0.060)	1.060($\pm$0.040)
WASP-98 b	0.830($\pm$0.070)	0.036	0	0.690($\pm$0.060)	0.700($\pm$0.020)
XO-1 b	0.900($\pm$0.070)	0.048	0	1.000($\pm$0.030)	0.928($\pm$0.030)
XO-5 b	1.077($\pm$0.037)	0.048	0	0.880($\pm$0.030)	1.060($\pm$0.050)

Table 3 Dynamical Characteristics of Exoplanets And Their Host Stars That are Used in Chapter 5.

Name	$v \sin i$ (m s^{-1})	$\log(L_p)$ (kg $m^2 s^{-1}$)	$\log(J_\star)$ (kg $m^2 s^{-1}$)	$\log(J_{spin})$ (kg $m^2 s^{-1}$)	$\log(J_{tot})$ (kg $m^2 s^{-1}$)
18 Del b	-	44.327	-	43.845	44.451
24 Sex b	2770($\pm$500)	43.229	43.063	43.116	43.477
24 Sex c	2770($\pm$500)	43.017	43.063	43.116	43.370
47 Uma b	2802($\pm$500)	43.489	42.297	42.384	43.522
47 Uma c	2802($\pm$500)	42.944	42.297	42.384	43.049
47 Uma d	-	43.680	-	42.384	43.702
51 Peg b	2572($\pm$500)	41.977	42.301	42.520	42.630
61 Vir b	2200($\pm-$)	40.454	42.036	42.237	42.244
61 Vir c	2200($\pm-$)	41.326	42.036	42.237	42.287
61 Vir d	2200($\pm-$)	41.611	42.036	42.237	42.329
70 Vir b	2684($\pm$500)	43.337	42.429	42.179	43.366
75 Cet b	1770($\pm-$)	43.755	43.408	43.989	44.189
81 Cet b	1800($\pm-$)	44.033	43.420	43.922	44.282
BD-10 3166 b	921($\pm$500)	41.916	41.936	42.312	42.459
CoRoT-1 b	5200($\pm$1000)	42.127	42.482	42.237	42.486
CoRoT-12 b	1000($\pm$1000)	42.205	41.823	42.467	42.656
CoRoT-13 b	4000($\pm$1000)	42.383	42.386	42.487	42.739
CoRoT-16 b	500($\pm$500)	42.0561	41.558	42.501	42.634
CoRoT-17 b	4500($\pm$500)	42.639	42.614	42.402	42.837
CoRoT-18 b	8000($\pm$1000)	42.691	42.623	42.237	42.822
CoRoT-2 b	11850($\pm$500)	42.655	42.758	42.275	42.806
CoRoT-20 b	-	43.057	-	42.569	43.179
CoRoT-22 b	-	41.012	-	42.502	42.516
CoRoT-23 b	9000($\pm$1000)	42.699	42.961	42.569	42.940
CoRoT-25 b	4300($\pm$500)	41.753	42.489	42.487	42.561
CoRoT-26 b	2000($\pm$1000)	41.982	42.334	42.487	42.605
CoRoT-27 b	4000($\pm$1000)	43.287	42.399	42.419	43.342
CoRoT-9 b	-($\pm$3500)	42.654	-	42.312	42.817
GJ 3021 b	-	43.275	-	42.139	43.306
HAT-P-1 b	2200($\pm$200)	42.040	42.216	42.586	42.695
HAT-P-13 b	2900($\pm$1000)	42.202	42.485	42.692	42.814
HAT-P-15 b	2000($\pm$500)	42.578	42.083	42.354	42.781
HAT-P-21 b	3500($\pm$500)	42.746	42.306	42.231	42.862
HAT-P-22 b	500($\pm$500)	42.547	41.421	42.171	42.700
HAT-P-23 b	8100($\pm$500)	42.456	42.815	42.553	42.808
HAT-P-25 b	500($\pm$500)	42.014	41.428	42.349	42.514
HAT-P-27 b	600($\pm$550)	41.971	41.450	42.228	42.419
HAT-P-28 b	200($\pm$500)	42.046	41.097	42.375	42.542
HAT-P-38 b	-	41.686	-	42.110	42.249
HD 100655 b	1600($\pm$1000)	43.271	43.295	43.922	44.010
HD 102117 b	878($\pm$500)	41.756	41.803	42.384	42.476
HD 104985 b	1670($\pm$90)	43.521	43.206	43.185	43.686
HD 106252 b	1925($\pm$500)	44.004	42.047	42.256	44.012
HD 106270 b	3130($\pm$500)	44.345	42.757	42.835	44.358

Table 3 Continue...

Name	$v \sin i$ (ms^{-1})	log(L_p) (kg m^2s^{-1})	log($J_\star$) (kg m^2s^{-1})	log(J_{spin}) (kg m^2s^{-1})	log(J_{tot}) (kg m^2s^{-1})
HD 10697 b	2480(±500)	43.929	42.433	42.585	43.948
HD 108874 b	2215(±500)	43.063	42.175	42.331	43.137
HD 108874 c	2215(±500)	43.149	42.175	42.331	43.210
HD 109246 b	3000(±1000)	42.525	42.233	42.349	42.747
HD 114729 b	2290(±500)	42.986	42.235	42.199	43.052
HD 11506 b	5000(±500)	43.694	42.657	42.647	43.731
HD 11506 c	-	42.76	-	42.647	43.012
HD 117207 b	1045(±500)	43.544	41.829	42.454	43.578
HD 117618 b	3194(±500)	41.794	42.344	42.419	42.512
HD 117618 c	-	42.222	-	42.419	42.633
HD 11964 b	2740(±500)	42.996	42.570	42.545	43.127
HD 11964 c	2740(±500)	41.530	42.570	42.545	42.585
HD 11977 b	2400(±1000)	44.026	43.518	43.507	44.141
HD 120084 b	2440(±−)	44.086	43.468	43.915	44.310
HD 125612 b	2100(±500)	43.487	42.127	42.504	43.530
HD 125612 c	2100(±500)	41.009	42.127	42.504	42.517
HD 125612 d	-	44.116	-	42.504	44.127
HD 12661 b	1301(±500)	43.061	41.936	42.454	43.157
HD 12661 c	1301(±500)	43.338	41.936	42.454	43.391
HD 134987 b	2173(±500)	42.996	42.206	42.454	43.106
HD 134987 c	2173(±500)	43.237	42.206	42.454	43.303
HD 136418 b	1660(±500)	43.350	42.618	42.849	43.469
HD 13931 b	2020(±500)	43.560	42.147	42.367	43.587
HD 14067 b	-	44.275	-	43.922	44.434
HD 141937 b	1880(±500)	44.025	42.084	42.504	44.038
HD 142 b	10352(±500)	43.046	42.734	42.504	43.156
HD 142 c	-	44.088	-	42.504	44.099
HD 142415 b	3427(±500)	43.155	42.328	42.487	43.239
HD 145377 b	3850(±0)	43.376	42.434	42.537	43.435
HD 1461 b	1600(±−)	40.723	42.020	42.470	42.478
HD 1461 c	-	40.707	-	42.470	42.478
HD 147513 b	1546(±500)	43.043	41.896	42.179	43.099
HD 149026 b	6000(±500)	41.849	42.810	42.808	42.853
HD 150706 b	-	43.759	-	42.218	43.772
HD 154672 b	540(±500)	43.526	41.604	42.436	43.560
HD 154857 b	1400(±500)	43.436	42.369	43.315	43.680
HD 154857 c	1400(±500)	43.798	42.369	43.315	43.922
HD 16141 b	1928(±500)	42.030	42.032	42.349	42.519
HD 16175 b	4800(±500)	43.796	42.826	42.876	43.846
HD 163607 b	1500(±500)	42.543	42.168	42.487	42.817
HD 163607 c	1500(±500)	43.412	42.168	42.487	43.461
HD 164509 b	2400(±50)	42.577	42.201	42.553	42.866
HD 168443 b	2200(±500)	43.543	42.262	42.321	43.569
HD 168746 b	-(±500)	41.633	-	42.098	42.226

Table 3 Continue...

Name	$v \sin i$ (ms^{-1})	$\log(L_p)$ (kg $m^2 s^{-1}$)	$\log(J_\star)$ (kg $m^2 s^{-1}$)	$\log(J_{spin})$ (kg $m^2 s^{-1}$)	$\log(J_{tot})$ (kg $m^2 s^{-1}$)
HD 170469 b	1700($\pm$500)	42.951	42.116	42.569	43.101
HD 171028 b	2299($\pm-$)	43.281	42.390	42.312	43.325
HD 17156 b	2800($\pm$500)	43.079	42.474	42.772	43.253
HD 173416 b	-	43.426	-	43.591	43.817
HD 175541 b	2900($\pm$500)	42.823	43.008	43.241	43.382
HD 179079 b	500($\pm$500)	41.344	41.648	42.482	42.513
HD 183263 b	1556($\pm$500)	43.609	42.086	42.616	43.651
HD 183263 c	1556($\pm$500)	43.857	42.086	42.616	43.881
HD 185269 b	6100($\pm$500)	42.379	42.909	42.779	42.925
HD 187123 b	2148($\pm$500)	41.970	42.168	42.436	42.564
HD 187123 c	2148($\pm$500)	43.583	42.168	42.436	43.613
HD 18742 b	2980($\pm$500)	43.602	43.111	43.185	43.743
HD 188015 b	-	43.083	-	42.487	43.181
HD 190360 b	2200($\pm$500)	43.409	42.181	42.402	43.449
HD 190360 c	2200($\pm$500)	41.230	42.181	42.402	42.430
HD 192699 b	1900($\pm$500)	43.425	42.875	43.274	43.657
HD 195019 b	2466($\pm$500)	43.049	42.300	42.436	43.144
HD 196050 b	3270($\pm$500)	43.524	42.436	42.616	43.574
HD 202206 c	2302($\pm$500)	43.544	42.167	42.553	43.586
HD 20367 b	-	43.008	-	42.402	43.104
HD 2039 b	3246($\pm$500)	43.776	42.328	42.294	43.790
HD 207832 b	3000($\pm-$)	42.539	42.148	42.218	42.708
HD 207832 c	3000($\pm-$)	42.939	42.148	42.218	43.015
HD 20794 b	1500($\pm$1500)	40.362	41.802	42.035	42.044
HD 20794 c	1500($\pm$1500)	40.423	41.802	42.035	42.045
HD 20794 d	1500($\pm$1500)	40.820	41.802	42.035	42.061
HD 208487 b	4608($\pm$500)	42.446	42.581	42.808	42.964
HD 209458 b	4490($\pm$500)	42.092	42.535	42.581	42.703
HD 210277 b	1801($\pm$500)	43.052	42.077	42.487	43.156
HD 212771 b	3580($\pm$500)	43.362	43.056	42.585	43.429
HD 213240 b	3972($\pm$500)	43.753	42.604	42.692	43.790
HD 216435 b	-	43.282	-	42.808	43.407
HD 216437 b	3133($\pm$500)	43.378	42.305	42.436	43.425
HD 217107 b	-($\pm$500)	42.486	-	42.367	42.731
HD 217107 c	-($\pm$500)	43.688	-	42.367	43.708
HD 219828 b	2900($\pm-$)	41.249	42.529	42.722	42.736
HD 222155 b	3200($\pm$1000)	43.586	42.524	42.553	43.624
HD 222582 b	2291($\pm$500)	43.875	42.159	42.312	43.886
HD 224693 b	3500($\pm$500)	42.524	42.641	42.849	43.017
HD 28185 b	-	43.734	-	42.722	43.774
HD 28254 b	2500($\pm$1000)	43.170	42.336	42.436	43.244
HD 290327 b	1440($\pm$1000)	43.576	41.855	42.139	43.592
HD 30177 b	2963($\pm$500)	44.007	42.241	42.237	44.015
HD 30669	-	42.793	-	42.179	42.888
HD 33283 b	3200($\pm$500)	42.059	42.420	42.722	42.807

Table 3 Continue...

Name	$v \sin i$ (ms^{-1})	$\log(L_p)$ (kg $m^2 s^{-1}$)	$\log(J_\star)$ (kg $m^2 s^{-1}$)	$\log(J_{spin})$ (kg $m^2 s^{-1}$)	$\log(J_{tot})$ (kg $m^2 s^{-1}$)
HD 34445 b	2700($\pm$500)	42.959	42.343	42.454	43.077
HD 37124 b	1217($\pm$500)	42.528	41.661	41.992	42.639
HD 37124 c	1217($\pm$500)	42.817	41.661	41.992	42.878
HD 37124 d	1217($\pm$500)	42.953	41.661	41.992	42.998
HD 38529 b	3903($\pm$500)	42.451	42.892	43.043	43.142
HD 39091 b	3135($\pm$500)	44.218	42.603	42.504	44.226
HD 4203 b	1227($\pm$500)	43.246	42.009	42.553	43.326
HD 4208 b	-	42.915	-	42.077	42.974
HD 4308 b	-	41.014	-	42.035	42.075
HD 4313 b	3370($\pm$500)	42.998	43.196	43.317	43.487
HD 43197 b	2180($\pm$1000)	42.677	42.063	42.256	42.817
HD 44219 b	2220($\pm$1000)	42.658	42.210	42.331	42.825
HD 45350 b	1368($\pm$500)	43.326	41.991	42.367	43.371
HD 49674 b	417($\pm$500)	41.323	41.366	42.454	42.485
HD 50499 b	4211($\pm$500)	43.505	42.611	42.765	43.578
HD 52265 b	4670($\pm$500)	42.826	42.588	42.662	43.053
HD 52265 c	-	42.258	-	42.662	42.806
HD 5319 b	3310($\pm$500)	43.433	42.969	43.139	43.611
HD 564 b	-	42.423	-	42.179	42.619
HD 5891 b	4950($\pm$500)	43.888	43.658	43.507	44.039
HD 6434 b	-	42.040	-	41.902	42.277
HD 6718 b	1760($\pm$1000)	43.387	41.979	42.256	43.418
HD 68988 b	2838($\pm$500)	42.619	42.332	42.662	42.942
HD 70642 b	300($\pm$500)	43.487	41.144	42.331	43.516
HD 72659 b	2205($\pm$500)	43.752	42.197	42.237	43.765
HD 73267 b	1650($\pm$0)	43.550	41.927	42.119	43.566
HD 73526 b	2623($\pm$500)	43.247	42.368	42.470	43.314
HD 73526 c	2623($\pm$500)	43.337	42.368	42.470	43.393
HD 73534 b	500($\pm$500)	43.292	41.975	42.794	43.412
HD 74156 b	4319($\pm$500)	42.927	42.686	42.722	43.137
HD 74156 c	4319($\pm$500)	44.144	42.686	42.722	44.160
HD 75289 b	4136($\pm$500)	41.940	42.477	42.419	42.544
HD 75898 b	4540($\pm$500)	43.401	42.711	42.779	43.494
HD 76700 b	1347($\pm$500)	41.596	41.996	42.331	42.404
HD 80606 b	1797($\pm$500)	43.338	41.980	42.294	43.376
HD 81040 b	2000($\pm$1000)	43.898	41.960	42.256	43.908
HD 82886 b	430($\pm$500)	43.162	42.083	42.436	43.237
HD 82943 b	1348($\pm$500)	43.673	41.994	42.631	43.710
HD 82943 c	1348($\pm$500)	43.578	41.994	42.631	43.625
HD 82943 d	-	42.591	-	42.631	42.913
HD 8535 b	1410($\pm$1000)	42.972	42.021	42.553	43.112
HD 88133 b	2200($\pm$500)	41.756	42.450	42.662	42.713
HD 89307 b	3210($\pm$500)	43.496	42.282	42.381	43.528
HD 92788 b	255($\pm$500)	43.527	41.199	42.553	43.571
HD 92788 c	-	42.791	-	42.553	42.989

Table 3 Continue...

Name	$v \sin i$ (ms^{-1})	$\log(L_p)$ (kg $m^2 s^{-1}$)	$\log(J_\star)$ (kg $m^2 s^{-1}$)	$\log(J_{spin})$ (kg $m^2 s^{-1}$)	$\log(J_{tot})$ (kg $m^2 s^{-1}$)
HD 9446 b	4000($\pm$1000)	42.398	42.345	42.331	42.667
HD 9446 c	4000($\pm$1000)	42.994	42.345	42.331	43.079
HD 96167 b	3800($\pm$500)	42.849	42.709	42.822	43.137
HIP 14810 b	540($\pm$500)	42.832	41.471	42.312	42.947
HIP 14810 c	540($\pm$500)	42.884	41.471	42.312	42.987
HIP 14810 d	540($\pm$500)	42.819	41.471	42.312	42.936
HR 810 b	-	43.285	-	42.520	43.354
Kepler-10 b	500($\pm$500)	40.038	41.428	42.159	42.162
Kepler-10 c	500($\pm$500)	41.331	41.428	42.159	42.219
Kepler-11 b	400($\pm$500)	40.100	41.364	42.237	42.240
Kepler-11 c	400($\pm$500)	40.379	41.364	42.237	42.243
Kepler-11 d	400($\pm$500)	40.877	41.364	42.237	42.256
Kepler-11 e	400($\pm$500)	40.907	41.364	42.237	42.257
Kepler-11 f	400($\pm$500)	40.404	41.364	42.237	42.244
Kepler-11 g	400($\pm$500)	42.725	41.364	42.237	42.847
Kepler-12 b	800($\pm$500)	41.961	41.884	42.610	42.698
Kepler-17 b	6000($\pm$2000)	42.526	42.606	42.600	42.866
Kepler-20 b	-	40.657	-	42.163	42.176
Kepler-20 c	-	41.082	-	42.163	42.198
Kepler-20 d	-	41.453	-	42.163	42.240
Kepler-20 e	400($\pm$500)	40.228	41.280	42.163	42.168
Kepler-20 f	400($\pm$500)	41.078	41.280	42.163	42.197
Kepler-22 b	600($\pm$100)	41.914	41.498	42.275	42.432
Kepler-4 b	2100($\pm$1000)	41.162	42.325	42.697	42.709
Kepler-41 b	4500($\pm$1500)	41.835	42.354	42.218	42.368
Kepler-412 b	5000($\pm$1000)	42.143	42.618	42.611	42.739
Kepler-43 b	5500($\pm$1500)	42.822	42.756	42.835	43.130
Kepler-44 b	4000($\pm$2000)	42.302	42.602	42.647	42.809
Kepler-66 b	-	41.987	-	42.398	42.541
Kepler-67 b	-	41.907	-	42.067	42.295
Kepler-75 b	3500($\pm$1500)	43.253	42.176	42.098	43.283
Kepler-77 b	1500($\pm$1000)	41.875	41.892	42.237	42.394
Kepler-78 b	2400($\pm$500)	39.595	41.901	41.947	41.949
KOI-192 b	-	41.850	-	42.256	42.400
KOI-195 b	-	41.746	-	42.159	42.301
ksi Aql b	-	43.448	-	43.764	43.935
mu Ara b	3117($\pm$500)	43.249	42.365	42.470	43.316
mu Ara c	3117($\pm$500)	40.929	42.365	42.470	42.483
mu Ara d	3117($\pm$500)	42.640	42.365	42.470	42.864
mu Ara e	3117($\pm$500)	43.553	42.365	42.470	43.588
OGLE-TR-56 b	-	42.232	-	42.616	42.766
ome Ser b	1890($\pm-$)	43.346	43.446	43.739	43.887
omi UMa b	3830($\pm-$)	44.080	43.965	44.382	44.558
TrES-2	2000($\pm$1500)	42.213	42.035	42.294	42.556
TrES-3	1000($\pm$1000)	42.367	41.618	42.187	42.587

Table 3 Continue...

Name	$v \sin i$ (ms^{-1})	$\log(L_p)$ (kg $m^2 s^{-1}$)	$\log(J_\star)$ (kg $m^2 s^{-1}$)	$\log(J_{spin})$ (kg $m^2 s^{-1}$)	$\log(J_{tot})$ (kg $m^2 s^{-1}$)
WASP-104 b	-	42.267	-	42.367	42.621
WASP-110 b	-	41.905	-	42.123	42.329
WASP-112 b	-	42.110	-	41.941	42.335
WASP-12 b	2200($\pm$1500)	42.317	42.419	42.876	42.982
WASP-16 b	3000($\pm$1000)	42.051	42.205	42.370	42.540
WASP-19 b	4000($\pm$2000)	42.055	42.303	42.147	42.404
WASP-21 b	1500($\pm$600)	41.761	41.948	42.349	42.448
WASP-25 b	3000($\pm$1000)	42.017	42.198	42.331	42.503
WASP-26 b	2400($\pm$1300)	42.264	42.299	42.537	42.722
WASP-32 b	3900($\pm$450)	42.793	42.420	42.504	42.973
WASP-34 b	1400($\pm$600)	41.987	41.862	42.349	42.505
WASP-36 b	3200($\pm$1300)	42.454	42.231	42.367	42.713
WASP-37 b	2400($\pm$1600)	42.465	42.042	42.033	42.602
WASP-39 b	1400($\pm$600)	41.701	41.809	42.199	42.319
WASP-4 b	2200($\pm$800)	42.180	42.114	42.199	42.490
WASP-41 b	1600($\pm$1100)	42.179	41.929	42.237	42.510
WASP-44 b	3200($\pm$900)	42.135	42.193	42.239	42.491
WASP-46 b	1900($\pm$1200)	42.431	41.964	42.249	42.650
WASP-47 b	3000($\pm$600)	42.345	42.316	42.477	42.717
WASP-5 b	3400($\pm$700)	42.351	42.309	42.331	42.642
WASP-50 b	2600($\pm$500)	42.284	42.025	42.058	42.487
WASP-58 b	2800($\pm$900)	42.175	42.231	42.218	42.498
WASP-6 b	1400($\pm$1000)	41.907	41.777	42.115	42.324
WASP-63 b	2800($\pm$500)	41.925	42.585	42.835	42.886
WASP-8 b	1590($\pm$85)	42.571	41.937	42.390	42.791
WASP-95 b	3100($\pm$600)	42.268	42.332	42.520	42.713
WASP-96 b	1500($\pm$1300)	41.947	41.965	42.436	42.558
WASP-97 b	1100($\pm$500)	42.331	41.859	42.537	42.747
WASP-98 b	-	42.042	-	41.656	42.192
XO-1 b	1110($\pm$67)	42.205	41.756	42.331	42.573
XO-5 b	1800($\pm$500)	42.275	41.968	42.098	42.496

Table 4 Physical And Orbital Characteristics of The Host Stars and Their Exoplanets Used in Chapter 6.

Name	M_p (M_J)	a (AU)	[Fe/H] dex	$M_\star$ ($M_\odot$)	Distance pc
47 Uma b	2.530($\pm$0.065)	2.100	0($\pm$0.07)	1.03($\pm$0.050)	13.97
47 Uma c	0.540($\pm$0.069)	3.600	0($\pm$0.07)	1.03($\pm$0.05)	13.97
47 Uma d	1.640($\pm$0.385)	11.60	0($\pm$0.07)	1.03($\pm$0.050)	13.97
51 Peg b	0.468($\pm$0.007)	0.052	0.2($\pm$0.07)	1.11($\pm$0.060)	14.70
61 Vir b	0.016($\pm$0.001)	0.050	-0.01($\pm$-)	0.95($\pm$0.030)	8.52
61 Vir c	0.057($\pm$0.003)	0.217	-0.01($\pm$-)	0.95($\pm$0.030)	8.52
61 Vir d	0.072($\pm$0.008)	0.476	-0.01($\pm$-)	0.95($\pm$0.030)	8.52
70 Vir b	6.600($\pm$0.660)	0.480	-0.11($\pm$-)	0.92($\pm$0.046)	22.00
CoRoT-1 b	1.030($\pm$0.120)	0.025	0.06($\pm$0.07)	0.95($\pm$0.150)	460.00
CoRoT-12 b	0.917($\pm$0.067)	0.040	0.16($\pm$0.10)	1.07($\pm$0.072)	1150.00
CoRoT-13 b	1.308($\pm$0.066)	0.051	0.01($\pm$0.07)	1.09($\pm$0.020)	1310.00
CoRoT-16 b	0.535($\pm$0.085)	0.061	0.19($\pm$0.06)	1.09($\pm$0.078)	840.00
CoRoT-17 b	2.430($\pm$0.160)	0.046	0($\pm$0.10)	1.04($\pm$0.100)	920.00
CoRoT-18 b	3.470($\pm$0.380)	0.029	-0.10($\pm$0.10)	0.95($\pm$0.150)	870.00
CoRoT-2 b	3.310($\pm$0.160)	0.028	-0.04($\pm$0.08)	0.97($\pm$0.060)	300.00
CoRoT-20 b	4.240($\pm$0.230)	0.090	0.14($\pm$0.12)	1.14($\pm$0.080)	1230.00
CoRoT-22 b	0.038($\pm$0.035)	0.092	0.17($\pm$0.09)	1.09($\pm$0.049)	592.00
CoRoT-23 b	2.800($\pm$0.250)	0.047	0.05($\pm$0.10)	1.14($\pm$0.080)	600.00
CoRoT-25 b	0.270($\pm$0.040)	0.057	-0.01($\pm$0.13)	1.09($\pm$0.080)	1000
CoRoT-26 b	0.520($\pm$0.050)	0.052	0.01($\pm$0.13)	1.09($\pm$0.060)	1670.00
CoRoT-27 b	10.390($\pm$0.550)	0.047	0.10($\pm$0.10)	1.05($\pm$0.110)	-
CoRoT-9 b	0.840($\pm$0.070)	0.407	-0.01($\pm$0.006)	0.99($\pm$0.040)	460.00
GJ 3021 b	3.370($\pm$0.090)	0.490	0.10($\pm$0.08)	0.90($\pm$0.045)	17.62
HAT-P-1 b	0.525($\pm$0.019)	0.055	0.13($\pm$0.008)	1.15($\pm$0.052)	139.00
HAT-P-15 b	1.946($\pm$0.066)	0.096	0.22($\pm$0.08)	1.01($\pm$0.043)	190.00
HAT-P-21 b	4.063($\pm$0.161)	0.049	0.01($\pm$0.08)	0.94($\pm$0.042)	254.00
HAT-P-22 b	2.147($\pm$0.061)	0.041	0.24($\pm$0.08)	0.91($\pm$0.035)	82.00
HAT-P-23 b	2.090($\pm$0.110)	0.023	0.16($\pm$0.03)	1.13($\pm$0.050)	393.00
HAT-P-25 b	0.567($\pm$0.056)	0.046	0.31($\pm$0.08)	1.01($\pm$0.032)	297.00
HAT-P-27 b	0.660($\pm$0.033)	0.040	0.29($\pm$0.10)	0.94($\pm$0.035)	204.00
HAT-P-28 b	0.626($\pm$0.037)	0.043	0.12($\pm$0.08)	1.02($\pm$0.047)	395.00
HAT-P-38 b	0.267($\pm$0.020)	0.052	0.06($\pm$0.10)	0.88($\pm$0.044)	249.00
HD 102117 b	0.172($\pm$0.018)	0.153	0.30($\pm$0.03)	1.03($\pm$0.050)	42.00
HD 106252 b	7.560($\pm$0.756)	2.700	-0.07	0.96($\pm$0.048)	37.44
HD 106270 b	11.000($\pm$0.800)	4.300	0.08($\pm$0.03)	1.32($\pm$0.092)	84.90
HD 10697 b	6.380($\pm$0.530)	2.160	0.10($\pm$0.06)	1.15($\pm$0.030)	32.56
HD 108874 b	1.360($\pm$0.130)	1.051	0.14	1.00($\pm$0.050)	68.50
HD 108874 c	1.018($\pm$0.300)	2.680	0.14	1.00($\pm$0.050)	68.50
HD 109246 b	0.770($\pm$0.090)	0.330	0.10	1.01($\pm$0.110)	65.60
HD 114729 b	0.840($\pm$0.084)	2.080	-0.22	0.93($\pm$0.046)	35.00
HD 11506 b	3.440($\pm$0.685)	2.430	0.31($\pm$0.03)	1.19($\pm$0.020)	53.82
HD 11506 c	0.820($\pm$0.405)	0.639	0.31($\pm$0.03)	1.19($\pm$0.020)	53.82
HD 117207 b	2.060($\pm$0.206)	3.780	0.27	1.07($\pm$0.053)	33.00
HD 117618 b	0.178($\pm$0.020)	0.176	0.04	1.05($\pm$0.052)	38.00

208

Table 4 Continue...

Name	M_p (M_J)	a (AU)	[Fe/H] dex	$M_\star$ $(M_\odot)$	Distance pc
HD 117618 c	0.200(±0.100)	0.930	0.04	1.05(±0.052)	38.00
HD 11964 b	0.622(±0.056)	3.160	0.17	1.12(±0.056)	33.98
HD 11964 c	0.079(±0.010)	0.229	0.17	1.12(±0.056)	33.98
HD 125612 b	3.000(±0.300)	1.370	0.24(±0.03)	1.10(±0.070)	52.82
HD 125612 c	0.058(±0.005)	0.050	0.24(±0.03)	1.10(±0.070)	52.82
HD 125612 d	7.200(±0.720)	4.200	0.24(±0.03)	1.10(±0.070)	52.82
HD 12661 b	2.300(±0.230)	0.830	0.29(±0.05)	1.07(±0.053)	37.16
HD 12661 c	1.570(±0.157)	2.560	0.29(±0.05)	1.07(±0.053)	37.16
HD 134987 b	1.590(±0.020)	0.810	0.25(±0.02)	1.07(±0.080)	22.20
HD 134987 c	0.820(±0.030)	5.800	0.25(±0.02)	1.07(±0.080)	22.20
HD 136418 b	2.000(±0.100)	1.320	-0.07(±0.03)	1.33(±0.090)	98.20
HD 13931 b	1.880(±0.150)	5.150	0.03(±0.04)	1.02(±0.020)	44.20
HD 141937 b	9.700(±0.970)	1.520	0.11	1.10(±0.055)	33.46
HD 142 b	1.250(±0.150)	1.020	0.04(±0.05)	1.10(±0.220)	20.60
HD 142 c	5.300(±0.700)	6.800	0.04(±0.05)	1.10(±0.220)	20.60
HD 142415 b	1.620(±0.162)	1.050	0.21(±0.05)	1.09(±0.054)	34.20
HD 145377 b	5.760(±0.100)	0.450	0.12(±0.01)	1.12(±0.030)	57.70
HD 1461 b	0.023(±0.003)	0.063	0.19(±0.01)	1.08(±0.040)	23.40
HD 1461 c	0.018(±0.002)	0.111	0.19(±0.01)	1.08(±0.040)	23.40
HD 147513 b	1.210(±0.121)	1.320	-0.03	0.92(±0.046)	12.90
HD 149026 b	0.356(±0.012)	0.042	0.36(±0.05)	1.30(±0.100)	78.90
HD 150706 b	2.710(±0.900)	6.700	-0.13	0.94(±0.800)	27.20
HD 154672 b	5.020(±0.170)	0.600	0.26(±0.04)	1.06(±0.090)	65.80
HD 16141 b	0.215(±0.030)	0.350	0.02	1.01(±0.050)	35.90
HD 16175 b	4.400(±0.440)	2.100	0.23(±0.07)	1.35(±0.090)	59.80
HD 163607 b	0.770(±0.040)	0.360	0.21(±0.03)	1.09(±0.020)	69.00
HD 163607 c	2.290(±0.160)	2.420	0.21(±0.03)	1.09(±0.020)	69.00
HD 164509 b	0.480(±0.090)	0.875	0.21(±0.03)	1.13(±0.020)	52.00
HD 168443 b	7.659(±0.097)	0.293	0.04(±0.03)	0.99(±0.019)	37.38
HD 168746 b	0.230(±0.023)	0.065	-0.06(±0.05)	0.88(±0.010)	43.12
HD 170469 b	0.670(±0.067)	2.240	0.30(±0.03)	1.14(±0.020)	64.97
HD 171028 b	1.980(±0.198)	1.320	-0.49(±0.02)	0.99(±0.080)	90.00
HD 17156 b	3.191(±0.033)	0.162	0.24(±0.05)	1.27(±0.018)	78.24
HD 179079 b	0.080(±0.008)	0.110	0.29(±0.04)	1.08(±0.100)	63.69
HD 183263 b	3.670(±0.300)	1.510	0.30	1.17(±0.058)	53.00
HD 183263 c	3.820(±0.590)	4.250	0.30	1.17(±0.058)	53.00
HD 185269 b	0.940(±0.094)	0.077	0.11(±0.05)	1.28(±0.100)	47.00
HD 187123 b	0.520(±0.040)	0.042	0.16	1.06(±0.053)	50.00
HD 187123 c	1.990(±0.250)	4.890	0.16	1.06(±0.053)	50.00
HD 188015 b	1.260(±0.126)	1.190	0.29	1.09(±0.054)	52.60
HD 190360 b	1.502(±0.130)	3.920	0.24(±0.08)	1.04(±0.052)	15.89
HD 190360 c	0.057(±0.015)	0.128	0.24(±0.08)	1.04(±0.052)	15.89
HD 195019 b	3.700(±0.300)	0.138	0.08(±0.04)	1.06(±0.053)	18.77
HD 196050 b	2.830(±0.283)	2.470	0.23	1.17(±0.058)	46.90
HD 202206 c	2.440(±0.244)	2.550	0.37(±0.07)	1.13(±0.056)	46.34

Table 4 Continue...

Name	M_p	a	[Fe/H]	$M_\star$	Distance
	(M_J)	(AU)	dex	$(M_\odot)$	pc
HD 20367 b	1.070(±0.107)	1.250	0.10	1.04(±0.060)	27.00
HD 2039 b	4.900(±1.000)	2.200	0.10(±0.16)	0.98(±0.050)	89.80
HD 207832 b	0.560(±0.045)	0.570	0.06	0.94(±0.100)	54.40
HD 207832 c	0.730(±0.115)	2.112	0.06	0.94(±0.100)	54.40
HD 20794 b	0.008(±0.0009)	0.120	-0.38(±0.06)	0.85(±0.040)	6.06
HD 20794 c	0.007(±0.0013)	0.203	-0.38(±0.06)	0.85(±0.040)	6.06
HD 20794 d	0.015(±0.0019)	0.349	-0.38(±0.06)	0.85(±0.040)	6.06
HD 208487 b	0.413(±0.050)	0.510	-0.06(±0.05)	1.30(±0.065)	45.00
HD 209458 b	0.690(±0.017)	0.047	0.02(±0.05)	1.14(±0.022)	47.00
HD 210277 b	1.230(±0.030)	1.100	0.19(±0.04)	1.09(±0.054)	21.29
HD 212771 b	2.300(±0.400)	1.220	-0.21(±0.03)	1.15(±0.080)	131.00
HD 213240 b	4.500(±0.450)	2.030	0.16	1.22(±0.061)	40.75
HD 216435 b	1.260(±0.130)	2.560	0.24	1.30	33.30
HD 216437 b	1.820(±0.182)	2.320	0.25	1.06(±0.053)	26.50
HD 217107 b	1.330(±0.050)	0.073	0.37(±0.05)	1.02(±0.051)	19.72
HD 217107 c	2.490(±0.250)	5.270	0.37(±0.05)	1.02(±0.051)	19.72
HD 219828 b	0.085(±0.008)	0.052	0.19(±0.03)	1.24(±0.062)	81.10
HD 222155 b	1.900(±0.600)	5.100	-0.11(±0.05)	1.13(±0.110)	49.10
HD 222582 b	7.750(±0.650)	1.350	-0.02	0.99(±0.049)	42.00
HD 224693 b	0.710(±0.071)	0.233	0.34(±0.03)	1.33(±0.100)	94.00
HD 28185 b	5.700(±0.570)	1.030	0.24	1.24(±0.062)	39.40
HD 28254 b	1.160(±0.080)	2.150	0.36(±0.03)	1.06(±0.053)	56.20
HD 290327 b	2.540(±0.155)	3.430	-0.11(±0.02)	0.90(±0.045)	54.90
HD 30177 b	7.700(±1.500)	2.600	0.19(±0.09)	0.95(±0.050)	55.00
HD 30669	0.470(±0.060)	2.690	0.13(±0.06)	0.92(±0.030)	57.00
HD 33283 b	0.330(±0.033)	0.168	0.36(±0.05)	1.24(±0.100)	86.00
HD 34445 b	0.790(±0.070)	2.070	0.14(±0.04)	1.07(±0.020)	46.50
HD 37124 b	0.675(±0.017)	0.533	-0.44	0.83(±0.041)	33.00
HD 37124 c	0.652(±0.052)	1.710	-0.44	0.83(±0.041)	33.00
HD 37124 d	0.696(±0.059)	2.807	-0.44	0.83(±0.041)	33.00
HD 38529 b	0.780(±0.078)	0.131	0.27(±0.05)	1.48(±0.050)	39.28
HD 39091 b	10.300(±1.030)	3.280	0.09	1.10(±0.055)	18.32
HD 4208 b	0.800(±0.080)	1.700	-0.28	0.87(±0.043)	33.90
HD 4308 b	0.040(±0.005)	0.118	-0.34	0.85(±0.042)	21.90
HD 44219 b	0.580(±0.050)	1.190	0.03(±0.01)	1.00(±0.050)	50.43
HD 45350 b	1.790(±0.140)	1.920	0.29	1.02(±0.051)	49.00
HD 49674 b	0.100(±0.010)	0.058	0.25	1.07(±0.053)	40.70
HD 50499 b	1.710(±0.200)	3.860	0.23	1.27(±0.063)	47.26
HD 52265 b	1.050(±0.030)	0.500	0.21(±0.06)	1.20(±0.060)	28.00
HD 52265 c	0.350(±0.090)	0.316	0.21(±0.06)	1.20(±0.060)	28.00
HD 564 b	0.330(±0.030)	1.200	0.13(±0.06)	0.92(±0.030)	54.00
HD 6434 b	0.390(±0.039)	0.140	-0.52	0.79(±0.039)	40.32
HD 6718 b	1.560(±0.105)	3.560	-0.06(±0.02)	0.96(±0.048)	55.90
HD 68988 b	1.900(±0.190)	0.071	0.24	1.20(±0.060)	58.00
HD 70642 b	2.000(±0.200)	3.300	0.16(±0.02)	1.00(±0.050)	28.80
HD 72659 b	3.150(±0.140)	4.740	-0.02(±0.01)	0.95(±2.000)	49.80

Table 4 Continue...

Name	M_p	a	[Fe/H]	$M_\star$	Distance
	(M_J)	(AU)	dex	$(M_\odot)$	pc
HD 73267 b	3.060($\pm$0.070)	2.198	0.03($\pm$0.02)	0.89($\pm$0.030)	54.91
HD 73526 b	2.900($\pm$0.200)	0.660	0.25($\pm$0.05)	1.08($\pm$0.050)	99.00
HD 73526 c	2.500($\pm$0.300)	1.050	0.25($\pm$0.05)	1.08($\pm$0.050)	99.00
HD 73534 b	1.150($\pm$0.115)	3.150	0.16($\pm$0.04)	1.29($\pm$0.100)	96.99
HD 74156 b	1.880($\pm$0.030)	0.294	0.13	1.24($\pm$0.040)	64.56
HD 74156 c	8.030($\pm$0.120)	3.400	0.13	1.24($\pm$0.040)	64.56
HD 75289 b	0.470($\pm$0.047)	0.046	0.29	1.05($\pm$0.052)	28.94
HD 75898 b	2.510($\pm$0.251)	1.190	0.27($\pm$0.05)	1.28($\pm$0.130)	80.58
HD 76700 b	0.230($\pm$0.023)	0.049	0.14	1($\pm$0.050)	59.70
HD 81040 b	6.860($\pm$0.710)	1.940	-0.16($\pm$0.06)	0.96($\pm$0.040)	32.56
HD 82886 b	1.300($\pm$0.100)	1.650	-0.31($\pm$0.03)	1.06($\pm$0.074)	125.00
HD 82943 b	4.800($\pm$0.480)	1.190	0.32	1.18($\pm$0.059)	27.46
HD 82943 c	4.780($\pm$0.478)	0.746	0.32	1.18($\pm$0.059)	27.46
HD 82943 d	0.290($\pm$0.031)	2.145	0.32	1.18($\pm$0.059)	27.46
HD 8535 b	0.680($\pm$0.055)	2.450	0.02	1.13($\pm$0.056)	52.50
HD 88133 b	0.300($\pm$0.030)	0.047	0.34($\pm$0.04)	1.20($\pm$0.200)	74.50
HD 89307 b	2.000($\pm$0.400)	3.340	-0.14($\pm$0.04)	1.02($\pm$0.040)	30.90
HD 92788 b	3.860($\pm$0.386)	0.970	0.32	1.13($\pm$0.056)	32.82
HD 92788 c	0.900($\pm$0.300)	0.600	0.32	1.13($\pm$0.056)	32.82
HD 9446 b	0.700($\pm$0.060)	0.189	0.09($\pm$0.05)	1.00($\pm$0.100)	53.00
HD 9446 c	1.820($\pm$0.170)	0.654	0.09($\pm$0.05)	1.00($\pm$0.100)	53.00
HD 96167 b	0.680($\pm$0.180)	1.300	0.09($\pm$0.05)	1.31($\pm$0.090)	84.00
HIP 14810 b	3.880($\pm$0.320)	0.069	0.26($\pm$0.03)	0.99($\pm$0.040)	52.90
HIP 14810 c	1.280($\pm$0.100)	0.545	0.26($\pm$0.03)	0.99($\pm$0.040)	52.90
HIP 14810 d	0.570($\pm$0.052)	1.890	0.26($\pm$0.03)	0.99($\pm$0.040)	52.90
HR 810 b	2.260($\pm$0.180)	0.925	0.25	1.11($\pm$0.070)	-
Kepler-10 b	0.010($\pm$0.001)	0.016	-0.15($\pm$0.04)	0.91($\pm$0.021)	173.00
Kepler-10 c	0.054($\pm$0.005)	0.241	-0.15($\pm$0.04)	0.91($\pm$0.021)	173.00
Kepler-11 b	0.005($\pm$0.003)	0.091	0.0	0.95($\pm$0.100)	-
Kepler-11 c	0.009($\pm$0.007)	0.106	0.0	0.95($\pm$0.100)	-
Kepler-11 d	0.022($\pm$0.003)	0.159	0.0	0.95($\pm$0.100)	-
Kepler-11 e	0.030($\pm$0.005)	0.194	0.0	0.95($\pm$0.100)	-
Kepler-11 f	0.006($\pm$0.002)	0.250	0.0	0.95($\pm$0.100)	-
Kepler-11 g	0.950($\pm$0.475)	0.462	0.0	0.95($\pm$0.100)	-
Kepler-12 b	0.431($\pm$0.041)	0.055	0.07($\pm$0.04)	1.16($\pm$0.054)	-
Kepler-17 b	2.450($\pm$0.014)	0.025	0.26($\pm$0.10)	1.16($\pm$0.060)	800
Kepler-20 b	0.026($\pm$0.006)	0.045	0.02($\pm$0.04)	0.91($\pm$0.035)	290.00
Kepler-20 c	0.049($\pm$0.007)	0.093	0.02($\pm$0.04)	0.91($\pm$0.035)	290.00
Kepler-20 d	0.060($\pm$0.006)	0.345	0.02($\pm$0.04)	0.91($\pm$0.035)	290.00
Kepler-20 e	0.009($\pm$0.0009)	0.050	0.02($\pm$0.04)	0.91($\pm$0.035)	290.00
Kepler-20 f	0.045($\pm$0.004)	0.110	0.02($\pm$0.04)	0.91($\pm$0.035)	290.00
Kepler-22 b	0.110($\pm$0.011)	0.849	-0.29($\pm$0.06)	0.97($\pm$0.060)	190.00
Kepler-4 b	0.082($\pm$0.0128)	0.045	0.17($\pm$0.06)	1.22($\pm$0.091)	550.00
Kepler-41 b	0.490($\pm$0.090)	0.029	-0.09($\pm$0.16)	0.94($\pm$0.090)	730.00
Kepler-412 b	0.939($\pm$0.085)	0.029	0.27($\pm$0.12)	1.16($\pm$0.091)	1056.00
Kepler-43 b	3.230($\pm$0.190)	0.044	0.33($\pm$0.11)	1.32($\pm$0.090)	1950.00

Table 4 Continue...

Name	M_p (MJ)	a (AU)	[Fe/H] dex	$M_\star$ ($M_\odot$)	Distance pc
Kepler-44 b	1.020($\pm$0.070)	0.045	0.26($\pm$0.10)	1.19($\pm$0.100)	2250.00
Kepler-66 b	0.310($\pm$0.070)	0.135	0.01($\pm$0.003)	1.03($\pm$0.051)	1107.00
Kepler-67 b	0.310($\pm$0.060)	0.117	0.01($\pm$0.003)	0.86($\pm$0.043)	1107.00
Kepler-75 b	9.900($\pm$0.500)	0.080	-0.07($\pm$0.15)	0.88($\pm$0.060)	1140.00
Kepler-77 b	0.430($\pm$0.032)	0.045	0.20($\pm$0.05)	0.95($\pm$0.040)	570.00
Kepler-78 b	0.005($\pm$0.001)	0.010	-0.14($\pm$0.08)	0.81($\pm$0.050)	-
KOI-192 b	0.290($\pm$0.090)	0.091	-0.19($\pm$0.07)	0.96($\pm$0.060)	1100.00
KOI-195 b	0.340($\pm$0.080)	0.041	-0.21($\pm$0.08)	0.91($\pm$0.060)	880.00
mu Ara b	1.676($\pm$0.167)	1.500	0.28($\pm$0.04)	1.08($\pm$0.050)	15.30
mu Ara c	0.033($\pm$0.003)	0.090	0.28($\pm$0.04)	1.08($\pm$0.050)	15.30
mu Ara d	0.521($\pm$0.052)	0.921	0.28($\pm$0.04)	1.08($\pm$0.050)	15.30
mu Ara e	1.814($\pm$0.181)	5.235	0.28($\pm$0.04)	1.08($\pm$0.050)	15.30
TrES-2	1.253($\pm$0.052)	0.035	-0.15($\pm$0.10)	0.98($\pm$0.062)	220.00
TrES-3	1.910($\pm$0.065)	0.022	-0.19($\pm$0.08)	0.92($\pm$0.040)	-
WASP-104 b	1.272($\pm$0.047)	0.029	0.32($\pm$0.09)	1.02($\pm$0.090)	143.00
WASP-110 b	0.515($\pm$0.064)	0.045	-0.06($\pm$0.10)	0.89($\pm$0.072)	320.00
WASP-112 b	0.880($\pm$0.120)	0.038	-0.64($\pm$0.15)	0.80($\pm$0.073)	450.00
WASP-12 b	1.404($\pm$0.099)	0.022	0.30($\pm$0.10)	1.35($\pm$0.140)	427.00
WASP-16 b	0.855($\pm$0.059)	0.042	0.01($\pm$0.10)	1.02($\pm$0.101)	-
WASP-19 b	1.114($\pm$0.040)	0.016	0.02($\pm$0.09)	0.90($\pm$0.045)	-
WASP-21 b	0.300($\pm$0.010)	0.052	-0.40($\pm$0.10)	1.01($\pm$0.025)	230.00
WASP-25 b	0.580($\pm$0.040)	0.047	-0.05($\pm$0.10)	1.00($\pm$0.030)	169.00
WASP-26 b	1.028($\pm$0.021)	0.039	-0.02(0.09)	1.12($\pm$0.030)	250.00
WASP-32 b	3.600($\pm$0.070)	0.039	-0.13($\pm$0.10)	1.10($\pm$0.030)	-
WASP-34 b	0.590($\pm$0.010)	0.052	-0.02($\pm$0.10)	1.01($\pm$0.070)	120.00
WASP-36 b	2.279($\pm$0.068)	0.026	-0.31($\pm$0.12)	1.02($\pm$0.032)	450.00
WASP-37 b	1.800($\pm$0.170)	0.043	-0.40($\pm$0.12)	0.84($\pm$0.040)	338.00
WASP-39 b	0.280($\pm$0.030)	0.048	-0.12($\pm$0.10)	0.93($\pm$0.030)	230.00
WASP-4 b	1.237($\pm$0.060)	0.023	-0.03($\pm$0.09)	0.93($\pm$0.050)	300.00
WASP-41 b	0.920($\pm$0.070)	0.040	-0.08($\pm$0.09)	0.95($\pm$0.090)	180.00
WASP-44 b	0.889($\pm$0.062)	0.034	0.06($\pm$0.10)	0.95($\pm$0.034)	-
WASP-46 b	2.101($\pm$0.073)	0.024	-0.37($\pm$0.13)	0.95($\pm$0.034)	-
WASP-47 b	1.140($\pm$0.050)	0.052	0.18($\pm$0.07)	1.08($\pm$0.370)	200.00
WASP-5 b	1.637($\pm$0.082)	0.027	0.09($\pm$0.09)	1.00($\pm$0.060)	297.00
WASP-50 b	1.437($\pm$0.068)	0.029	-0.12($\pm$0.08)	0.86($\pm$0.057)	230.00
WASP-58 b	0.890($\pm$0.070)	0.056	-0.45($\pm$0.09)	0.94($\pm$0.100)	300.00
WASP-6 b	0.503($\pm$0.028)	0.042	-0.20($\pm$0.09)	0.88($\pm$0.080)	307.00
WASP-63 b	0.380($\pm$0.030)	0.057	0.08($\pm$0.07)	1.32($\pm$0.050)	330.00
WASP-8 b	2.244($\pm$0.086)	0.080	0.17($\pm$0.07)	1.03($\pm$0.050)	87.00
WASP-95 b	1.130($\pm$0.070)	0.034	0.14($\pm$0.16)	1.11($\pm$0.090)	-
WASP-96 b	0.480($\pm$0.030)	0.045	0.14($\pm$0.19)	1.06($\pm$0.090)	-
WASP-97 b	1.320($\pm$0.050)	0.033	0.23($\pm$0.11)	1.12($\pm$0.060)	-
WASP-98 b	0.830($\pm$0.070)	0.036	-0.6($\pm$0.19)	0.69($\pm$0.060)	-
XO-5 b	1.077($\pm$0.037)	0.048	0.18($\pm$0.03)	0.88($\pm$0.030)	-

Table 4 Continue...

Name	M_p (M_J)	a (AU)	[Fe/H] dex	$M_\star$ ($M_\odot$)	Distance pc
Kepler-66 b	0.310(±0.070)	0.135	0.01(±0.003)	1.03(±0.051)	1107.00
Kepler-67 b	0.310(±0.060)	0.117	0.01(±0.003)	0.86(±0.043)	1107.00
Kepler-75 b	9.900(±0.500)	0.080	-0.07(±0.15)	0.88(±0.060)	1140.00
Kepler-77 b	0.430(±0.032)	0.045	0.20(±0.05)	0.95(±0.040)	570.00
Kepler-78 b	0.005(±0.001)	0.010	-0.14(±0.08)	0.81(±0.050)	-
KOI-192 b	0.290(±0.090)	0.091	-0.19(±0.07)	0.96(±0.060)	1100.00
KOI-195 b	0.340(±0.080)	0.041	-0.21(±0.08)	0.91(±0.060)	880.00
mu Ara b	1.676(±0.167)	1.500	0.28(±0.04)	1.08(±0.050)	15.30
mu Ara c	0.033(±0.003)	0.090	0.28(±0.04)	1.08(±0.050)	15.30
mu Ara d	0.521(±0.052)	0.921	0.28(±0.04)	1.08(±0.050)	15.30
mu Ara e	1.814(±0.181)	5.235	0.28(±0.04)	1.08(±0.050)	15.30
TrES-2	1.253(±0.052)	0.035	-0.15(±0.10)	0.98(±0.062)	220.00
TrES-3	1.910(±0.065)	0.022	-0.19(±0.08)	0.92(±0.040)	-
WASP-104 b	1.272(±0.047)	0.029	0.32(±0.09)	1.02(±0.090)	143.00
WASP-110 b	0.515(±0.064)	0.045	-0.06(±0.10)	0.89(±0.072)	320.00
WASP-112 b	0.880(±0.120)	0.038	-0.64(±0.15)	0.80(±0.073)	450.00
WASP-12 b	1.404(±0.099)	0.022	0.30(±0.10)	1.35(±0.140)	427.00
WASP-16 b	0.855(±0.059)	0.042	0.01(±0.10)	1.02(±0.101)	-
WASP-19 b	1.114(±0.040)	0.016	0.02(±0.09)	0.90(±0.045)	-
WASP-21 b	0.300(±0.010)	0.052	-0.40(±0.10)	1.01(±0.025)	230.00
WASP-25 b	0.580(±0.040)	0.047	-0.05(±0.10)	1.00(±0.030)	169.00
WASP-26 b	1.028(±0.021)	0.039	-0.02(0.09)	1.12(±0.030)	250.00
WASP-32 b	3.600(±0.070)	0.039	-0.13(±0.10)	1.10(±0.030)	-
WASP-34 b	0.590(±0.010)	0.052	-0.02(±0.10)	1.01(±0.070)	120.00
WASP-36 b	2.279(±0.068)	0.026	-0.31(±0.12)	1.02(±0.032)	450.00
WASP-37 b	1.800(±0.170)	0.043	-0.40(±0.12)	0.84(±0.040)	338.00
WASP-39 b	0.280(±0.030)	0.048	-0.12(±0.10)	0.93(±0.030)	230.00
WASP-4 b	1.237(±0.060)	0.023	-0.03(±0.09)	0.93(±0.050)	300.00
WASP-41 b	0.920(±0.070)	0.040	-0.08(±0.09)	0.95(±0.090)	180.00
WASP-44 b	0.889(±0.062)	0.034	0.06(±0.10)	0.95(±0.034)	-
WASP-46 b	2.101(±0.073)	0.024	-0.37(±0.13)	0.95(±0.034)	-
WASP-47 b	1.140(±0.050)	0.052	0.18(±0.07)	1.08(±0.370)	200.00
WASP-5 b	1.637(±0.082)	0.027	0.09(±0.09)	1.00(±0.060)	297.00
WASP-50 b	1.437(±0.068)	0.029	-0.12(±0.08)	0.86(±0.057)	230.00
WASP-58 b	0.890(±0.070)	0.056	-0.45(±0.09)	0.94(±0.100)	300.00
WASP-6 b	0.503(±0.028)	0.042	-0.20(±0.09)	0.88(±0.080)	307.00
WASP-63 b	0.380(±0.030)	0.057	0.08(±0.07)	1.32(±0.050)	330.00
WASP-8 b	2.244(±0.086)	0.080	0.17(±0.07)	1.03(±0.050)	87.00
WASP-95 b	1.130(±0.070)	0.034	0.14(±0.16)	1.11(±0.090)	-
WASP-96 b	0.480(±0.030)	0.045	0.14(±0.19)	1.06(±0.090)	-
WASP-97 b	1.320(±0.050)	0.033	0.23(±0.11)	1.12(±0.060)	-
WASP-98 b	0.830(±0.070)	0.036	-0.6(±0.19)	0.69(±0.060)	-
XO-5 b	1.077(±0.037)	0.048	0.18(±0.03)	0.88(±0.030)	-

Table 5 Stellar mass versus metallicity

Different laws	All systems					Multiplanetary systems					Single planetary systems				
	C1	$\lvert\frac{\delta C1}{C1}\rvert$	C2	$\lvert\frac{\delta C2}{C2}\rvert$	χ^2	C1	$\lvert\frac{\delta C1}{C1}\rvert$	C2	$\lvert\frac{\delta C2}{C2}\rvert$	χ^2	C1	$\lvert\frac{\delta C1}{C1}\rvert$	C2	$\lvert\frac{\delta C2}{C2}\rvert$	χ^2
linear-linear	0.855	0.018	0.147	0.081	10.100	0.801	0.014	0.161	0.136	1.35	0.858	0.025	0.156	0.108	1.693
linear-log	1.021	0.005	0.377	0.066	7.831	0.995	0.022	0.396	0.242	0.50	1.036	0.007	0.370	0.083	14.878
log-log	0.007	0.857	0.165	0.157	1.376	-0.003	7.333	0.173	0.578	0.10	0.014	0.571	0.159	0.201	2.806

Table 6 Physical Characteristics of Exoplanets and Their Host Stars Used In Analysis of Chapter 7.

Name	M_p (M$_J$)	$M_\star$ (M$_\odot$)	Spectral Type	$\log(R_{HK})$	$T_\star$ (Gyrs)
47 Uma b	2.530($\pm$0.060)	1.03($\pm$0.05)	G0V	-5.024	7.40($\pm$1.90)
47 Uma c	0.540($\pm$0.073)	1.03($\pm$0.05)	G0V	-5.024	7.40($\pm$1.90)
47 Uma d	1.640($\pm$0.480)	1.03($\pm$0.05)	G0V	-5.024	7.40($\pm$1.90)
51 Peg b	0.470($\pm$0.067)	1.11($\pm$0.06)	G2IV	-5.079	4.00($\pm$2.50)
70 Vir b	6.600($\pm$-)	0.92($\pm$-)	G4V	-4.986	7.09($\pm$-)
BD-10 3166 b	0.460($\pm$-)	0.99($\pm$-)	G4V	-4.907	4.18($\pm$-)
HAT-P-1 b	0.525($\pm$0.019)	1.15($\pm$0.05)	GOV	-5.030	3.6($\pm$-)
HAT-P-25 b	0.567($\pm$-)	1.01($\pm$0.03)	G5	-4.990	3.20($\pm$2.30)
HAT-P-38 b	0.267($\pm$0.020)	0.88($\pm$0.04)	G	-5.124	10.10($\pm$4.80)
HD 10697 b	6.830($\pm$0.984)	1.15($\pm$0.03)	G5IV	-5.082	6.90($\pm$0.60)
HD 108874 b	1.360($\pm$0.130)	1.00($\pm$-)	G5	-5.081	7.26($\pm$-)
HD 108874 c	1.018($\pm$0.300)	1.00($\pm$-)	G5	-5.081	7.26($\pm$-)
HD 114729 b	0.840($\pm$-)	0.93($\pm$-)	G3V	-5.066	4.58($\pm$-)
HD 11506 b	3.440($\pm$0.470)	1.19($\pm$0.10)	G0V	-4.990	5.40($\pm$1.60)
HD 11506 c	0.820($\pm$0.500)	1.19($\pm$0.10)	G0V	-4.980	5.40($\pm$1.60)
HD 117207 b	2.060($\pm$-)	1.07($\pm$-)	G8VI/V	-5.063	6.68($\pm$2.20)
HD 117618 b	0.178($\pm$0.020)	1.05($\pm$-)	G2V	-4.907	3.88($\pm$-)
HD 11964 b	0.622($\pm$0.056)	1.12($\pm$-)	G5	-5.160	9.56($\pm$-)
HD 11964 c	0.079($\pm$0.010)	1.12($\pm$-)	G5	-5.160	9.56($\pm$-)
HD 125612 b	3.000($\pm$-)	1.10($\pm$0.07)	G3V	-4.850	2.10($\pm$-)
HD 125612 c	0.058($\pm$-)	1.10($\pm$0.07)	G3V	-4.850	2.10($\pm$-)
HD 125612 d	7.200($\pm$-)	1.10($\pm$0.07)	G3V	-4.850	2.10($\pm$-)
HD 12661 b	2.300($\pm$-)	1.07($\pm$-)	G6V	-5.079	7.05($\pm$-)
HD 12661 c	1.570($\pm$-)	1.07($\pm$-)	G6V	-5.079	7.05($\pm$-)
HD 134987 b	1.590($\pm$0.020)	1.07($\pm$0.08)	G5V	-5.093	9.70($\pm$3.70)
HD 134987 c	0.820($\pm$0.030)	1.07($\pm$0.08)	G5V	-5.093	9.70($\pm$3.70)
HD 136418 b	2.000($\pm$0.100)	1.33($\pm$0.09)	G5	-5.190	4.00($\pm$1.00)
HD 13931 b	1.880($\pm$0.150)	1.02($\pm$0.02)	G0	-4.990	8.40($\pm$2.00)
HD 141937 b	9.700($\pm$-)	1.10($\pm$-)	G2/G3V	-4.935	2.55($\pm$-)
HD 142 b	1.250($\pm$0.150)	1.10($\pm$-)	G1IV	-4.920	5.93($\pm$-)
HD 142 c	5.300($\pm$0.700)	1.10($\pm$-)	G1IV	-4.920	5.93($\pm$-)
HD 142415 b	1.620($\pm$-)	1.09($\pm$-)	G1V	-4.665	1.49($\pm$-)
HD 145377 b	5.760($\pm$0.100)	1.12($\pm$0.03)	G3V	-4.620	1.30($\pm$1.00)
HD 1461 b	0.020($\pm$0.002)	1.02($\pm$-)	G0V	-5.020	6.30($\pm$-)
HD 1461 c	0.017($\pm$0.002)	1.02($\pm$-)	G0V	-5.020	6.30($\pm$-)
HD 147513 b	1.210($\pm$-)	0.92($\pm$-)	G3/G5V	-4.520	0.65($\pm$-)
HD 16141 b	0.215($\pm$0.030)	1.01($\pm$-)	G5IV	-5.108	7.76($\pm$-)
HD 16175 b	4.770($\pm$0.370)	1.35($\pm$0.09)	G0	-5.130	5.30($\pm$1.00)
HD 163607 b	0.770($\pm$0.040)	1.09($\pm$0.02)	G5IV	-5.010	8.60($\pm$6.00)
HD 163607 c	2.290($\pm$0.160)	1.09($\pm$0.02)	G5IV	-5.010	8.60($\pm$6.00)
HD 164509 b	0.480($\pm$0.090)	1.13($\pm$0.02)	G5V	-4.880	1.10($\pm$1.00)
HD 164922 b	0.338($\pm$0.015)	0.87($\pm$0.01)	G9V	-5.047	13.40($\pm$-)
HD 164922 c	0.040($\pm$0.005)	0.87($\pm$0.01)	G9V	-5.047	13.40($\pm$-)
HD 168443 b	7.659($\pm$0.097)	0.99($\pm$0.01)	G5	-5.088	9.80($\pm$1.00)

Table 6 Continue...

Name	M_p (M$_J$)	a (AU)	$M_\star$ (M$_\odot$)	Spectral Type	$T_\star$ (Gyrs)
HD 168746 b	0.230($\pm$-)	0.88($\pm$0.01)	G5	-5.045	3.75($\pm$-)
HD 170469 b	0.670($\pm$-)	1.14($\pm$0.02)	G5IV	-5.060	6.70($\pm$1.10)
HD 171028 b	1.980($\pm$-)	0.99($\pm$0.08)	G0	-4.920	8.00($\pm$2.00)
HD 17156 b	3.195($\pm$0.033)	1.27($\pm$0.02)	G0	-5.040	3.38($\pm$0.47)
HD 183263 b	3.670($\pm$0.300)	1.17($\pm$-)	G2IV	-5.108	8.10($\pm$-)
HD 183263 c	3.820($\pm$0.590)	1.17($\pm$-)	G2IV	-5.108	8.10($\pm$-)
HD 185269 b	0.940($\pm$-)	1.28($\pm$0.10)	G0IV	-4.500	4.20($\pm$-)
HD 187123 b	0.520($\pm$0.040)	1.06($\pm$-)	G5	-5.034	5.33($\pm$-)
HD 187123 c	1.990($\pm$0.250)	1.06($\pm$-)	G5	-5.034	5.33($\pm$-)
HD 188015 b	1.260($\pm$-)	1.09($\pm$-)	G5IV	-5.048	6.20($\pm$2.32)
HD 190360 b	1.495($\pm$0.150)	1.04($\pm$-)	G6IV	-5.093	12.11($\pm$-)
HD 190360 c	0.063($\pm$0.009)	1.04($\pm$-)	G6IV	-5.093	12.11($\pm$-)
HD 195019 b	3.700($\pm$0.300)	1.06($\pm$-)	G3IV-V	-5.085	5.33($\pm$)
HD 196050 b	2.830($\pm$-)	1.17($\pm$-)	G3V	-5.040	3.17($\pm$-)
HD 2039 b	6.110($\pm$0.820)	0.98($\pm$0.05)	G2/G3IV-V	-4.910	5.28($\pm$-)
HD 207832 b	0.560($\pm$0.030)	0.94($\pm$0.10)	G5V	-4.620	4.50($\pm$4.50)
HD 207832 c	0.730($\pm$0.050)	0.94($\pm$0.10)	G5V	-4.620	4.50($\pm$4.50)
HD 20794 b	0.008($\pm$0.001)	0.85($\pm$0.04)	G8V	-4.976	14.00($\pm$5.00)
HD 20794 c	0.007($\pm$0.001)	0.85($\pm$0.04)	G8V	-4.976	14.00($\pm$5.00)
HD 20794 d	0.015($\pm$0.002)	0.85($\pm$0.04)	G8V	-4.976	14.00($\pm$5.00)
HD 208487 b	0.413($\pm$0.050)	1.30($\pm$-)	G2V	-4.911	3.88($\pm$-)
HD 209458 b	0.690($\pm$0.017)	1.14($\pm$0.02)	G0V	-5.014	4.00($\pm$2.00)
HD 210277 b	1.230($\pm$0.030)	1.09($\pm$-)	G0	-5.055	6.93($\pm$-)
HD 212771 b	2.300($\pm$0.400)	1.15($\pm$0.08)	G8IV	-5.090	6.00($\pm$2.00)
HD 213240 b	4.500($\pm$-)	1.22($\pm$-)	G4IV	-5.013	5.11($\pm$-)
HD 216437 b	1.820($\pm$-)	1.06($\pm$-)	G4IV-V	-5.010	12.960($\pm$-)
HD 217107 b	1.330($\pm$0.050)	1.02($\pm$-)	G8IV	-5.082	7.32($\pm$-)
HD 217107 c	2.490($\pm$0.250)	1.02($\pm$-)	G8IV	-5.082	7.32($\pm$-)
HD 219828 b	0.066($\pm$0.004)	1.24($\pm$-)	G0IV	-5.040	5.80($\pm$1.20)
HD 222155 b	1.900($\pm$0.530)	1.13($\pm$0.11)	G2V	-5.060	8.20($\pm$0.70)
HD 222582 b	7.750($\pm$0.650)	0.99($\pm$-)	G5	-5.008	6.16($\pm$-)
HD 224693 b	0.710($\pm$-)	1.33($\pm$0.10)	G2IV	-5.150	2.00($\pm$0.50)
HD 30177 b	8.070($\pm$0.120)	1.05($\pm$0.08)	G8V	-5.070	11.60($\pm$2.20)
HD 30177 c	3.000($\pm$0.3000)	1.05($\pm$0.08)	G8V	-5.070	11.60($\pm$2.20)
HD 33283 b	0.330($\pm$-)	1.24($\pm$0.10)	G3V	-5.600	3.20($\pm$2.30)
HD 34445 b	0.790($\pm$0.070)	1.07($\pm$0.02)	G0	-5.070	8.50($\pm$2.00)
HD 37124 b	0.675($\pm$0.017)	0.83($\pm$-)	G4V	-4.900	3.33($\pm$-)
HD 37124 c	0.652($\pm$0.052)	0.83($\pm$-)	G4V	-4.900	3.33($\pm$-)
HD 37124 d	0.696($\pm$0.059)	0.83($\pm$-)	G4V	-4.900	3.33($\pm$-)
HD 38529 b	0.930($\pm$0.110)	1.48($\pm$0.05)	G4IV	-4.964	3.28($\pm$0.30)
HD 39091 b	10.300($\pm$-)	1.10($\pm$-)	G1IV	-4.978	3.83($\pm$-)
HD 4203 b	1.820($\pm$0.050)	1.13($\pm$-)	G5	-5.178	9.41($\pm$-)
HD 4203 c	2.170($\pm$0.520)	1.13($\pm$-)	G5	-5.178	9.41($\pm$-)
HD 4208 b	0.804($\pm$0.073)	0.87($\pm$-)	G5V	-4.945	4.47($\pm$-)
HD 45350 b	1.790($\pm$0.140)	1.02($\pm$-)	G5IV	-5.099	5.59($\pm$-)
HD 49674 b	0.100($\pm$-)	1.07($\pm$-)	G5V	-4.801	2.38($\pm$-)

Table 6 Continue...

Name	M_p (M$_J$)	a (AU)	$M_\star$ (M$_\odot$)	Spectral Type	$T_\star$ (Gyrs)
HD 50499 b	1.710($\pm$0.200)	1.27($\pm$-)	GIV	-5.029	6.00($\pm$-)
HD 52265 b	1.050($\pm$0.030)	1.20($\pm$-)	G0V	-5.037	4.88($\pm$-)
HD 52265 c	0.350($\pm$0.090)	1.20($\pm$-)	G0V	-5.037	4.88($\pm$-)
HD 6434 b	0.390($\pm$-)	0.79($\pm$-)	G3IV	-4.895	3.80($\pm$-)
HD 68988 b	1.860($\pm$0.160)	1.20($\pm$-)	G0	-5.035	6.78($\pm$-)
HD 70642 b	2.000($\pm$-)	1.00($\pm$0.05)	G5IV-V	-4.900	3.88($\pm$-)
HD 72659 b	3.150($\pm$0.140)	0.95($\pm$2.00)	G2V	-5.024	6.50($\pm$1.50)
HD 74156 b	1.778($\pm$0.020)	1.24($\pm$0.04)	G1V	-5.090	3.70($\pm$0.40)
HD 74156 c	7.997($\pm$0.095)	1.24($\pm$0.04)	G1V	-5.090	3.70($\pm$0.40)
HD 75289 b	0.470($\pm$-)	1.05($\pm$-)	G0V	-5.011	4.96($\pm$-)
HD 75898 b	2.510($\pm$-)	1.28($\pm$0.13)	G0	-5.020	3.80($\pm$0.80)
HD 80606 b	3.940($\pm$0.110)	0.98($\pm$0.10)	G5	-5.088	7.63($\pm$-)
HD 81040 b	6.860($\pm$0.710)	0.96($\pm$0.04)	G2/G3	-4.480	4.18($\pm$-)
HD 82943 d	0.290($\pm$0.031)	1.18($\pm$)	G0	-4.917	3.08($\pm$-)
HD 88133 b	0.300($\pm$-)	1.20($\pm$0.20)	G5IV	-5.160	9.56($\pm$-)
HD 89307 b	2.000($\pm$0.400)	1.02($\pm$0.04)	G0V	-4.962	6.76($\pm$-)
HD 92788 c	0.900($\pm$0.300)	1.13($\pm$-)	G5	-5.052	3.78($\pm$-)
HD 96167 b	0.680($\pm$0.180)	1.31($\pm$0.09)	G5D	-5.210	3.80($\pm$1.00)
Kepler-17 b	2.450($\pm$0.014)	1.16($\pm$0.06)	G2V	-4.470	1.78($\pm$-)
Kepler-20 b	0.030($\pm$0.004)	0.912($\pm$0.035)	G8	-4.930	8.80($\pm$2.70)
Kepler-20 c	0.040($\pm$0.007)	0.912($\pm$0.035)	G8	-4.930	8.80($\pm$2.70)
Kepler-20 d	0.031($\pm$0.011)	0.912($\pm$0.035)	G8	-4.930	8.80($\pm$2.70)
Kepler-20 e	0.009($\pm$-)	0.91($\pm$0.03)	G8	-4.930	8.80($\pm$2.70)
Kepler-20 f	0.045($\pm$-)	0.91($\pm$0.03)	G8	-4.930	8.80($\pm$2.70)
Kepler-20 g	0.062($\pm$0.011)	0.91($\pm$0.03)	G8	-4.930	8.80($\pm$2.70)
mu Ara b	1.676($\pm$-)	1.08($\pm$0.05)	G3IV-V	-5.016	6.41($\pm$-)
mu Ara c	0.033($\pm$-)	1.08($\pm$0.05)	G3IV-V	-5.016	6.41($\pm$-)
mu Ara d	0.521($\pm$-)	1.08($\pm$0.05)	G3IV-V	-5.016	6.41($\pm$)
mu Ara e	1.814($\pm$)	1.08($\pm$0.05)	G3IV-V	-5.016	6.41($\pm$)
WASP-58 b	0.890($\pm$0.070)	0.94($\pm$0.10)	G2V	-4.400	3.20($\pm$4.50)